

DISSERTATION

# Ultrafast Magneto-Optical Studies of Remagnetisation Dynamics in Transition Metals

LISA WILLIG

Submitted in fulfilment of the requirements for the degree of  
*doctor rerum naturalium* (Dr. rer. nat.)

In the scientific discipline *experimental physics*

Supervisor: Prof. Dr. Matias Bargheer  
Second Assessor: Prof. Dr. Bert Koopmans  
Third Assessor: Prof. Dr. Stéphane Mangin

University of Potsdam  
Faculty of Science  
Institute of Physics and Astronomy  
May 2019

*The left hand side of the coverpage shows an enhanced image of magnetic domains of YIG measured with MOKE microscopy. ©Lisa Willig*

*„The unanswered mystery is what stays with us the longest,  
and it's what we'll remember in the end.“*

Alan Wake



# Abstract

Ultrafast magnetisation dynamics have been investigated intensely for two decades. The recovery process after demagnetisation, however, was rarely discussed. The focus of this work lies on the investigation of the magnetisation on long timescales after laser excitation. It combines two ultrafast time resolved methods to study the relaxation of the magnetic and lattice system after excitation with a high fluence ultrashort laser pulse.

The magnetic system is investigated by time resolved measurements of the magneto-optical Kerr effect. The experimental setup has been implemented in the scope of this work. The lattice dynamics were obtained with ultrafast X-ray diffraction. The combination of both techniques leads to a better understanding of the mechanisms involved in magnetisation recovery from a non-equilibrium condition.

Three different groups of samples are investigated in this work: Thin Nickel layers capped with non-magnetic materials, a continuous sample of the ordered L10 phase of Iron Platinum and a sample consisting of Iron Platinum nano particles embedded in a carbon matrix. The study of the remagnetisation reveals a general trend for all of the samples: The remagnetisation process can be described by two time dependences. A first exponential recovery that slows down with an increasing amount of energy absorbed in the system until an approximately linear time dependence is observed. This is followed by a second exponential recovery. In case of low fluence excitation the first recovery is faster than the second. With increasing fluence the first recovery is slowed down and can be described as linear function. If the pump-induced temperature increase in the sample is sufficiently high, a phase transition to a paramagnetic state is observed. In the remagnetisation process the transition into the ferromagnetic state is characterised by a distinct transition between the linear and exponential recovery.

From the combination of the transient lattice temperature  $T_p(t)$  obtained from ultrafast X-ray measurements and magnetisation  $M(t)$  gained from magneto-optical measurements we construct the transient magnetisation versus temperature relations  $M(T_p)$ . If the lattice temperature remains below the Curie temperature the remagnetisation curve  $M(T_p)$  is linear and stays below the  $M(T)$  curve in equilibrium in the continuous transition metal layers. When the sample is heated above phase transition, the remagnetisation converges towards the static temperature dependence. For the granular Iron Platinum sample the  $M(T_p)$  curves for different fluences coincide, i.e. the remagnetisation follows a similar path irrespective of the initial laser-induced temperature jump.



# Kurzfassung

Ultraschnelle Magnetisierungsdynamiken wurden in den letzten zwei Jahrzehnten intensiv untersucht. Hingegen der Wiederherstellungsprozess der Magnetisierung nach einer ultraschnellen Demagnetisierung wird selten thematisiert. Der Fokus dieser Arbeit liegt auf der Untersuchung der Magnetisierung auf langen Zeitskalen nach der Anregung durch einen Laserpuls. Dazu werden zwei ultraschnelle zeitaufgelöste Techniken verwendet, um die Relaxierung von dem magnetischen System und dem System des Gitters nach Anregung mit einem hochenergetischen ultrakurzen Laserpuls zu untersuchen.

Das magnetische System wurde untersucht mithilfe von Messungen des zeitaufgelösten magneto-optischen Kerr Effekts. Der experimentelle Aufbau wurde im Rahmen dieser Arbeit entwickelt. Die Gitterdynamik wurde mittels ultraschneller Röntgendiffraktometrie aufgenommen. Die Kombination beider Techniken liefert ein besseres Verständnis von den Prozessen involviert in Magnetisierungsrelaxation aus einem Nicht-Gleichgewichtszustand.

Drei unterschiedliche Probensysteme wurden im Rahmen dieser Arbeit untersucht: Dünne Nickel Schichten umgeben von nicht-magnetischen Schichten, eine kontinuierliche Schicht aus einer Eisen Platin Legierung und eine Probe bestehend aus Eisen Platin Nanopartikeln eingebettet in einer Kohlenstoffmatrix. Die Studie der Remagnetisierung zeigt einen generellen Trend für alle diese Systeme auf: Der Remagnetisierungsprozess kann mit zwei Zeitabhängigkeiten beschrieben werden. Eine erste exponentielle Zeitabhängigkeit, die mit zunehmender Menge an absorbiertener Energie verlangsamt wird bis ein lineares Verhalten beobachtet wird. Darauf folgend gibt es eine zweite exponentielle funktionale Abhängigkeit in der Zeit. Im Falle einer geringen Energieabsorption ist die erste Remagnetisierung schneller als die zweite. Mit steigender Fluenz wird die Remagnetisierung in der ersten Zeitabhängigkeit verlangsamt und kann als lineare Funktion beschrieben werden. Wenn der durch den Pump Puls induzierte Temperatursprung in der Probe ausreichend groß ist, wird ein Phasenübergang in die paramagnetische Phase beobachtet. In dem Remagnetisierungsprozess wird dieser Übergang durch einen deutlich sichtbaren Wechsel zwischen linearem und exponentiellen Verhalten sichtbar.

Mithilfe der Kombination aus der von Röntgendaten gewonnener Gittertemperatur  $T_p(t)$  und der Magnetisierung  $M(t)$  erhalten wir die zeitliche Abhängigkeit der Magnetisierung von der Gittertemperatur  $M(T_p)$ . Falls die Gittertemperatur unter der Curietemperatur bleibt, ist die Remagnetisierungskurve  $M(T_p)$  linear und bleibt unterhalb der statischen Gleichgewichtskurve  $M(T)$  für die kontinuierlichen Übergangsmetalle. Wenn die Probe über den Phasenübergang geheizt wird, nähert sich die Remagnetisierung der statischen Kurve an.

Die transiente Remagnetisierungskurven  $M(T_p)$  der granularen Eisen Platin Probe folgen immer einem der statischen Magnetisierungskurve ähnlichen Verlauf, unabhängig von dem laser-induzierten Temperatursprung.



## Abbreviations

2TM	two temperature model
3TM	three temperature model
AO-HDS	all-optical helicity-dependent switching
BBO	beta-barium borite
DAQ	data acquisition
DOS	density of states
FePt	Iron Platinum
GdFeCo	Gadolinium Iron Cobalt
HAMR	heat assisted magnetic recording
MOKE	magneto-optical Kerr effect
PXS	plasma X-ray source
SHG	second harmonic generation
SLAC	Stanford Linear Accelerator Center
SQUID	superconducting quantum interference device
UXRD	ultrafast X-ray diffraction
VSM	vibrating sample geometry
XCD	X-ray circular dichroism
XMCD	X-ray magnetic circular dichroism
XRD	X-ray diffraction
YIG	Yttrium Iron Garnett



## List of Figures

2.1	Magnetic field units at a thin metal film.....	5
2.2	Spectroscopic picture for magneto-optical transitions.....	7
2.3	Effects on linear polarized light induced by a magnetic material.....	10
2.4	Theoretical MOKE spectra for Nickel and FePt.....	11
2.5	Density of states for Nickel and Iron, Stoner criterion calculation.....	12
3.1	Visualization of the three temperature model (3TM), hot electron thermalization .....	17
3.2	Specific heat capacity for Nickel.....	17
3.3	Timescales of magnetisation interaction and dynamics.....	18
3.4	Ultrafast demagnetisation of Nickel.....	19
4.1	Optical pump probe MOKE setup.....	23
4.2	Schematic magnetisation direction of the magnetic layer determined by external magnetic field .....	24
4.3	Technical MOKE signal generation .....	27
4.4	Software user interface .....	28
4.5	Software flowchart.....	29
4.6	Sample environment with pump and probe pulse incidence.....	30
4.7	Electronical Kerr signal $I_{\text{electronic Kerr}}$ of rotating molecules.....	31
4.8	Back Reflection visible in MOKE demagnetisation .....	32
5.1	Schematic sample structure of the investigated FePt samples .....	35
5.2	Static characterisation of FePt samples .....	35
5.3	SEM images of FePt samples .....	36
5.4	Absorption of the granular FePt film .....	36
5.5	Static and transient hysteresis measured before time zero of continuous FePt .....	37
5.6	Transient hysteresis of continuous FePt.....	38
5.7	Initial magnetisation after pump excitation of the continuous FePt film.....	39
5.8	Time resolved, fluence dependent hysteresis measurements of continuous FePt.....	40
5.9	Time resolved, fluence dependent hysteresis measurements of granular FePt.....	42
5.10	Transient reference hysteresis measured before time zero of granular FePt .....	43
5.11	Transient hysteresis of the granular FePt film.....	44
5.12	Major and minor hysteresis measurements on the continuous FePt film .....	45
5.13	Time resolved hysteresis of FePt granular measured at $F_{\text{inc}} = 8.5 \text{ mJ/cm}^2$ .....	45
5.14	Comparison of the time dependent evolution of hysteresis versus time resolved MOKE signal.....	46
5.15	Static heating effect on magnetisation after excitation .....	47
5.16	Fluence dependent time resolved MOKE measurements of continuous FePt at 0.3 T.....	48
5.17	Normalized fluence dependent time resolved MOKE measurements of continuous FePt at 0.75 T. ....	48
5.18	External field dependent time resolved MOKE measurements of continuous FePt at $F_{\text{inc}} = 7.0 \text{ mJ/cm}^2$ .....	49
5.19	External field dependent time resolved MOKE measurements of continuous FePt, at $F_{\text{inc}} = 3.0, 5.0 \text{ and } 9.0 \text{ mJ/cm}^2$ .....	50

5.20	Fluence dependent time resolved MOKE measurements of granular FePt at $B_{\text{ext}} = 0.75 \text{ T}$ ...	52
5.21	Fluence dependent time resolved MOKE measurements of granular FePt at $B_{\text{ext}} = 0.3 \text{ T}$ ...	52
5.22	External field dependent time resolved MOKE measurements of granular FePt at $F_{\text{inc}} = 5.2 \text{ mJ/cm}^2$ .....	53
5.23	External field dependent time resolved MOKE measurements of granular FePt at $F_{\text{inc}} = 10.0 \text{ mJ/cm}^2$ .....	53
5.24	Fluence dependent remagnetisation fits for continuous FePt at $B_{\text{ext}} = 0.3 \text{ T}$ .....	55
5.25	Fluence dependent remagnetisation fits for continuous FePt at $B_{\text{ext}} = 0.75 \text{ T}$ .....	55
5.26	Incident fluence dependence of remagnetisation time constants for Continuous FePt .....	56
5.27	External Field Dependent Remagnetisation Fits for Continuous FePt at $7.0 \text{ mJ/cm}^2$ .....	56
5.28	External Field Dependent Remagnetisation Fits for Continuous FePt at $F_{\text{inc}} = 9.0 \text{ mJ/cm}^2$ .....	57
5.29	External Field Dependent Remagnetisation Fits for Continuous FePt at $F_{\text{inc}} = 5.0 \text{ mJ/cm}^2$ .....	57
5.30	External field dependent remagnetisation fits for continuous FePt at $F_{\text{inc}} = 3.0 \text{ mJ/cm}^2$ .....	58
5.31	External field dependence of remagnetisation time constants for continuous FePt .....	58
5.32	Interception of the two remagnetisation time dependencies for continuous FePt .....	59
5.33	Fluence dependent remagnetisation fits for granular FePt at $B_{\text{ext}} = 0.3 \text{ T}$ .....	60
5.34	Fluence dependent remagnetisation fits for granular FePt at $B_{\text{ext}} = 0.75 \text{ T}$ .....	60
5.35	External field dependence of remagnetisation time constants for granular FePt.....	60
5.36	External field dependent remagnetisation fits for granular FePt at $F_{\text{inc}} = 5.2 \text{ mJ/cm}^2$ .....	61
5.37	External field dependent remagnetisation fits for granular FePt at $F_{\text{inc}} = 10.0 \text{ mJ/cm}^2$ .....	61
5.38	External field dependence of remagnetisation time constants for granular FePt.....	62
5.39	Interception of the two remagnetisation time dependencies for granular FePt .....	62
6.1	Schematic sample structure of the investigated AuNi samples .....	66
6.2	VSM Measurements for Nickel samples GN1 and GN2 .....	67
6.3	Time resolved MOKE measurements depending on fluence for three Nickel samples .....	70
6.4	Magneto-optical time resolved measurements and fits of Nickel sample GN1 .....	71
6.5	Magneto-optical time resolved measurements and fits of Nickel sample GN2 .....	72
6.6	Magneto-optical time resolved measurements and fits of Nickel sample GMN .....	72
6.7	Fit results for the remagnetisation slope and the time constant for Nickel samples.....	73
6.8	Interception time of the Nickel samples.....	73
7.1	X-ray diffraction measurements for the Nickel sample GN1 .....	76
7.2	Time resolved X-ray diffraction measurements of strain and calculated temperature and energy density for the Nickel sample GN1 .....	78
7.3	Schematic ultrafast X-ray diffraction (UXRD) and magneto-optical Kerr effect (MOKE) experimental measurement geometries .....	79
7.4	Concept for the combination of UXRD and MOKE measurement to calculate magnetisation dependence on the lattice temperature $T_p$ .....	81
7.5	Calculated $M(T_p)$ and statically obtained $M(T)$ for the Nickel sample GN2 .....	84
7.6	Calculated $M(T_p)$ and statically obtained $M(T)$ for the Nickel sample GN1 .....	86
7.7	Calculated $M(T_p)$ and statically obtained $M(T)$ for the FePt continuous film.....	88
7.8	Calculated $M(T_p)$ and statically obtained $M(T)$ for the FePt granular film depending on the thermal expansion coefficient $\alpha^{uf}$ .....	89
7.9	Calculated $M(T_p)$ and statically obtained $M(T)$ for the FePt granular film .....	90
7.10	UXRD and MOKE measurements for sample GN2 (Nickel).....	91
7.11	UXRD and MOKE measurements for sample GMN (Nickel) .....	92
7.12	UXRD and MOKE measurements for sample GN1 (Nickel).....	93
7.13	Summary figure for the Nickel sample GN1.....	97

7.14	Concept for correlation between fluence dependent transient hysteresis and switching particle fractions of the FePt granular film .....	99
7.15	Summary figure for the FePt continuous film .....	101
7.16	Summary figure for the FePt granular film .....	102
A.1	Hardware components of MOKE-setup .....	A-1
B.1	Pump beam profile of the MOKE setup .....	B-2
C.1	Screenshot of the MOKE application side panel. ....	C-1
C.2	Tabs of the main data window for switching between different measurements. ....	C-3
D.1	Electronic Kerr signal measured from the rotational alignment of molecules .....	D-1
E.1	Hysteresis Measurements of MgO and GN1 .....	E-1
E.2	Hysteresis Measurement for 5 nm and 50 nm Gold Films .....	E-1
F.1	Magnetisation precession animations. ....	F-1
F.2	Iron Platinum unit cell animations. ....	F-1



## List of Tables

2.1	Magnetic properties for the materials discussed in this thesis. $T_c$ is the Curie temperature, $B_{mf}$ represents the magnitude of mean Weiss field, and $M_s$ the saturation magnetisation reached at 4.2 K. ....	6
5.1	Sample structures and designations of FePt films discussed in this chapter. ....	34
6.1	Sample structures and designations of AuNi-Bilayers discussed in this chapter. ....	66
7.1	Thermal expansion coefficients after ultrafast excitation used for calculations of the lattice temperature $T_p$ in the following sections. ....	83
B.1	Fluence determination and comparison for UXRD and MOKE.....	B-1



# Contents

List of Figures	VII
List of Tables	XI
<b>1 Introduction</b>	<b>1</b>
<b>2 Magnetisation in Equilibrium Conditions</b>	<b>3</b>
2.1 Magnetic Energies	3
2.1.1 Exchange Interaction	4
2.1.2 Spin-Orbit Interaction	4
2.1.3 Zeeman Interaction	4
2.1.4 Demagnetization and Stray Fields	5
2.2 Weiss Mean-Field Theory	6
2.3 Magneto-Optical Effects	7
2.4 Ferromagnetism in Transition Metals	11
<b>3 Magnetisation Dynamics in Metals</b>	<b>13</b>
3.1 Timescales of Magnetisation Dynamics	13
3.2 Ultrafast Heating of a Magnetic Metal	15
3.3 Ultrafast Magnetisation Dynamics	18
<b>4 Experimental Setups</b>	<b>21</b>
4.1 Laser system	21
4.2 Optical Setup	21
4.3 Hysteresis Measurements	24
4.4 Time-Resolved MOKE Measurements	25
4.5 Data Acquisition	25
4.6 Software	28
4.7 Additional Kerr Signal Contributions	30
4.7.1 Molecules	30
4.7.2 Second Excitation	32
<b>5 Magnetisation Dynamics in Iron Platinum</b>	<b>33</b>
5.1 Motivation	34
5.2 Sample Characterization	34
5.3 Time-Resolved Hysteresis Measurements	36
5.3.1 Continuous FePt Film	37
5.3.2 Granular FePt Film	41
5.3.3 Minor Hysteresis Loops	44
5.4 Time-Resolved MOKE Measurements	45
5.4.1 Continuous Film	46
5.4.2 Granular Film	51
5.5 Timescales of the Remagnetisation Dynamics	54
5.5.1 Continuous Film	54

5.5.2 Granular Film .....	59
5.6 Summary .....	63
<b>6 Magnetisation Dynamics in Nickel-Gold Bilayers</b>	<b>65</b>
6.1 Motivation .....	65
6.2 Sample Characterization .....	66
6.3 Magneto-Optical Detection of Remagnetisation Dynamics .....	68
6.4 Summary .....	74
<b>7 Interpretation of Spin Dynamics</b>	<b>75</b>
7.1 Determination of the Lattice Temperature .....	75
7.1.1 Ultrafast X-ray Diffraction Measurements .....	75
7.1.2 Absorption Comparison .....	79
7.2 Dependence of the Magnetisation on the Transient Lattice Temperature .....	80
7.2.1 Expansion Coefficient $\alpha$ .....	82
7.2.2 Nickel GN2 .....	83
7.2.3 Nickel GN1 .....	85
7.2.4 FePt Continuous .....	87
7.2.5 FePt Granular .....	89
7.3 Comparison of Lattice and Spin Dynamics .....	90
7.4 Summary .....	94
7.4.1 Nickel .....	95
7.4.2 Iron Platinum .....	98
<b>8 Conclusion</b>	<b>103</b>
<b>Bibliography</b>	<b>105</b>
<b>Appendix</b>	
A Hardware Setup .....	A-1
B Fluence Determination .....	B-1
C Labware UDKM .....	C-1
D Molecule Excitation .....	D-1
E Hysteresis Measurements of Nickel, Gold and MgO .....	E-1
F Animations .....	F-1
<b>Acknowledgement</b>	<b>XV</b>
<b>Declaration of Authorship</b>	<b>XVII</b>

# 1 | Introduction

The phenomenon *magnetism* intrigues humans since ancient times [1]. But not only does it represent a puzzle in understanding the origin of its properties, it also can be exploited for numerous devices and technological modules. This started as a useful tool for navigating the oceans [2] and nowadays many everyday objects and daily routines depend on the functionality of magnetic data storage and processing as well as sensors. The main challenges faced by enhancing the current technology are dominated by the wish to make new devices smaller, faster and more energy efficient without the loss of stability. Not only is this development promoted by the understanding of the underlying concepts, but also by the ability to manufacture new alloys and nanoscale objects, introducing additional possibilities to manipulate magnetic and non-magnetic properties.

Besides the immense interest of the industry for the improvement and employments of magnetic material manipulation it raises countless scientific questions. Since the development of ultrafast laser sources and evolution in measurement techniques like pump probe spectroscopy it is possible to observe the behaviour of materials on very short timescales. This enables investigations of the interaction of different properties on an atomic level in non-equilibrium conditions. The comparison of dynamic non-equilibrium and static equilibrium conditions enriches the understanding of solid matter.

The first experiment showing the demagnetisation of a thin nickel film on a timescale shorter than a picosecond was published by Beaurepaire et al. in 1996 [3]. It sparked great interest and many experiments on magnetic materials investigating the origin of this fast phenomenon and also the search for the limits of ultrafast manipulation followed. Many of these experiments employ the measurement of magneto-optical effects as indicator for the processes in the magnetic system of a material. The non-equilibrium state of a material excited with an ultrafast laser pulse is often modelled with the definition of three subsystems: The three temperature model (3TM) assigns a temperature to the systems of electrons, lattice (phonons) and spins (magnetic systems). The dynamic response is determined by the interaction of all subsystems on the associated timescales. For this reason it is of immense value not only to observe the subsystems individually but in direct comparison to each other.

This work represents the basis for combining the measurements of magneto-optical signals as reference for the spin subsystem as well as ultrafast X-ray diffraction (UXRD) measurements as tool for investigating the lattice dynamics. As part of this work a new time resolved magneto-optical Kerr effect (MOKE) setup was developed and implemented. The magnetic systems investigated are several transition metal thin films. The first set of samples is formed by the ordered L10 phase of Iron Platinum (FePt), which exhibits promising qualities for the manufacturing of new hard drive storage techniques [4]. The samples are distinguished in their morphology: A thin continuous film is compared to an equally thin film consisting of nanoparticles surrounded by a carbon matrix. The second set of samples is a series of Nickel Gold bi- and trilayers. Such samples are of interest due to the interface interaction of a paramagnet and a ferromagnet during ultrafast excitation [5] or heat transport [6].

The temperatures increase in the sample during laser excitation can reach very high values on a short timescale. Electron temperatures of thousand Kelvin can be reached [7]. Nevertheless, despite those high temperatures of hot electrons it is not clear, if the lattice and spin systems can reach a significant temperature raise to full demagnetisation magnetic thin films. Some experimental results indicate a full demagnetisation [8, 9], while other findings imply a remaining threshold magnetisation, which does not decrease further even with increasing excitation density [10, 11]. Theoretical investigations predict a dependence on the magnetic layer thickness [12].

As part of the 3TM the lattice plays an important role in the energy distribution of the electrons and the temperature equilibration process. However, it is often neglected in measurements of the magnetic system and the analysis depends on uncertain quantities like the value of the phonon heat capacity. To understand the importance of the lattice and the connection between lattice temperature and spin dynamics the magneto-optical measurements of this thesis are compared to UXRD measurements performed at a table top plasma X-ray source (PXS). They allow an estimation of the lattice temperature by relating the lattice expansion with the thermal expansion coefficient. To pass the Curie temperature of the respective sample the measurements were performed under high incident fluence. The relation of time resolved MOKE and UXRD data is not only of interest for the demagnetisation on a short timescale, but also for investigating the remagnetisation on long timescales. A timescale of tens of picoseconds is typical for experiments focused on the magneto-optical response to ultrafast laser excitation. The recovery of magnetisation is rarely presented or discussed [13, 14].

This thesis will first introduce important key concepts and properties of static magnetisation in chapter 2 followed by an overview of ultrafast mechanisms and previous experiments and models in chapter 3. In chapter 4 the new time resolved MOKE setup is described, including hardware, software and an explanation of the evolution of the signal at the balanced photodiode to the resulting discussed transient MOKE trace. The following chapter 5 displays the MOKE measurements on Iron Platinum with a focus on the combination of transient hysteresis and time resolved MOKE traces. Another important aspect are the fits of the remagnetisation dynamics depending on the applied external magnetic field and the pump fluence. Chapter 6 presents the measurement results and fits for the Nickel samples. Static measurements of the temperature dependence of the magnetisation are also included to compare remagnetisation dynamics with static properties. Finally in chapter 7 the measurements regarding the lattice dynamics is compared with the magneto-optical measurements of both sample systems.

## 2 | Magnetisation in Equilibrium Conditions

The phenomenon of magnetism is recorded in human history since ancient times. The natural magnetised material Magnetite ( $\text{Fe}_3\text{O}_4$ ) enabled an access to the attractive force of magnets long before the correlation between electric wires and magnetic fields were investigated. The earliest mentioning is attributed to the Greek philosopher Thales of Miletus (634-546 BCE). He is now considered to be "the first Western scientist and philosopher" [15]. It is said that he got his Iron-attracting rock from a town named Magnesia, and therefore called it the "magnesian rock" [16]. This might indicate the origin of the word magnetism. But in the earlier times this material was called *lodstone* (also *loadstone*). In the philosophy of Thales everything that has the "capacity to produce movement" ([1] as cited in [15]) must have a soul. The soul of lodstone was also adopted by the Chinese literature, which called it *ci shi*, the loving stone because of its attraction to Iron. But despite the mysterious origin of its properties, it was used as direction pointer. The first known device was created in the time of the Qin dynasty, which lasted from 221-206 BCE). Starting from the 11th century, it was used as regular navigation compass on ships from the Chinese empire and later in the 12th century also in European fleets. [2]

Until 1819 the lodstone and its activating force on Iron was the only known form of magnetism. After that the investigation of electric currents and their connection of magnetism began with the main contributors of Hans Christian Oersted, Jean-Baptiste Biot, Felix Savart and André Marie Ampère. Also the connection of light waves and magnetic properties was developed, Mary Somerville published a paper in 1825 titled "The Magnetic Properties of the Violet Rays of the Solar Spectrum".

With the evolution of quantum physics, the property of the electron called spin emerged in the time of 1925-1928. It was first mentioned in the context of understanding atomic spectra.

This chapter will focus on the properties and energies defined today to describe the equilibrium condition of a magnetic system. Also it will discuss the origin of magneto-optical Kerr effect (MOKE), which is used to measure changes in the magnetic system. Chapter 3 will continue the historical overview of the field of ultrafast magnetism as well as describe the underlying concepts and theories.

Our understanding of solid state physics and magnetism has improved vastly since the time of the first compass devices, but the general state is not so different: magnetism is a fascinating field, which has a lot of unsolved mysteries and no coherent theory exists to describe the non-equilibrium behaviour, but nevertheless the technological devices make extensive use of those properties.

The descriptions of properties in this chapter are focused on cubic unit cells, as this is a good approximation for all the investigated 3d transition metals in this thesis. For the complex structures that can be found for example in the lanthanide elements the discussion needs to be adapted.

### 2.1 Magnetic Energies

The electron possesses both an intrinsic angular momentum *spin*  $s$  which is connected to an antiparallel *magnetic moment*  $\mu_B$ . The interaction of the electrons with each other according to several interaction mechanisms and energies defines the resulting magnetism of a material. The interaction of two magnetic dipoles separated by a distance of  $\mathbf{r}$  is too weak to explain any form of spontaneous magnetisation at room temperature [17], therefore other forms of interaction energies have to be the dominant ones. They are discussed in the following sections. This description follows the textbooks of Stöhr et al. [2], Blundell et al. [17], Coey et al. [18] and Gross et al. [19].

### 2.1.1 Exchange Interaction

While all materials have magnetic moments, either originating from electrons or nucleons, only some experience spontaneous magnetisation in the absence of an external magnetic field. The long-range order of electron spins is created by the exchange interaction. It is a consequence of the Coulomb interaction between neighbouring spins and the symmetrization postulate by Pauli. The combination of kinetic and Coulomb energies defines the resulting, favourable spin alignment for the material. It can be described in the Heisenberg model as exchange Hamiltonian:

$$\mathcal{H}_{ex} = - \sum_{i,j=1} J_{ij} S_i S_j \quad (2.1)$$

Here  $S_i$  and  $S_j$  are the spin operators and  $J_{ij}$  the exchange integral. This Hamiltonian is valid for neighbouring spins with distinct atomic positions. A parallel (ferromagnetic) order is favoured for a positive value of  $J_{ij}$ , an antiparallel (antiferromagnetic) order is energetically preferred when  $J_{ij}$  evaluates negative. The value of the exchange integral decreases rapidly for increasing distance between atoms. For this reason only the direct neighbour atoms are considered in calculations for materials with a cubic unit cell. The exchange interaction itself is isotropic in a cubic arrangement of spins and is responsible for the alignment of neighbouring spins, but the direction preferences occurring in a crystal arise from the spin-orbit interaction. [2, 17, 18, 20]

### 2.1.2 Spin-Orbit Interaction

The spin-orbit interaction couples the spin  $\mathbf{S}$  to the direction of the orbital angular momentum  $\mathbf{L}$ . This coupling favours the parallel alignment of the directions of  $\mathbf{S}$  and  $\mathbf{L}$ . This leads to the magneto-static energy:

$$\mathbf{E}_{so} = -m_S \cdot \mathbf{H}_{orb}. \quad (2.2)$$

The direction of  $\mathbf{L}$  is tied by the crystal field. Together with the exchange interaction which aligns spins relative to each other, this so-called *magneto-crystalline anisotropy* is the origin of the preferred direction for the magnetisation orientation in a crystal. The preferred orientation of the orbital  $\mathbf{L}$  is determined by the lattice potential. A reduction in symmetry at interfaces can therefore strongly change the direction of orbital alignment and consequently the spin direction. Additionally other changes in the crystal field potential alter the preferred magnetisation direction. The anisotropy consequently has a contribution from the shape of the sample, the *shape anisotropy*. For bulk materials the interface effects are insignificant, but for thin films or nano particles this is not the case. The magneto-crystalline anisotropy  $\mathbf{E}_{an}$  for a cubic system can be determined by equation 2.3, where the parameters  $K_{1,z}$  and  $K_{2,z}$  are material specific anisotropy constants,  $\alpha_i$  represents the magnetisation direction cosines [18, 20].

$$\mathbf{E}_{an} = K_{1,z}(\alpha_1^2\alpha_2^2 + \alpha_2^2\alpha_3^2 + \alpha_3^2\alpha_1^2) + K_{2,z}(\alpha_1^2\alpha_2^2\alpha_3^2) + \text{higher order} \quad (2.3)$$

Not only the shape and interface effects can influence the crystal field potential. This results in many contributions from other parameters to the anisotropy, like stress present in the crystal (*the stress-induced anisotropy*). Typically the interaction energy is around 10 to 100 times smaller than the exchange energy [2].

### 2.1.3 Zeeman Interaction

When an external magnetic field is applied it influences the orientation and energy of the magnetisation. If the external field is sufficiently large, it can dominate over the spin orbit coupling so that the magnetisation

is no longer aligned along the preferred crystal axis, but along the external field direction. Its energy is defined as

$$E_Z = -\mathbf{B}_{\text{ext}} \cdot \mathbf{M} \quad (2.4)$$

It also causes a splitting in the energy levels of the atom depending on the orbital momentum. The Hamiltonian for the Zeeman interaction of an magnetic moment inside a magnetic field  $\mathbf{H}$  is given by equation 2.5 [2]:

$$\mathcal{H}_Z = \frac{\mu_B}{\hbar} \mathbf{H} \cdot \mathbf{g}_s \quad (2.5)$$

If calculated for an external field of  $B_{\text{ext}} = 1 \text{ T}$ , a typical strength of interaction is in the order of  $E_Z \approx 0.1 \text{ meV}$ . Compared with the spin-orbit coupling energy  $E_{\text{so}}$  for cubic Sodium (Na) of  $2.1 \text{ meV}$  it is clear that the energy contribution of the Zeeman energy is smaller. [2]

#### 2.1.4 Demagnetization and Stray Fields

Figure 2.1 is a visualization of the magnetic units that are commonly used to describe the magnetism of a material. The grey block represents a thin magnetic film. It was magnetised such that the internal magnetisation is oriented perpendicular to the film surface. The magnetisation  $\mathbf{M}$  describes the magnetic moments in a material aligned in the direction of observation. The magnitude of  $\mathbf{M}$  represents a volume density of magnetic moments, and thereby it also determines the maximum magnetisation that can be reached in a specific material,  $M_s$ . It is only defined inside matter. The magnetic flux density  $\mathbf{B}$  determines the induced force on a moving particle by the magnetic field. The unit  $\mathbf{H}$  is the representation of the magnetic field strength. The magnetic flux  $\mathbf{B}$  follows the Maxwell equation  $\nabla \cdot \mathbf{B} = 0$ , postulating the non-existence of magnetic monopoles. This means that the number of flux lines going into matter are equal to the number of lines exiting the material.  $\mathbf{B}$  can be represented as a sum of the other two units, so that equation 2.6 also follows. [2, 19]

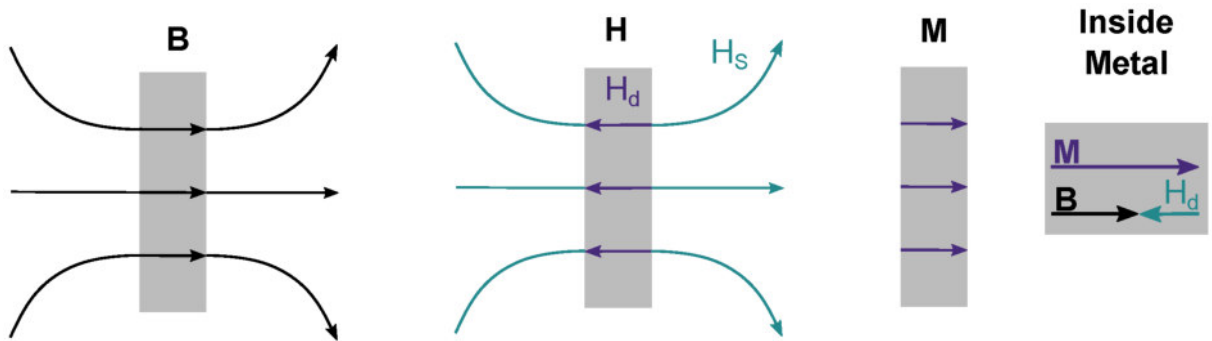


**Figure 2.1: Magnetic field units at a thin metal film.** This sketch shows the different units used to describe magnetism of a material on the example of a thin magnetic film (grey block).  $\mathbf{B}$  is the magnetic flux,  $\mathbf{H}$  the magnetic field strength and  $\mathbf{M}$  the magnetisation of a material.  $\mathbf{H}_s$  shows the stray field direction in relation to the corresponding demagnetisation field  $\mathbf{H}_d$ . Image after [2] and [19].

$$\nabla \cdot \mathbf{B} = \mu_0 \nabla \cdot (\mathbf{H} + \mathbf{M}) = 0 \quad (2.6)$$

Equation 2.6 is valid for matter. If there is no material,  $\mathbf{M}$  vanishes and  $\mathbf{B}$  and  $\mathbf{H}$  only differ by a constant.

Inside of the thin film, a demagnetisation field  $\mathbf{H}_d$  is created by the magnetic moments, see equation 2.7.

$$\mathbf{H}_d = \frac{1}{\mu_0} (\mathbf{B} - \mathbf{M}) \quad (2.7)$$

It is directed opposite to the magnetisation direction, it therefore weakens the integrity and stability of the magnetisation orientation. Additionally the magnetisation itself creates a stray field outside of the sample,  $H_s$  (equation 2.8). The demagnetisation field of a thin film is lowest, when the magnetisation is directed along the surface of the disk-like shape. It is maximized when the magnetisation is perpendicular to the surface, as shown in figure 2.1.

$$H_s = \frac{1}{\mu_0}(\mathbf{B}) \quad (2.8)$$

The stray field exhibits the same behaviour: It is largest in the perpendicular, and lowest in the parallel orientation. This is one of the challenges for the creation of hard drives, that are supposed to get smaller and smaller: The demagnetisation field is an undesired property, because it weakens the orientation of the domains representing a logical bit and increases the impact of thermal fluctuations, which means larger domains are needed to retain the information. On the other hand a strong and stable stray field is needed, to read out the information.

## 2.2 Weiss Mean-Field Theory

The phenomenological description of the exchange force driven by quantum physics is provided by the Weiss mean-field or molecular field theory. It was developed as the response to the observation that the dipole-dipole interaction could not be responsible for the spontaneous magnetisation above the small temperature range of few Kelvins, much less at room temperature. The theory was developed by Weiss in 1906 [21, 22], who postulated the existence of a magnetic field called *molecular field*,  $B_{mf}$ . This was developed into the theory of mean-fields, in which a virtual field is created by all electron spins. This virtual field also acts on all spins as contribution to the effective field, leading to a much higher stability against thermal fluctuations. This mean-field is able to describe the temperature dependence of the net magnetisation and the phase transition at the temperature called *Curie temperature*,  $T_c$ . Below that temperature, the long-range interatomic ordering is established. When the thermal energy  $k_B T$  is larger than the field energy  $\mu \mathbf{B}$  of a magnetic dipole in a magnetic field, the long range order is destroyed and a paramagnetic behaviour occurs. That means the spins are no longer coordinated regarding each other, but they will align along an external magnetic field. The amplitude of the necessary external field to reach the saturation value of magnetisation in the paramagnetic phase is several orders of magnitude larger than compared to a ferromagnet. In table 2.1 the properties for the elements investigated in this work are collected. [2, 18]

$$B_{mf} = \lambda \mathbf{M} \quad (2.9)$$

Element	$T_c$ [K]	$B_{mf}$ [T]	$M_s$ @4.2 K [T]
Fe (bcc)	1043	1553	2.199
Ni (fcc)	631	949	0.665

**Table 2.1:** Magnetic properties for the materials discussed in this thesis.  $T_c$  is the Curie temperature,  $B_{mf}$  represents the magnitude of mean Weiss field, and  $M_s$  the saturation magnetisation reached at 4.2 K.

The mean-field theory gives a good approximation to calculate the temperature behaviour of the magnetisation, but it neglects the influence of spin wave excitations at low temperatures and the critical fluctuations for high temperatures close to the Curie temperature. Therefore the calculated Curie point is generally overestimated. Also it determines the Curie temperature to be a distinct point with all long range order eliminated above the transition. In real ferromagnets, the transition is smoother with local order still intact above phase transition [23].

## 2.3 Magneto-Optical Effects

The measurement of magnetisation can be performed by many different experimental methods. Methods like the vibrating sample geometry (VSM) can obtain an absolute value of magnetisation. Other methods related to X-ray circular dichroism (XCD) can make estimations of absolute values by calculating the sum rules and are intended to be element specific [24]. But those methods are lacking the flexibility of all-optical setups. Magneto-optical measurements do not yield absolute values, but a relative change in magnetisation. The possibility to measure changes of magnetisation with time and spatial resolution allows for microscopic studies of magnetic domains, domain formation and domain wall propagation [25–27]. It is also possible to detect magnetisation dynamics on ultrafast timescales like precession, demagnetisation and magnetisation reversal. The investigation of the magneto-optical effects themselves as interaction between magnetic matter and light is also of high interest for improving understanding of fundamental questions [28].

The foundation for magneto-optical measurements was set in 1845, when Michael Faraday investigated the properties of transmitted light in glass samples. He observed a rotation of the polarization plane of the light when an external magnetic field was applied [29]. This effect is now called Faraday effect. In 1877 John Kerr published his results on the same observation for reflected light [30], introducing the effect known as MOKE. The discoveries of these effects were an important key point for the theory of electromagnetism created by Maxwell, as they sparked the interpretation of light as an electromagnetic entity [31].

In brief MOKE is a consequence of energy splitting for left and right hand circular polarized light absorption due to spin-orbit and exchange interaction. To understand the effect of magneto-optical change in

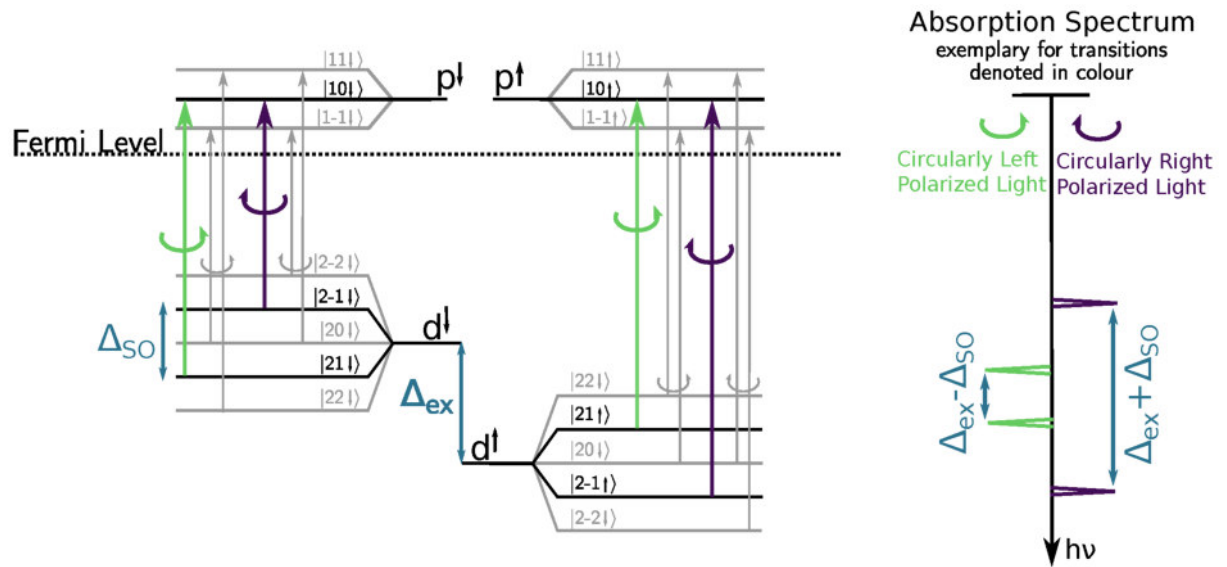


**Figure 2.2: Spectroscopic picture for magneto-optical transitions with distinct energies.** Energy levels on the left side demonstrate the splitting caused by exchange ( $\Delta_{ex}$ ) and spin orbit interaction ( $\Delta_{SO}$ ). This creates a different absorption spectrum for left (green) and right hand circular polarized light (purple), shown on the right hand side. The transition for an atom with a localised 3d electron is shown. Image after [32]

reflection, the microscopic electronic band structure of a material has too be considered. The reflection of light is determined by the allowed and excited optical transitions. The equations of Maxwell give the theoretical framework for calculations. A sketch of the microscopic structure of a theoretical transition metal is shown in figure 2.2 for the case of localised, sharp energy distribution. The allowed optical transitions have the initial state in the 3d band and the final state in the 4p orbital. The energy degeneration of the 3d band is lifted for the orbitals with opposite spin orientations, because the spin-orbit coupling energetically favours one orbital orientation above the other. That introduces the energy difference  $\Delta_{SO}$ .

In addition to the spin-orbit coupling another energy splitting for the different spin orientations originating from the exchange interaction,  $\Delta_{\text{ex}}$ , occurs. The arrows in figure 2.2 indicate all allowed optical transitions. The coloured transitions represent the difference for left (purple) and right hand circular polarized light (green) that are also considered in the absorption spectra on the right. The energy difference for these transitions is the microscopic origin of the MOKE signal, which therefore depends on both the exchange energy splitting and spin orbit interaction. If either of these is zero in this simple picture, the energy for left and right hand circular polarized light is equivalent. [31–33]

So the presence of both energy contributions cause the left and right hand circular light to be absorbed differently at each energy. This leads to a non-zero Kerr effect. The process is illustrated for well defined energy levels, but the concept is also applicable for the band structure of the delocalized 3d electrons in a real transition metal.

The phenomenological description of the interaction of light and magnetic matter starts with the Maxwell equations. The optical response of a layer can be described by both quantities equally: the optical susceptibility  $\underline{\chi}$ , which relates the induced change of polarization  $\mathbf{P}$  with the electric field  $\mathbf{E}$ , and the dielectric tensor  $\underline{\epsilon}$ . This correlates the dielectric displacement  $\mathbf{D}$  with the electric field  $\mathbf{E}$ . The electric displacement  $\mathbf{D}$  (equation 2.10) and the polarization  $\mathbf{P}$  (equation 2.11) follow from the material equations, with the relation between  $\underline{\chi}$  and  $\underline{\epsilon}$  given by equation 2.12.

$$\mathbf{D} = \underline{\epsilon} \mathbf{E} \quad (2.10)$$

$$\mathbf{P} = \underline{\chi} \mathbf{E} \quad (2.11)$$

$$\underline{\epsilon} = 1 + \underline{\chi} \quad (2.12)$$

The following equation 2.13 describes the relation between the permittivity  $\underline{\epsilon}$ , optical conductivity  $\underline{\sigma}$  and the wavevector  $\omega$ . For Nickel and Iron the calculation of the conductivity tensor  $\underline{\sigma}(\omega)$  has been done for example with ab initio calculations from Oppeneer et al. [34].

$$\underline{\epsilon}(\omega) = \frac{i\underline{\sigma}(\omega)}{\omega} \quad (2.13)$$

The difference in energy absorption results in off-diagonal elements in the dielectric tensor  $\underline{\epsilon}$  or equivalently the optical conductivity tensor  $\underline{\sigma}$ . The form of the dielectric tensor  $\underline{\epsilon}$  depends on the underlying crystal symmetry and magnetisation orientation in the frame of reference of the crystal axis [31]. For a magnetic medium the polarization change introduced by the static magnetisation  $\mathbf{M}$  is as follows:

$$\mathbf{P}_M = \underline{\epsilon}(\mathbf{M} \times \mathbf{E}). \quad (2.14)$$

The magnetisation  $\mathbf{M}$  is a vector with the components relative to the frame of reference of sample and incoming light. Here polar and  $\mathbf{M}_{\text{polar}}$  refers to the situation of the light being incident normal to the material surface and the magnetisation direction along the z-axis, so out of the sample plane.

$$\mathbf{M} = \begin{pmatrix} m_x \\ m_y \\ m_z \end{pmatrix} \stackrel{\text{polar}}{=} \begin{pmatrix} 0 \\ 0 \\ 1 \end{pmatrix}. \quad (2.15)$$

The interaction of the static magnetisation  $\mathbf{M}$  and the electric field  $\mathbf{E}$  leads to an dielectric tensor  $\underline{\epsilon}$  with symmetric and antisymmetric parts, illustrated in equation 2.16. Only the antisymmetric parts contribute to the MOKE signal, as the symmetric ones are equal for left and right hand polarized light. The diagonal components with an even dependence in  $\mathbf{M}$  are a measure for the average absorption of both left and right hand circular light, while the off diagonal elements are a measure for the difference between those

absorptions [31]. In this explanation the media is assumed to be homogeneous and a monochromatic wave is taken into consideration.

$$\underline{\epsilon} = \begin{pmatrix} \epsilon_{xx} & \epsilon_{xy}m_z & \epsilon_{xz}m_y \\ \epsilon_{yx}m_z & \epsilon_{xx} & \epsilon_{yz}m_x \\ \epsilon_{zx}m_y & \epsilon_{zy}m_x & \epsilon_{zz} \end{pmatrix} \quad (2.16)$$

The tensor describes the change of polarization for different measurement geometries. The MOKE measurements in this thesis are only performed in the polar MOKE geometry, which reduces the relevant entries of the tensor to 2.17 [33, 35–38].

$$\underline{\epsilon}_{\text{polar}} = \begin{pmatrix} \epsilon_{xx} & \epsilon_{xy}m_z & 0 \\ -\epsilon_{xy}m_z & \epsilon_{xx} & 0 \\ 0 & 0 & \epsilon_{zz} \end{pmatrix} \quad (2.17)$$

The electromagnetic light wave can be described in the base of the polarisations  $s$  and  $p$ , giving the modal amplitudes  $E_s$  and  $E_p$ . The Jones framework can be utilized to describe the change of the polarization state when passing optical elements [39]. The Jones vector  $\mathbf{J}_{\text{in}}$  for the incoming light is expressed in equation 2.18

$$\mathbf{J}_{\text{in}} = \begin{pmatrix} E_{s,i}(\omega) \\ E_{p,i}(\omega) \end{pmatrix} \quad (2.18)$$

In the case of a reflection of light from an object, the incoming and outgoing light waves are connected via the reflection matrix  $\underline{R}$  (see equation 2.19) [36, 39].

$$\mathbf{J}_{\text{out}} = \underline{R} \cdot \mathbf{J}_{\text{in}} \quad (2.19)$$

As a result the reflectivity matrix  $\underline{R}$  describes the reflection at the interface of the whole sample with Fresnel coefficients. In the basis of linear  $s$ - and  $p$ -polarized light it takes the form of the matrix 2.20.

$$\underline{R} = \begin{pmatrix} r_{pp} & r_{ps} \\ r_{sp} & r_{ss} \end{pmatrix} \quad (2.20)$$

The diagonal components represent the fraction of incoming  $p$ - and  $s$ -polarized light and the reflection of the respective polarization. The off-diagonal entries describe the reflection of changed polarisation, so  $r_{sp}$  describes the amount of  $s$ -polarized incident light which is reflected as  $p$ -polarized light. This matrix can be simplified to the matrix  $\underline{R}_{\text{polar}}$  2.21 if the magnetisation is oriented along the  $z$ -axis in the plane of incidence and the light is incident at normal incidence. In this geometry  $s$ - and  $p$ -polarized light can no longer be distinguished.

$$\underline{R}_{\text{polar}} = \begin{pmatrix} r_{pp} & r_{sp} \\ r_{sp} & -r_{pp} \end{pmatrix} \quad (2.21)$$

The off-diagonal elements originate from the spin-orbit coupling, so for a non-magnetic medium those elements vanish. The Fresnel equation describes the link between the dielectric tensor  $\underline{\epsilon}$  and the refraction index  $n$ . The solutions for the polar MOKE geometry are presented in equation 2.22 [31].

$$n_{\pm}^2 = \epsilon_{xx} \pm i\epsilon_{xy} \quad (2.22)$$

It is clear that the existence of the off-diagonal elements creates a difference in the complex refractive index for left and right hand circular light.

As a macroscopic result, the former linear polarized light as superposition of equal amounts of right and left hand circular light is altered: The microscopic change due to spin-orbit coupling and exchange

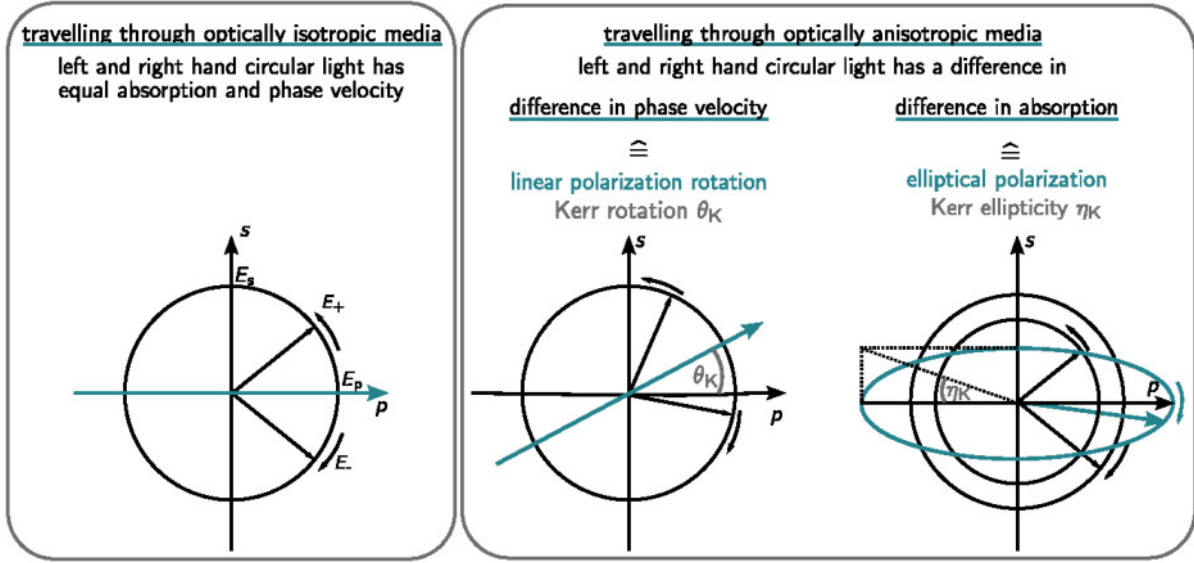


**Figure 2.3: Effects on linear polarized light induced by a magnetic material.** The electric field of light in the left box is a combination of equal amplitudes for left ( $E_+$ ) and right hand ( $E_-$ ) circular light. The equal phase velocity in an optically isotropic medium creates linear p-polarization (blue). If the medium is anisotropic for example due to the presence of a magnetic field, the right box described two effects. On one hand the phase velocity for left and right hand circular light is uneven, which causes a rotation of the polarization plane. In case of MOKE this quantity is described by the Kerr angle  $\theta_K$ . Additionally a difference in absorption is present, which creates different amplitudes in  $E_+$  and  $E_-$ . Consequently the unequal amplitudes create an elliptical polarization. This quantity is described as ellipticity  $\eta_K$ . A superposition of both effects create the magneto-optical effect. Inspiration from [38].

interaction creates unequal absorption and a difference in phase velocity. Figure 2.3 shows schematically the changes of the polarization. The unequal absorption leads to a difference in amplitude for the right and left hand circular modes,  $E_+$  and  $E_-$ . As a result, the linear polarized light gets elliptical. The ellipticity is described with the parameter  $\eta_K$ .

A difference in phase velocity creates a phase change between the polarizations. This leads to a tilt of the polarization plane around the angle  $\theta_K$ . A combination of both effects is the complex Kerr angle  $\Theta_K$ . A detailed description of the process reflection of light can be found in [40]. The influence of the magnetic field is described by Oppeneer [31].

Under the polar MOKE geometry no difference between s- and p-polarized light appears. In case of experimental setups with a small change from normal incidence the measured difference is also neglectable [31]. The experimentally measured quantity of the complex Kerr angle depends on the detection method [32].

$$\begin{aligned}\Theta_K &= \theta_K + i\eta_K \\ &= \frac{r_{ps}}{r_{pp}}\end{aligned}\tag{2.23}$$

Ebert showed a framework to calculate the MOKE spectra for the transition metals based on the calculated band structure in reference [41]. The results for Nickel and an Iron Platinum alloy  $\text{Fe}_{0.5}\text{Pt}_{0.5}$  are shown in figure 2.4. The black line in the Nickel spectra represents the theoretical result, the coloured lines are experimental results for comparison. In the graph on the right for FePt the results are presented the disordered state as well as the crystal orientations (001) and (100).

The amplitude of the Kerr rotation indicates that FePt has a larger magneto-optical effect, so the experimentally measured amplitude of a MOKE signal is larger compared to Nickel. This is expected

because the strength of the spin-orbit coupling is larger in FePt, and this influences the strength of the magneto-optical effect. These graphs also indicate that in particular for Nickel the probing wavelength should be different than the often available 800 nm. The effect at this wavelength is very small. In this work 400 nm were used for both materials, which shows a significant effect.

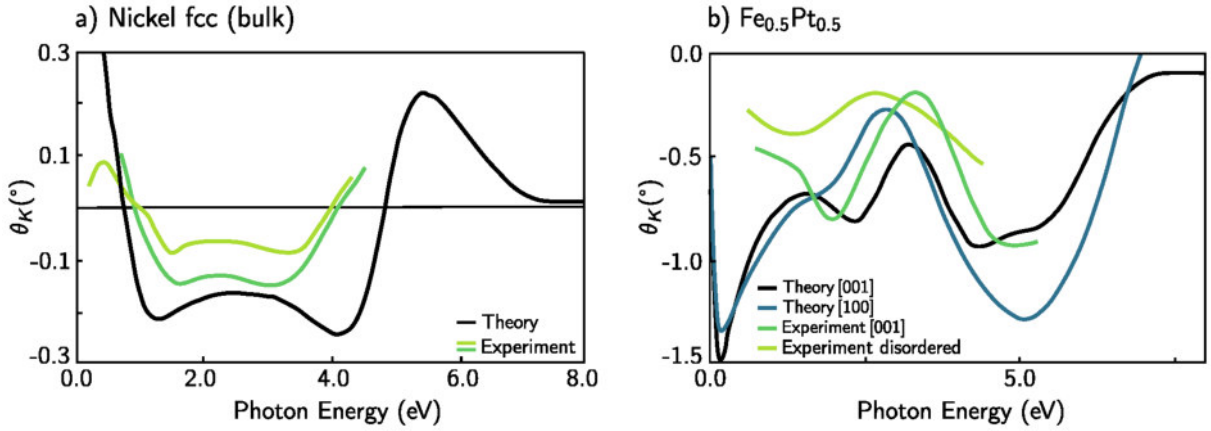


**Figure 2.4: Theoretical MOKE spectra for Nickel (bulk) and Iron Platinum (Fe<sub>0.5</sub>Pt<sub>0.5</sub>).** The black line in a) and lines marked as *Theory* in b) represent calculated results for the rotation of the light, in b) shown for different crystal orientations. The rest of the curves are experimental data for comparison. Data is taken from [41].

## 2.4 Ferromagnetism in Transition Metals

The magnetic elements investigated in this thesis, Nickel and Iron, are both transition metals. Their magnetism is created by unpaired electrons in the 3d-orbitals. These electrons are called itinerant, as the wavefunctions of neighbouring atoms overlap. This causes electrons to be delocalized. So instead of being bound to an atom, they exist as majority and minority band electrons filling the energy levels up to the Fermi energy. Consequently the simplified picture given in figure 2.2 for optical transitions between localised states does not apply directly. Instead the energies for minority and majority spins are distributed over a broad spectrum defined by the density of states (DOS). The calculated DOS for Iron (bcc) and Nickel (fcc) in figure 2.5 shows the density for minority (here: spin down) and majority (spin up) band. Nickel is considered a strong ferromagnet, because the majority band does not cross the Fermi energy, whereas Iron is a weak ferromagnet with the majority band not fully occupied [18]. A ferromagnetic state is reached when the two bands are not equally occupied without an external field applied, as for Iron and Nickel. A paramagnetic state is described by equal energy and spin distributions, which are shifted when a field is applied.

The transition of spins from the majority band to the minority band leads to an unfavourable increase in the kinetic energy, since the energy levels are now filled until  $E_F + \delta E$  and not only to the Fermi level. But the energy increase is overcompensated by the mean-field  $B_{mf}$ , which favours the parallel orientation of spins [42]. If a transition metal exhibits ferromagnetic or paramagnetic behaviour is described by the *Stoner criterion*. It is determined by the parameter  $U$  describing the strength of the Coulomb energy of the molecular field (see equation 2.24) and the DOS  $N(E_F)$  at the Fermi level. If the multiplication of these parameters is larger or equal to one, a transition metal is ferromagnetic. Equation 2.25 shows the resulting condition from the energy calculations.

$$U = \mu_0 \mu_B^2 \lambda \quad (2.24)$$

$$U \cdot N(E_F) \geq 1 \quad (2.25)$$

In the right panel of figure 2.5 the calculation for  $U$  as well as the Stoner criterion are plotted against the atomic number. It is clear that the itinerant ferromagnetism is only expected for the metals Nickel, Iron and Cobalt.

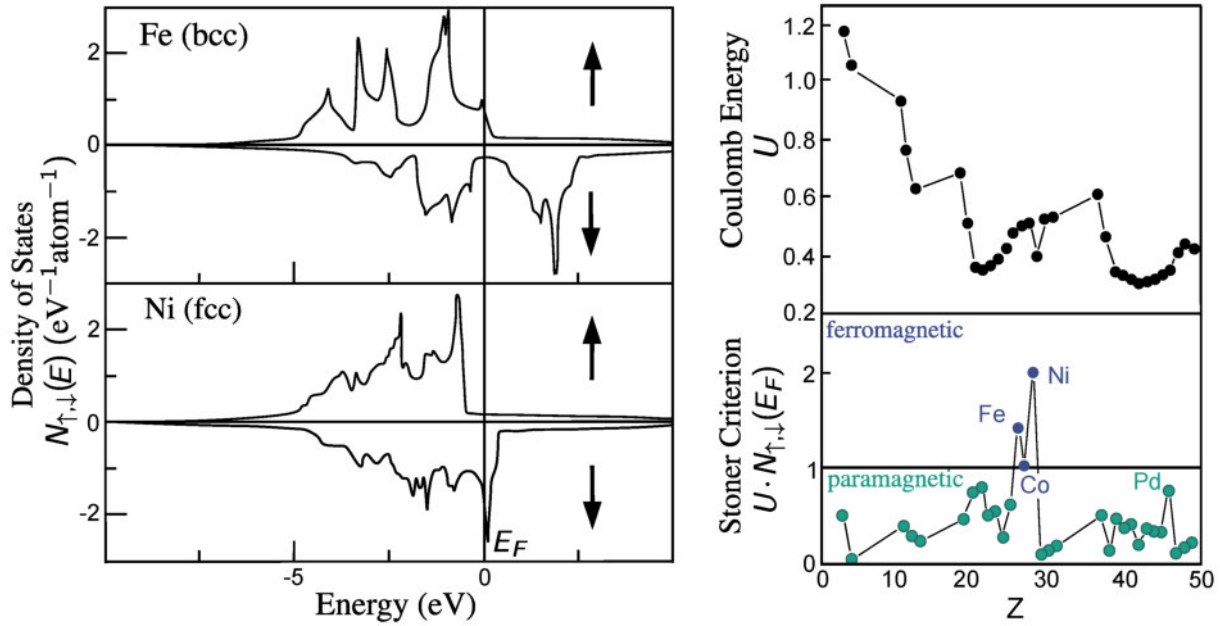


**Figure 2.5:** Left: Spin dependent density of states for Nickel (fcc) and Iron (bcc), the Fermi level is indicated with  $E_F$ . Figure adapted from [18]. Right: Stoner criterion calculations.  $U$  represents the Coulomb energy created by the mean-field  $\mathbf{B}_{\text{mf}}, N_{\uparrow,\downarrow}(E_F)$  the DOS at Fermi level. The bottom graph shows the calculation of the Stoner criterion for the atom numbers with the resulting magnetic state. Adapted from [42]

### 3 | Magnetisation Dynamics in Metals

The understanding of magnetism and its associated interactions in matter has been of research interest for a long time. Since the development of ultrafast laser systems and the general search for faster and smaller technological devices the field of ultrafast magnetisation reversal and manipulation has gained a lot of attraction and attention. Besides possible advantages for new applications it also enables a better understanding of solid state materials and the interaction of the various subsystems determining the properties of materials. The investigation of non-equilibrium dynamics has been benefiting greatly from the evolution of femtosecond lasersystems, which enable experiments in a non-equilibrium regime.

In this chapter the time and temperature dependent mechanisms of magnetisation are discussed. It will start with slow equilibrium conditions and continue to the ultrafast, non-equilibrium topics up to the recently discussed topics in this field.

#### 3.1 Timescales of Magnetisation Dynamics

**Energy minimization** In equilibrium conditions a magnetic system reaches a stable state where changes only occur as thermal fluctuations. The configuration of a magnetic structure in this condition is described by minimizing the Gibbs free energy  $\mathbf{G}$ , see equation 3.1. The energy is defined by the Helmholtz free energy  $\mathbf{F}$  of the system and the Zeeman energy imposed by the external applied field [20].

$$\mathbf{G} = \mathbf{F} - \mu_0 \int_V \mathbf{H}_{\text{ext}} \mathbf{M} d^3\mathbf{r} \quad (3.1)$$

In a thermal state far away from the Curie temperature the energy  $\mathbf{F}$  can be set to equal the total internal energy  $\mathbf{U}$  of the system. When the temperature rises, the entropy  $\mathbf{S}$  can no longer be neglected and has to be taken into account, see equation 3.2.

$$\mathbf{F} = \mathbf{U} - T\mathbf{S} \quad (3.2)$$

**Magnetic Domains** The stable state is microscopically achieved by magnetic domains, areas with the same magnetisation direction. The size and shape of the domains are the result of the energy minimization. For example generally avoiding large stray fields is energetically favourable, so the domains at the interface of a magnetic material tend to form in plane. The solutions of the energy optimization allow a large set of possible domain configurations, with which the equilibrium condition is reached. A metastable state is reached, when the effective field strength  $\mathbf{H}_{\text{eff}}$  creates no torque  $\mathcal{T}$  at any point inside the sample (equation 3.3) [20].

$$\mathcal{T} = \mathbf{M} \times \mathbf{H}_{\text{eff}} \stackrel{\text{metastable}}{=} 0 \quad (3.3)$$

The effective field  $\mathbf{H}_{\text{eff}}$  is determined by equation 3.4. It is a combination of all components acting on a spin, namely the exchange energy contribution (first term), anisotropy energy contribution (second term), the demagnetisation field  $\mathbf{H}_d$  and the applied external field  $\mathbf{H}_{\text{ext}}$ . Here  $\mathbf{m}$  represents the magnetisation relative to the saturation magnetisation  $\mathbf{M}/M_s$  and  $A$  is the material dependent exchange stiffness constant [20].

$$\mathbf{H}_{\text{eff}} = \frac{2A}{\mu_0 M_s^2} \nabla^2 \mathbf{M} - \frac{1}{\mu_0 M_s^2} \frac{\partial \mathbf{E}_{\text{an}}}{\partial \mathbf{m}} + \mathbf{H}_d + \mathbf{H}_{\text{ext}} \quad (3.4)$$

If the effective field is changed, for example by a variation of the applied field, the resulting torque  $\mathcal{T}$  on the previously stable configuration is not zero anymore. As a result the magnetic moments reorient until stability is reached again. This describes the magnetisation process observed in a ferromagnetic hysteresis: If an external field is applied, it changes the state of magnetisation inside the sample in order to minimize energy. The reorientation as seen in a hysteresis loop is the result of domain nucleation, movement of domain walls as well as rotation of domains.

**Magnetisation Reversal** The change of a magnetic configuration can be both reversible and irreversible, coherent and non-uniform. The two mechanisms most likely to occur are domain nucleation and domain wall motion. If the induced torque causes a rotation of spins, this can act inside a domain or at a domain wall. A domain wall can move rigidly: When the shape of the wall is not changed, only a displacement occurs. The energy necessary to move the wall from the previously favourable position equalizes with the energy gained by aligning with the external field. Still a threshold energy is necessary to move the wall even in perfect crystals, so the applied fields for driving the movement cannot be vanishingly small [20]. The coherent domain rotation for the whole sample is only expected for specific situations of magnetisation reversal and frustration inside the sample, for example measured by Grolier et al. [43]. The original state of a domain structure with no net magnetisation is altered by an increasing external field until the saturation magnetisation is reached. The initial magnetisation is described by the susceptibility  $\chi_i$ , which relates the applied field  $\mathbf{B}_{\text{ext}}$  with the magnetisation  $\mathbf{M}$  with equation 3.5. The initial virgin hysteresis branch (magnetisation from a state of zero net magnetisation) as well as the first part of the recoil curve are typically linear.

$$\chi = \frac{\partial \mathbf{M}}{\partial \mathbf{B}} \stackrel{\text{reversible}}{=} \frac{\Delta \mathbf{M}}{\Delta \mathbf{B}} \quad (3.5)$$

The linear part of a recoil curve (change of magnetisation direction from any point of the major hysteresis loop) is described by the reversible susceptibility  $\chi_{\text{rev}}$ . Microscopically this is caused by defects in the sample: internal stresses, point and extended defects, grain boundaries, sample surface and interfaces and many others. These disruptions of the energy gradient cause domain walls to be pinned. A domain wall will interact and stick to these defects and a slight variation in the external field causes the wall to bend and bulge. In terms of Gibbs free energy this is represented in a parabolic shape in a one dimensional expression of the average coordinate of the domain wall. The reversibility in this phase is given by the landscape of  $G$ : local minima of parabolic potentials can be recovered. This reversible, linear behaviour can also be modelled for domain rotations. [20]

Whether the initial magnetisation of a magnet is dominated by domain wall movement or domain rotation depends on the material constants. For Iron with positive cubic anisotropy it could be determined that not rotation, but the movement of domain walls is the main contribution in the reversible magnetisation. On the other hand Nickel with its negative cubic anisotropy has a larger wall stiffness, so the domain wall mobility is low and rotation is dominating [20]. The velocity of a domain wall depends on the shape of wall and sample, but in an ideal ferromagnet without defects it has two linear regimes in which it increases with the applied field [44]. In a realistic thin film ferromagnet with defects causing domain wall pinning the dependence is less linear for low fields [45].

If the magnetisation process is determined by domain wall propagation, only few nucleation events are needed to drive the switching process from saturation magnetisation. This creates square-like hysteresis loops. If the domain wall mobility is limited, the necessary number of nucleation events increase. The reversal occurs over a larger applied field range, the hysteresis loop gets flatter and rounder [18, 46]. The speed of domain wall movement is determined by the applied external field. The domain nucleation represents a coherent rotation of a uniformly magnetised domain. It can act on much faster timescales than domain wall movement at moderate fields, between  $10^{-12}$  to  $10^{-8}$  s. The precessional reversal of a granular sample excited by the ultrafast electron beam of the Stanford Linear Accelerator Center (SLAC)

was determined to be limited by 9 ps [47]. Faster timescales in the dynamics of magnetisation have been observed and the underlying mechanisms are still under debate.

The impact of defects on a magnet interface can be seen in the image on the left hand side of the cover of this thesis. The typical regular domain structure of Yttrium Iron Garnett (YIG) is interrupted by long stretching scratches on the surface. They cause the domains at the top-centre to be irregular and also expand in size compared to the regular labyrinth structure at the bottom.

**Magnetisation Temperature Dynamics** Besides the dynamics of a magnetic system induced by an altered effective magnetic field the magnetic system is influenced by temperature. The relation of magnetisation and temperature for a simple ferromagnet shows a decrease of the saturation magnetisation starting at low temperatures. This decrease has a first regime which is attributed to magnons (spin wave excitations) and is described by a  $T^{3/2}$ -law. The following regime is a faster decrease of magnetisation until a sharp edge followed by a soft tail is marking the phase transition from ferromagnet to paramagnet. This behaviour is dominated by thermal fluctuations (see section 2.2) [18, 48]

**Slow Dynamics** The thermal relaxations at low temperatures far below the Curie point allow a system to keep its original state for millions of years. This discovery beginning with the pioneering works of Bernard Brunhes in the early 20th century lead to the research field of palaeomagnetism, which is the reconstruction and investigation of the earth's magnetic field from the magnetisation orientation of rocks. The process of magma cooling and hardening as new ocean ground makes the Atlantic ridge and floor the largest hard drive, storing the direction of the earth magnetic field.[49]

**Precession** The most elementary dynamics of a magnetic system can be represented by a single spin. If an external field is applied, the spin expectation value starts to precess around the axis of the external field. The damping introduced from dissipation of energy causes the spin axis to align with the external field. This behaviour also describes an ensemble of spins. An often used equation for calculating the magnetisation precession over time is the Landau-Lifshitz-Gilbert equation (3.6).

$$\frac{d\mathbf{M}}{dt} = \gamma\mu_0(\mathbf{M} \times \mathbf{H}_{\text{eff}}) + \frac{\alpha}{M_s} \left( \mathbf{M} \times \frac{d\mathbf{M}}{dt} \right) \quad (3.6)$$

The parameter  $\gamma$  is the gyromagnetic ratio, the ratio between magnetic moment  $\mu$  and angular momentum  $j = g\mu_B\mu/\hbar$ , and  $\alpha$  represents the Gilbert damping parameter. If no damping occurs, a spin would not align to the external field. According to this equation, an antiparallel field would not cause the spin to reverse sign. But in a real ferromagnet a large enough field will not only act on the magnetic moment of the spin, but also alter other variables like the spin orbit coupling [48]. Consequently, a field antiparallel to the effective field  $\mathbf{B}_{\text{eff}}$  will result in a change of orientation of the spin.

The manipulation and understanding of magnetisation precession and the damping is an active field of research, as summarized amongst others in the reviews by Azzawi et al. [50] and Lobsy et al [51].

## 3.2 Ultrafast Heating of a Magnetic Metal

A model to describe the excitation of a metal with an ultrafast laser pulse is the two temperature model (2TM) [52]. In this model the metal is divided in two subsystems that interact with each other with defined mechanisms and timescales. Initially, the energy is absorbed by the electron system before it is redistributed to the lattice system (phononic system) via electron-phonon interactions. This model of subsystems is defined by the parameter temperature, which is assigned to each subsystem. [52]

In the transition metals an additional subsystem has to be taken into account: the spin system. The spins of paramagnets do not contribute significantly to the total energy, they can be neglected. But for the

ferromagnetic transition metals the energy is no longer insignificant. With an additional separate energy bath the model is extended as three temperature model (3TM) .

The electrons follow a Fermi-Dirac distribution at equilibrium conditions, see equation 3.7.

$$f(E) = e^{-\frac{E - \mu}{kT_{e,0}(t < t_0)}} + 1 \quad (3.7)$$

$T_{e,0}$  represents the temperature of the electron subsystem before a pump pulse arrives,  $\mu$  the chemical potential. In this case the temperature of the lattice and the sample itself are equal to the electron temperature. Figure 3.1 represents a schematic version of the 3TM and an illustration of the process of thermalization of hot electrons.

The excitation with the pump pulse, denoted with  $P(t)$ , deposits energy in the system, because the pumping photons are absorbed by electrons below the Fermi level. This leads to populated states above the Fermi energy. This is illustrated as 2D distribution of electrons in figure 3.1. The left circle represents the cool state with only occupied states inside of the Fermi level. The right circle represents the hot, excited state with several electrons excited above the Fermi level. The right column shows the density of states depending on energy. After excitation a sharp increase in electrons in higher energetic levels is observed, the Fermi-Dirac distribution is distorted.

In the process of cooling, the heated electrons scatter and cool to a distribution that fulfils Fermi-Dirac at higher temperatures  $\Delta T + T_{e,0}$ . In Nickel, this thermalization happens on a timescale of  $\tau_e = 10$  fs [53]. The distribution of electron levels is smoothed compared to the initial distribution.

Further cooling down is now accompanied by transferring energy to the other subsystems. This describes the connected subsystems with a set of coupled differential equations. The model described by the equations 3.8 assumes temperatures that can be assigned for each of the subsystems,  $T_e$ ,  $T_p$  and  $T_s$ , and heat capacities associated with each individual subsystem ( $C_e$ ,  $C_s$ ,  $C_p$ ). The excitation via a laser pulse is expressed with the term  $P(t)$ , describing the power absorbed to the electron system.

$$\begin{aligned} C_e(T_e) \frac{dT_e}{dt} &= -g_{ep}(T_e - T_p) - g_{es}(T_e - T_s) + P(t) \\ C_s(T_s) \frac{dT_s}{dt} &= -g_{es}(T_s - T_e) - g_{sp}(T_s - T_p) \\ C_p(T_p) \frac{dT_p}{dt} &= -g_{ep}(T_p - T_e) - g_{ps}(T_p - T_s) \end{aligned} \quad (3.8)$$

The coupling of the subsystems is described with the material specific coupling constants:  $g_{es}$  (electron-spin),  $g_{sp}$  (spin-phonon) and  $g_{ep}$  (electron-phonon). The strength of the coupling constants determines the speed of energy transfer between the subsystems, expressed by the respective time constants  $\tau$ .

Energy transferred to the lattice system can be detected via coherent and incoherent excitation, which moved the atoms out of their original lattice position. The later is mostly observed as temperature increase usually accompanied by a thermal expansion, while the former represents the excitation of a phonon.

The excitation of the spin system can also be coherent (with excitation of spin waves) or incoherent, where heating creates spin disorder.

There exist several models altering this simple approach to include the electron thermalization [54] or the transfer of angular momentum included in the microscopic three temperature model [55]. Another approach allows for much longer equilibration times by calculating the energy distribution including nonequilibrium processes [56]. This model was applied to Iron Platinum and predicts a out of equilibrium time of picoseconds. The specific heat capacities of the subsystems are shown in the graph a) of figure 3.2 for Nickel [18]. In the plot b) the change of the spin heat capacity with an applied external field is shown [57]. The total heat capacity  $C$  sums the contribution of all subsystems. The heat contributions from the subsystems vary strongly with the temperature. The specific heat of the magnetic system has a maximum

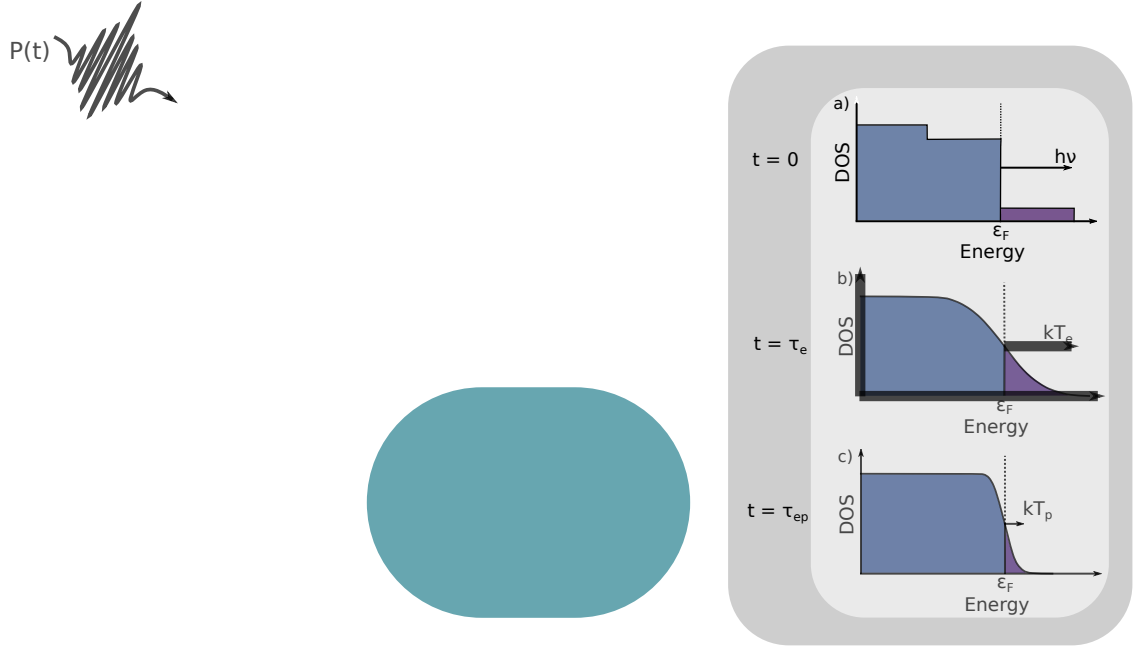


**Figure 3.1: Visualization of the 3TM, hot electron thermalization.** Left: Subsystems of the three temperature model and their respective time constants. Right: Thermalization of hot electrons. Image after [5].

around the Curie temperature  $T_c$ . The lattice dominates the lower temperature until several thousands Kelvin. At higher temperatures of a few thousand Kelvin the electron system is dominating the specific heat. The addition of an external field causes the sharp peak at the Curie point to be rounded and stretched over a wider temperature range. Nevertheless, the changes are not significant for the measurement in this thesis and are neglected in the data analysis. Figure 3.3 taken from Bigot et al. [58] provides an overview

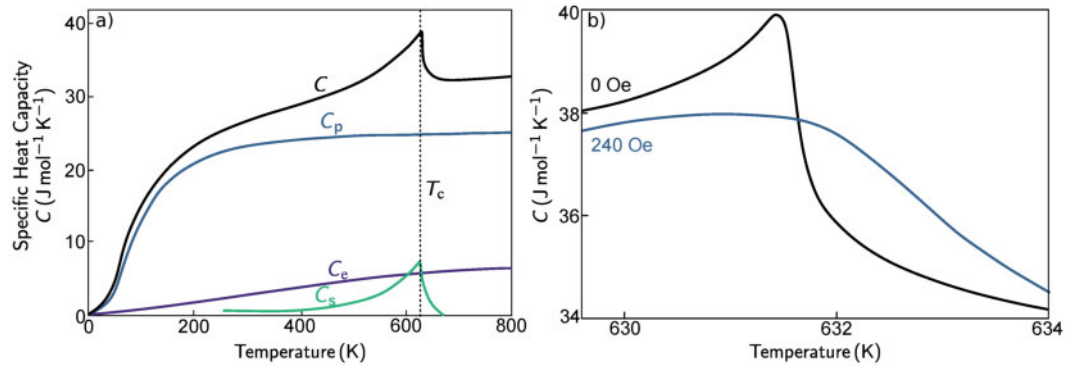


**Figure 3.2: Specific heat capacity of Nickel.** Left: Total heat capacity of Nickel over temperature with the individual contributions of the electronic ( $C_e$ ), phononic ( $C_p$ ) and spin ( $C_s$ ) subsystem. The Curie temperature  $T_c$  is added as dashed line. Data from [18]. Right: Measured dependence of the specific heat capacity for Nickel on an external applied magnetic field. Data from [57].

of the discussed timescales and interactions important for the description of a magnetic sample in ultrafast, non-equilibrium conditions. The short timescales of around 1 fs are determined by the excitation of electrons into higher energy states. The timescale is determined by the dipolar transition dephasing time  $T_{2e}$ . The difference in the inter- or intraband transitions for various materials is responsible for the spectral dependence of magneto-optical Kerr effect (MOKE) measurements [58]. On a similar timescale quantum fluctuations resulting in local change of magnetism can be observed. The following timescale of a few

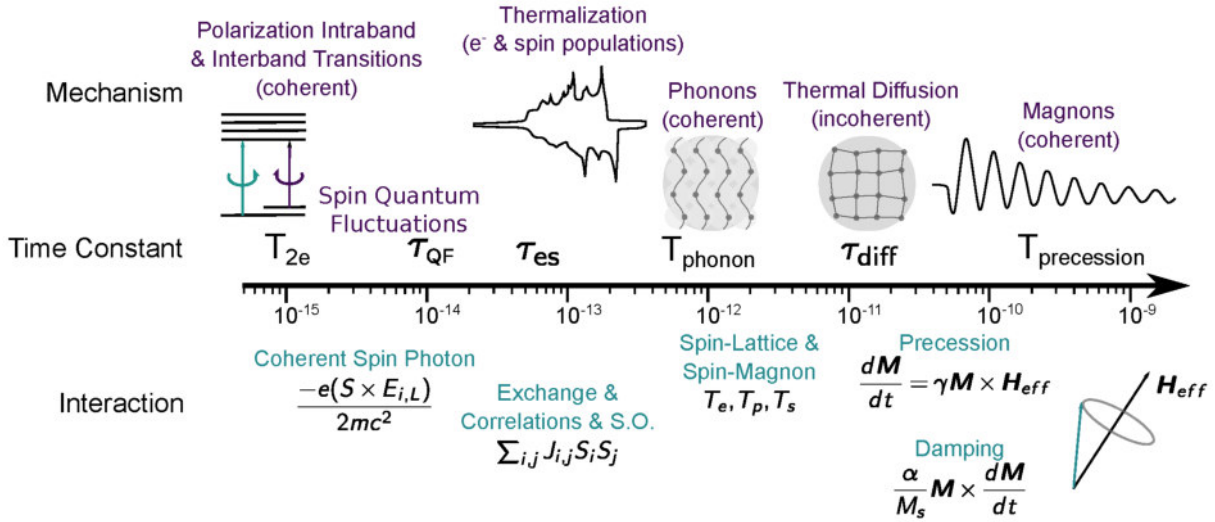


**Figure 3.3:** Overview of the processes and their corresponding timescales in magnetism and magnetisation dynamics. Figure taken from [58]

hundred femtoseconds is determined by the cooling of hot electrons and spins. The excited electrons are redistributed in  $k$ -space and populate again the levels below the Fermi energy. The dominating interactions around this time are exchange and Coulomb interactions, mediating the cooling via scattering events. At a time of 1 ps after laser excitation the lattice shows the effects of general heating and also coherent expansion via acoustic pulses in the sample, if the thickness is sufficient. The strength and direction of change of the lattice planes are determined by the specific heat. On long timescales of several picoseconds up to nanoseconds the magnetisation dynamics is driven by magnetisation precession. The lifetime of these coherent magnons depends on the damping, it is therefore a material specific time. [58]

### 3.3 Ultrafast Magnetisation Dynamics

Agranat et al. used the 3TM first as an explanation for the temperature of the spin system in Nickel when heated with a picosecond laser pulse [59]. This experiment was one of the first to utilise the pump probe technique for investigating the dynamics of magnetisation after excitation with a laser pulse. Even though the electron and lattice temperature was determined to be higher than the Curie temperature of Nickel, the 50-100 nm film did not show a complete demagnetisation. Thus the average spin temperature was determined to be lower than the Curie temperature.

Beaurepaire et al. used the high time resolution of femtosecond laser pulses with the combination of pump probe techniques to show the ultrafast demagnetisation of Nickel for the first time in a subpicosecond resolution [3]. The data shown in figure 3.4 a) was the origin for numerous experiments and theories to understand the mechanisms regarding the subsystems in materials and the possible limits of demagnetisation timescales. This experiment sparked the development and growth of the research field of ultrafast magnetism. The data shows that the drop in the magnetisation signal appears in less than 1 ps, which is surprising regarding the timescales of the interactions. But nevertheless the result was repeatedly reproduced in many different experiments, for example by Hohlfield et al. [60] and Koopmans et al. [61]. Figure 3.4 a) presents both the inspirational measurement of Beaurepaire et al. from 1996 and a more recent measurement from Koopmans et al. [55] in 2010 in b). It highlights the improvements in time resolution and signal quality over the past two decades. It also confirms the initially observed behaviour for a thin Nickel layer.

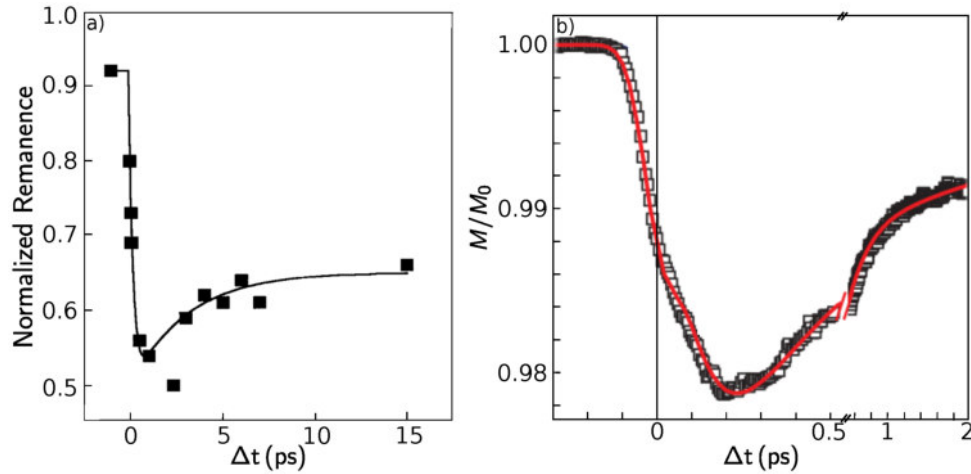


**Figure 3.4: Ultrafast demagnetisation of Nickel.** Left: First measurement of the ultrafast demagnetisation of Nickel after excitation with a short laserpulse, measured by Beaurepaire et al. in 1996. Image after [62]. Right: Measurement from Koopmans et al. in 2010 for a low fluence excitation. Image after [55]

The investigations of demagnetisation of a single ferromagnetic thin layer were soon accompanied by many experiments about the control and manipulations of magnetisation properties in complex systems. The laser-driven control of coherent precession is particularly of interest for the field of spintronics. It therefore is often performed in insulators with low magnetisation precession damping. This is fulfilled for the garnet samples, for example investigated by van Kampen et al. [63], Hansteen et al. [64], Kalashnikova et al. [65] and Atoneche et al. [66].

Another attractive field of research is invested in using laser pulses to switch the orientation of ferromagnetic compounds or multilayered systems. The mechanism triggering the switching depends on the material. A variety of rare earth alloys and ferromagnetic multilayers were investigated using the effect of all-optical helicity-dependent switching (AO-HDS). This exploits the impact of the helicity of the exciting laser pulse on the magnetic layer for controlling the domain orientation [67–69]. Of special interest is the alloy Gadolinium Iron Cobalt (GdFeCo), which is to date the only material, where a deterministic single pulse toggle-switching of the magnetisation state is possible without the assistance of an external magnetic field [70]. The switching can also be triggered with indirect laser excitation of a back layer (Platinum) with a buffer layer of Gold, so that the switching is only triggered by heat traversing the sample [71]. It was also possible to reproduce this effect only with electrical currents [72].

Besides the ultrafast magnetic quenching, experimental results also revealed that the demagnetisation process of ferrimagnets and ferromagnetic alloys is element specific. The sublattices of different materials exhibit different demagnetisation timescales [73, 74].

The ultrafast experiments on the demagnetisation of various magnetic materials could reproduce the original result from Beaurepaire consistently: The quenching of the magnetisation is faster than 1 ps, most extracted values are in range of 100 - 500 fs. The results were obtained by different time resolved methods like magneto-optical measurements, element specific X-ray magnetic circular dichroism (XMCD) [73, 75], angle-, spin and energy resolved photoelectron spectroscopy [76–78] or angle-resolved photoemission [13].

After two decades of experiments regarding ultrafast demagnetisation it is still unclear and debated, which physical mechanisms are relevant. The magnetisation changes on a timescale faster than any equilibrium dynamics driven by magnetisation precession. The models developed for explaining the observations include scattering processes like the Elliot-Yafet spin flip, during which the angular momentum distributes via interaction with the lattice: A spin flip is accompanied by the emission or absorption of a phonon

[54, 79]. A similar scattering process excludes the phonon contribution by only taking electron-electron scattering via Coulomb interaction into account [80]. Another scattering process is given by the interaction between electronic and spin system: inelastic electron-magnon scattering [81]. Stoner excitations are also a low-spin excitation, during which the majority band electrons take a place in the minority band, creating electron-hole pairs at the Fermi-level [82].

An alternative approach to scattering as driving process are spin transport phenomena. Where the main differences in modelling are the electron properties. The spin current into the magnetic media could be described as diffusive, super-diffusive or ballistic [5, 83–86].

Another recent approach assumes a dynamic exchange splitting, which is affected at similar timescales as the demagnetisation process [78], [87].

Currently, both experiments and models give contradictory results. The interpretation of the data is often not trivial, because only one degree of freedom is measured while the model analysis is based on at least two of the subsystems established in the 3TM. Another uncertainty in measurements arises from using of layers with a thickness above the penetration depth. If the probed layers are excited inhomogeneously, the signal is composed of the response by different excited layers. If the observation technique is not depth sensitive, effects like magnetic phase transition can be masked. An additional masking of the magnetic signal obtained with MOKE measurements can be expected in the first timescale of a few hundreds of femtoseconds. This originates from the electronic system in a non equilibrium [61, 88]. The origin of the MOKE signal explained in section 2.3 indicates that any change of the optical conductivity tensor during laser excitation would lead to a different MOKE signal. This may lead to a signal which is no longer proportional to the magnetisation, especially at very high pump fluences. Nevertheless, the discussion in this thesis focuses on timescales far beyond 1 ps, so it can be assumed that the relaxation process of electrons does not play a significant role in the MOKE signal and can be neglected.

The aim of this work is to combine the structural measurements of the lattice obtained with ultrafast X-ray diffraction (UXRD) and the magnetic signal measured with MOKE. The samples all share the property of being thin, so that the approximation of a homogeneous excited layer is valid. The measurements are performed at high incident fluences, to investigate the remagnetisation process above and close to the phase transition. Although a complete demagnetisation of the magnetic layer would be expected from high lattice temperature, the results from literature show that the maximum demagnetisation observed with MOKE measurements at high fluences up to the sample damage threshold is not unambiguous. Cheskis et al. [10] have found a saturation value for the magneto-optical contrast after demagnetising Nickel with high fluence pump pulses. They investigate a 30 nm polycrystalline Nickel sample with an applied field of 50 Oersteds and found a magnetisation of around 10 % of the saturation value at room temperature remaining in the first 3 picoseconds of the demagnetisation. Also Atxitia et al. [11] noticed that the demagnetisation with high fluence changes the timescale for remagnetisation, but the total demagnetisation could only be reduced to 60 % with a fluence of 50 mJ/cm<sup>2</sup>. However, their determination of lattice and electron temperature predicts that they do not surpass the Curie temperature of the 15 nm Nickel sample for a significant time. In contrast to those results Conrad et al. [8] reported a full demagnetisation of Nickel thin films with less than 7 monolayers, measured with time resolved second harmonic generation (SHG) measurements. Also Roth et al. [9] observe a full demagnetisation of Nickel with experiments performed under increased ambient temperature.

Besides the question regarding the temperature of the three subsystems after laser excitation, it is noticeable that many experiments are only presenting the results of ultrafast demagnetisation, but not the remagnetisation on long timescales. Also the focus of experiments is mostly set to low to medium fluence excitation. This thesis addresses both of the questions and presents results for low to high fluence over a long timescale close to 1 ns.

## 4 | Experimental Setups

The investigation of properties of solid state materials is often performed with the help of lasers. Not only the static properties are of interest but also the dynamic behaviour is an important factor for a huge variety of technical applications. Also the understanding of the interaction of the subsystems of the sample can be enhanced if the ultrafast dynamics are observed. The timescales of these interactions are far beyond traditional detector resolutions for observing changes in time in form of videos.

For that reason, the method of pump-probe spectroscopy is employed. This is a stroboscopic method. To measure the time resolved evolution of a quantity, two laser pulses are created: A pump pulse with high intensity which induces the desired effect in the material, and a less intense probe pulse measuring the response. Between the pump and probe pulse a delay is created by altering the length of the beam path on the optical table. The time of the arrival of the probe pulse relative to the pump pulse is changed, so every delay position of the length variation corresponds to a different step of the process in time.

In order to produce a coherent series of events in time the original state of the probed parameter has to recover before every pumped state.

Combining this time resolving method with the measurement of change in polarization enables an observation of the magnetisation dynamics following an excitation. The time resolution is mainly limited by the duration of the laser pulse.

As part of this work a new setup and data acquisition routine was developed. The setup is shown in figure 4.1 and will be described in the following section. The data acquisition procedure and the software design are outlined in section 4.5.

### 4.1 Laser system

The laser system used for the optical experiments is an amplified titanium sapphire laser with a central wavelength of 800 nm. The laser pulses are generated at a frequency of 1 kHz. The laser system from *Coherent Inc.* consists of a mode-locked Ti:Sapphire oscillator (*MIRA 900*). It is pumped with a continuous wave pump laser (*VERDI V5*) and generates on average 600 mW pulses with a frequency of 80 MHz. Approximately 300 mW are amplified with a Q-switched pump laser of 1 kHz (*Evolution*) inside the *Legend Elite* regenerative amplifier system. This results in a total output power of 1 W with a duration of 100-130 fs and a repetition rate of 1 kHz. The laser power is divided for several experiments. Around 500 mW are used for the MOKE pump probe setup, which will be described in the following section.

Additionally the position of the outgoing laser beam is stabilised with a self-made beam stabilisation. It uses the transmission on two optical mirrors for detecting beam movement. The corrections are made with two *Newport* piezo motorized mirrors.

### 4.2 Optical Setup

The optical setup measuring the Kerr rotation is shown in figure 4.1. The laser pulse used for this MOKE pump probe setup is divided into two parts by a 20:80 beam splitter. The first part is used as a low intensity probe pulse with which static measurements are performed and the dynamics of the sample is monitored. The second beam is a high intensity pump pulse, which rapidly deposits energy in the sample.

The probe wavelength is set to 400 nm for investigations of Nickel and Iron Platinum. This ensures a high magneto-optical contrast by probing relevant electron spins, as can be seen in the data in figure 2.4. Low

intensity in the probe beam is used to avoid pumping additional dynamics. For all investigated samples these conditions are fulfilled for 400 nm. Additionally it is possible to separate pump and probe beam by wavelengths using bandpass optics in the setup. To generate the 400 nm second harmonic generation (SHG) in a beta-barium borate (BBO) crystal is used. For that the probe pulse passes through a telescope to reduce its beam diameter to ensure a sufficient energy density to optimize the SHG. A lambda-half waveplate in combination with a polarizer enables controlling the probe fluence precisely. To reduce the remaining content of 800 nm in the probe pulse, it passes longpass dichroic mirrors with a cutoff wavelength of 490 nm. They transmit more than 90% of the 800 nm and reflect 95% of 400 nm light. The type I SHG creates 400 nm p-polarized light from the incoming s-polarized 800 nm light.

The probe beam is focused onto the sample at nearly 0° incidence through a hole in the pole shoe of the magnet. A lens with a large focus length is used, so that Faraday rotation introduced by the magnetic field is avoided. After reflection from the sample the probe beam is separated from the incoming beam with a 50:50 beam splitter. This means that 50% of the incoming probe beam are splitted and do not hit the sample. This beam can be utilized to monitor the spot size on the sample or to measure intensity variation and detect movement of the laser pulse.

The p-polarized probe beam reflected from the sample passes a detection setup consisting of a lambda-half waveplate and a Wollaston prism. It is then detected by a balanced photodiode. The Wollaston prism separates the s- and p-polarized light components, which are then detected by the diodes of the balanced photodiode. To maximize the sensitivity to the magnetic component the lambda-half waveplate in front of the Wollaston prism is tuned to produce an equal amount of s- and p-polarized light on the respective diodes. This results in a zero signal voltage at the difference output of the balanced photodiode. A small change in polarization will lead to a significant change in the detected signal.

The signals from each diode as well as the difference signal are passed into boxcar integrators. The boxcars are triggered with the laser frequency of 1 kHz and integrate the diode signal in a boxcar gate of several nanoseconds adjusted to the response time of the photodiodes. The integration result is measured with a data acquisition (DAQ) measurement card. The *last sample* output of the boxcar is used, which does not average multiple pulses. A detailed flowchart of the hardware setup can be found in Appendix A. The boxcar signal is described in further detail in section 4.5.

The pump pulse passes through a motorized lambda-half waveplate and a polarizer set to p-polarization. This enables an automated way of changing the fluence for each measurement by changing the angle of the waveplate and therefore the power of the laser pulse. A reference diode is used to monitor the power of the pump pulse during every measurement. Both during changing of the fluence and for static hysteresis measurements a shutter is used, which is automatically activated if one of the above tasks is performed. A delay stage varies the length of the path on the optical table and thereby creates the time delay between pump and probe pulse. Additionally the pump pulse passes a chopper, which is set to a frequency of 500 Hz synchronized with the laser to block every second pump pulse.

With a minimal angular separation of 1° from the probe pulse the pump pulse passes through the pole shoe and is focused onto the sample. If the two beams are overlapping in air, it is possible to detect the rotation of molecules which are Raman excited at high fluences. A further description will be given in section 4.7.

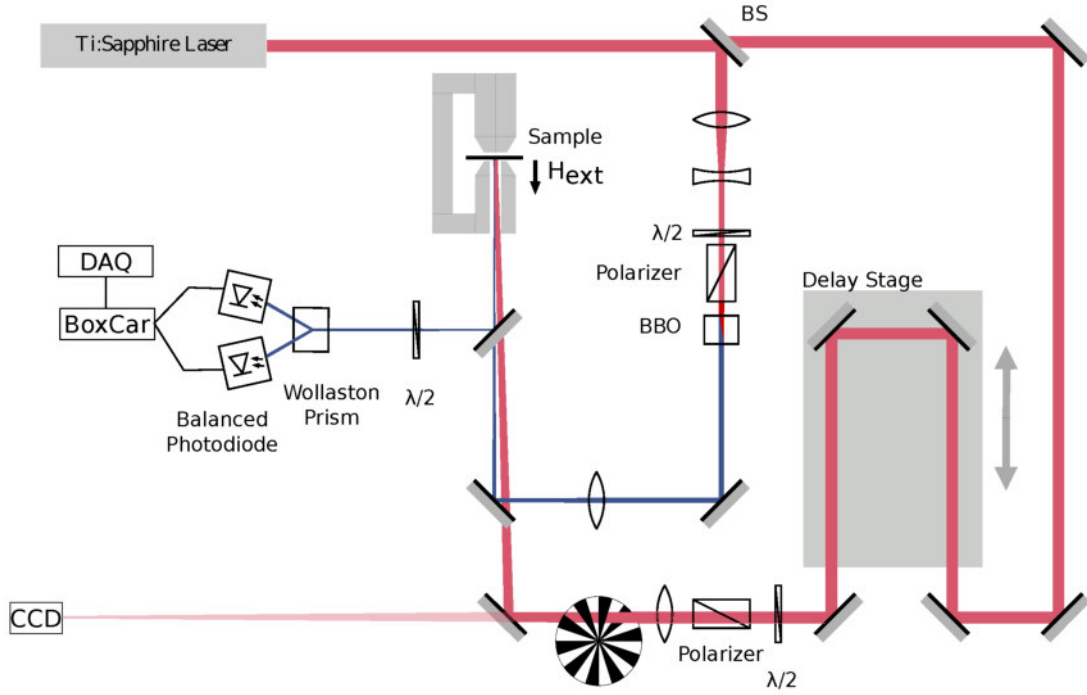


**Figure 4.1: Optical pump probe MOKE setup.** A polar MOKE geometry with a 400 nm probe pulse and a 800 nm chopped and delayed pump pulse is used. A balanced photodiode measures the Kerr rotation. The signal is analysed with a boxcar integrator.

**Sample Geometry** The measurements discussed in this thesis were taken in a polar MOKE geometry. This refers to the external magnetic field being applied perpendicular to the sample surface and the probe pulse being incident at close to  $0^\circ$ . The advantage of this geometry compared to longitudinal or transverse geometries is the conceptual simplicity of the analysis. While the longitudinal signal is a mixture of longitudinal and polar components of the sample magnetisation, in the polar geometry the signal is only sensitive to the out of plane component [89]. This allows an investigation of demagnetisation along the out of plane direction. In this geometry the observation of magnetic precessional movement is possible, when the effective field  $\mathbf{B}_{\text{eff}}$  is not perpendicular to the sample surface. Equation 4.1 shows that it is composed of the external applied field  $\mathbf{B}_{\text{ext}}$  and the anisotropy field  $\mathbf{B}_{\text{ani}}$ .

$$\mathbf{B}_{\text{eff}} = \mathbf{B}_{\text{ext}} + \mathbf{B}_{\text{ani}} \quad (4.1)$$

This implies that at high external fields the saturation magnetisation is reached out of plane, even if the anisotropy is aligned in plane. If the sample magnetisation is not completely tilted out of plane and therefore has an in plane component, a precession can be observed. The two possibilities are sketched in figure 4.2. In picture a) the anisotropy contributions are large compared to the applied external field  $\mathbf{B}_{\text{ext}}$ . This leads to a partial change of the effective field  $\mathbf{B}_{\text{eff}}$  towards the out of plane alignment. An excitation inducing magnetisation dynamics leads to a precession of  $\mathbf{M}$  around  $\mathbf{B}_{\text{eff}}$ , causing the projection of  $\mathbf{M}$  on the axis of observation  $\mathbf{M}_z$  to oscillate as well. In case of b) the external field is large compared to the anisotropy. This causes the effective field  $\mathbf{B}_{\text{eff}}$  to be parallel to the external field. Even if a precession of the magnetisation is caused in the sample, the measurement along the z-axis would not change the amplitude with the precession, so no oscillation is measured. In the pump probe experiments we see a second excitation under certain conditions. It is caused by the pump pulse which is reflected at the backside of the sample substrate and introduces a second excitation in the investigated layer. This is in particular the case when the layer is very thin, so that the pump pulse is partially transmitted. To delay and

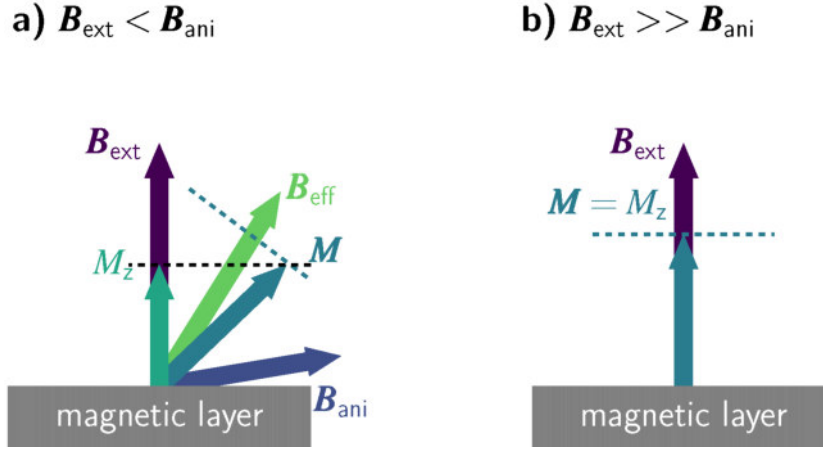


**Figure 4.2: Schematic magnetisation direction of the magnetic layer determined by external magnetic field.** The direction of the internal magnetisation  $\mathbf{M}$  is determined by the anisotropy contribution  $\mathbf{B}_{\text{ani}}$  (dark blue) and the external applied magnetic field  $\mathbf{B}_{\text{ext}}$  (purple) to the effective magnetic field  $\mathbf{B}_{\text{eff}}$  (green). In this setup the polar magneto-optical Kerr effect (MOKE) geometry is implemented, so the external field is applied along the z-axis along the surface normal of the sample. If the two contributions  $\mathbf{B}_{\text{ani}}$  and  $\mathbf{B}_{\text{ext}}$  are in the same orders of magnitudes, the resulting magnetisation is tilted when the anisotropy is directed in plane. This is presented in figure a). The polar MOKE measurement is sensitive to the projection of the magnetisation to the z-axis,  $M_z$ , represented by the turquoise arrow and the black dashed line. If the magnetisation starts to precess, indicated by the blue dashed line, the projection of the MOKE signal changes and therefore an oscillation is visible. If the applied external field is large compared to the internal magnetic anisotropy, as shown in figure b) the net magnetisation direction is aligned parallel to the field direction. In this case no precessional motion would be detected, as the projection of the magnetisation does not change. Cinematic animations of both processes can be found in appendix F, playable in the electronic file of the thesis.

weaken this effect an index matching fluid is used to connect the substrate of the sample to an additional substrate with a thickness of 2 mm. For further explanation see section 4.7.2.

**Fluence determination** The diameter of the pump pulse ( $\approx 1000 \mu\text{m}$ ) on the sample is roughly 3 times as large as the probing spot size ( $\approx 300 \mu\text{m}$ ). Both spot sizes are determined with a CCD placed at the same distance from the lenses as the sample. For determination of the fluence we use the values where the 2D-Gaussian profile of the pump pulse is reduced to  $1/e$ . For our experiments a good approximation of the fluence is necessary in order to make an assumption about the temperature increase in the sample. For a detailed description of the fluence comparison see the appendix chapter B.

### 4.3 Hysteresis Measurements

To measure the static and dynamic magnetisation properties hysteresis measurements are performed. A hysteresis relates the applied external magnetic field with the internal sample magnetisation. The conducted MOKE experiments do not yield an absolute value for the magnetisation, but a relative change. However if a static hysteresis can be measured the dynamic changes can be quantified in relation to that equilibrium value. The setup of the time resolved evolution of the magnetisation and the hysteresis measured at different time delays is the same, so in both cases a reference value is available at the closed chopper position.

**Static Hysteresis** For static hysteresis measurements the electromagnet is ramped to the maximum value of  $\pm 5.1 \text{ A}$  on a minute timescale. The resulting field at the sample position depends on the distance of the poleshoes. The static measurements are performed without signal modulation. The hysteresis measurements give a normalisation value for the relative demagnetization observed in the time resolved

signals. The static measurements are performed with the shutter of the pump pulse closed. Each point on the hysteresis is acquired around 50 times and additionally the hysteresis loop is measured repeatedly to reduce the signal to noise ratio.

**Transient Hysteresis** To gather additional information about the time resolved behaviour of the magnetisation change we measure the hysteresis after excitation with a laser pump pulse. Two MOKE values at each external magnetic field value  $B$  are measured: the value  $M$  for the transient hysteresis at the stage delay  $t$ , but also the reference value  $M$  at the closed chopper position, thus measured  $\approx 1$  ms after excitation. This measurement is a transient reference hysteresis. Between the different measurements of the excited states the sample is not saturated again.

## 4.4 Time-Resolved MOKE Measurements

The difference between the magnetisation value measured for the transient reference hysteresis and transient hysteresis at a set external magnetic field can be converted into the time resolved MOKE trace. When the external magnetic field is sufficiently large, the sample is saturated and during time resolved measurements the original magnetic state can be reproduced for every delay position by the applied external field  $B_{\text{ext}}$ . The direct comparison of the signal for the pumped and unpumped state of the sample reduces the noise compared to hysteresis measurements. A detailed description of the relation between the two measurement methods can be found in section 5.4.

## 4.5 Data Acquisition

The MOKE-Signal is created by measuring the change of polarization depending on the external magnetic field. The polarization change is detected by a balanced photodiode. The output intensity difference  $I_{\text{Diode}}$  is proportional to the ratio of s- and p-polarized light reflected from the sample while simultaneously the two single diodes detect the change in reflectivity (equation 4.2). An illustration of the timing sequences during the signal acquisition and the MOKE data generation is sketched in figure 4.3.

$$I_{\text{Diode}} = I_{\text{spol}} - I_{\text{ppol}} \quad (4.2)$$

Subfigure a) shows the timing of events relative to each other. The main laser trigger corresponding to an emitted laser pulse has a frequency of 1 kHz, so it is repeated every millisecond. The chopper is opening and closing at half of the frequency, so with every laser pulse it changes its state. The chopper position is shown in yellow (closed). The exact timing of the chopper window is determined by the position of the chopper in the laser path. While the chopper is synchronized to the laser trigger, it is positioned in the laser path such that one pulse passes through without being blocked for the open pumped state. The trigger for the DAQ card (green) is shifted by  $500 \mu\text{s}$ , so the data point of one measurement is taken in between two pulses.

Subfigure b) displays the diode signal (green) obtained at the boxcar. The integration gate of the boxcar (blue) indicates the area under which the data is integrated. The gate is larger than the actual diode peak to compensate for potential irregularities in the trigger position.

In subfigure c) the actual output of the boxcar is shown in blue. The green lines indicate the timing of the measurement card, so the moment one data point is measured. Corresponding to the chopper position it is clear to see that after one millisecond the signal changes slightly, but every two milliseconds a larger fluctuation in the signal is visible. The origin for this modulation is currently unknown, but the signal quality can be improved drastically with the pump probe comparison.

These boxcar outputs are measured for about 100 laser pulses for one measurement of the averaged intensity with open chopper window  $I_{\text{Diode, pumped}}$  and closed window  $I_{\text{Diode, unpumped}}$ . The delay-time

trace for both chopper positions is shown in subplot d). The excited state are shown in purple and the correlated unpumped states in blue. Here the time axis does no longer correspond to real time, but to the delay time introduced by the stage position change. For this measurement the magnetic field was applied in one direction, and the pump probe trace was measured once with each data point averaged over 100 laser pulses. The resulting time resolved pump probe measurements calculated by equation 4.3 are shown by subplot e).

$$I_{\text{PumpProbe}} = I_{\text{Diode, pumped}} - I_{\text{Diode, unpumped}} \quad (4.3)$$

It is clearly visible that the signal quality increases largely by this subtraction of the laser fluctuation. The combination of boxcar and chopper running at 500 Hz enables single pulse measurement. That means the usage of a lockin does not improve the quality of measurement and instead the real measured amplitude of the trace is preserved. The pump probe measurements are shown for two opposite external magnetic fields. The sign of the traces changes as expected, showing the magnetic origin of the signal.

In the last subfigure f) the resulting MOKE signal (dark green) and electronic Kerr signal (bright green) [90] are plotted. These signals are calculated according to equation 4.5.

$$I_{\text{magnetoOptical Kerr}} = I_{\text{PumpProbe, M+}} - I_{\text{PumpProbe, M-}} \quad (4.4)$$

$$I_{\text{electronic Kerr}} = I_{\text{PumpProbe, M+}} + I_{\text{PumpProbe, M-}} \quad (4.5)$$

The electronic Kerr signal indicates that a small non-magnetic contribution is measured. The origin for that is discussed in 4.7.1. An additional contribution to the magnetic signal is visible in the MOKE trace as well, the origin of that is described in 4.7.2. The time axis is shifted, so that the time zero  $t_0 = 0$  ps is related to the temporal overlap of pump and probe pulse. For these experiments this is equivalent to the beginning of the ultrafast demagnetisation.

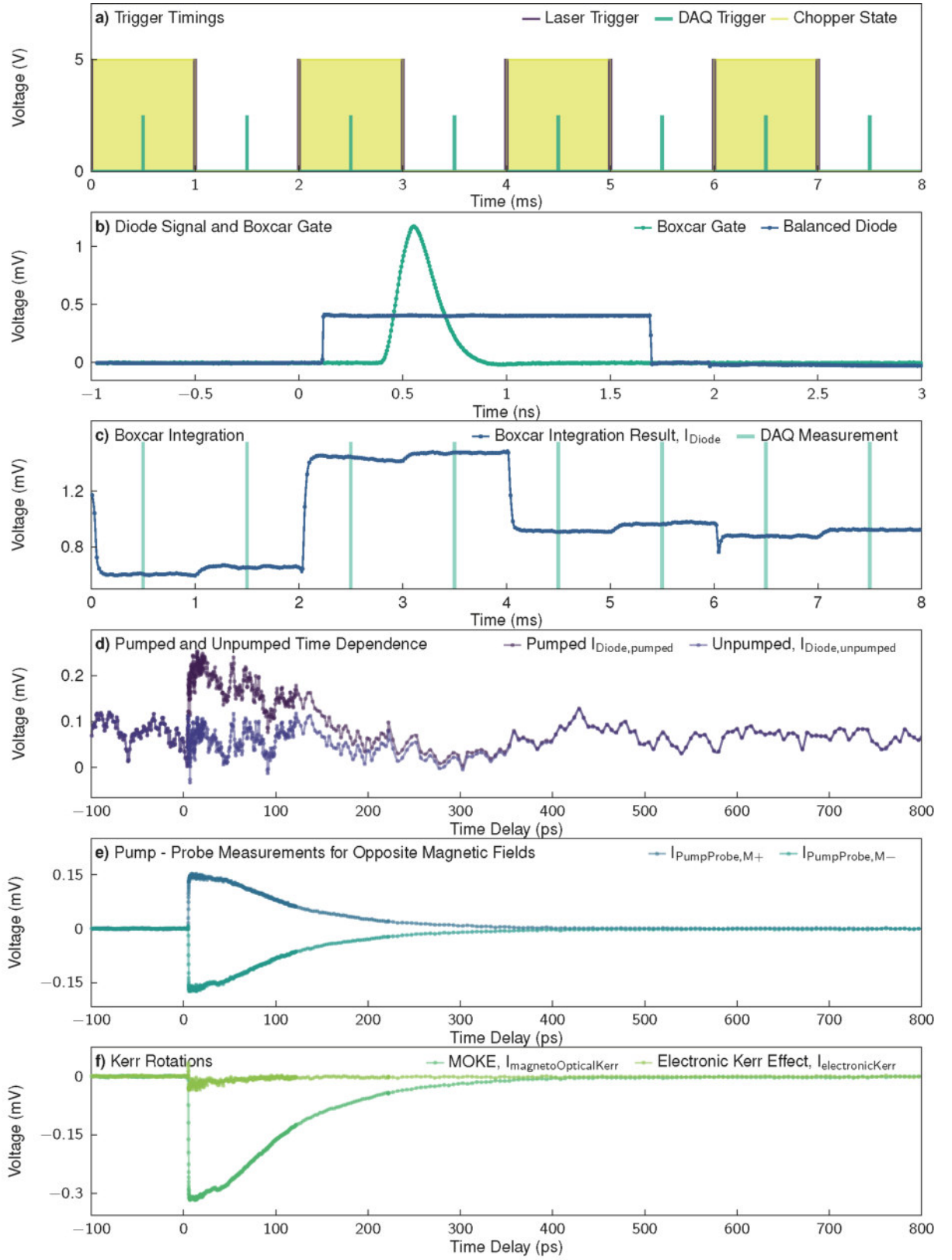


**Figure 4.3: Technical MOKE signal generation.** The detailed description can be found in the text.

## 4.6 Software

To measure the signals acquired by the hardware setup, a software was designed and implemented using the programming language *Python*. The latest version of this software *Labware - UDKM* used in this thesis can be found on *github.com* as release version v0.9 [91]. It consists of several applications for different experiments and hardware components such as beam stabilization and laser control panels.

The complete measurement flowchart of the MOKE software is presented in figure 4.5. The graphical user interface can be seen in figure 4.4. It consists of three main components. The side panel allows the setting of the measurement parameters and displays the current status of the measurement progress. The main window allows the choice of different tabs for displaying the current data. In the screen shot the resulting MOKE signal is displayed in the main window in the centre. The bottom panel displays the results for the pump probe measurements for each magnetic field direction. The tabs on top of each window allow the switching between the average of all loops and all single measurements layered on top of each other. The latter allows for a fast confirmation during the measurement that the loops are still probing the same undamaged spot on the sample. A detailed description can be found in the appendix C. Each of the three main measurement components (static hysteresis, time resolved hysteresis and time

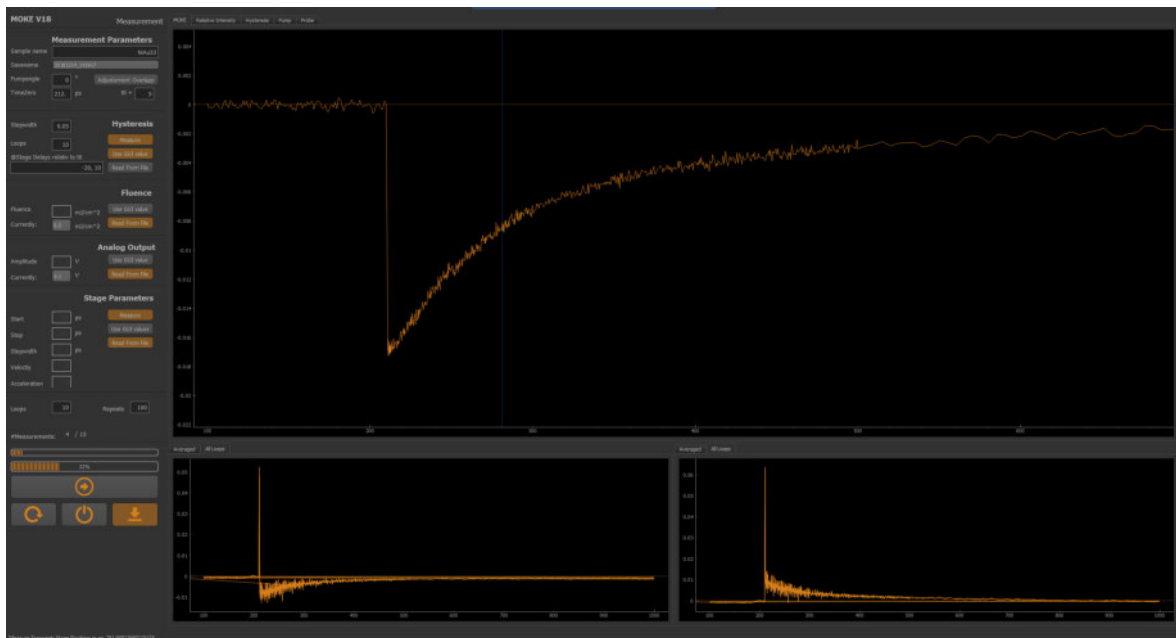


**Figure 4.4: Software user interface** Screenshot of the graphical user interface for the MOKE application of the *Labware - UDKM* framework.

resolved pump probe) can be performed independent of each other. Typical values for repeats and loops are indicated in the flowchart in figure 4.5. The exact values used depend on the signal-to-noise ratio of the investigated sample.

To measure the time resolved trace the stage position is changed according to the desired vector defining stepsize and position. At each position of the stage the measurement point for both chopper positions is repeated 100 times and averaged. The complete stage vector is now looped repeatedly. This can be performed at several values for the external applied field and several values for a set fluence.

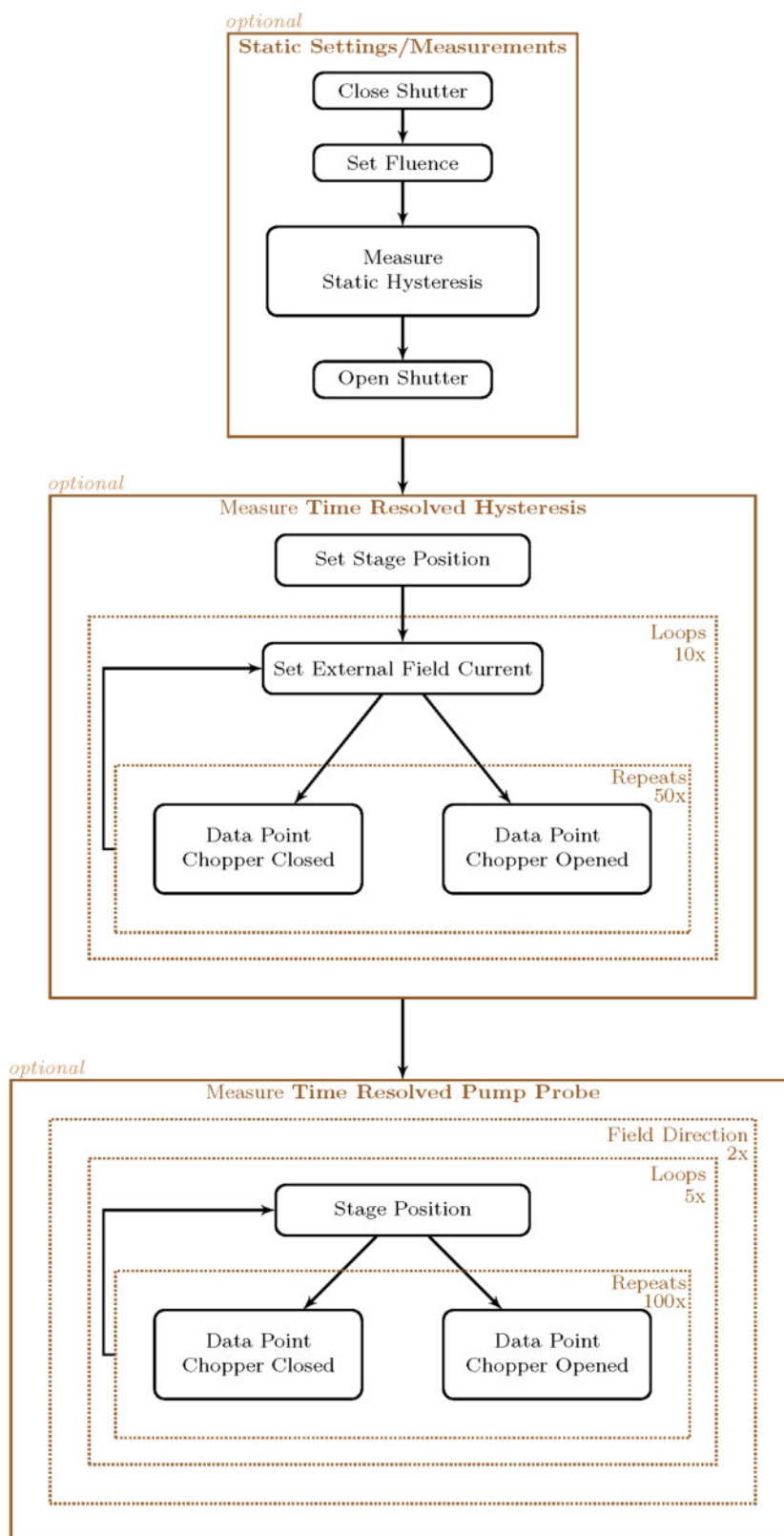


**Figure 4.5: Software flowchart.** Flowchart describing the order of measurement and physical parameters involved.

## 4.7 Additional Kerr Signal Contributions

Besides the desired magneto-optical response of the investigated sample, other signals can contribute to the rotation of the polarization. Two of those additional contributions are presented here, as they partially interfered with the signal analysis.

### 4.7.1 Molecules

As can be seen in figure 4.6, the nearly parallel alignment in the polar MOKE geometry can lead to a partial overlap of pump and probe pulse in air. When the fluences used for excitation are relatively high, this can lead not only to an excitation of the sample, but also of the air molecules. The probe beam can measure the response of the excited molecules as seen in figure 4.7.

This signal is independent of the magnetic field direction, which means it is only visible in the single pump probe traces,  $I_{\text{PumpProbe, M+}}$  and  $I_{\text{PumpProbe, M-}}$ , and the electronic Kerr signal  $I_{\text{electronic Kerr}}$ . The features are very sharp in time and have a considerable amplitude for at least 300 ps. The amplitude of the electronic Kerr signal compared to the magnetic Kerr signal depends on the exact alignment and the pump fluence. As these contributions are present in the sum of the Kerr measurements, they can be removed by taking the difference. Therefore they are not present in the MOKE traces. However, due to the sharpness of the feature, the molecules can introduce additional noise, because a slight change of the overlap after several loops or a less precise stage movement leads to a remaining signal in the resulting MOKE signal.

The excitation of air molecules is caused by the interaction of the electric field vector of the short laser pulse and the molecular polarizability.

Because air molecules are non-spherical they experience a torque from the electrical field acting on the rotational degree of freedom. The molecule is spatially aligned by the propagating vector of the pump pulse and the probe pulse measures birefringence in air. The signal manifests itself as peaks and dips in the electronic Kerr trace. The molecules keep rotating after the initial pump pulse passed so that the alignment is revived after the rotation period. See Renard et al. [92] for further explanation.

The molecule alignment can be detected with the method of electronic Kerr measurements [90], because the molecule alignment in space creates a birefringence, as explained by Marceau et al. [93]. The signal is therefore related to the alignment factor  $\langle \cos^2\theta \rangle(r, t)$ . From the numerical calculations by Marceau et al. the peaks of nitrogen and oxygen in the first picoseconds can be identified. From the measurements of Renard et al. [92] the revivals of carbon oxide can be determined. In the figure 4.7 the clearly identified peaks from these papers are marked in the respective colours. The other features can be identified with the knowledge of the rotation period of the molecules as well, but the analysis is not topic of this thesis.

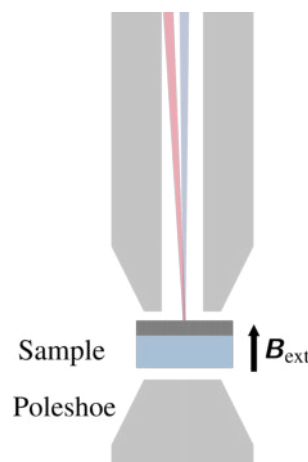


**Figure 4.6: Sample Environment.** Pump and probe pulse hitting the sample. Because the beams are passing the pole shoe through a small hole they overlap partially in air.

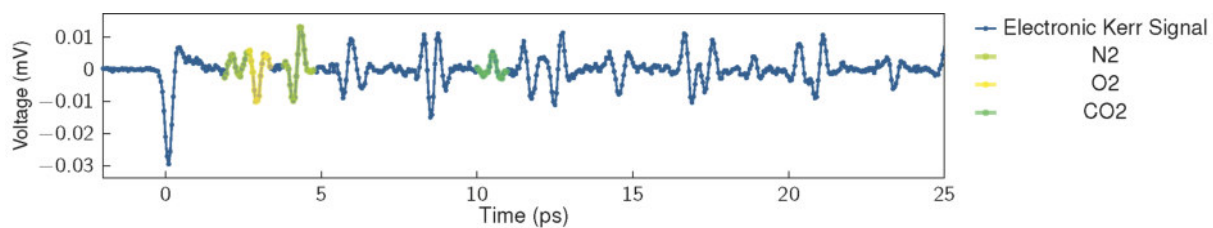


**Figure 4.7: Electronical Kerr signal  $I_{\text{electronic Kerr}}$  of rotating molecules.** Electronic Kerr signal  $I_{\text{electronic Kerr}}$  from excited rotating air molecules in the overlap region of pump and probe pulse. From the references identified features are highlighted and assigned to specific rotating molecules.

### 4.7.2 Second Excitation

In some of the magneto-optical measurements presented in this thesis a second excitation of the sample can be observed, as shown in figure 4.8 in a measurement of a continuous Iron Platinum film (see chapter 5) pumped with an incident fluence of  $F_{\text{inc}} = 8.0 \text{ mJ/cm}^2$  in green, and a measurement of granular Iron Platinum excited with  $F_{\text{inc}} = 10.0 \text{ mJ/cm}^2$  in blue. This excitation is present either around 5 ps (green) or around 25 ps (blue) after the time zero. As can be seen in the zoomed figure, the shape of the feature is

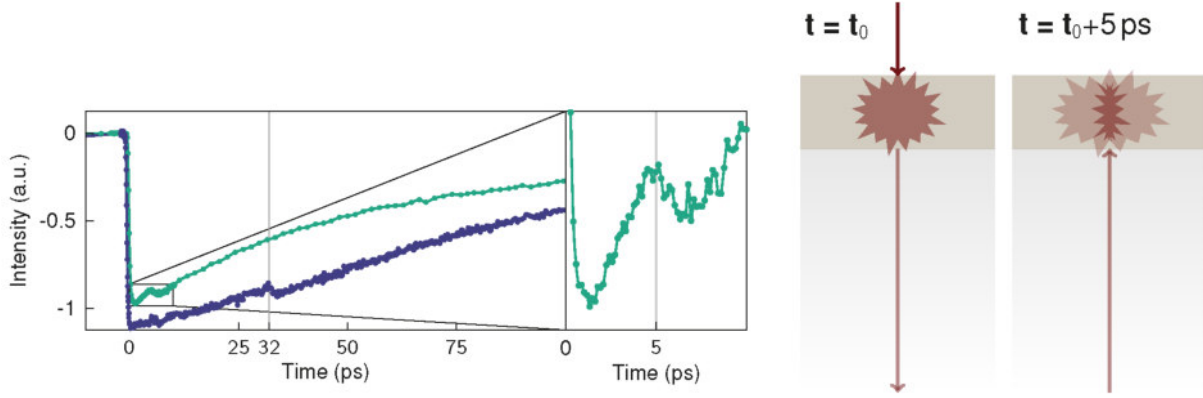


**Figure 4.8: Back Reflection.** Additional demagnetisation introduced in the sample after 5 ps and 32 ps, corresponding to the pump pulse entering the probed layer for a second time after being reflected from the back of the thin and thick substrate, respectively.

not symmetrical, but rather a second rapid demagnetisation. According to the occurring time of 5 ps for the green curve, it is possible to trace the origin to the reflection of the incoming pump pulse from the back of the substrate. In all of the samples investigated in this thesis the film is thin and the transmission is sufficiently large to introduce a second excitation. The substrate that was used in all experiments is Magnesium oxide (MgO) with thicknesses of around  $d = 500 \mu\text{m}$ . These back reflection artefacts are also visible when an incident angle of  $45^\circ$  is used, as the refraction index causes the light to be refracted towards a steeper angle. To prevent this excitation to appear, we used an index matching oil and an additional MgO substrate with a thickness of 2 mm. This reduced the second excitation, but in some measurements a second demagnetisation can be observed after about 30 ps.

The travelling time  $t$  of the pump pulse through the sample is given by equation 4.6. The velocity is the speed of light  $c$ ,  $d$  is the total thickness of the sample ( $d = 500 \mu\text{m} + 2 \text{ mm}$ ) and the refractive index of MgO,  $n_{\text{MgO}}$ , which is around 1.73 [94]. With these parameters the second excitation with a thick substrate would be expected after  $t \approx 29 \text{ ps}$ . In the blue measurement, the second excitation is observed approximately 32 ps after time zero. The shift might be added by a longer travel path caused by a thick layer of index matching fluid.

$$t = \frac{2dn_{\text{MgO}}}{c} = 28.9 \text{ ps} \quad (4.6)$$

## 5 | Magnetisation Dynamics in Iron Platinum

Iron has been an important material for humans and their development. The oldest artefacts created of Iron could be dated to 3200 BCE. The Iron reached the surface of the earth as meteorites, which gave it at first names translated to stone from heaven. Later on the ore was extracted from mountains and wrought Iron was utilised, marking the beginning of the Iron Age (around 1500 BCE). [95, 96]

On the contrary Platinum was unknown for a much longer time. It was used in South America to create jewellery for hundreds of years, before European sailors and Spanish settlers discovered the "little silver" (span. *platina*) and brought it to Europe in 1745. [97]

Since 3000 BCE the idea of mixing elements or alloys together to improve the properties of a material was known. The first popular mixing of Copper and Tin to bronze also marked the beginning of the so-called Bronze Age [96]. However, the technological possibilities for manufacturing materials like alloys of Iron Platinum on a nanoscale are only present for the past 30 years.

The material Iron Platinum (FePt) is of great interest for industry applications, as it is used in hard drives as magnetic material to store binary data. The technological challenges in creating more storage space with better properties in terms of environmental impact, durability and cost efficiency promote the investigations on this system. However, extensive knowledge about parameters like heat capacity  $C_p$ , thermal expansion coefficients  $\alpha$  and other properties characterized by bulk experiments is currently not available.

The set of samples presented in this chapter consist of a thin continuous film and a granular film of FePt. The structural investigations with time resolved UXRD measurements presented by von Reppert et al. [98] were performed on the same samples as the magneto-optical measurements discussed in this chapter.

Similar samples have been studied with electron diffraction by Reid et al. [99] and with ultrafast small-angle X-ray scattering by Granitzka et al. [100]. A study by Hovorka et al. [101] investigates the Curie temperature of granular FePt depending on the size of the nanoparticles.

Additionally, time resolved magneto-optical measurements have been performed by Becker et al. [102] and He et al. [103], investigating precession dynamics in granular FePt. Similar experiments have been conducted by Chen et al. [104], Mizukami et al. [105] and Iihama et al. [106] on a continuous FePt sample. Time resolved investigations of the demagnetisation depending on the incident fluence has been performed by Mendil et al. [7] and by Zhao et al. [14], who also investigated time resolved hysteresis and remagnetisation on longer timescales.

In this thesis the magnetisation dynamics of FePt were investigated by measuring the static and time resolved hysteresis as well as time resolved MOKE pump probe. The influence of both fluence and external applied magnetic field were investigated by measuring systematic series. The results will be compared to the structural dynamics in chapter 7.

The following section 5.1 will briefly discuss the interest in this alloy. The characteristics of our samples are described in section 5.2. Section 5.3 will present the results for the hysteresis measurements for both samples. Section 5.4 will discuss the connection of the time resolved trace related to the hysteresis measurements and present the time resolved traces for the continuous and granular film. In the last section of the chapter 5.5 the time resolved remagnetisation signal and the time constants are shown.

## 5.1 Motivation

A main objective for the development of hard drives is the increase in efficiency, thus the materials are optimized in order to fulfil the requirements. Currently one logical bit is saved by the magnetic orientation of nanoscale grains. These grains have a stable magnetic orientation at room temperature and are switched under the influence of a magnetic field. To increase the stability of the grain orientation a larger number of nanoparticles represents a single bit. The efficiency of a magnetic hard drive storage is limited by the balance of grain size to thermal stability. It would be ideal to use as little grains as possible and also a small number of grains per written bit, but the increase in thermal fluctuations would decrease the stability of the saved data. One promising method for writing long time stable data in small volumes is *Heat Assisted Magnetic Recording* (HAMR). In this process a laser pulse is utilized to heat the material locally above the Curie temperature and write new information to a bit during the cooling phase. Because the magnetic grains are only heated locally for a short period of time, their size can be reduced and the thermal stability is increased with Curie temperatures far above room temperature. [4, 107]

The material of the nanoparticles ideally possess properties such as high magnetic saturation fields as well as a medium Curie temperature with high coercive fields and out of plane anisotropy, as the reading head is measuring the stray field emitted by the granular media. These criteria are well met by the alloy of Iron and Platinum, FePt. It can be grown in an ordered L10 phase with a simple unit cell configuration (see figure 5.1) with high anisotropy and a large saturation value originating from the Iron 3d band [108].

Another important question for applications and the understanding of the origin of the magnetic properties is the speed of de- and remagnetisation. The magnetisation dynamics for the FePt alloy was modelled by Kazantseva et al. [109], who included a combination of atomistic and micromagnetic simulations to use a multimacrosin approach for describing the behaviour of FePt grains. They predict on short timescales of picoseconds a slower recovery of the magnetisation after excitation with high fluence than with low fluence. This has been observed by Zhao et al. [14], who also saw a complete demagnetisation in the transient hysteresis at high fluence for the first picoseconds. Also Mendil et al. [7] reported a slowing down of the remagnetisation with high fluence on a short timescale. However, they did not observe a complete demagnetisation of their 3 nm thick FePt layer.

## 5.2 Sample Characterization

The samples investigated in this chapter are summarized in table 5.1. The first FePt sample consists of a FePt layer of 9.7 nm and 1 nm Aluminium as protecting capping layer on top grown on a MgO substrate with (100) orientation. The second FePt sample consists of FePt nanoparticles. Those grains have a height of approximately 9.5 nm, their average lateral size is 10 nm. The particles are embedded in a matrix of amorphous carbon.

	Magnetic Layer	Capping Layer	Substrate	Internal Identifier
1	FePt 9.7 nm continuous	Al 1 nm	MgO(100) $\approx 500 \mu\text{m}$	CH2281b
2	FePt 9.5 nm granular islands		MgO(100) $\approx 500 \mu\text{m}$	OH140

**Table 5.1:** Sample structures and designations of FePt films discussed in this chapter.

A schematic version of the sample structures can be seen on the left in figure 5.1. The right image shows the unit cell of FePt. The standard unit cell is a face-centred cubic lattice arrangement with a statistical occupation by Fe and Pt atoms. In case of low temperatures an ordered FePt L10-phase is formed. This ordered phase has a tetragonal unit cell with a Pt-atom in the centre surrounded by Fe-atoms. The anisotropy of both samples leads to an easy axis out of plane. The corresponding out of plane static

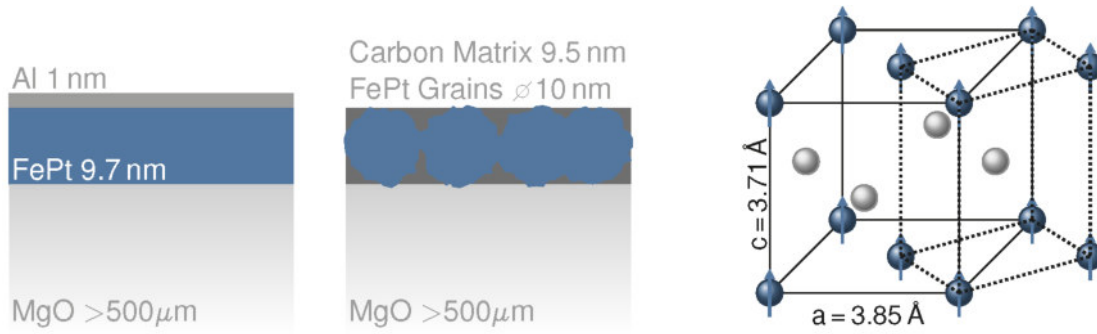


**Figure 5.1: Schematic sample structure of the investigated FePt samples.** Left: Structure of the continuous film and granular sample with respective layer thickness as described in table 5.1. Right: Unit cell of FePt in the ordered L10 phase with the Iron atoms in blue and Platinum atoms in grey.

hysteresis is shown in figure 5.2. Comparing the static hysteresis of both samples in figure 5.2 a) the difference in amount of FePt in the granular film and continuous film can also be confirmed: The total magnetisation value per cubic centimetre is reduced by a factor of approximately 1/3-rd. According to the sample growth process this is the estimated amount of volume taken by the carbon matrix. The continuous sample has a coercive field of around 500 mT and a rapid change to the other magnetisation direction. The switching of magnetic direction in a continuous film is done not only by magnetic domain rotation but also domain wall movement [20] (see section 3.1). In contrast, the granular film has a high coercive field of at least 5 T. The domain wall movement is not possible across particle boundaries so every particle has to be switched on its own. As it can be seen in the hysteresis loop of the granular sample, the field necessary for switching the particles is distributed over a range of 2-3 T, so that the saturation magnetisation is reached at a high value of 8 T. The ferromagnetic behaviour versus temperature in figure 5.2 b) shows that the

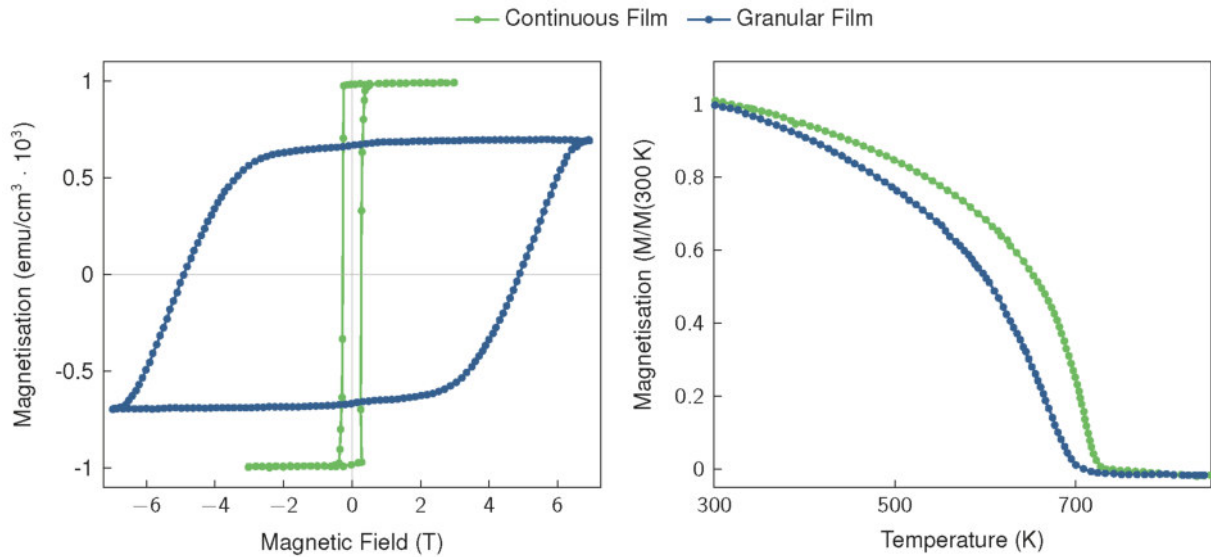


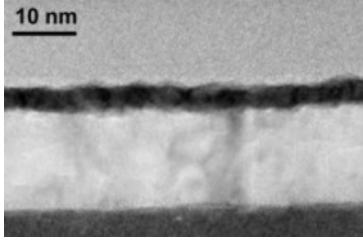
**Figure 5.2: Static characterisation of FePt samples.** a) Static hysteresis loop measured with a superconducting quantum interference device (SQUID)-vibrating sample geometry (VSM) (*Quantum Design*). b) Temperature dependence measured with PPMS (Physical Property Measurement System, *Quantum Design*). The blue line corresponds to the granular, the green line to the continuous film. These static characterisations were provided by the sample growers Fabian Ganss and Olav Hellwig (TU Chemnitz).

Curie temperature of both samples is very similar. The continuous film starts the magnetic ordering at a temperature of  $T_C = 725$  K, the granular film at  $T_C = 700$  K. The static demagnetisation is steeper for the granular film than for the continuous film. This can be attributed to the particles having a distribution of Curie temperatures and partially acting as isolated, single magnets. As Hovorka et al. [101] have shown,

the Curie temperature distribution depends on the average particle sizes and it gets more significant for smaller average diameter. The temperature dependent data were measured on samples comparable to the investigated ones. The hysteresis measurements are taken from the two investigated samples.

The distribution of size and position of the particles to each other is not completely equal, as can be seen in the image 5.3 b) obtained with a scanning electron microscope (SEM) measurement. It has been

a) Continuous Film



b) Granular Film

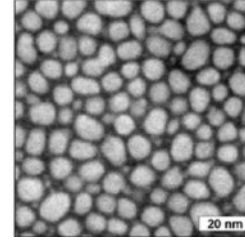
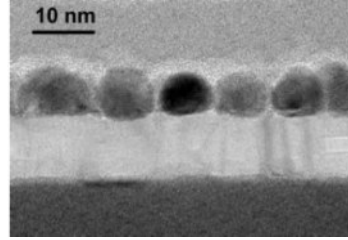


**Figure 5.3:** SEM images of similar FePt samples from Mendil et al.[7]. a) continuous film from side view, b) granular film in side and top view.

shown by Granitzka et al. [100] that the position of the grains to each other influences their absorption behaviour. Figure 5.4 a) shows that the optical absorption of grouped particles is locally enhanced by nearly 10% compared to isolated particles. The enhancement occurs when particles are close enough to exhibit plasmonic resonance [100].

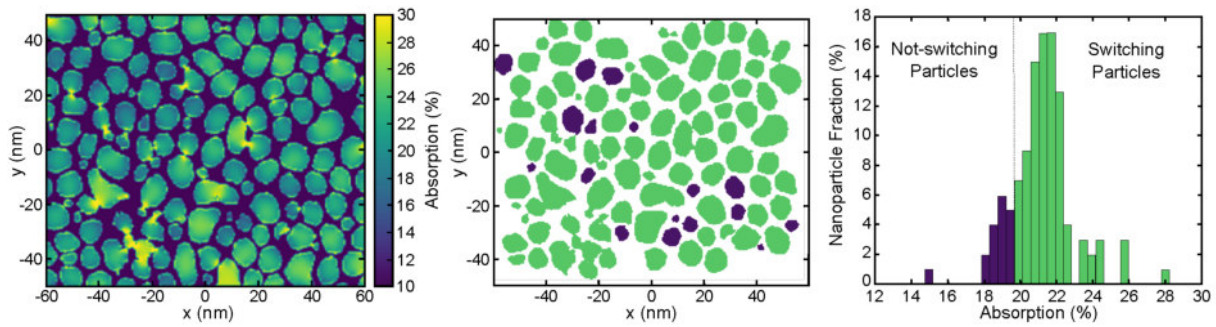


**Figure 5.4: Absorption of the FePt granular film.** a) Optical absorption of 800 nm. If the grains are close to each other, the absorption is enhanced by plasmonic resonance. This leads to a different amount of switching grains at the same incident fluence and applied magnetic field. b) shows the resulting magnetisation switch. Some isolated grains are not switched (purple) while the majority is oriented in the new magnetisation direction (green). The incident fluence is reported to be 11 mJ/cm<sup>2</sup> and the applied field was 0.4 T. Subfigure c) shows the percentage fraction of particles at a certain absorption value. The dashed line indicates the threshold for the applied incident fluence and magnetic field. The position of this value will shift depending on fluence and field. Images from [100]

### 5.3 Time-Resolved Hysteresis Measurements

The figures 5.8 and 5.9 display a matrix of MOKE hysteresis measurements for the continuous and granular film, measured with the optical setup described in chapter 4. Vertically, the plots show the measurement for different fluences, whereas horizontally the pump probe delay is varied.

For the continuous film the measurement highlighted by the grey rectangle in the first column displays the static hysteresis loop without any pump pulse excitation as reference.

The grey hysteresis represents the transient reference measurement at the closed chopper position 1 ms after excitation. The second column is a measurement of the transient hysteresis before time zero, so nearly 2 ms after the last pump pulse excited the sample. The grey reference hysteresis and the coloured transient hysteresis are overlapping in this column, indicating that no change in the magnetisation can be

resolved between 1 ms and 2 ms after excitation. The coloured hysteresis represent the transient hysteresis measurements at the time delay. The colour code indicates the excitation fluence and is also used for other MOKE traces with fluence variations.

The hysteresis measurements were performed during pumping the sample, so at each measurement point the sample was pumped before the last magnetic field value was applied. The sample was not saturated in between. So the coloured hysteresis is a collection of virgin hysteresis branches (pumped state) and their recovery (unpumped state). Depending on the used fluence the starting value for the remagnetisation is varied (see figure 5.7).

In short, the two matrices of hysteresis measurements give a series of snapshots in time of the magnetisation recovery for each fluence.

### 5.3.1 Continuous FePt Film

Figure 5.5 shows the static hysteresis (first column of the matrix 5.8) in a) and the transient reference hysteresis (second column) in b). This makes it possible to compare the change from the static hysteresis to the hysteresis before the time zero depending on the incident fluence. The sample is no longer in an excited state but has a reduced coercive field due to the previous excitation. A difference in shape of the transient hysteresis to the static hysteresis is only visible, when a certain threshold fluence is crossed. Before that, the hysteresis shape is not changed. The static hysteresis can be described with two distinct parts: a flat component describing the change of magnetisation between saturation magnetisation to remanence magnetisation described by a linear slope  $m_{\text{rem}}$  at remanence; and the transition to a large change of internal magnetisation when an external field above the coercive field value is applied in the opposite direction, described by the linear slope  $m_{\text{coer}} = \partial M / \partial B_{\text{coer}}$ . The two slopes are indicated in figure 5.5 a) as black lines. They will be used as reference values to describe the hysteresis.

The hysteresis of the continuous sample shows a nearly square like behaviour. So the magnetisation loss between the saturation magnetisation and no external field applied is small, therefore  $m_{\text{rem}}$  is small, and a rapid change in a small range of field close to the coercive field described by a large value for the slope  $m_{\text{coer}}$ . Above the fluence threshold, which can be determined as larger than  $2 \text{ mJ/cm}^2$  but lower than  $5 \text{ mJ/cm}^2$ , the coercive field starts to decrease, the hysteresis loop gets narrow. Also the slope  $m_{\text{coer}}$  decreases while  $m_{\text{rem}}$  increases. Figure 5.6 depicts the change of the hysteresis shape at certain values

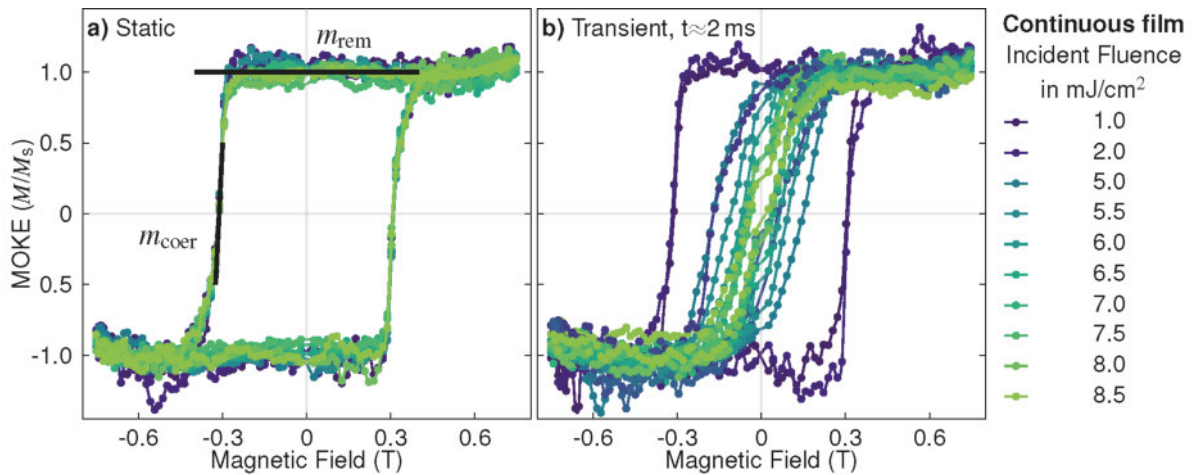


**Figure 5.5: Static and transient hysteresis measured before time zero of continuous FePt.** Comparison of a) the static hysteresis without excitation and b) the transient hysteresis loop obtained before time zero with different incident fluences. The two slopes  $m_{\text{coer}}$  and  $m_{\text{rem}}$  used for describing the shape of the hysteresis loops are indicated in black in figure a).

for the time delay for different fluences. Roughly 1 ps after time zero in subplot a), the magnetisation

for fluences higher than  $6.5 \text{ mJ/cm}^2$  is close to zero over the range of the applied external field. In this measurement the hysteresis deviates slightly from zero. Comparing the transient vs transient reference hysteresis in figure 5.8, it is apparent that this deviation is largely a noise contribution, as the transient reference hysteresis measured simultaneously for each transient hysteresis exhibits this shape as well. It seems to be correlated with the 500 Hz-fluctuations of the laser mentioned in section 4.5, as it changes for every fluence but is consistent for the direct pumped-unpumped comparison.

For low fluences below  $2 \text{ mJ/cm}^2$  the coercive field of the transient hysteresis does not shrink. The pump pulse only induces a reduction of the total net magnetisation. The slopes  $m_{\text{coer}}$  and  $m_{\text{rem}}$  are equal to the static measurement. The recovery is comparably fast: At a time of roughly 25 ps after the excitation the low fluence hysteresis have already reached their original amplitude and therefore have fully recovered their initial state. With increasing fluence the differences in shape from static to transient hysteresis are getting more pronounced: The open part of the loop is narrowed as a result of smaller coercive fields and a reduction in  $m_{\text{coer}}$ . Also the saturation magnetisation is reduced. In addition the transient hysteresis before time zero (nearly two milliseconds after the last pump pulse) has a lower coercive field and a small slope  $m_{\text{coer}}$ .

Transient hysteresis for fluences in the medium regime of  $5.5$  to  $6.5 \text{ mJ/cm}^2$  are growing faster in their magnetisation amplitude and also change their shape from closed to open square-like hysteresis. In the high fluence regime the recovery of the original hysteresis loop takes longer, the magneto-optical signal stays small for a longer time period. At 25 ps in figure 5.6 b), the hysteresis loop is still mostly closed and the amplitude grew only slightly. After 100 ps this behaviour continues: Figure 5.6 c) shows that the medium excited signals have not fully recovered to the original saturation value, but the hysteresis is clearly open. The high fluence hysteresis are lower in amplitude, but the slope  $m_{\text{coer}}$  increases.

At a certain fluence the transient hysteresis around time zero is closed (so  $M_{\text{rem}} = 0$  and  $B_{\text{coer}} = 0$ ) and has a linear dependence on the external field. This means both slopes are equal,  $m_{\text{coer}} = m_{\text{rem}}$ . It is fluence dependent at which time they start to be different again. For higher fluence they are indistinguishable on a longer timescale. In figure 5.7 the static hysteresis measurements after demagnetisation with the respective

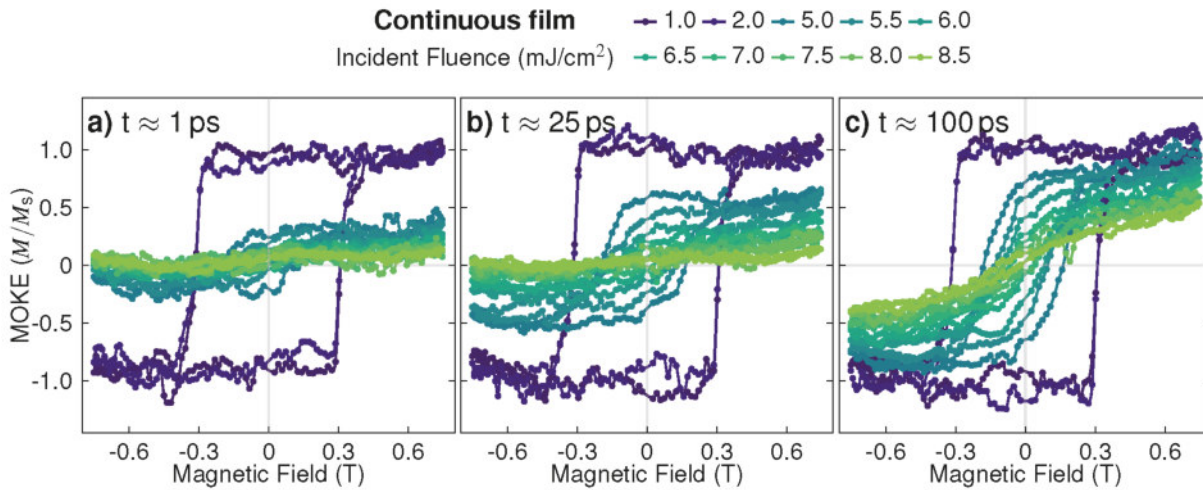


**Figure 5.6: Transient hysteresis of continuous FePt.** Hysteresis obtained at delay times of a) 1, b) 25 and c) 100 ps with different incident fluences.

fluence are shown. These measurements are recorded as follows: After laser excitation without an external magnetic field applied, the pump laser is blocked and the external field is increased to saturation. There is no averaging of loops performed, only the data points at one field value are averaged. They represent the initial magnetisation dependence after disorder, the virgin magnetisation branches after full demagnetisation. A complete static reference hysteresis is indicated in grey.

As before it shows that a fluence of  $3.0 \text{ mJ/cm}^2$  and lower does not change the magnetisation order in the sample irreversible. The initial magnetisation value is equal to the remanent magnetisation of the reference hysteresis, so the measured transient magnetisation reduction was not permanent. Starting with a fluence of  $4.0 \text{ mJ/cm}^2$  the initial magnetisation state is reduced compared to the reference. The magnetisation disorder induced with the excitation pump pulse has created a metastable domain state with a net magnetisation. At higher fluence the initial net magnetisation is reduced further until it reaches zero.

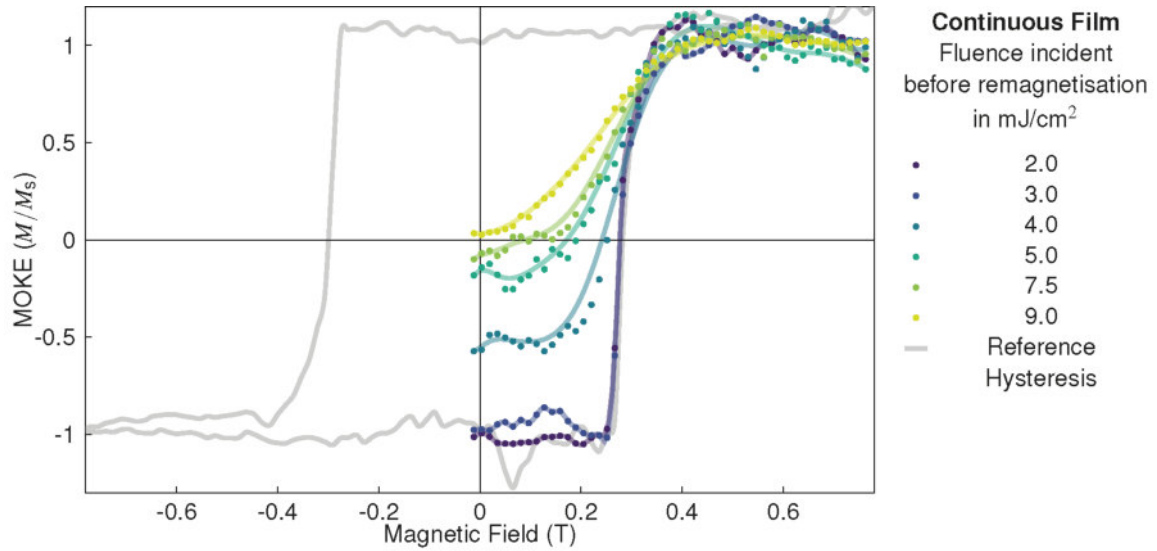


**Figure 5.7: Initial magnetisation after pump excitation of the continuous FePt film.** The grey line represents a static reference hysteresis loop, the coloured lines are the initial magnetisation branches after pump excitation with the fluence values indicated in the legend.

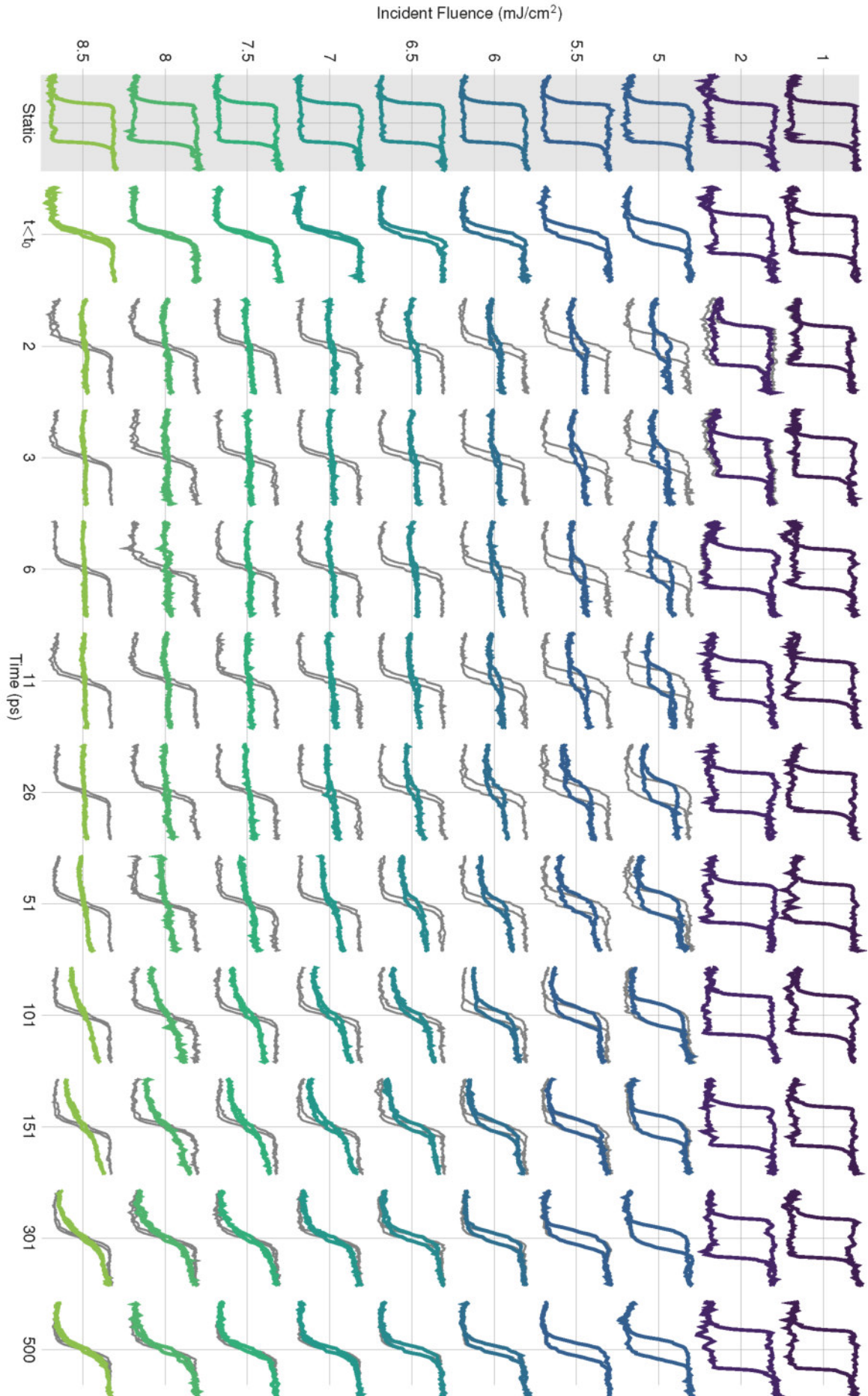


**Figure 5.8:** Time resolved, fluence dependent hysteresis measurements of continuous FePt. Caption continues on next page.

**Figure 5.8: Time resolved, fluence dependent hysteresis measurements of continuous FePt.** The static hysteresis in column 1 (grey rectangle, no laser excitation) and the transient hysteresis before time zero ( $\approx 2$  ms after excitation) in column 2 are shown as reference. The grey hysteresis is the corresponding transient reference hysteresis (last pump pulse excited the sample  $\approx 1$  ms before the measurement). The coloured hysteresis represents the hysteresis of the excited sample at a certain fluence. The transient reference hysteresis in column 2 is identical to the transient hysteresis, it is therefore hidden below the transient measurement.

### 5.3.2 Granular FePt Film

For the granular film shown in figure 5.9 no static measurement can be performed in this MOKE setup, as the external magnetic field required to change the magnetisation direction of the nanoparticles statically would be 8 T. Nevertheless the magnetisation dynamic and recovery can be investigated by using the effect of heat assisted switching. The grey coloured reference column displays the hysteresis measured nearly 2 ms after the last excitation. Due to the reduction of the coercive field upon laser heating, a transient hysteresis can be measured (coloured). As with the continuous sample the colourcode indicates the fluence used for the laser excitation. In the range of the available external magnetic field the static minor hysteresis loop is shifted along a flat part of the major hysteresis loop shown in blue in figure 5.2 a). The flat part refers to the region close to the remanent magnetisation, where the slope of the hysteresis,  $m_{\text{rem}}$ , is close to zero. The minor loop for the continuous sample is discussed in section 5.3.3. An example for comparison of static minor and major hysteresis loops on a similar sample (nanoparticles of FePtAg-C) can be found published by Pisana et al. [110]. During static measurements the signal is only shifted along the flat part of the square-shaped hysteresis. With an excitation pump pulse the minor hysteresis loop also changes in shape and amplitude and it is possible to measure an open loop for this granular sample, as well.

Figure 5.10 a) shows a summary of the transient hysteresis before time zero. The analysis of the amplitude of the MOKE signal in b) indicates a threshold under which the majority of grains is not switched by the chosen combination of external field and incident fluence. The fluence for switching a significant amount of grains at a field of  $B_{\text{ext}} \approx 1$  T must be higher than  $2.5 \text{ mJ/cm}^2$ , but lower than  $5.0 \text{ mJ/cm}^2$ . This is indicated by the open hysteresis in the second row of the hysteresis matrix, which can be obtained with  $5.0 \text{ mJ/cm}^2$  laser-heating. However the available data points for the demagnetisation amplitude do not indicate a saturation value for the MOKE amplitude.

As seen before for the continuous sample the shape of the transient hysteresis before time zero changes with more absorbed energy (fig. 5.10 a)): At low fluence no hysteresis is visible, so only a slight change of saturation magnetisation caused by the movement along the remanent slope of the major hysteresis branch is measured during a time resolved pump probe measurement. At  $5.0 \text{ mJ/cm}^2$ , the hysteresis is opened widest for all the presented fluences. This means the coercive field  $B_{\text{coer}}$  for the switching grains is still large, but already reduced compared to the static hysteresis. For higher fluences the field is reduced further, so that the hysteresis loop is narrow. The slope  $m_{\text{coer}}$  is growing continuously with the fluence increase. Compared to the continuous film the transient reference hysteresis of the granular sample is not similar to a square, so the two slopes  $m_{\text{coer}}$  and  $m_{\text{rem}}$  are very similar. In figure 5.9 the column for the lowest fluence of  $2.5 \text{ mJ/cm}^2$  reveals only a small decrease in the magneto-optical signal after excitation, but the majority of grains does not switch the magnetisation to the opposite field.

At  $5.0 \text{ mJ/cm}^2$  the reduction in the magneto-optical magnitude is still visible, as the hysteresis measurement is not centred around zero. This indicates that only a small fraction of grains switches. The offset to zero is not visible for the two higher fluences, indicating that the amount of switching particles is high enough, so that the contribution to the signal from not-switching particles is insignificant and hidden in the noise. The increase in the magneto-optical amplitude of the complete hysteresis loop is also indicating that more particles switch at higher fluences.

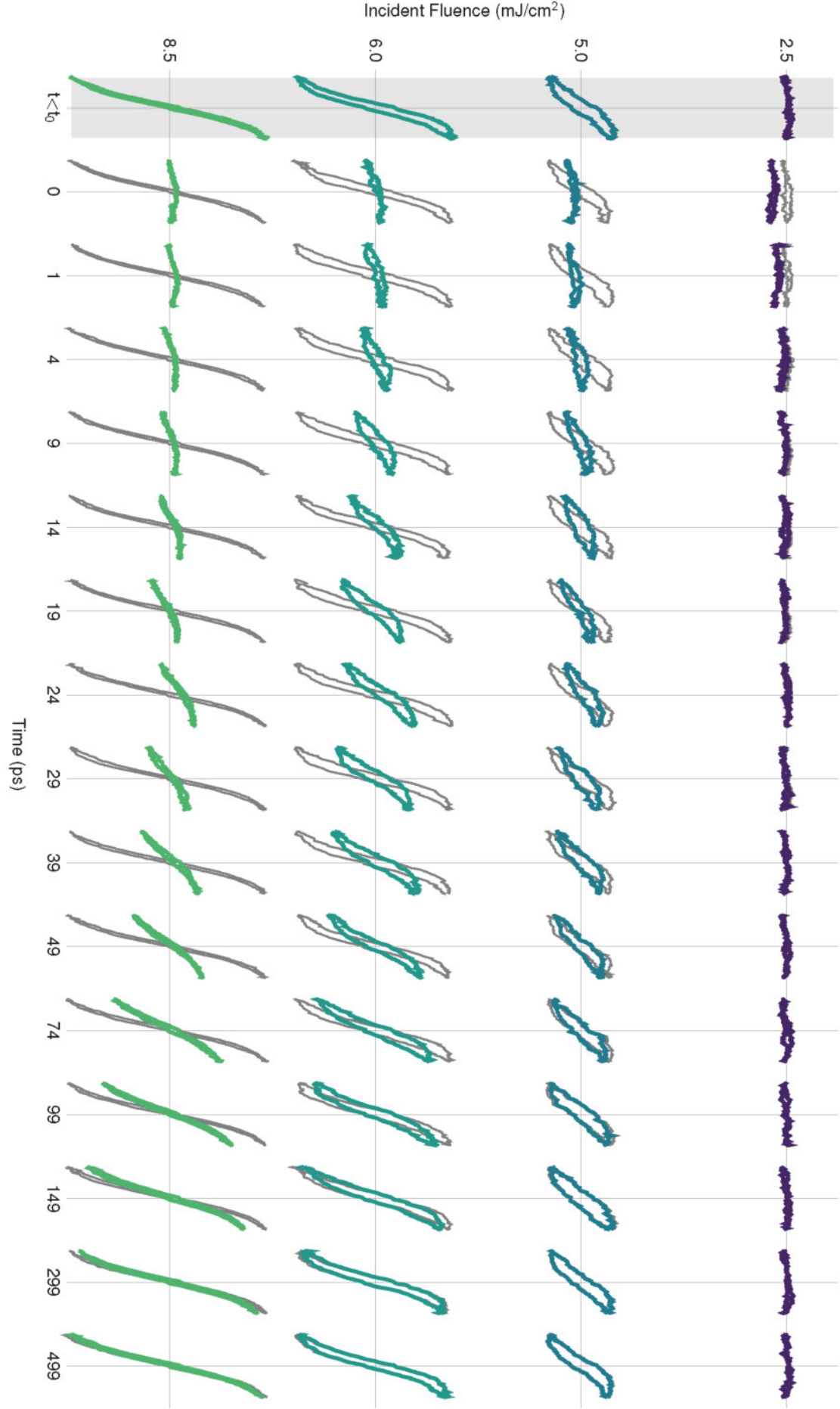
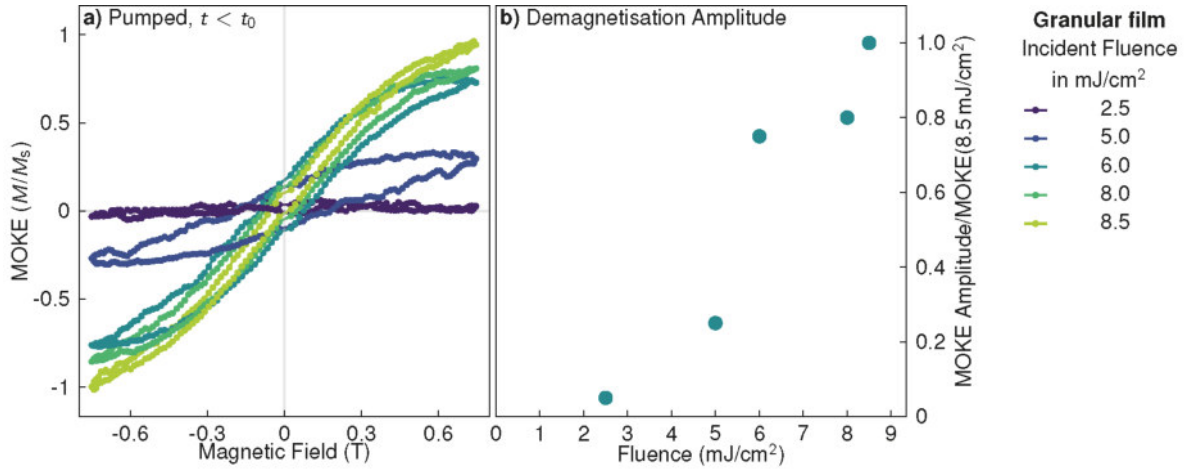


Figure 5.9: Time resolved, fluence dependent hysteresis measurements of granular FePt. The caption continues on the next page.

**Figure 5.9: Time resolved, fluence dependent hysteresis measurements of granular FePt.** The static hysteresis in column 1 (grey rectangle, no laser excitation) and the transient hysteresis before time zero ( $\approx 2$  ms after excitation) in column 2 are shown as reference. The grey hysteresis is the corresponding transient reference hysteresis (last pump pulse excited the sample  $\approx 1$  ms before the measurement). The coloured hysteresis represents the hysteresis of the excited sample at a certain fluence. The transient reference hysteresis in column 2 is identical to the transient hysteresis, it is therefore hidden below the transient measurement.



**Figure 5.10: Transient reference hysteresis measured before time zero of granular FePt.** a) Comparison of the transient reference hysteresis obtained before time zero measured with different fluences, b) comparing the MOKE hysteresis magnitude of each of the hysteresis in a) to the highest magnitude measured with  $F_{\text{inc}} = 8.5$  mJ/cm².

The evolution of the hysteresis at the times of 1, 29 and 99 ps after excitation is summarized in figure 5.11. At time zero the hysteresis loop is closed for all fluences and does not show a significant slope  $m_{\text{coer}}$ . For the two lower fluences an offset from zero is measured, which can be explained by the before mentioned not-switching particles. The excitation of particles without switching leads to a lowering of the overall magnetisation due to the temperature increase in the sample. After about 30 ps, the hysteresis loops for 5.0 and 6.0 mJ/cm² have reached roughly half of their transient reference magnetisation value, while the hysteresis loop for 8.5 mJ/cm² has only recovered a small fraction of its relaxation value. The increase of the magneto-optical magnitude at higher sample temperatures can be explained by two effects: the grains show a variation of size and shape, which could lead to a distribution of Curie temperatures. That would cause some grains to switch at lower incident fluences for an equal amount of absorbed energy as their threshold for switching the magnetisation direction is reached at lower temperatures.

On the other hand the study of Granitzka et al. [100] has shown that this effect is not the prominent mechanism. They show that the absorption of the grains cannot be assumed equal for all grains. Instead the neighbourhood of the grains is dominating the switching behaviour: The grains with immediate neighbours can absorb a higher amount of energy due to plasmonic enhancement effects. That means for equal incident fluence isolated grains are less likely to switch at a field below the coercive field than grains closely surrounded.

Unfortunately, because no static hysteresis can be measured, the time resolved traces cannot be normalized to a percentage of magnetisation change. They can be analysed in the amplitudes relative to each other, which introduces uncertainty due to experimental shifts.

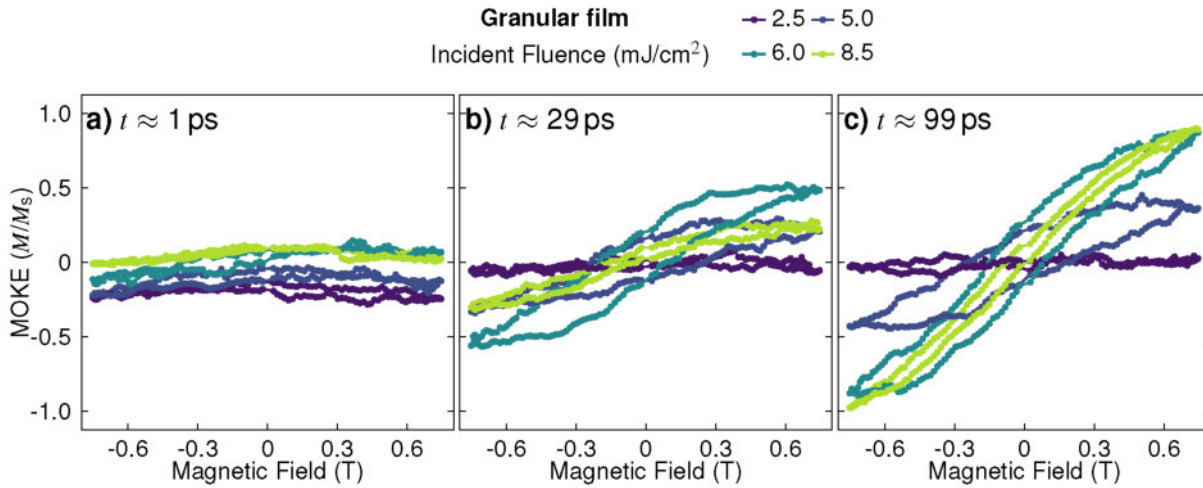


**Figure 5.11:** Transient hysteresis of the granular FePt film at the delay times of a) 1, b) 29 and c) 99 ps at different fluences.

### 5.3.3 Minor Hysteresis Loops

Figure 5.12 shows the effect of a maximum magnetic field  $B_{\max}$  than the saturation field  $B_{\text{sat}}$  used for hysteresis loop measurements. This data was obtained from the continuous FePt thin film.

Subfigure a) shows the static hysteresis. The largest hysteresis represents the major hysteresis loop with a saturated sample. With a maximum field  $B_{\max}$  smaller than saturation  $B_{\text{sat}}$  the measured hysteresis represents a minor loop which never reaches saturation. Consequently the maximum magnetisation of the hysteresis loop is smaller than the saturation value  $M_{\text{sat}}$ . When  $B_{\max}$  is significantly smaller than the coercive field  $B_{\text{coer}}$  the magnetisation changes along the flat part of the square-like hysteresis, depending on the starting value of the internal magnetisation. The smallest loop measured only between  $\pm 200$  mT would have a magnetisation amplitude of 0.2. For clarity this loop is shifted to zero.

In subfigure b) the transient hysteresis is shown. This represents the hysteresis measured at  $t \approx 2$  ms after a pump pulse excited the sample. In general the coercive field  $B_{\text{coer}}$  is reduced compared to the static hysteresis and the magnetisation saturation is reached at a significantly lower applied magnetic field. The minor hysteresis loops are exhibiting the same trend with variation of the maximum field as before: For a smaller field  $B_{\max}$  the reached maximum magnetisation is reduced and for a very small field below the coercive field  $B_{\text{coer}}$  the magneto-optical signal only changes very slightly. Because the slope  $m_{\text{rem}} = \partial M / \partial B_{\text{ext}}$  at zero applied field is larger compared to the static square-like hysteresis, the hysteresis loop for very small fields of  $\pm 50$  mT reaches significantly larger magnetisation values than for the static measurement.

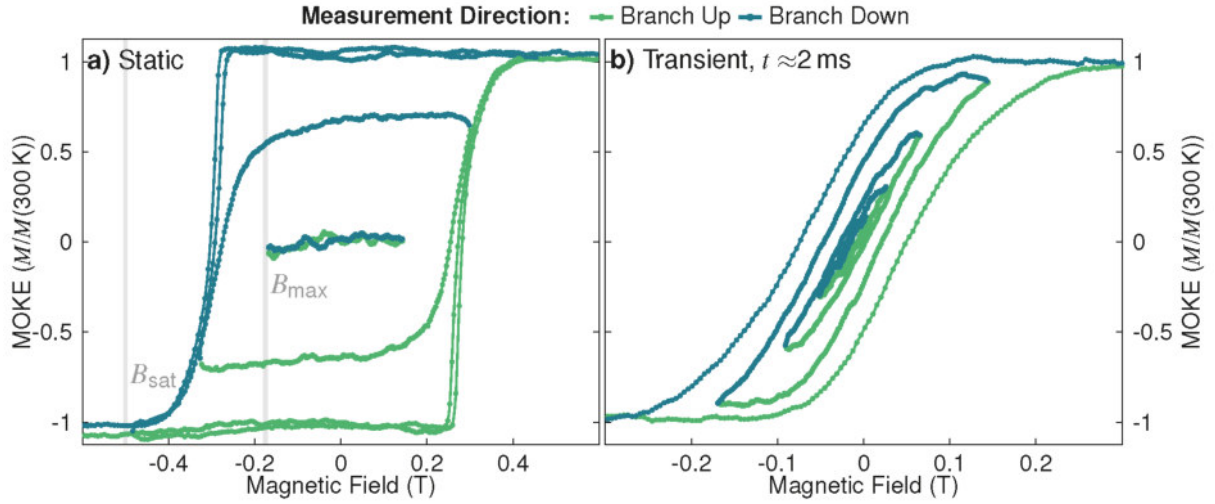


**Figure 5.12: Major and minor hysteresis measurements on the continuous FePt film.** The measurements in a) are taken under static conditions (no excitation) and in b) transient measurements ( $t \approx 2$  ms after excitation) are shown. The minor loops have been shifted to centre around zero for clarity.

## 5.4 Time-Resolved MOKE Measurements

Instead of the complete hysteresis loops at several time delays (figure 5.13) only the change of the magnetisation  $\Delta M$  at one external field value  $\pm B_{\text{ext}}$  is measured to create a time trace displaying the dynamic behaviour of the magnetisation. To increase the signal to noise ratio, it is preferred to measure

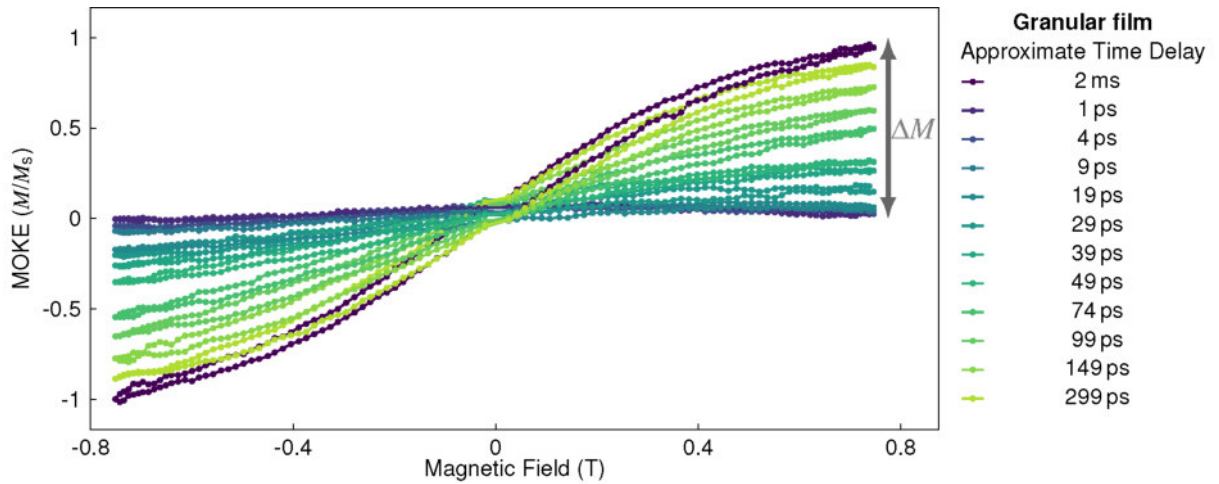


**Figure 5.13: Time resolved hysteresis of FePt granular measured at  $F_{\text{inc}} = 8.5 \text{ mJcm}^{-2}$ .** Hysteresis from the granular FePt film, measured at different time delays of pump and probe. The MOKE amplitude value is indicated with the grey arrow.

the transient signal with reference to the signal obtained with closed chopper ( $\approx 1$  ms after excitation). As shown in figure 4.3, this eliminates the majority of noise contribution by laser fluctuations. So for the measurement of a time dependent MOKE trace, we only investigate the change  $\Delta M$  at a set external magnetic field value  $B_{\text{ext}}$ . The MOKE magnitudes extracted from the hysteresis in 5.13 at the external field of 800 mT are inserted as cross marks in 5.14. The underlying graph is a pump probe MOKE trace measured at a comparable fluence. The trace obtained from the hysteresis magnitude changes are in good agreement with the time resolved MOKE trace. Small deviations are expected as the hysteresis measurements are not corrected with a transient reference value. For the time resolved measurements

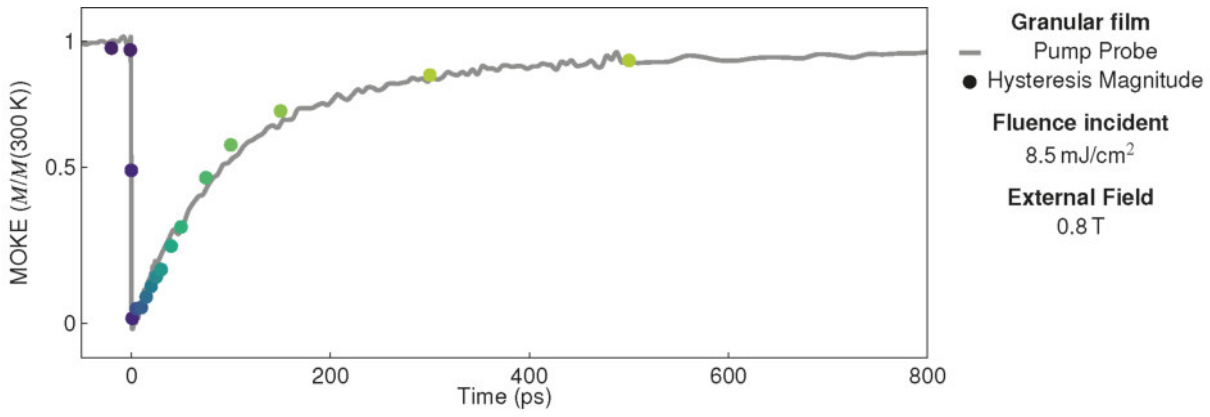


**Figure 5.14:** Comparison of time dependent evolution of MOKE signal determined with hysteresis amplitude changes (cross marks) and the pump probe trace (solid line) at an external field value of  $B_{\text{ext}}=0.8$  T and a fluence of  $8.5 \text{ mJ/cm}^2$  on the granular sample.

presented in this thesis the number of data points was reduced by binning multiple points on the time axis together in addition to the data analysis described in section 4.5.

#### 5.4.1 Continuous Film

Figures 5.16 and 5.17 both display the demagnetisation and magnetisation recovery over time depending on the incident fluence. The first series was measured with an external field of  $B_{\text{ext}}=0.3$  T (fig. 5.16), the second series was measured at a field of  $B_{\text{ext}}=0.8$  T (fig. 5.17). For the first series it was not possible to normalize the amplitude of the time resolved magnetic response to a static hysteresis, so the values on the magnetisation axis represent the original measured amplitude. The second fluence series is normalized according to the MOKE amplitude of the static hysteresis. This magnetisation axis displays the magnetisation change relative to the saturation magnetisation. The bottom graph plots are scaled to the maximum of demagnetisation after 1 ps to compare the relative remagnetisation dynamics.

For low fluence measurements in the first series the magnetisation recovery can be described with a fast component in the first picoseconds and a following slow component. With an increase in fluence the first recovery begins to slow down and transitions into the opposite behaviour: It is recovering slowly in the beginning and after a certain threshold in time the magnetisation gain is increased again.

A similar behaviour can be observed in the second series in figure 5.17. In both cases, the change of the timescale from fast to slow appears at a certain threshold: Between  $2.0$  and  $3.0 \text{ mJ/cm}^2$  the remagnetisation changes significantly.

The normalized values for magnetisation show a decrease in the total magnetisation for the highest fluences of  $8.5$  and  $9.0 \text{ mJ/cm}^2$ . Most likely this is an indication for a static heating effect. The actual decrease in magnetisation triggered by the pump pulse is not reduced, as seen clearly in the corresponding hysteresis measurements: The transient hysteresis at time zero is suppressed completely. But the static saturation magnetisation  $M_{\text{sat}}$  at higher temperature is smaller. In figure 5.15 the static hysteresis (green) and the transient hysteresis before the time zero (blue) show a slightly different amplitude.

Figures 5.18 and 5.19 display measurement series depending on the external applied magnetic field at fixed fluences. The first series in 5.18 was taken with an incident fluence of  $7.0 \text{ mJ/cm}^2$ . The applied magnetic field ranges from small fields of  $70$  mT to  $350$  mT. In the bottom graph the scaled plots show a clear influence of the magnetic field on the second recovery timescale. With a higher field applied, the remagnetisation is getting faster, the static saturation value is reached earlier compared to smaller fields. The magnetic field dependence for incident fluences of  $3.0$ ,  $5.0$  and  $9.0 \text{ mJ/cm}^2$  are shown in figure 5.19. Here only the shape of the curves are compared, they are scaled to the highest demagnetisation

value. The y-axis corresponds to the normalisation of the curve measured with the highest applied field of 0.75 T. Compared to the previously discussed measurements, this graph has a linear time axis without a logarithmic break. In all measurements a second demagnetisation after 20 ps is visible. This is caused by a back reflection from the backside of the second MgO substrate, as explained in section 4.7.2.

For the low fluence  $3.0 \text{ mJ/cm}^2$  the influence of the magnetic field is visible, but only marginal. At the higher fluence of  $5.0 \text{ mJ/cm}^2$  the trend becomes clearer: A higher magnetic field increases the speed of magnetisation recovery. For the highest fluence of  $9.0 \text{ mJ/cm}^2$  it is evident that the magnetic field has a huge impact on the remagnetisation behaviour. The second recovery rate is increased largely. But also the linear part is altered: a larger applied field leads to a faster recovery.

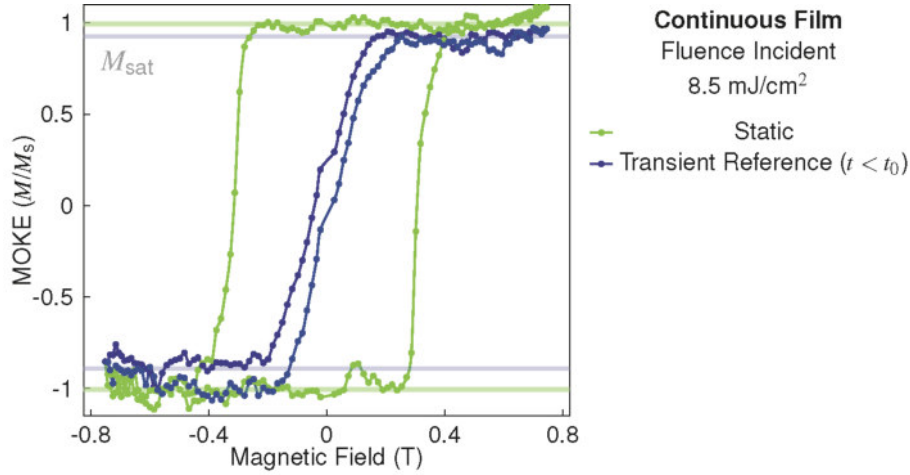


**Figure 5.15: Static heating effect on magnetisation after excitation.** The static hysteresis (green) compared to the transient hysteresis at  $t \approx 2 \text{ ms}$  after the last pump pulse excited the layer (blue) show a small difference in the saturation magnetisation. This is most likely caused by a static temperature increase in the sample which takes longer than 2 ms to cool to the substrate and reduces the saturation magnetisation.

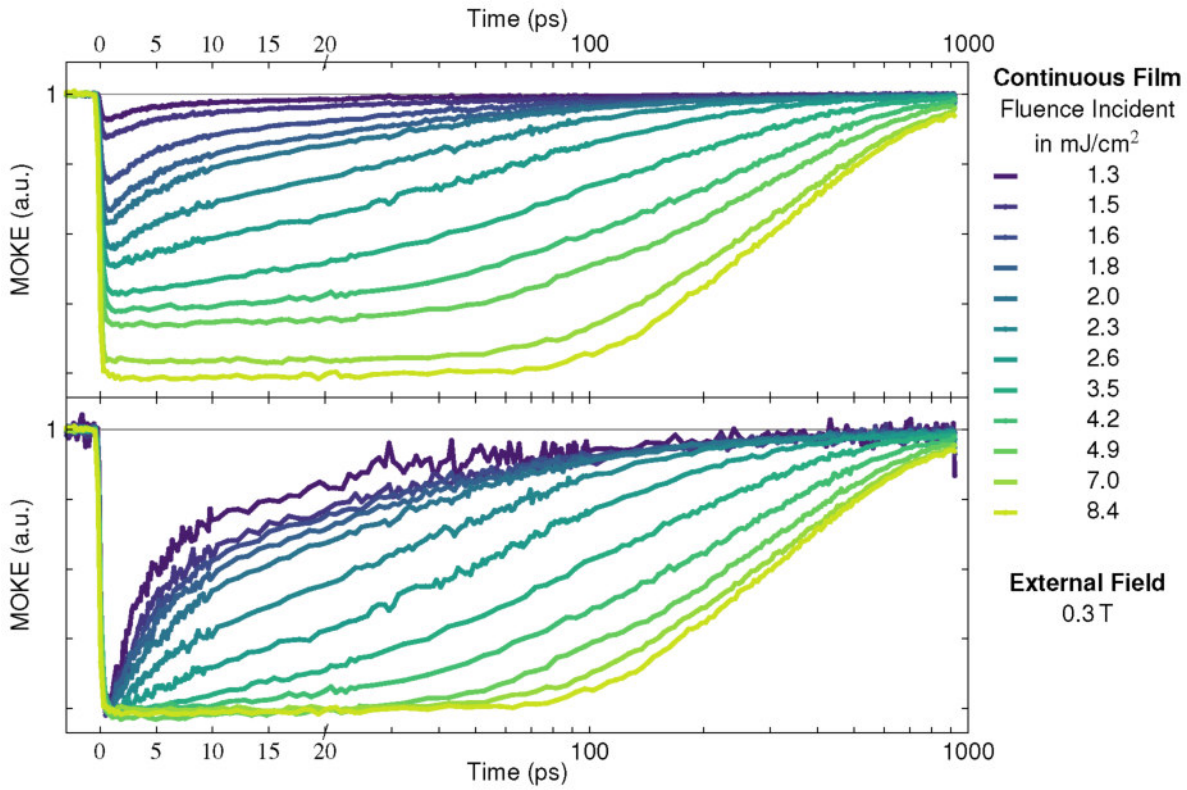


**Figure 5.16: Fluence dependent time resolved MOKE measurements of continuous FePt.** Top: Measurements with original measured MOKE value b) Measurements scaled to the maximum demagnetization. Measured at  $B_{\text{ext}} = 0.3 \text{ T}$ .

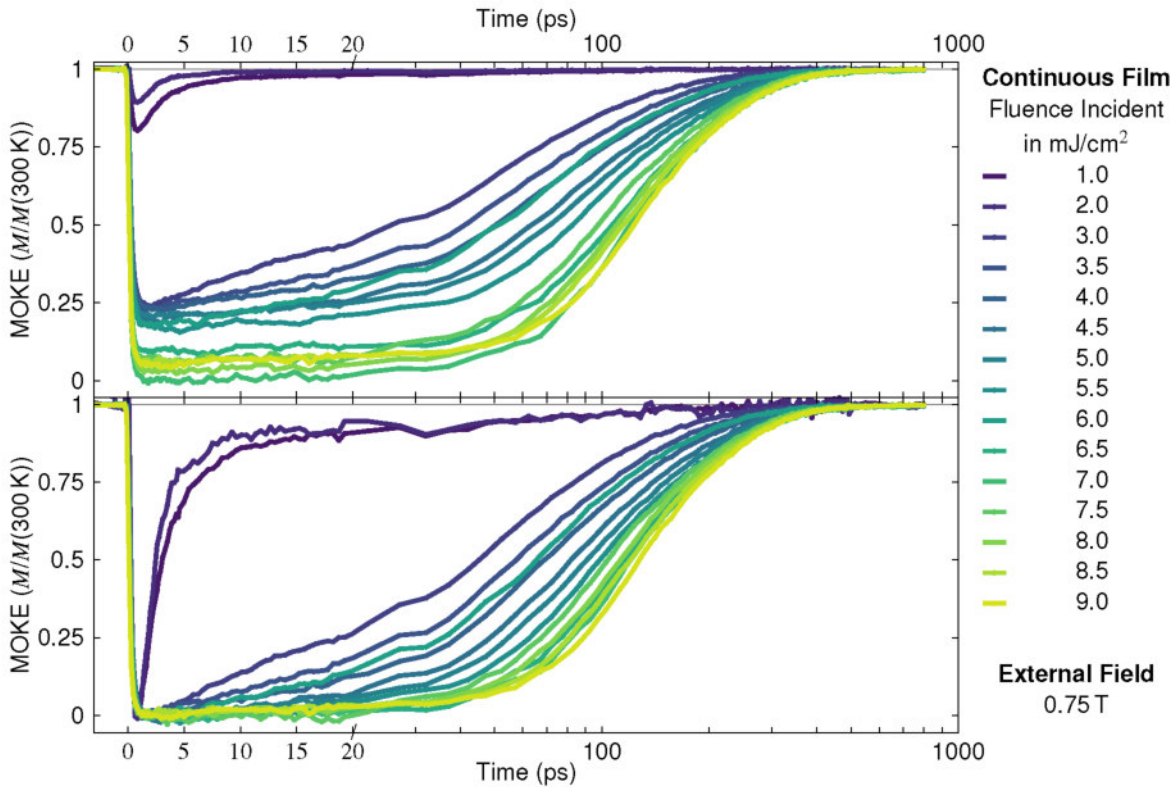


**Figure 5.17: Normalized fluence dependent time resolved MOKE measurements of continuous FePt.** Top: Measurements normalized to the hysteresis measurements, b) measurements scaled to the maximum demagnetization. Measured at  $B_{\text{ext}} = 0.75 \text{ T}$ .

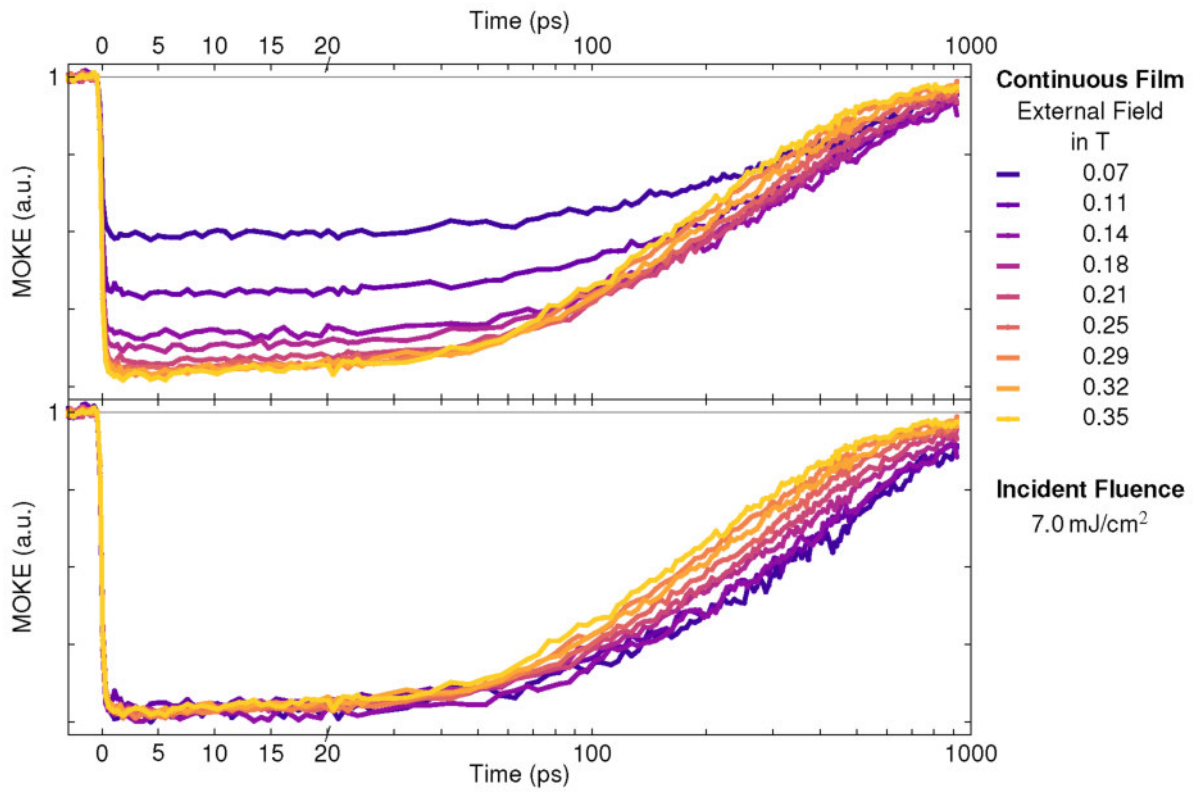


**Figure 5.18: External field dependent time resolved MOKE measurements of continuous FePt,  $F_{\text{inc}} = 7.0 \text{ mJ/cm}^2$ .** a) External field dependent measurements with measured amplitude, b) external field dependent measurements scaled to the largest amplitude. Measured at an incident fluence of  $F_{\text{inc}} = 7.0 \text{ mJ/cm}^2$ .

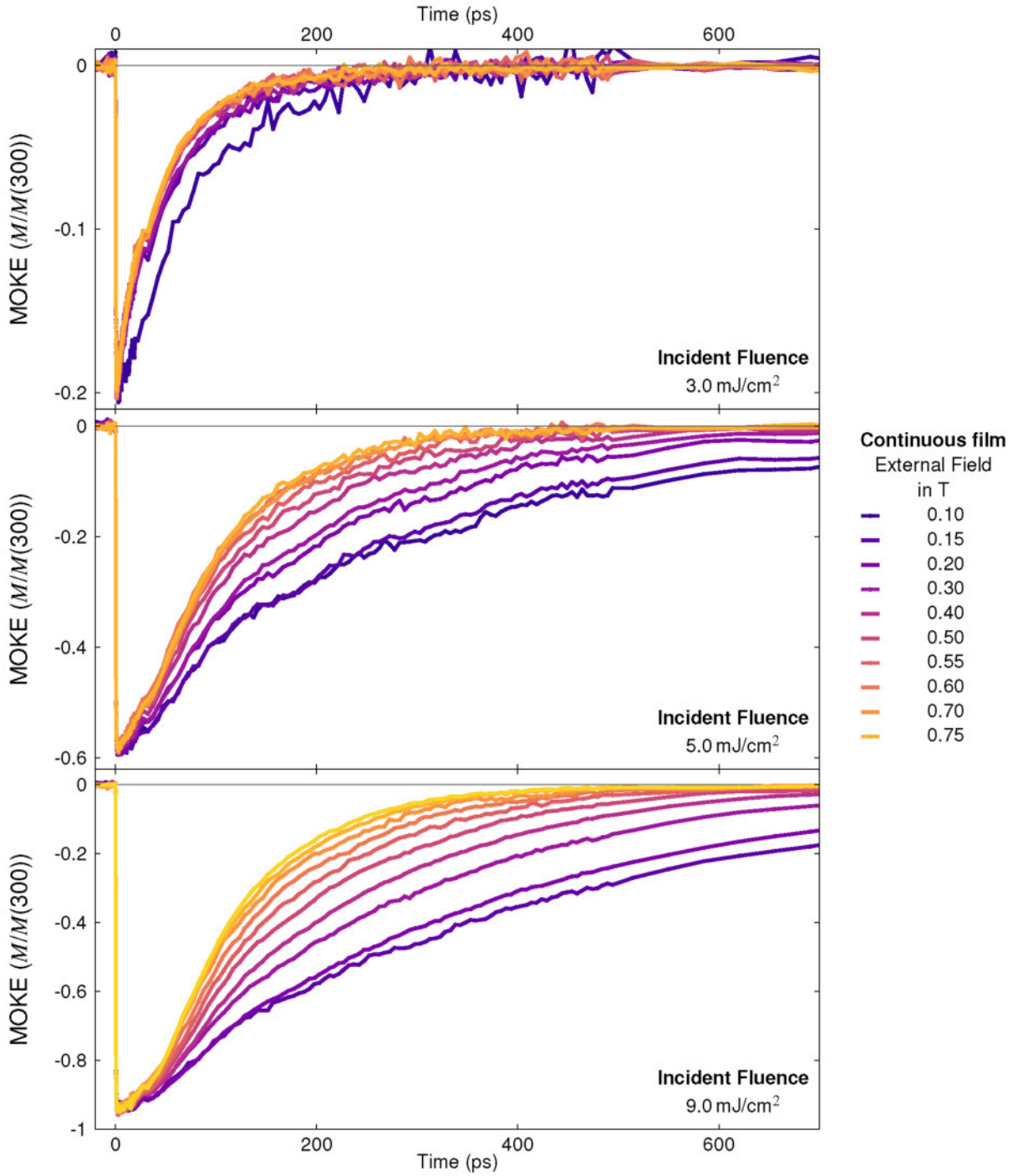


**Figure 5.19: External field dependent time resolved MOKE measurements of continuous FePt, at  $F_{\text{inc}} = 3.0$ ,  $5.0$  and  $9.0 \text{ mJ/cm}^2$ . Incident fluence of a)  $3.0 \text{ mJ/cm}^2$ , b)  $5.0 \text{ mJ/cm}^2$  and c)  $9.0 \text{ mJ/cm}^2$ . All measurements are scaled to the amplitude of the highest magnetic field of  $B_{\text{ext}} = 0.75 \text{ T}$ .**

### 5.4.2 Granular Film

As before for the continuous film the figures 5.20 and 5.21 show the fluence dependent change in magnetisation measured with an external applied field  $B_{\text{ext}}$  of 1.2 T and 0.3 T. As explained in section 5.3.2 a normalisation to the saturation hysteresis could not be performed, so the magnetisation axis shows the relative original measured amplitude. Several consecutive measurements have reproduced the behaviour of the 13.0 mJ/cm<sup>2</sup> curve in figure 5.21, which shows a decrease of total demagnetisation compared to lower fluences. This could possibly also hint to a static heating effect of the laser, as seen for the continuous film.

In comparison to the fluence change of the continuous film the very fast timescales for low fluences are not present. The time resolved hysteresis measurements showed that the fluence of 2.5 mJ/cm<sup>2</sup> is not a measurement of switching grains, but mainly of the magnetisation amplitude reduction of the hysteresis introduced by the laser. The shape of the remagnetisation curve is similar to the continuous sample: A faster recovery at low fluences is getting gradually slower and is delayed with an additional slow recovery contribution emerging in the first picoseconds at high fluences.

The comparison of the magnetic field dependent remagnetisation at incident fluences of 5.2 mJ/cm<sup>2</sup> in figure 5.22 and of 10.0 mJ/cm<sup>2</sup> in figure 5.23 exhibit a less pronounced behaviour compared to the continuous film, but a similar trend: For the lower fluence a low magnetic field has no detectable influence in altering the remagnetisation shape. At higher fluence measurements and a higher range in the applied magnetic fields the remagnetisation is faster with increasing field strength.

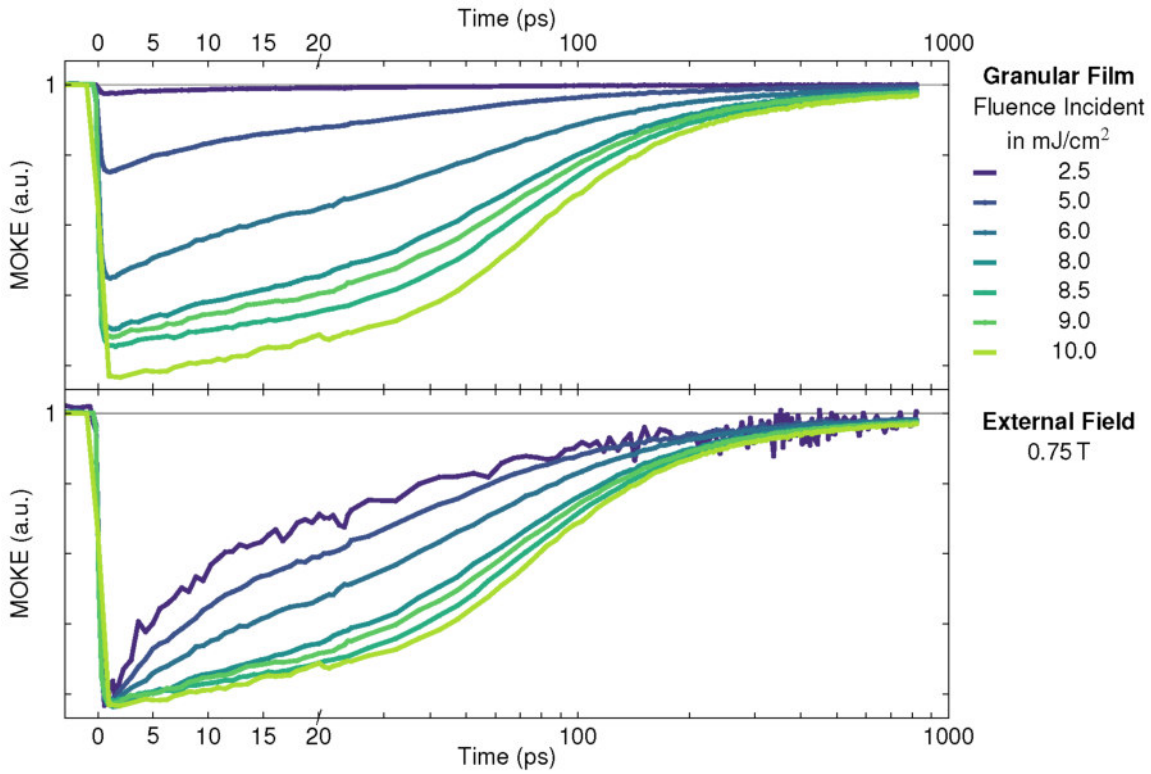


**Figure 5.20: Fluence dependent time resolved MOKE measurements of granular FePt at  $B_{\text{ext}} = 0.75$  T.** a) Measurements with original amplitude, b) measurements scaled to the maximum amplitude. Measured with the applied external field of  $B_{\text{ext}} = 0.75$  T.

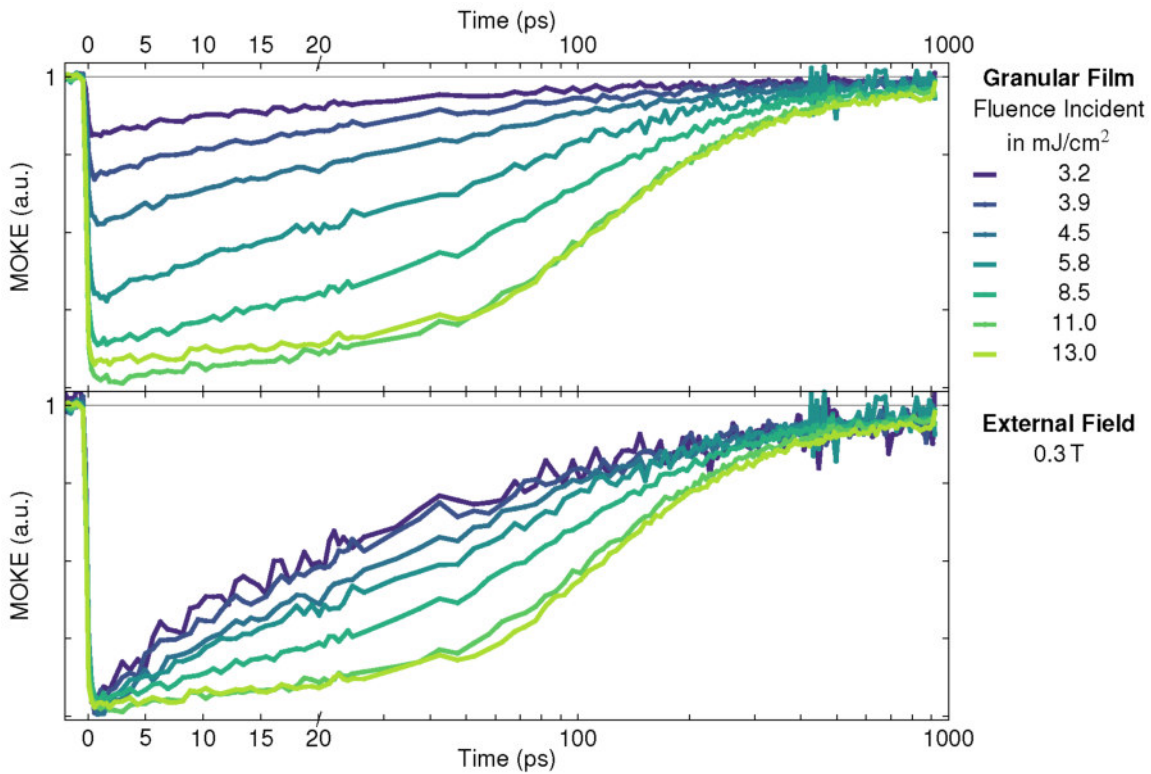


**Figure 5.21: Fluence dependent time resolved MOKE measurements of granular FePt at  $B_{\text{ext}} = 0.3$  T.** a) Measurements with original amplitude, b) measurements scaled to the maximum amplitude. Measured with the applied external field of  $B_{\text{ext}} = 0.3$  T.

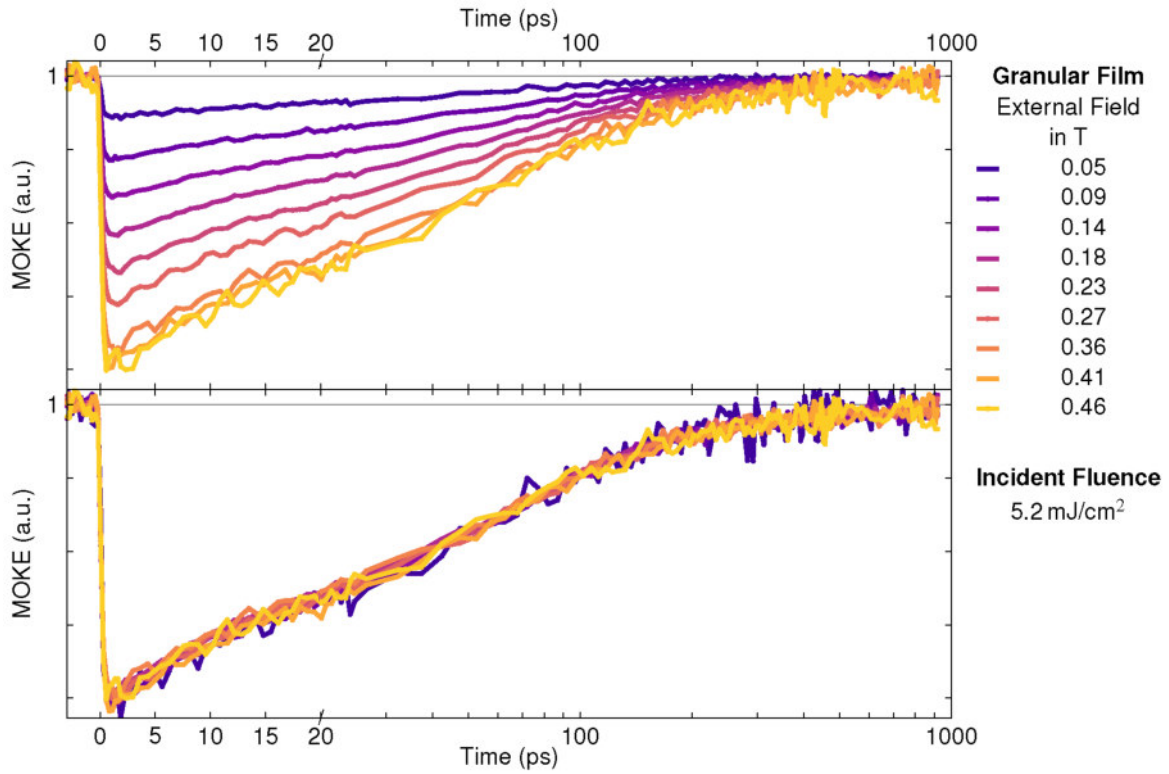


**Figure 5.22: External field dependent time resolved MOKE measurements of granular FePt.** a) Measurements with original amplitude, b) measurements scaled to the maximum amplitude. Measured after excitation with excitation fluence of  $F_{\text{inc}} = 5.2 \text{ mJ/cm}^2$ .

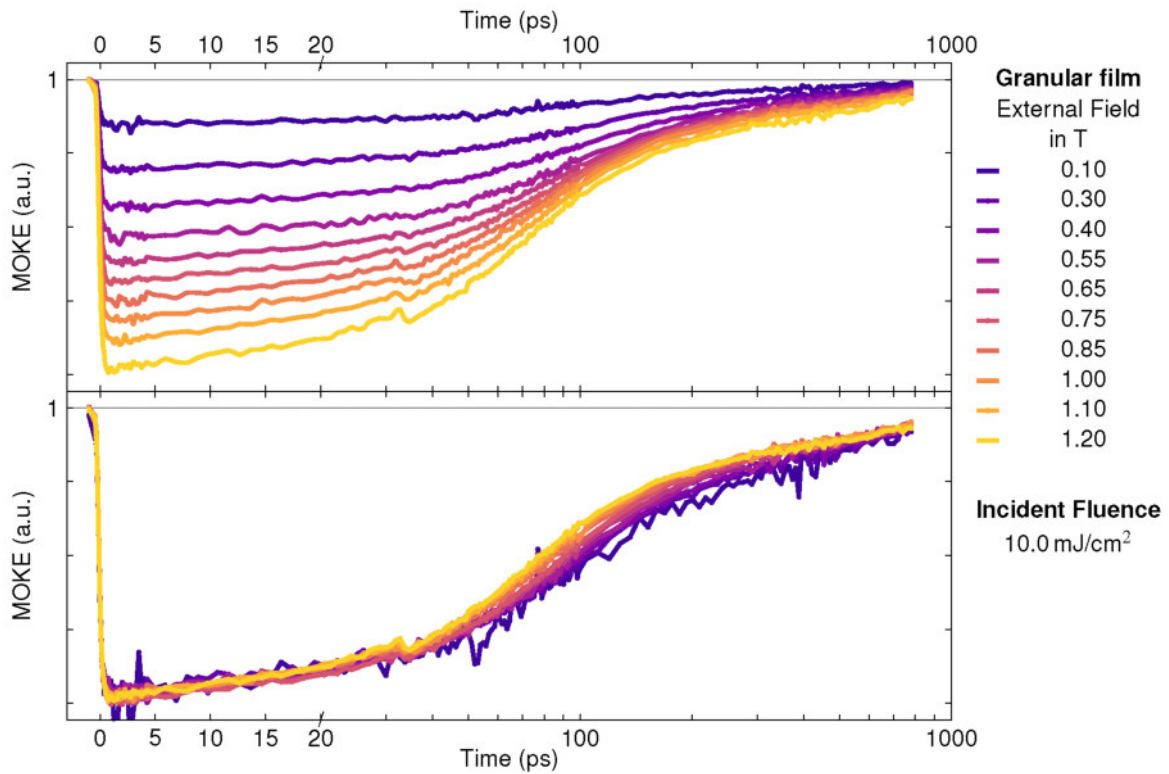


**Figure 5.23: External field dependent time resolved MOKE measurements of granular FePt.** a) Measurements with original amplitude, b) measurements scaled to the maximum amplitude. Measured after excitation with excitation fluence of  $F_{\text{inc}} = 10.0 \text{ mJ/cm}^2$ .

## 5.5 Timescales of the Remagnetisation Dynamics

The dynamics of all presented de- and remagnetisation curves in this thesis can be described with three distinct behaviours in time. The first one is the ultrafast demagnetisation. It occurs faster than the first picosecond after the pump pulse arrives. The length of the pump pulse in the presented measurements is too long to investigate the dependence of the first demagnetisation on the applied external field or the pump fluence, so the dynamics of the demagnetisation is not part of the analysis.

The initial shape of the remagnetisation dynamics depends strongly on the fluence and the applied magnetic field. For high pump pulse intensity a linear function is a good approximation. For lower fluence this approximation is getting inaccurate and an exponential behaviour is observed. Nevertheless to compare the high and low fluence curves the linear function expressed in equation 5.1 was used as the fit function for all analysed measurements. The parameter  $m$  as the slope of the linear function is the parameter expressing the magnetisation recovery over time.

$$M(t) = m \cdot t - \text{offset} \quad (5.1)$$

The following long term magnetisation recovery does also depend on the incident fluence and the external magnetic field. For the majority of measurements, the simple exponential function in equation 5.2 was sufficient to fit the recovery. However, for very high magnetic fields the measured magneto-optical trace deviates from the shape of an exponential function. As before for the linear function, to compare the remagnetisation timescales the exponential evaluation was kept for the data analysis. The parameter  $b$  is the inverse time constant  $\tau$ , which reflects the speed of remagnetisation.

$$M(t) = -\text{Amp} \cdot e^{-t/b} - \text{offset} \quad (5.2)$$

For the majority of measurements the change of dynamics between the two timescales is a distinct point in time,  $t_{\text{int}}$ . Whether or not the linear or the exponential recovery is the faster component is determined by the combination of magnetic field and energy in the sample. In the measurements where no clear distinction between both functions can be made, the slope of the linear function is similar to the exponential function. The linear fit range was set manually for each curve. The exponential fit had a variable start point and was set to find the best range by minimizing the errors of the fit results.

In the following sections the fit results for both samples are discussed. For all series a choice of fit functions with the respective measurement data is shown. The results for all fits are summarized in the plots of the parameters.

### 5.5.1 Continuous Film

Figures 5.24 and 5.25 show the fits for the remagnetisation occurring during the fluence series measurements at different magnetic fields. Only three curves are shown exemplary to increase the visibility of the changes. The dashed lines show the interception times  $t_{\text{int}}$  for both remagnetisation components. The linear function fits the data points only in the range of about 100 ps at maximum. After that, the long term recovery is dominated by a single exponential time dependence. The time constant  $\tau$  fit results for all curves are shown in figure 5.26 and their corresponding time of interception  $t_{\text{int}}$  can be found in 5.32.

The first fits show that an increase in fluence leads to a longer time of the slow linear recovery. The interception  $t_{\text{int}}$  of both functions is delayed to later times. However, the second timescale describing the remagnetisation with an exponential behaviour is increasing for higher energy deposited in the sample. The value for magnetisation is not normalized for this measurement, so the demagnetisation values are determined by the measured signal.

For the measurements at high magnetic field in figure 5.25 a similar behaviour is observed. The linear recovery slope  $m$  is decreasing and accompanied by an increase in the second remagnetisation time  $\tau$ . It is

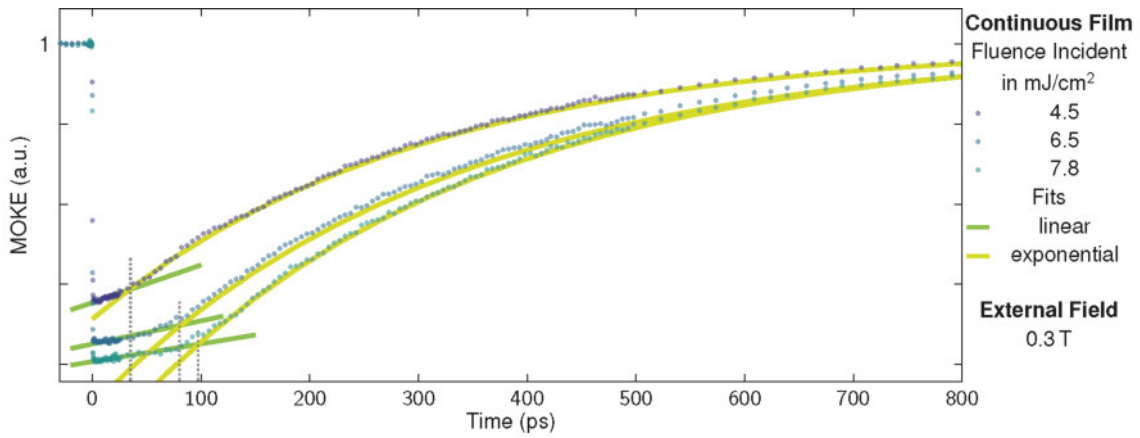
clearly visible that the simple exponential approach is less accurate for high external fields. The deviation is increasing for higher fluence measurements.

The interception  $t_{\text{int}}$  between the two timescales still shifts to later times with higher fluence, but the transient shows an overall faster remagnetisation than for low magnetic fields. It is apparent that the linear remagnetisation slope  $m$  increases compared to the low field measurements. So the remagnetisation speed strongly depends on the fluence and the external field strength. Compared with the first fits in figure 5.24  $t_{\text{int}}$  appears at earlier times for similar incident fluences.

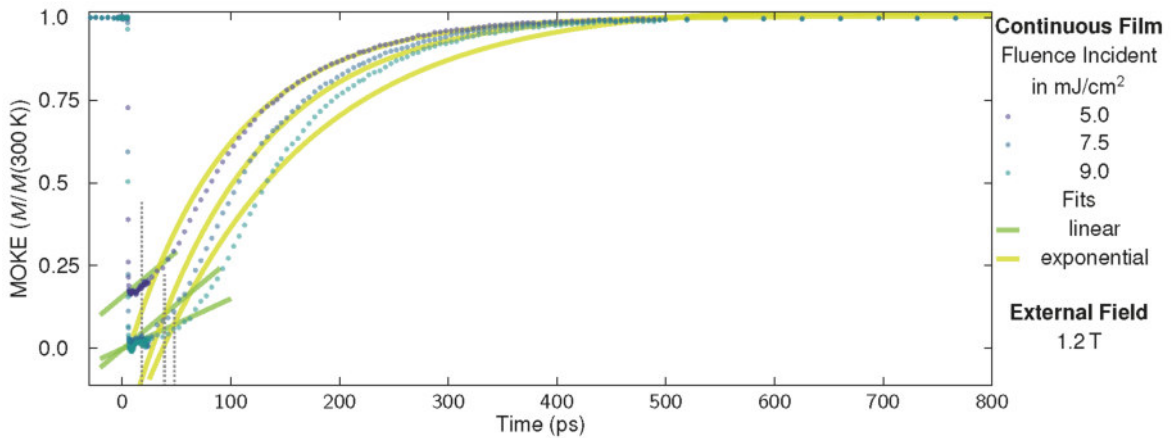
The exponential function depends on the external field similar as the linear function: With a higher field strength the time for magnetisation recovery is faster. This is true even though both magnetic fields are higher than the saturation field for the excited sample.

There is a combination of fluence and external field, at which the linear and exponential function are approximately described with the same remagnetisation slope for the first 100 ps. For these measurements it is difficult to determine the exact interception  $t_{\text{int}}$ .

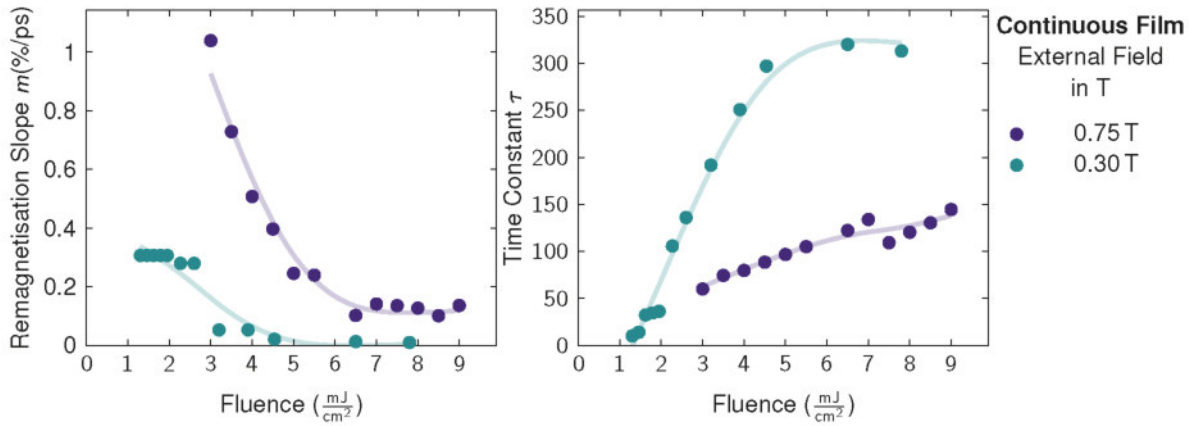
In figure 5.26 an additional threshold value for low fluence measurements is visible in the low magnetic field data. This implies that there is a threshold fluence at which a slowing down of the remagnetisation in the first picoseconds occurs.



**Figure 5.24:** Fits for the fluence dependent remagnetisation of the continuous film with an applied external field of  $B_{\text{ext}} = 0.3 \text{ T}$ . The dashed line indicates the intersection time  $t_{\text{int}}$  of the linear and exponential fit. The y-axis represents the original measured signal amplitude.



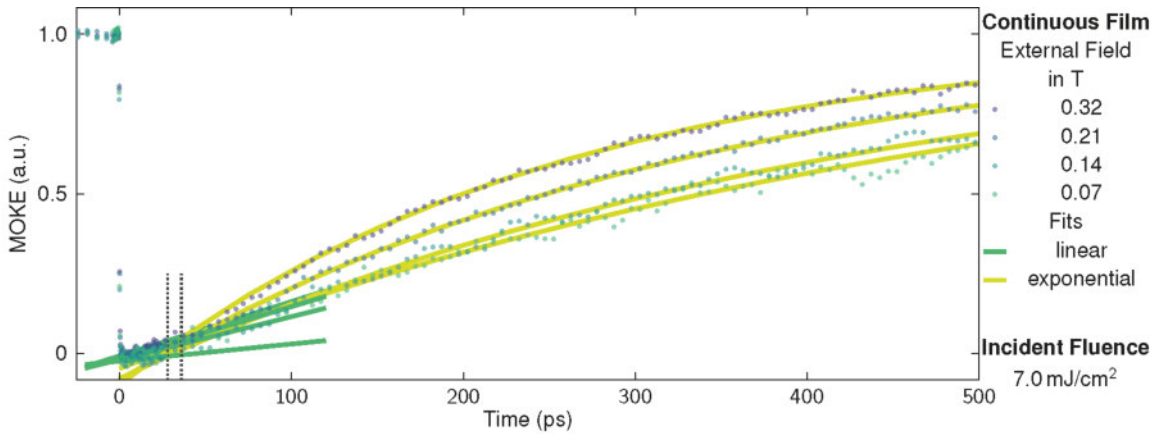
**Figure 5.25:** Fits for the fluence dependent remagnetisation of the continuous film with an applied external field of  $B_{\text{ext}} = 0.75 \text{ T}$ . The dashed line indicates the intersection time  $t_{\text{int}}$  of the linear and exponential fit. The y-axis is normalized to the saturation magnetisation of the hysteresis.



**Figure 5.26: Incident fluence dependence of remagnetisation time constants for the continuous sample.** Left: linear remagnetisation slope  $m$ , right: exponential time constant  $\tau$ .

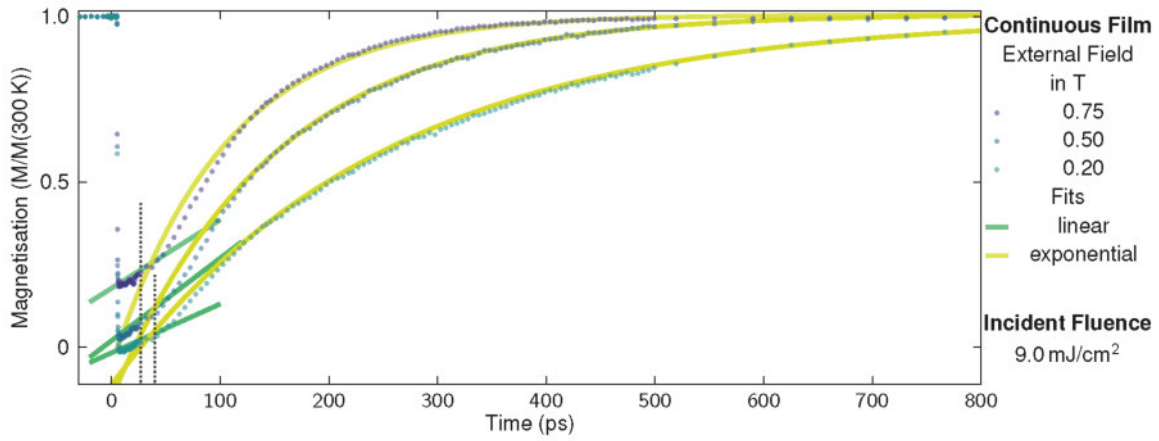
The following figures 5.27, 5.28, 5.29 and 5.30 all display external magnetic field dependent measurement at fixed incident fluence values. The first measurement at  $F_{\text{inc}} = 7.0 \text{ mJ}/\text{cm}^2$  was only performed at relatively low magnetic fields and in a previous version of the setup, while the other three were measured in an identical configuration and at the same sample position.

In figure 5.27 the data was scaled to the same amplitude to compare the changes in the dynamics. The exponential demagnetisation displays a clear trend of increasing with higher applied fields. Two values of the field were beneath the saturation magnetisation value in the static hysteresis and their change in remagnetisation slope  $m$  is not as large compared to the dynamics of the fields above the coercive field. The linear slope is decreasing with increasing field, as observed for the two fluence series as well. Only the lowest field of 70 mT is different in that aspect: It shows an increase in remagnetisation recovery compared to a field twice as large. Because the signal to noise ratio of the measurement is worse for lower fields the uncertainty in finding the most accurate boundaries for the fits is larger.



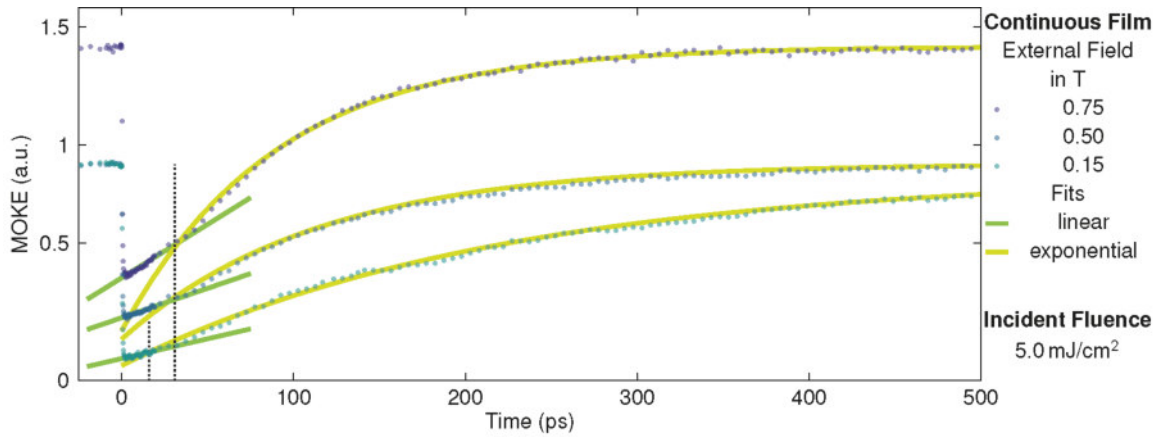
**Figure 5.27: Fits for the magnetic field dependent remagnetisation of the continuous film with an incident fluence of  $7.0 \text{ mJ}/\text{cm}^2$ .** The y-axis values were shifted to improve visibility.

Figure 5.28 contains the data for an incident fluence of  $9.0 \text{ mJ}/\text{cm}^2$ . The demagnetisation values were normalized according to the static hysteresis. The interception  $t_{\text{int}}$  of the two fit functions is only slightly varying in time with the applied field. This can also be seen in figure 5.29, which was measured with an incident fluence of  $5.0 \text{ mJ}/\text{cm}^2$ . The curves are shifted in their magnetisation values on the y-axis to increase visibility. The interception in this case seems to have two possible positions: For high values in the applied field it shifts to later times compared to fields below the coercive field. The interception



**Figure 5.28:** Fits for the magnetic field dependent remagnetisation of the continuous film with an incident fluence of  $F_{\text{inc}} = 9.0 \text{ mJ/cm}^2$ . The dashed line indicates the intersection time  $t_{\text{int}}$  of the linear and exponential fit. The y-axis is normed to demagnetisation of hysteresis.

$t_{\text{int}}$  is earlier compared to higher fluence measurements. Otherwise the dependence of the dynamics is as described before.



**Figure 5.29:** Fits for the magnetic field dependent remagnetisation of the continuous film with an incident fluence of  $F_{\text{inc}} = 5.0 \text{ mJ/cm}^2$ . The dashed line indicates the intersection time  $t_{\text{int}}$  of the linear and exponential fit. The y-axis values were shifted to improve visibility.

The series measured at the lowest fluence of figure 5.30 has a slower exponential recovery component compared to all other measurements. This means at the interception point  $t_{\text{int}}$  the linear function has a higher remagnetisation slope  $m$  than the following rate  $\tau$  given by the exponential fit. This is true for all of the applied fields, even though the difference increases for higher fields. So the exponential time constant  $\tau$  is increasing with the applied field as well, but the linear slope increases even faster. This indicates that an excitation with low intensity and only a small demagnetisation is described by a fast recovery transitioning into a slow component, while a high fluence excitation with stronger reduced net magnetisation is following the opposite behaviour.

In figure 5.31 the time constants for all external field dependent measurements are plotted. In the left graph the linear remagnetisation slope  $m$  is plotted. It displays the described behaviour of increasing remagnetisation speed with increasing applied field. For most fluences this can be described as approximately linear, with the exception of the lowest fluence,  $3.0 \text{ mJ/cm}^2$ . This graph shows a maximum in  $m$  at 300 mT. On the other hand the decrease of the exponential time constant  $\tau$  with higher fields is only significantly for high fluence. The initial difference in the remagnetisation time constants at low applied

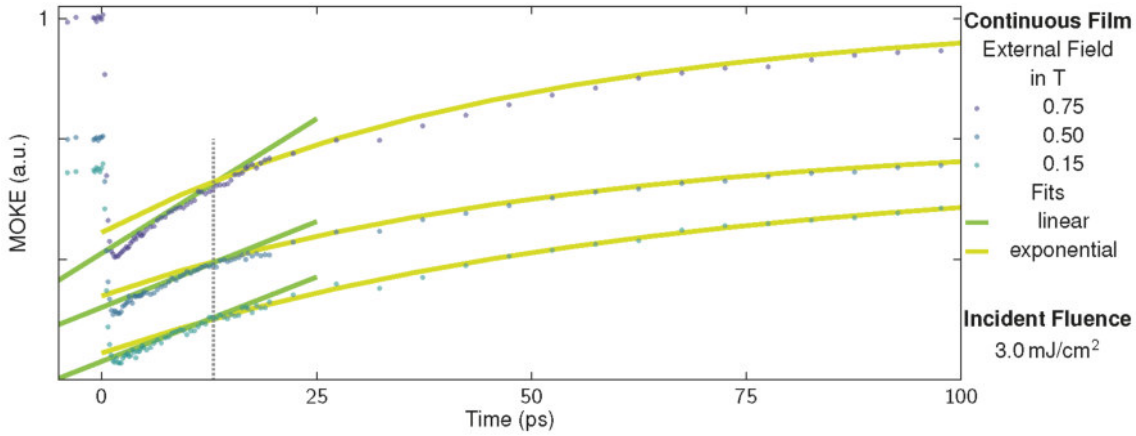


**Figure 5.30:** Fits for the magnetic field dependent remagnetisation of the continuous film with an incident fluence of  $3.0 \text{ mJ/cm}^2$ . The dashed line indicates the intersection time  $t_{\text{int}}$  of the linear and exponential fit. The y-axis value were shifted to improve visibility.

field stretches over 300 ps for the fluence range from  $3.0 \text{ mJ/cm}^2$  to  $9.0 \text{ mJ/cm}^2$ . At a high applied field of 0.75 T the difference between the highest and lowest time constant is only 50 ps.

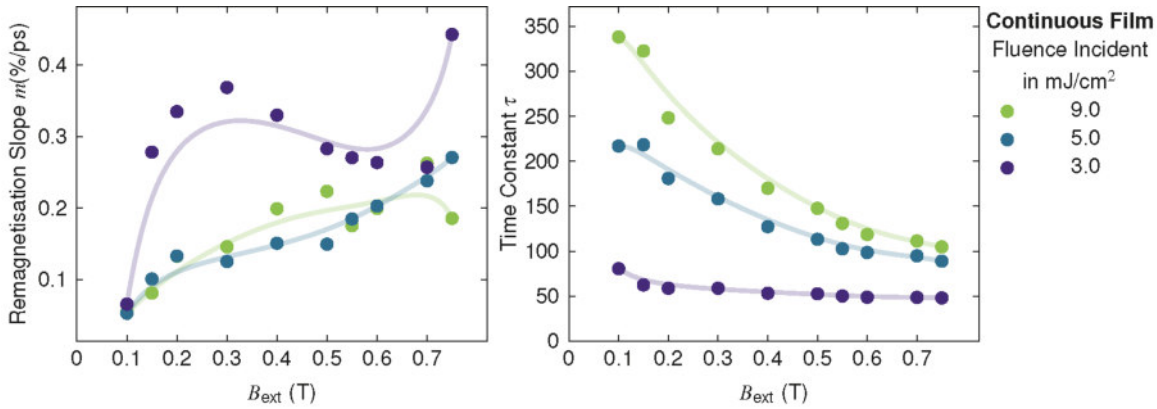


**Figure 5.31: External field dependence of remagnetisation time constants for the continuous sample.** Left: linear remagnetisation slope  $m$ , right: exponential time constant  $\tau$ .

The resulting times of transition between the linear and exponential remagnetisation behaviour for all measurements on the thin continuous FePt film are compared in figure 5.32. The dependence of the interception  $t_{\text{int}}$  on the external applied field is insignificantly low. An exception is the medium fluence of  $5.0 \text{ mJ/cm}^2$ , where a larger shift of the transition is observed. In contrast, the time of transition  $t_{\text{int}}$  is strongly shifted to higher values for increasing fluence, which can be seen both in the fluence measurements in the left plot as well as in the applied field dependence in the right plot.

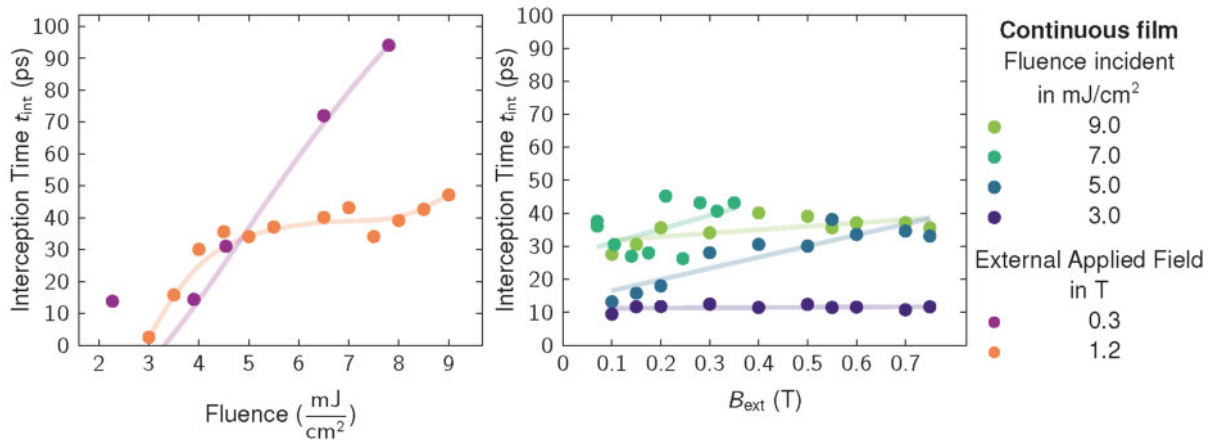


**Figure 5.32: Interception of the two remagnetisation time dependencies for the continuous sample.** Left: variation with incident fluence, right: variation with external applied field.

### 5.5.2 Granular Film

The dynamics of the granular sample are qualitatively comparable to the continuous layer of Iron Platinum. In figures 5.33 and 5.34 the two fluence series are shown.

It is noticeable that the transition in speed for the linear and exponential remagnetisation slope happens at higher fluences compared to the continuous sample. While the data for a fluence of 13.0  $mJ/cm^2$  indicates a slow linear recovery which is followed by the faster exponential growth with a low applied field of 0.3 T, already a fluence of 8.5  $mJ/cm^2$  indicates the opposite behaviour. For the high magnetic field of 0.75 T this is also visible: At a fluence of 9.0  $mJ/cm^2$  but also at 8.0  $mJ/cm^2$  the remagnetisation rate of the linear and exponential recovery is nearly identical.

The linear dependence on the incident fluence presents a different behaviour than for the continuous film, as can be seen by the comparison of figure 5.26 and figure 5.35. The slope is small for high fluences and for low fluences, but it increases in between to a maximum value. This is observed for both field dependent measurements with a maximum at the same fluence of  $F_{inc} = 6.0 \text{ mJ/cm}^2$ . The magnitude of the effect is different however: The high magnetic field leads to an overall increase in the remagnetisation slope  $m$ . The time of interception  $t_{int}$  for both components displayed in figure 5.39 is shifting towards later times as previously observed as well. Compared to the continuous film the transition between the two remagnetisation regimes happens at earlier times.

For the measurement at higher applied magnetic field the nearly identical slope of exponential and linear function can be observed for two fluences: 9.0  $mJ/cm^2$  and 8.0  $mJ/cm^2$ . The data measured for the fluence in between, however, exhibits a clear difference. One possible influence could be the effect of static heating, as observed for the normalized measurements of the continuous sample. But additionally the difference in fluence is not large, a small shift in the laser intensity during the measurement could also contribute to wrong identification of the incident energy.

The exponential recovery shows an increase in time constant  $\tau$  for higher fluences, as was seen for the continuous sample as well. The influence of the magnetic field however is much smaller. The tendency is still clearly visible: At high fluences an increase in applied field decreases the recovery time. The magnitude of the time constant  $\tau$  is small compared to the continuous film. So both varied parameters, fluence and external applied field, have a limited effect on the dynamics of the nanostructured sample in comparison to the continuous film.

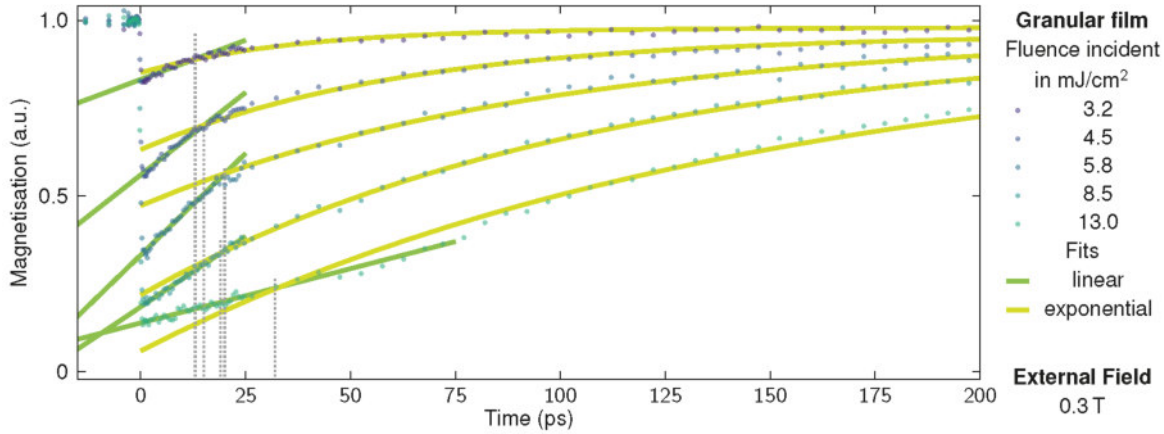


**Figure 5.33:** Fits for the fluence dependent remagnetisation of the granular sample with 0.3 T applied external field. The dashed line indicates the intersection point of the linear and exponential fit. The y-axis value were shifted to improve visibility.

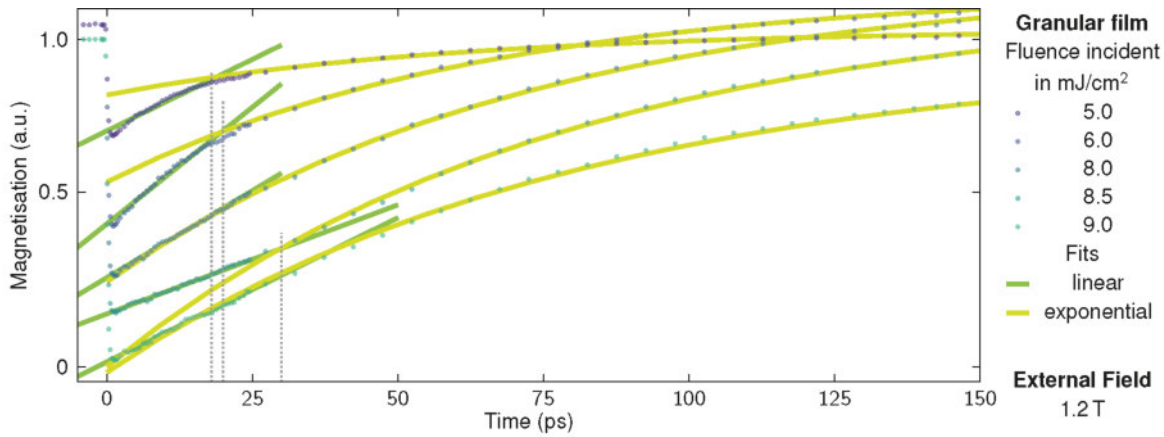


**Figure 5.34:** Fits for the fluence dependent remagnetisation of the granular sample with 0.75 T applied external field. The dashed line indicates the intersection time  $t_{\text{int}}$  of the linear and exponential fit. The y-axis value were shifted to improve visibility.

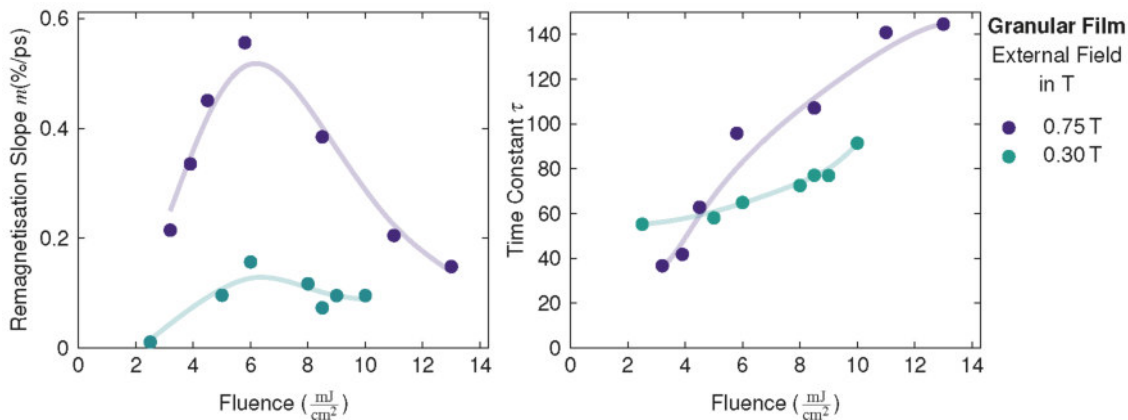


**Figure 5.35:** External field dependence of remagnetisation time constants for the granular sample. Left: linear remagnetisation rate  $m$ , right: exponential time constant  $\tau$ .

The dependence of the remagnetisation on the external applied field is shown in figures 5.36 and 5.37. It is clearly illustrating the same characteristics as seen for the continuous sample: The linear remagnetisation slope  $m$  increases with an increase in external field. The time  $t_{\text{int}}$  at which the dynamic changes the behaviour is not significantly influenced by the applied field, but it depends on the incident fluence: For the lower fluence of  $F_{\text{inc}} = 5.2 \text{ mJ/cm}^2$  it is fitted to a value of around 15 ps and shifted to about 25 ps for the higher fluence of  $F_{\text{inc}} = 10.0 \text{ mJ/cm}^2$ . The exponential recovery is getting faster for higher fields. All measurements in figure 5.36 have a steeper slope of the linear contribution than the initial slope of the exponential recovery. On the contrary all measurements in the second dataset in 5.37 have a slow first recovery exchanged with a fast exponential component. Solely the measurement at the lowest field has equal remagnetisation rates.

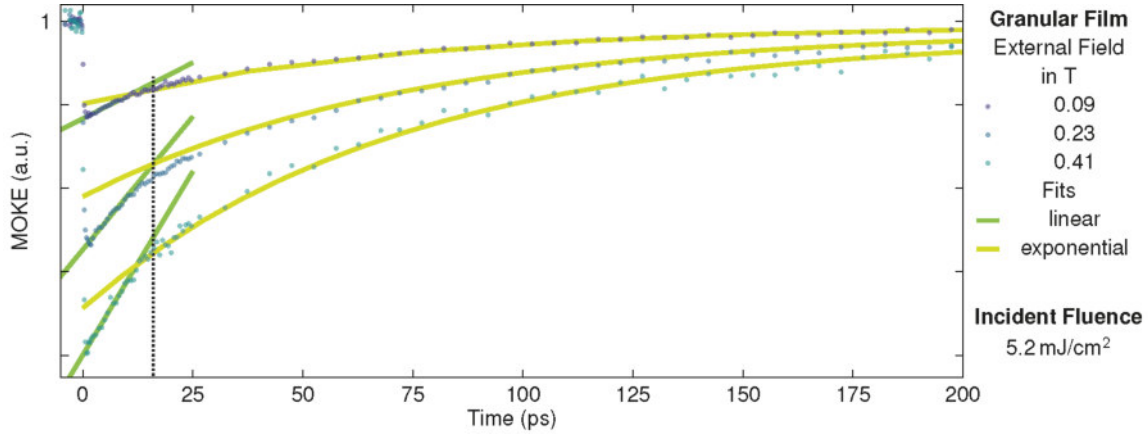


**Figure 5.36:** Fits for the magnetic field dependent remagnetisation of the granular sample with an incident fluence of  $F_{\text{inc}} = 5.2 \text{ mJ/cm}^2$ . The dashed line indicates the intersection time  $t_{\text{int}}$  of the linear and exponential fit. The y-axis represents the original measured signal.

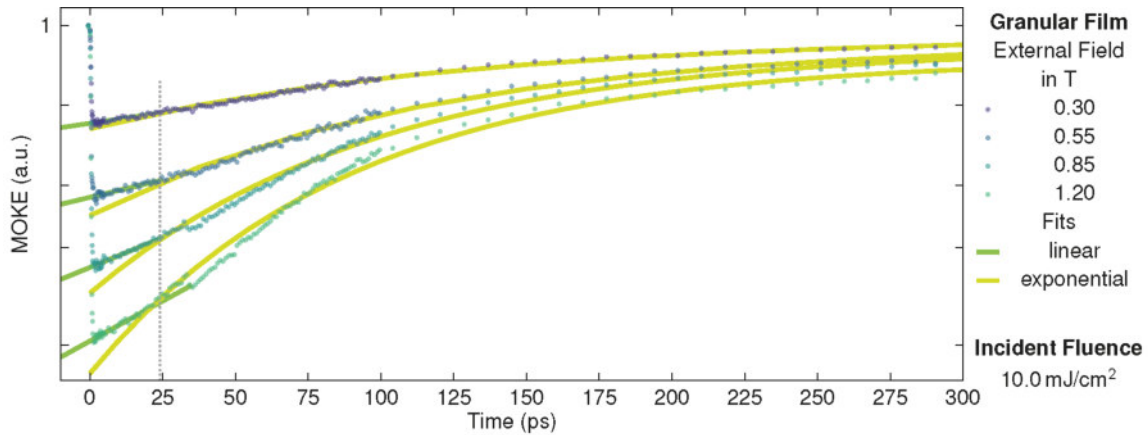


**Figure 5.37:** Fits for the magnetic field dependent remagnetisation of the granular sample with an incident fluence of  $F_{\text{inc}} = 10.0 \text{ mJ/cm}^2$ . The dashed line indicates the intersection time  $t_{\text{int}}$  of the linear and exponential fit. The y-axis represents the original measured signal.

The time constants for the external field dependent measurements are shown in Figure 5.38. The linear remagnetisation slope shows a clear trend for both the high and mid-regime fluence measurements. In both cases it can be approximated as linear increase with increasing external applied field. The data for the lower fluence of  $5.2 \text{ mJ/cm}^2$  has an increased remagnetisation recovery than the high fluence data of  $10.0 \text{ mJ/cm}^2$  at equal field strengths. The low fluence recovery might reach a threshold at around  $0.5 \text{ T}$ , at which the increase in recovery speed is slowing down. But for a conclusive statement more data points beyond  $500 \text{ mT}$  point would be necessary.

The exponential recovery rate of the lower fluence measurement is not influenced by the external field, however the higher fluence shows a decrease in time constant. As before the amplitude for this time constant difference is small compared to the continuous film.

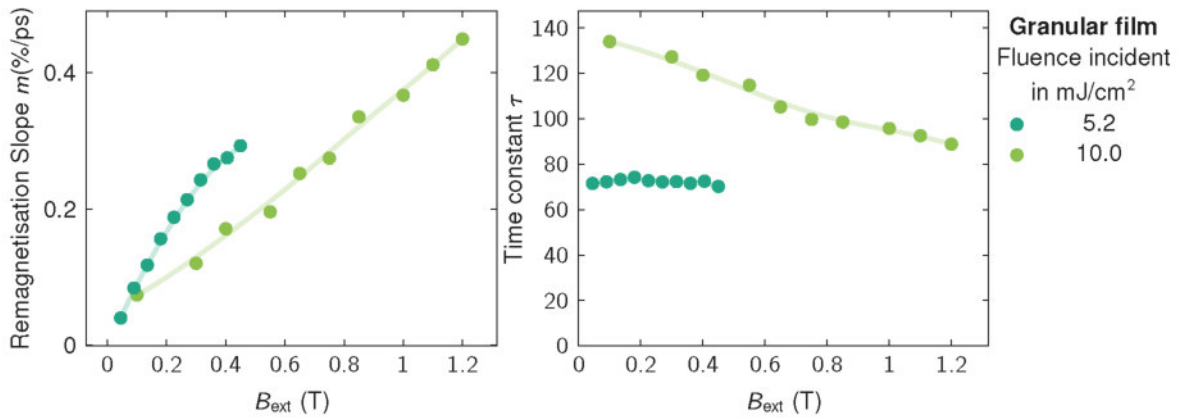


**Figure 5.38: External field dependence of remagnetisation time constants for the granular sample.** Left: linear remagnetisation slope  $m$ , right: exponential time constant  $\tau$ .

The interception points of the fits are shown in 5.39. The general trend is similar to the continuous film: Increasing the fluence shifts the transition to an exponential recovery  $\tau$  to later times, and a higher field shifts it to earlier times. The exception for the data point at a fluence of 8.0 mJ/cm<sup>2</sup> for an applied field of 0.3 T reflects the difficulty to determine a clear point of interception, if both functions have a very similar slope in the beginning of remagnetisation.

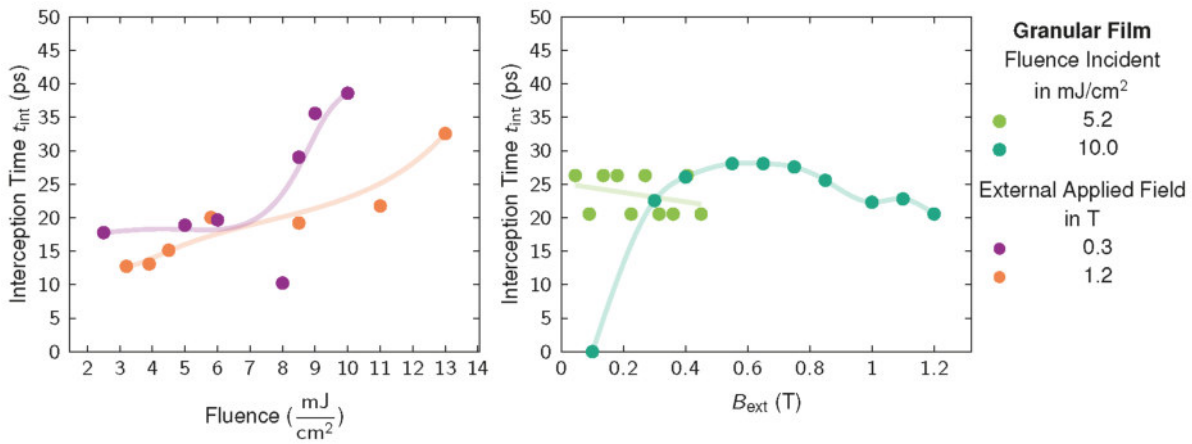


**Figure 5.39: Interception of the two remagnetisation time dependencies for the granular FePt sample.** Left: variation of interception time  $t_{\text{int}}$  with incident fluence, right: variation of interception time  $t_{\text{int}}$  with the external applied field.

## 5.6 Summary

The analysis of the remagnetisation behaviour has revealed several characteristics in both samples. This section will summarize the findings and identify similar as well as reversed characteristics for the granular and continuous film.

### Similarities

- The coercivity field  $B_{\text{coer}}$  of both samples is reduced with higher fluence, starting at a certain fluence threshold.
- low fluence excitations reduces the saturation magnetisation  $M_s$ , but the shape of hysteresis is not changed.
- The demagnetization occurs on an ultrafast timescale in less than 1 ps.
- The remagnetisation is divided in two sections:
  1. A slow remagnetisation for high fluence excitations, which transitions into a fast recovery for low fluences. In the slow regime it is best described by a linear function, in the fast regime an exponential function describes the remagnetisation most accurately.
  2. An exponential remagnetisation on long timescales.
- The two sections are divided by a distinct interception time  $t_{\text{int}}$ , which is particularly visible for high fluence excitations.
- The external field  $B_{\text{ext}}$  has a significant effect on the dynamics: An increase causes a faster in remagnetisation.
- The effect of the external field is enhanced with increasing fluence.
- The interception time  $t_{\text{int}}$  between the two sections is shifted to later times when the fluence is increased
- The interception time  $t_{\text{int}}$  is not influenced significantly by the external field.
- A static heating effect occurs at the highest fluence excitations, which causes a decrease in absolute demagnetisation amplitude due the static reduction in the saturation magnetisation.

### Differences

- An increasing fluence leads to a decrease in the linear remagnetisation slope for the continuous film. The granular sample has an increasing recovery until a threshold fluence of  $F_{\text{inc}} = 6 \text{ mJ/cm}^2$ , after which the remagnetisation slope  $m$  decreases again.
- For the second timescale the dynamics are reversed: The continuous film recovers faster with higher fluence, while the granular sample is fastest at low fluences, according to the exponential time constant  $\tau$ .
- The amplitude of the influence of the external applied field is larger for the continuous film. The granular sample exhibits this less pronounced.
- The transition between the speed difference of the linear slope of the first remagnetisation section and the initial slope of the exponential section is occurring for the granular sample at significant higher fluence values than for the continuous sample.



## 6 | Magnetisation Dynamics in Nickel-Gold Bilayers

Nickel has been present in human society for a significant amount of time. It was found naturally in alloys with many other elements like Copper, Iron or Zinc, so it is contained in ancient bronzes from 4000 BCE, for example made in Sumeria and Syria. Its properties regarding the persistence against everyday forces made it a good candidate for currency coins. China utilized this in combination with Copper as early as 700 BCE, calling it "white copper". However, for a long time Nickel was not recognized as a single element. This discovery was made first by the Swedish chemist and mineralogist Cronstedt in 1751. Even after his discovery it was debated until 1775 if it is indeed a pure element. [111–113]

Nowadays Nickel is present in numerous devices and structures, mainly due to its electric and magnetic properties. It is also the element on which Beaurepaire et al. made the ground-breaking experiment discovering the ultrafast nature of demagnetisation after laser excitation in 1996 [3]. Numerous experiments on Nickel and other magnetic layers have followed (see chapter 3), and even after extensive research the mechanisms behind the process of ultrafast magnetisation dynamics are not clear. Nickel continues to be a good candidate to investigate magnetic and other properties due to its relatively simple structure and strong ferromagnetism (see section 2.4).

In this work a variety of Nickel and Gold bi- and trilayers were investigated with time resolved MOKE measurements to analyse the remagnetisation dynamics after excitation with a wide range of fluences. This system was chosen with the aim to combine the magnetisation dynamics of the ferromagnetic Nickel layer with the structural response of the lattice of Gold and Nickel measured with ultrafast X-ray diffraction (UXRD). This combination allows a closer look at the magnetic phase transition after excitation with high fluence. After a short motivation concerning the investigated sample system the static characterisation of the samples will be presented. Subsequently, the magneto-optical measurements of the fluence dependent de- and remagnetisation are shown and finally discussed in combination with the respective fits. The comparison of the lattice response to the magnetic excitation will be the topic of chapter 7.

### 6.1 Motivation

Despite numerous experiments on Nickel, its magnetisation dynamics still provides many scientific questions. To address these, a magnetic layer can be investigated in a layered system, in which non-magnetic materials surround Nickel. For example, experiments were performed on systems with a thick non-magnetic layer, back site pumping and probing of the magnetic layer to investigate the effect of heat transport or magnon excitation [114, 115]. The spin injection in the non-magnetic layer after laser excitation was observed with element selective MOKE [5]. One of the often utilized non-magnetic elements is Gold. The structural investigations on the samples used in this work delivered new insights about the heat transport on the nanoscale and picosecond timescales, published by Pudell et al. [6]. Similar samples were discussed in the topic of heat dependent demagnetisation by Eschenlohr et al. [116]. The cited work also sparked discussions regarding the absorbed energy density profile of a multilayer system, in which the absorption of a layer depends considerably on the real part of the refractive index of the material and not purely on the penetration depth profile [117]. In order to investigate the importance of the neighbouring layer of the thin magnetic layer, the presented samples combine both Nickel connected to Gold and MgO as well as Nickel being surrounded by MgO.

## 6.2 Sample Characterization

We investigated Gold Nickel bilayers (AuNi) with varying thicknesses and a trilayer with MgO in between Gold and Nickel. The samples are summarized in the table 6.1 and shown in figure 6.1. The thickness of the layers were determined with X-ray reflectivity (XRR). The samples were grown by molecular beam epitaxy onto a MgO(100) substrate.

The magnetic layer in this system is ferromagnetic Nickel. It has a face-centred cubic (fcc) unit cell, as shown in figure 6.1 b). The lattice constant is  $a=3.52 \text{ \AA}$ . The easy axis of the magnetisation is oriented in plane. This corresponds to an effective field  $B_{\text{eff}}$  oriented in plane, if no external field is applied. According to the description of the sample geometry in the developed MOKE setup (see chapter 4), the magnitude of the external field  $B_{\text{ext}}$  determines the angle of the magnetisation to the surface normal. The available range of the applied magnetic field is sufficient to reach a full magnetisation saturation out of plane. The static behaviour of the magnetisation in dependence of temperature is shown for the samples

	Magnetic Layer	Capping Layer	Buffer Layer	Substrate	Internal Identifier
GN1	Ni 12.4 nm	Au 5.6 nm		MgO(100)	NiB/NiAu 1.2
GN2	Ni 12.0 nm	Au 11.2 nm		MgO(100)	NiAu 3.3
GMN	Ni 10.6 nm	Au 10.8 nm	MgO(100) 7.6 nm	MgO(100)	NiAu 3.1

**Table 6.1:** Sample structures and designations of AuNi-Bilayers discussed in this chapter.

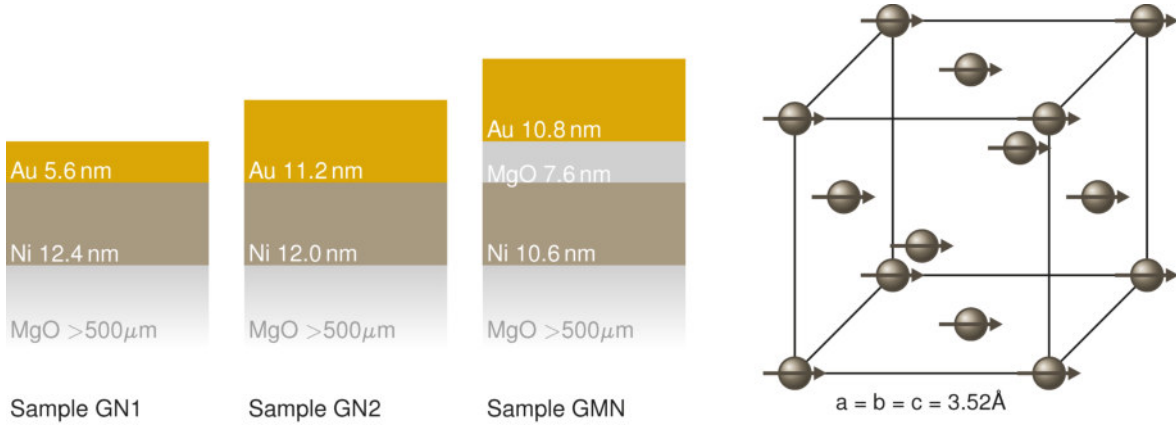


**Figure 6.1:** Schematic sample structure of the investigated AuNi samples. Left: Geometry of the samples presented in table 6.1. Right: Cubic unit cell of the ferromagnetic Nickel layer in the samples. The anisotropy results in an in plane effective field  $B_{\text{ext}}$  and therefore the spins are oriented in plane when no external field is applied.

GN1 and GN2 in figure 6.2. It was measured by Vibrating Sample Magnetometry (VSM) in a SQUID (Quantum Design) at the Université de Lorraine in Nancy. The magnetic field was applied in plane during the measurements, that is unlike in the MOKE measurements, the easy axis of the system is measured.

In the first row of figure 6.2 the raw data is shown. The linear dependence of the magnetisation signal on the applied magnetic field visible at high fields is caused by the dia- and possible paramagnetic contributions. In this measurement the diamagnetic behaviour of the sample holder is predominant. When the ferromagnetic material is saturated, only the dia- and paramagnetic contributions are visible, so after fitting of the saturated data this contribution can be subtracted from the whole field range of the raw data.

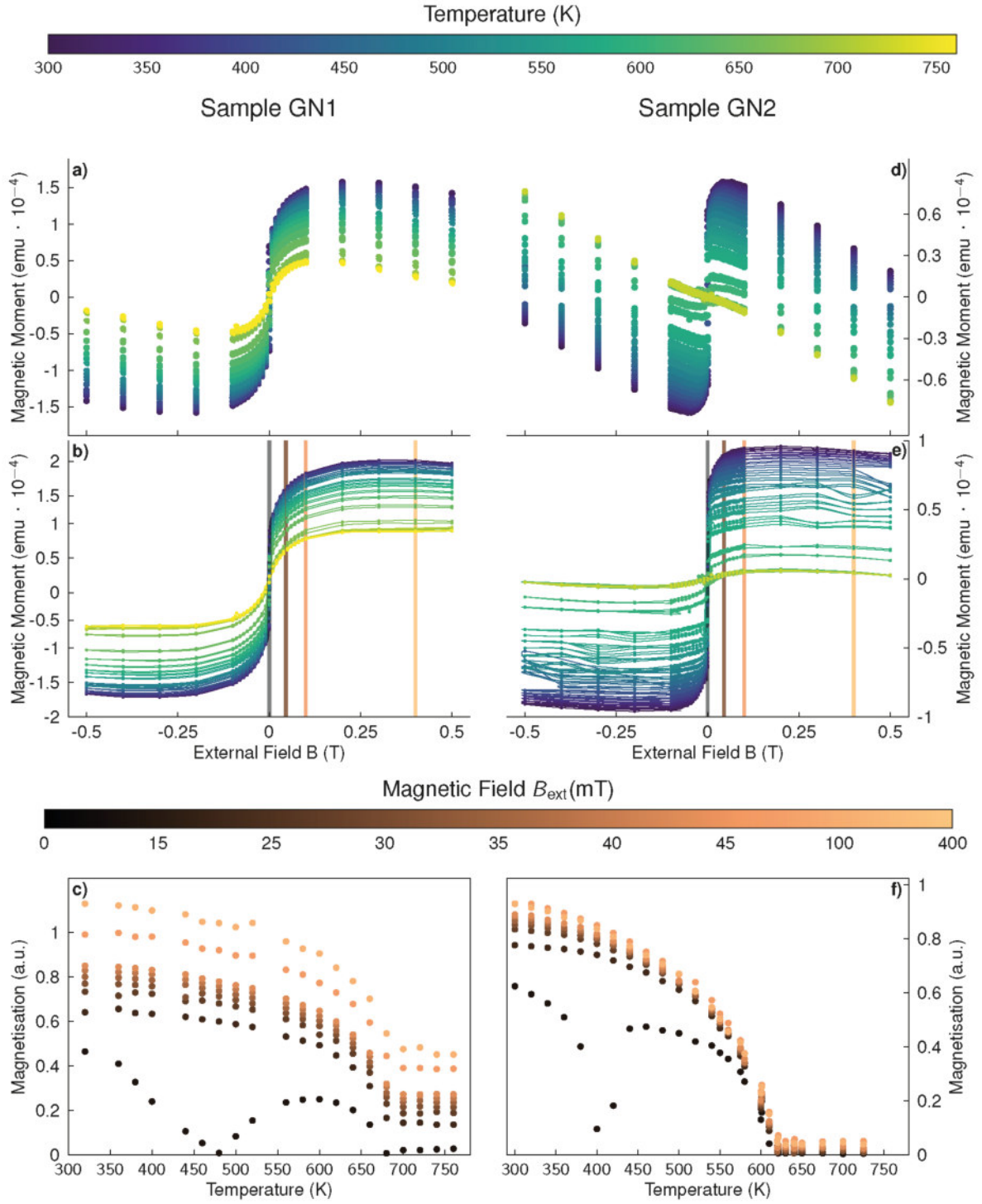


**Figure 6.2: VSM Measurements for determination of the Curie temperature for samples GN1 and GN2.** Left column: sample GN1, right column: sample GN2. The top row subfigures a) and d) show the raw data of the superconducting quantum interference device (SQUID) magnetisation measurement at each temperature. The second row figures b) and e) display the corrected ferromagnetic hysteresis. The correction involved removing the linear function caused by dia- and paramagnetic contributions, extracted from the ferromagnetic saturation magnetisation range. In the third row figures c) and f) depict the extracted values for the temperature dependent magnetisation behaviour including the estimated Curie temperature for sample GN1 in c) and sample GN2 in f).

The second row of the figure represents the resulting ferromagnetic hysteresis depending on the ambient temperature. The two samples with a similar structure and identical materials exhibit significantly different behaviours at high temperatures. This is also true for the extracted magnetisation over temperature data in the third row. The magnetic fields of 0, 45, 100 and 400 mT are highlighted in the hysteresis plots of the second row. While the sample GN2 on the right has a clearly visible Curie temperature at an expected value for this film thickness of  $T_c = 610$  K, the sample GN1 on the left has a highly magnetic field dependent magnetisation far beyond the expected Curie temperature. Even at temperature larger than 750 K the hysteresis is only reduced to half of the equivalent saturation magnetisation at room temperature. The other sample GN2 also has a small contribution of around 8% at higher fields, but the effect is clearly stronger in sample GN1. Also the Curie temperature of around  $T_c = 680$  K extracted for sample GN1 is higher than for bulk Nickel, which would be at  $T_c = 627$  K. Figure 6.2 shows that the diamagnetic effect of the sample holder is significantly larger in the measurement of sample GN2. This might point to an additional paramagnetic counterpart in GN1, which adds a second linear dependence with opposing sign to the high field region. The sample holder was identical in both measurements and the physical size of the two samples is comparable.

It is possible that the lattice mismatch between MgO and Nickel introduced a partially granular morphology of Nickel. As mentioned before, the lattice constant for Nickel is around  $a = 3.52$  Å, while the lattice constant for MgO in the crystal direction 100 is around  $a = 4.2$  Å. This could create geometric boundaries during epitaxial growth which could favour the formation of so-called macro spins, that bind the magnetisation direction of single spins together to one large spin. This superparamagnetic behaviour reduces the external field necessary to align the spins compared to paramagnetic alignment of single spins. A superparamagnetic phase in granular Nickel was observed by Gittleman et al. [118]. They created Nickel grains surrounded by a matrix of SiO<sub>2</sub>. The phase diagram relating temperature and Nickel volume concentration reveals the existence of ferromagnetism for low temperatures and high concentration of Nickel, superparamagnetism for medium temperatures and lower concentration of Nickel, and paramagnetism for high temperatures. They do not report a shift in the Curie temperature, so even in a superparamagnetic state of granular Nickel the observed transition to the paramagnetic phase occurs at the expected bulk Curie temperature [118].

Additionally a surprising feature can be observed at  $B_{\text{ext}} = 0$  mT. Both samples show a drop to vanishing magnetisation at a certain temperature. For sample GN1 this appears at  $T = 480$  K, for sample GN2 at  $T = 400$  K. After the drop both samples recover their magnetisation again until the Curie temperature is reached. It is striking that the temperature difference in these values is quite similar to the temperature difference of the respective Curie temperatures. A magnetisation signature like the observed one might be expected for magnetic systems with coupled sublattices, as those encountered in ferrimagnets. Then this temperature is equivalent to a compensation temperature, at which both sublattices have the same magnetisation magnitude with opposing directions. However, it is not expected that the thin Nickel layer is divided in sublattices with different temperature dependence.

### 6.3 Magneto-Optical Detection of Remagnetisation Dynamics

The magneto-optical response was measured with the pump probe MOKE technique described in chapter 4 and demonstrated in chapter 5. The magnetisation of Nickel is tilted out of plane due to the presence of an out of plane external field. The applied external field of  $B_{\text{ext}} = 0.28$  T was sufficiently large to saturate the magnetisation out of plane, because no precessional motion can be detected in the following measurements.

For the Nickel samples no static reference hysteresis measurements from the MOKE setup are available to normalize the time resolved magnetisation signal. This is partially due to the development process of the setup. Additionally the hysteresis measurements of the sample GN1 have been dependent on the investigated spot on the sample, which does not allow comparison of hysteresis and time-dependent

response measured on different setup conditions. Specifically on this sample the measurements revealed a surprising quadratic dependence on the whole sample to the magnetic field, presented in appendix E.

Figure 6.3 contains the time resolved magneto-optical measurements for all samples obtained at different incident fluences. The three plots at the bottom highlight the first 20 ps of the remagnetisation process, while the other plots show the complete development on a long timescale. Plot 6.3 a) shows the result for the GN1 bilayer, 6.3 b) for the second bilayer GN2 and c) for the trilayer GMN. Overall a similar trend is present, nevertheless the three samples have also differing behaviour.

The remagnetisation for sample GN1 in figure 6.3 a) changes, depending on the amount of absorbed energy. The short timescale enables observing the dynamics of the low fluence measurement of  $1.8 \text{ mJ/cm}^2$ . The remagnetisation for this fluence consists of a fast remagnetisation in the first 5 ps, followed by a slow component until full recovery. With an increase in fluence this first remagnetisation time dependence is slowed down, until the first and second remagnetisation regimes have the same slope. With further increase in fluence the first recovery of magnetisation is described well by a linear recovery. After a certain time depending on the fluence the recovery enters a faster exponential remagnetisation.

In the measurements for sample GN2 in b) the back reflection explained in section 4.7.2 is more strongly present than in the other measurements. The fluence dependence differs from the measurements of sample GN1: While an incident fluence of  $5.0 \text{ mJ/cm}^2$  for sample GN1 in plot a) already shows a significant slowing down compared to lower fluences, the fast remagnetisation occurs in the first 10 ps before it slows down for sample GN2 in figure b). Also the measured remagnetisation at the highest fluence of  $8.5 \text{ mJ/cm}^2$  has a steeper slope compared to the measurements of GN1 with the incident fluences of  $9.0$  and  $7.2 \text{ mJ/cm}^2$ . Nevertheless the general trend of remagnetisation behaviour is the same, the fluence dependence is shifted in comparison to GN1. This might indicate a lower absorption of the Nickel layer. It has to be noted that these measurements were taken at a higher external magnetic field. As seen in chapter 5, an increased magnetisation recovery would be expected for higher fields.

A possible absorption difference is unlikely to be caused by the thicker Gold layer, because a similar Gold layer also covers the trilayer GMN. The fluence dependence of the remagnetisation for this sample shown in plot c) resembles the sample GN1 in plot a). The remagnetisation curve for an incident fluence of  $4.7 \text{ mJ/cm}^2$  is already slowed down to a relatively flat slope at the beginning of remagnetisation. At the highest fluence of  $9.6 \text{ mJ/cm}^2$  the first 20 ps are not showing a significant remagnetisation, it is even possible to detect a further reduction in the magnetisation.

The analysis of the magneto-optical remagnetisation traces is performed as explained in section 5.5, as the time dependence shows very similar time scales. To summarize, two regimes in the time domain have been identified. The first part of the remagnetisation is described as a linear function, see equation 6.1. At high fluence this is a good approximation, whereas at low fluence the reproduction of the fast remagnetisation could be improved by choosing a second exponential recovery. However, the fit of high fluence dynamics is performed sufficiently well with the approximated linear function.

$$M(t) = m \cdot t - \text{offset} \quad (6.1)$$

The second regime of remagnetisation dynamics is fitted with an exponential function, see equation 6.2. Here  $b$  describes the inverse rate of the remagnetisation, in the following denoted as time constant  $\tau = 1/b$ . In the fit process the range of the exponential function was determined by the least error fit, the linear fit boundaries were set manually.

$$M(t) = -\text{Amp} \cdot e^{-t/b} - \text{offset} \quad (6.2)$$

In figure 6.4 these fits are shown for sample GN1 and for all high fluences measurements where a linear recovery can be identified in addition to the exponential remagnetisation. The fluence has an impact on the

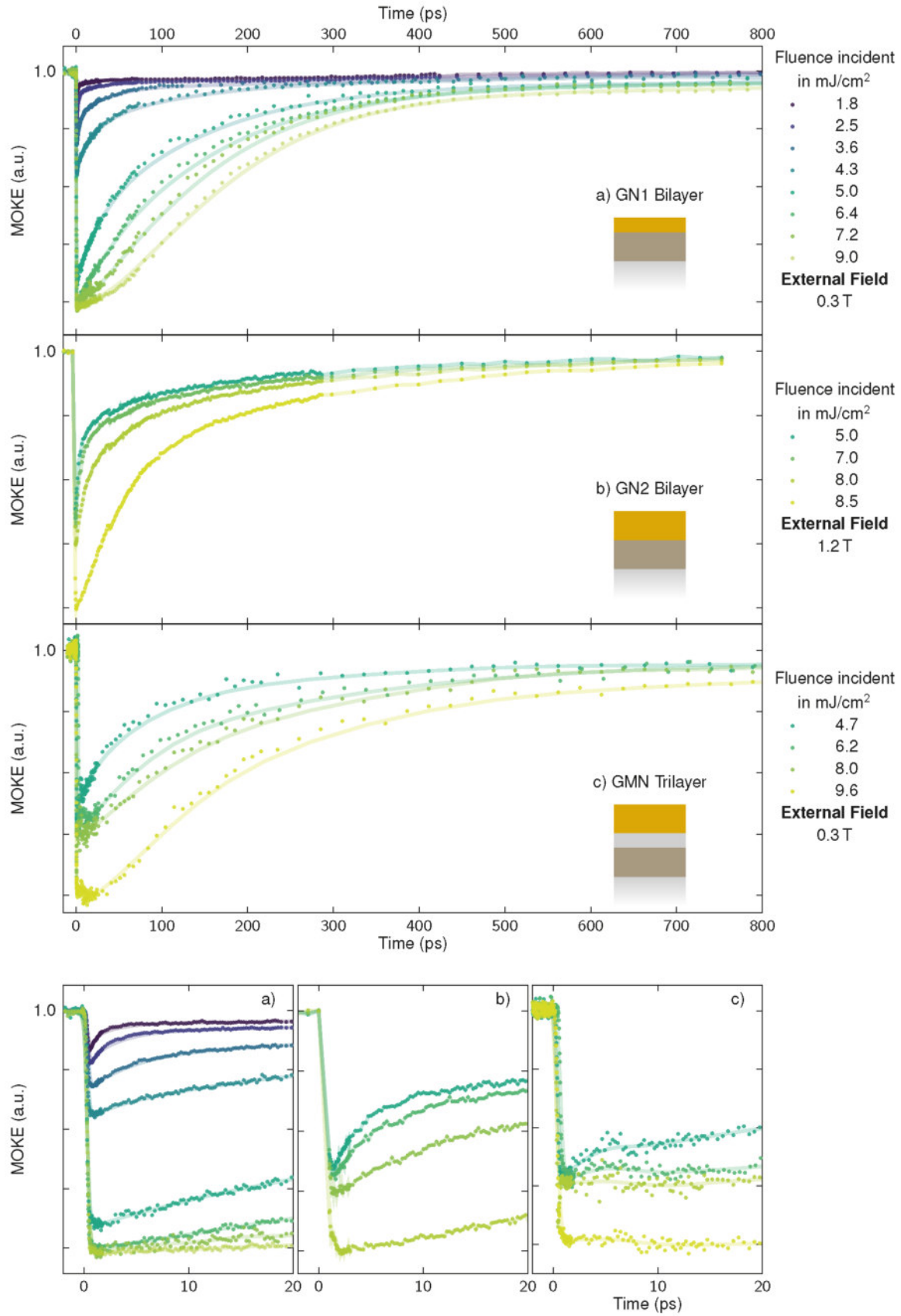


**Figure 6.3: Time resolved MOKE measurements depending on fluence for three Nickel samples a) Sample GN1, b) sample GN2 and c) sample GMN.** The insets show the layers of the respective samples, the upper graphs show the long timescale, the graphs at the bottom present a short timescale up to 20 ps.

intersection time of both fit functions, which was also determined for the FePt samples. The intersection is marked with the dashed black lines. The higher the deposited energy in the sample is, the later the first remagnetisation component changes into the second remagnetisation behaviour. With higher fluence the linear slope of the first remagnetisation slope is slowed down. At a certain fluence this means that the initial linear slope of the exponential function is the steeper remagnetisation slope.

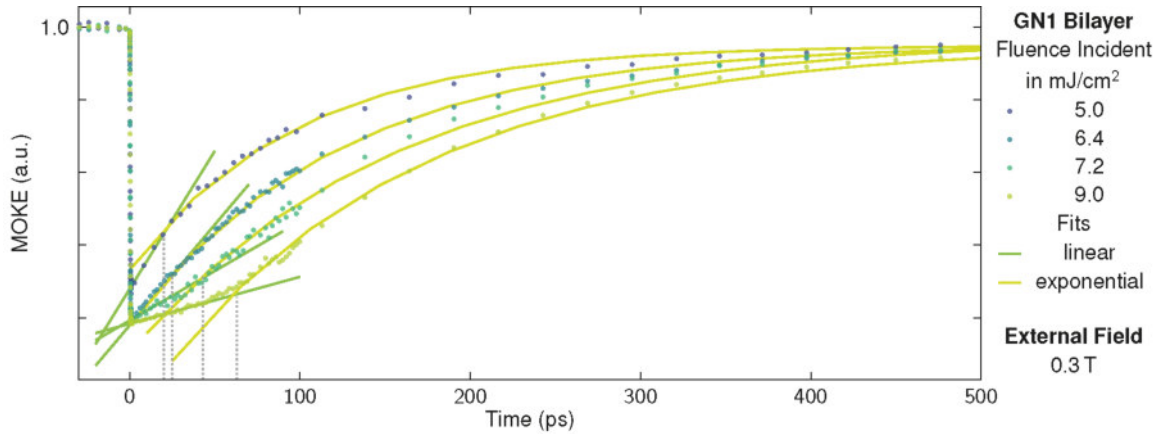


**Figure 6.4: Magneto-optical time resolved measurements and fits of Nickel sample GN1.** The remagnetisation dynamics can be divided into two parts: A slow, linear component in the beginning of the remagnetisation (green) and a following fast, exponential part (yellow). The intersection  $t_{int}$  of the fits of both sections is dependent on the fluence and is indicated with the black dashed line.

In general a similar behaviour can be observed for the Nickel sample GN2, the fit results are shown in figure 6.5. As mentioned before the magnetisation dependence on fluence seems to be shifted compared to sample GN1: At the much higher incident fluence value of 7.0 mJ/cm<sup>2</sup> the first remagnetisation is still very fast and exhibits a stronger exponential behaviour. The shape is comparable to the 1.8 mJ/cm<sup>2</sup> measurement of sample GN1. Yet, the distinct crossover in the remagnetisation behaviour is observed for all measurements. The time trace for remagnetisation after excitation with 9.0 mJ/cm<sup>2</sup> has a slow first recovery followed by the faster second remagnetisation. Compared to sample GN1 the interception time  $t_{int}$  is shifted to significantly earlier times. Even with an uncertainty in the fluence determination between the two measurements it is clear that neither a lower nor a higher fluence could reproduce an identical shape to the GN1 measurements. The damage threshold of both samples was reached at approximately 10.0 mJ/cm<sup>2</sup>. However, the magneto-optical signal for the GN2 sample was not vanishing completely above this energy, but the absorbed fluence was clearly reduced and the sample was visibly damaged after the measurement. It also has to be considered that the measurements for GN2 were performed with a higher external magnetic field. As seen before for Iron Platinum this can have an impact on the speed of recovery.

The fits for the time resolved remagnetisation of the third investigated sample GMN are shown in figure 6.6. As this sample has an insulating MgO layer between Gold and Nickel it might be expected to see a significant difference in remagnetisation compared to the previous samples. However, the fluence dependence of the dynamics are very similar to the GN1 sample in figure 6.4. The interception time  $t_{int}$  between the first slow and fast second component are shifted to earlier times compared to sample GN1. This was also observed for sample GN2. From all Nickel samples the measurement at the incident fluence of 9.6 mJ/cm<sup>2</sup> has the smallest linear remagnetisation slope. Depending on the chosen boundaries for the linear fit it is also possible that the slope is negative in the first 20 ps. This could only be observed for the GMN trilayer.

Figure 6.7 displays the values for the fitted remagnetisation slope  $m$  and time constant  $\tau$ . It can be seen that the linear remagnetisation shows the same trend in all samples: A higher fluences decreases the

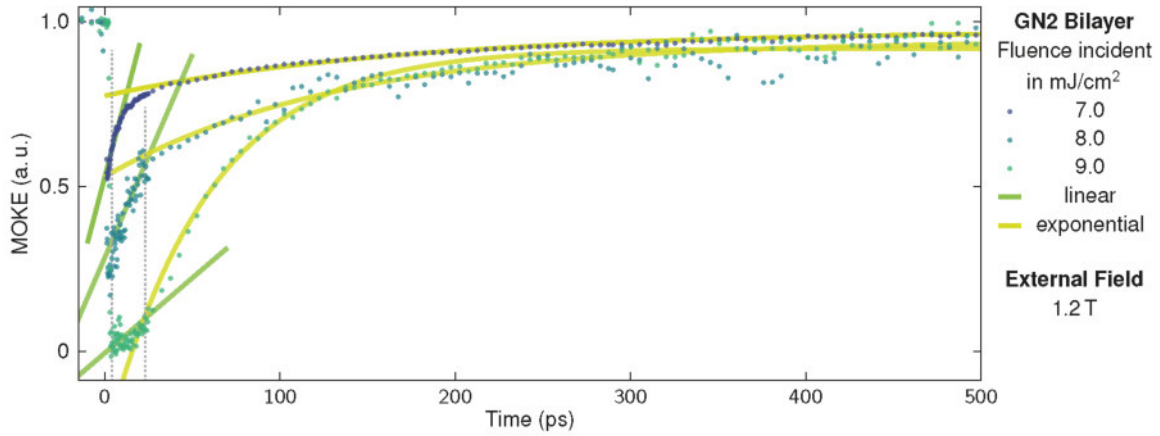


**Figure 6.5: Magneto-optical time resolved measurements and fits of Nickel sample GN2.** The remagnetisation dynamics can be divided into two parts: A linear component in the beginning of the remagnetisation (green) and a second exponential part (yellow). The intersection  $t_{\text{int}}$  of the fits of both sections is dependent on the fluence and is indicated with the black dashed line.

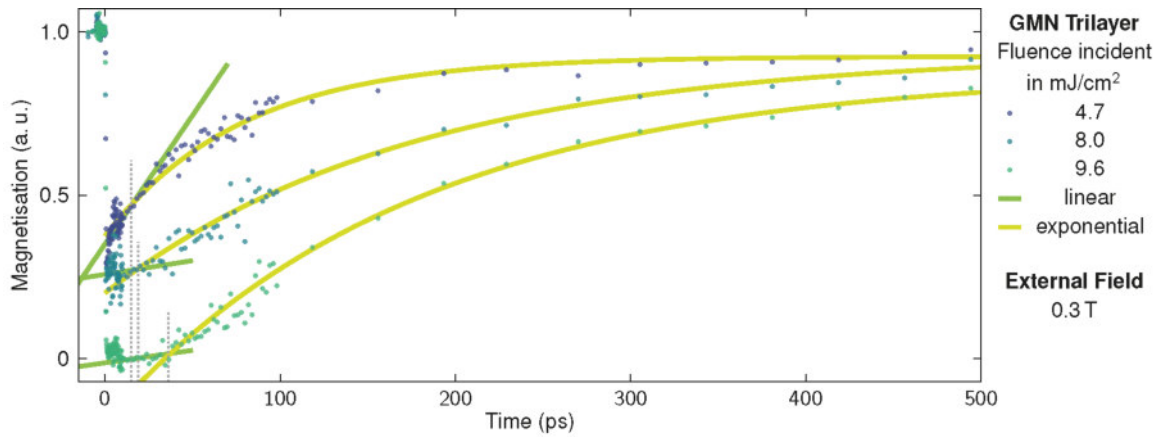


**Figure 6.6: Magneto-optical time resolved measurements and fits of Nickel sample GMN.** The remagnetisation dynamics can be divided into two parts: A linear component in the beginning of the remagnetisation (green) and a second exponential part (yellow). The intersection  $t_{\text{int}}$  of the fits of both sections is dependent on the fluence and is indicated with the black dashed line.

speed of remagnetisation in the first picoseconds. Yet, the trilayer GMN shows a significantly slower remagnetisation compared to the two bilayers of AuNi.

The trends in the exponential time constant  $\tau$  are not unambiguous. The bilayer GN2 demonstrates a decreasing time constant with increasing fluence. This could be equivalent for the sample GN1, but the data points are scattered, so that the trend is not clearly visible. This is also the case for GMN, but the few datapoints correlate well with the GN1 bilayer. Nevertheless the range of variation in  $\tau$  is mostly 100 – 200 ps. Noticeable this is a very significant difference to the Iron Platinum sample fit results. The continuous FePt film slowed down with increasing fluence.

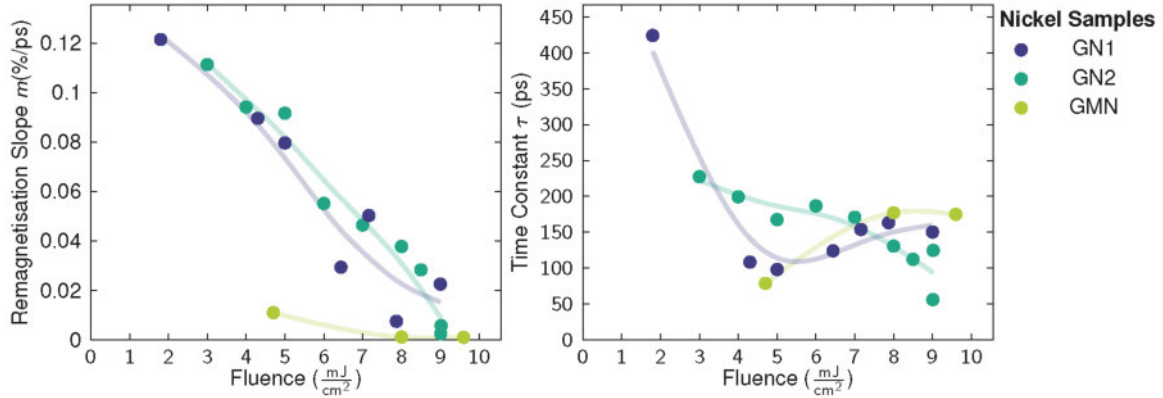


**Figure 6.7: Fit results for the remagnetisation slope  $m$  and the time constant  $\tau$  for the Nickel samples.** The left plot shows the remagnetisation slope  $m$  extracted from the linear remagnetisation regime. The right plot displays the time constant  $\tau$  of the exponential magnetisation recovery.

The time for the interception between both remagnetisation signatures is depicted in figure 6.8. The general trend is equivalent for all samples: A higher fluence leads to a later crossing of both functions. The bilayer GN1 stays longer in the first remagnetisation regime and therefore has a later interception time than the other two samples. It might be that the dependence of crossing time to fluence is not a linear, but rather an exponential function. However, the determination of low fluence linear contributions is more uncertain than for the high fluence data.

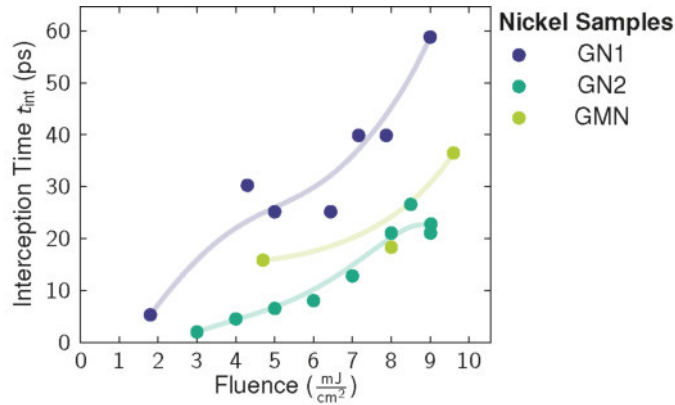


**Figure 6.8: Interception time  $t_{\text{int}}$  for the Nickel samples.** Indicates the interception of both remagnetisation time regimes for all measured Nickel samples depending on the fluence.

## 6.4 Summary

This section will summarize the main observations regarding the static and dynamic remagnetisation behaviour of the AuNi bi- and trilayers. The focus lies on similarities and difference in characteristics.

### Similarities

- For the external applied field of 0.3 mT for samples GN1 and GMN and 1.2 T for sample GN2 no magnetisation oscillations on long timescales could be observed, therefore all samples are saturated in the out of plane direction.
- The demagnetization occurs on an ultrafast timescale in less than 1 ps.
- Two remagnetisation regimes could be identified in all samples:
  1. A fast remagnetisation observed in the first picoseconds for low fluence excitations which is slowed down with increasing fluence. For low fluence an exponential function is most accurate, whereas at high fluences a linear fit is sufficient for earlier times.
  2. An exponential remagnetisation lasting hundreds of picoseconds.
- Both functions cross at a distinct interception time  $t_{\text{int}}$ , which is particularly pronounced for high fluence excitations.
- This interception time  $t_{\text{int}}$  is shifted to later times when the fluence is increased.
- The exponential time constant  $\tau$  varies in a small range from 100 – 200 ps
- Static magnetisation measurements at zero field suggest an anomaly for samples GN1 and GN2 200 K below their respective Curie temperature.

### Differences

- The exponential time constant  $\tau$  of the sample GN2 shows a clear decrease with increasing fluence. A trend is less obvious for the other two samples.
- For sample GN1 static magnetisation measurements identify a large superparamagnetic contribution of 50% also well above an additionally increased Curie temperature, while sample GN1 exhibits only a small external field dependent magnetisation above a typical Curie temperature.
- The GMN trilayer is the only investigated sample, where a negative linear magnetisation change after excitation at high fluence could be observed.

## 7 | Interpretation of Spin Dynamics

All five samples measured and presented in this thesis exhibit similar overall remagnetisation dynamics. All of the elements creating magnetisation in the investigated layers belong to the category of transition metals, in which the 3d electrons determine the magnetisation dynamics. Another similarity between the samples is the very thin magnetic layer. The layer thickness is less than 15 nm, which means the penetration depth of the infrared laser light is not surpassed. Because of the thin films and the large excitation spot compared to the probing spot, a homogeneous excitation of the investigated layer can be assumed. The granular Iron Platinum sample is the only exception, caused by the geometrical confinements of the grains. It is reasonable to assume that the individual grains are homogeneously excited, but their absorption behaviour as described in Granitzka et al. [100] creates a distribution of temperature jumps.

The measured time resolved magnetisation response is not only a measure of the magnetisation of the sample, but can also be interpreted as a spin temperature according to the three temperature model (3TM), relating a certain magnetisation to a transient temperature. With the assumption that the different subsystem energy reservoirs are in thermal equilibrium after at maximum a few picoseconds, the lattice temperature and the spin temperature are expected to be identical after a short time. We extract the lattice temperature from ultrafast X-ray diffraction (UXRD) measurements and project this temperature to the magnetisation curve of the time dependent magneto-optical Kerr effect (MOKE) measurements.

In the first section of this chapter the UXRD measurement procedure and following data analysis to extract the lattice temperature is outlined on the example of the Nickel sample GN1. In the following section 7.2 the mentioned projection between lattice temperature and magnetisation is sketched and discussed. The closing section will conclude the information obtained about each sample system and describe the complete picture of magnetisation processes obtained from the measurements and analysis of this thesis.

### 7.1 Determination of the Lattice Temperature

For the determination of the time dependent temperature of the lattice ultrafast X-ray Diffraction (UXRD) measurements were performed. The process of the measurement and the data analysis are not part of this thesis, so this section will give a brief overview of the method and extraction of the lattice temperature with references to the appropriate sources. After the presentation of the UXRD results the comparison of the fluence between the MOKE and UXRD setups will be described, as this is an important value for calculating the lattice and spin temperature measured at two different setups.

#### 7.1.1 Ultrafast X-ray Diffraction Measurements

The periodic arrangement of atoms in a crystalline material leads to constructive and destructive interference of an incoming X-ray beam. The probe beam must have a wavelength in the same order of magnitude or smaller than the distance  $d$  of the lattice planes. Typically lattice constants are in the order of several Angström, so hard X-ray wavelengths are necessary. The relation between incoming wavelength  $\lambda$ , diffraction angle  $\theta$  and distance of the lattice planes is described by the Bragg condition (7.1).

$$n\lambda = 2d\sin(\theta) \quad (7.1)$$

Here  $n$  refers to the order of the positive interference.

Compared to most methods using optical light this enables a deeper understanding of multilayered systems, as the penetration depth of X-rays is much larger than that of light in the visible spectrum. Additionally for several materials with different lattice constants in a heterostructure the behaviour of the single layers can be studied separately. But a significant disadvantage lies in the necessity of periodicity in atoms for lab-based sources, excluding amorphous and other non-crystalline samples.

The measurements used in this work were performed at the table-top plasma X-ray source (PXS) at Potsdam. Both, experiments and data analysis, were conducted by Alexander von Reppert and Jan-Etienne Pudell. The detailed description of the functionality and theory of this experimental setup can be found in the publications of Schick et al. [119] and Zamponi et al. [120]. The data analysis routine can be found in a publication by Schick et al. [121].

The grey line in the top graph of figure 7.1 shows a  $\theta$ - $2\theta$  scan with an area detector: The intensity of the diffracted X-rays are measured in dependence of the sample rotation. If the Bragg condition is fulfilled and positive interference occurs, a Bragg peak is detected and from its position the corresponding distance of the lattice planes can be determined. In this measurement the layers for Gold (Au), Nickel (Ni) and the substrate MgO can be identified. The intensity of the Bragg peak is given by the structure factor. The shape of the Bragg peak is determined by the layer thickness as well as crystallinity and defects of the sample. A perfect bulk crystal without impurities would create a very sharp peak. The measured lattice constant in the symmetric Bragg geometry is the out of plane direction. For the time depended

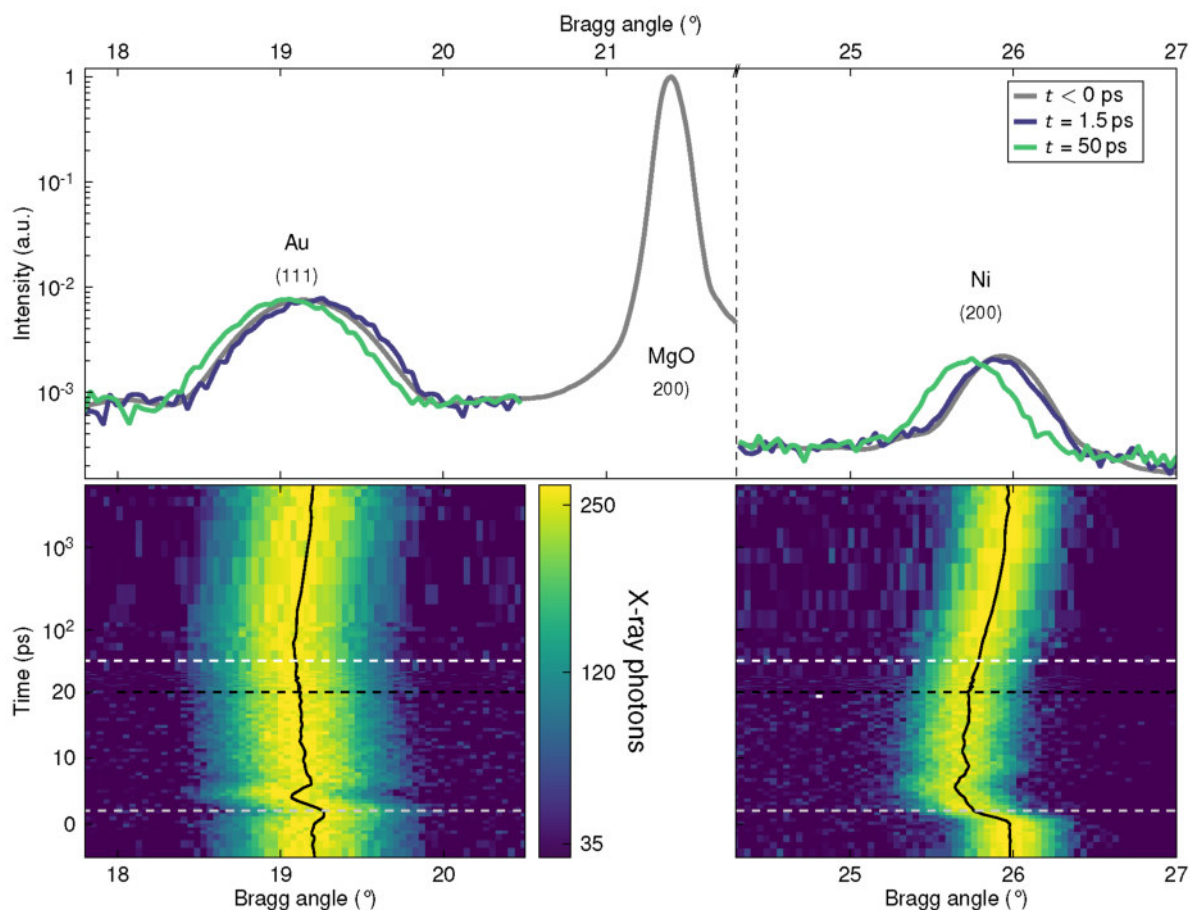


**Figure 7.1: X-ray Diffraction measurements for the Nickel sample GN1.** Top Panel: X-ray  $\theta$ - $2\theta$  scan. It depicts the Bragg peaks for the two layers and the substrate peak. At the bottom panel the time resolved evolutions of the Bragg peaks for Gold (left) and Nickel (right) are displayed. The grey and white dashed lines represent the blue and red Bragg peak in the top Panel at 1.5 and 50 ps respectively, the black line indicates an axis break from linear to logarithmic at 20 ps. Original figure from reference [6].

measurement the advantage of an area detector is utilized and the measurement is performed on a single

incident angle  $\theta$  of the sample [121]. The measurement of the Bragg peak position of Nickel and Gold is repeated for each delay time between pump and probe pulses. This creates the traces shown in the bottom of figure 7.1. The left image corresponds to the Gold layer (111) orientation, the image on the right to the diffraction of the (200) oriented Nickel layer. The centre of the Bragg peaks corresponding to the mean lattice constant of the layer shown with the black lines, is the extracted time resolved response of the lattice constant. Two slices of the time resolved measurements are also presented in the top of figure 7.1. The blue line represents the Bragg peaks a short time after excitation:  $t = 1.5$  ps. The red lines are taken from a measurement at later times:  $t = 50$  ps. A shift to lower Bragg angles is equivalent to a lattice expansion, whereas a higher Bragg angle indicates lattice contraction. Therefore the two slices show that the Gold layer is first compressed and afterwards expanded, while Nickel shows a lattice expansion at all times.

From the change in lattice constant the amount of energy deposited in the layer can be estimated. The induced strain  $\epsilon$  is equivalent to equation 7.2, the relation between measured change of the lattice constant  $\Delta c = c - c_0$  to the static lattice constant  $c_0$ .

$$\epsilon = \frac{\Delta c}{c_0} \quad (7.2)$$

Equation 7.3 relates the strain induced by the pump pulse to the specific heat  $C$  and the effective expansion coefficient in out of plane direction for an ultrafast heating of the sample,  $\alpha^{uf}$ . This expansion coefficient is corrected due to the in plane clamping detected by the symmetry of the excitation: a lattice, which is excited with a femtosecond laser pulse and heated, cannot expand directly in all lattice directions equally. The in plane stress is instantaneously equal at all sides until the soundwave travelled to the edges of the excited laser spot. Therefore only the out of plane direction is able to expand, which increases the value of the coefficient compared to static heating. All of those variables depend on the material of the layer.

$$\epsilon_{Ni,Au} = \frac{\alpha_{Au,Ni}^{uf}}{C_{Au,Ni}} \rho_{Au,Ni}^Q \quad (7.3)$$

From the relation of energy density  $\rho^Q$  and the specific heat  $C$  it is possible to assign a temperature increase to the lattice subsystem, see equation 7.4. Taking the ambient start temperature into consideration allows an assignment of absolute temperature in each layer at each point in time excluding the signal variation by the coherent dynamic.

$$\epsilon_{Ni,Au} = \alpha_{Au,Ni}^{uf} \Delta T_{Au,Ni} \quad (7.4)$$

Figure 7.2 includes all of the described quantities for both layers. The time resolved Bragg peak position shift calculated as strain  $\epsilon$  for Gold is shown in subfigure a), the equivalent for Nickel in subfigure b), the energy density  $\rho^Q$  is given on the outer right y-axis and the assigned lattice temperature at the inner right y-axis.

In the first 20 ps the Nickel strain shows oscillations originating from a strain pulse created by the rapid expansion after excitation, which is travelling from the Gold/Nickel interface through the sample structure. The temperature on this timescale is approximated to be the mean value without oscillation.

The above description of the analysis of the strain, sound as well as a detailed discussion about the heat flow observed in this bilayer can be found in reference [6]. For further comparison of the lattice and the spinsystem the time resolved strain, temperature and energy density for Nickel pumped at 800 nm is used as reference.

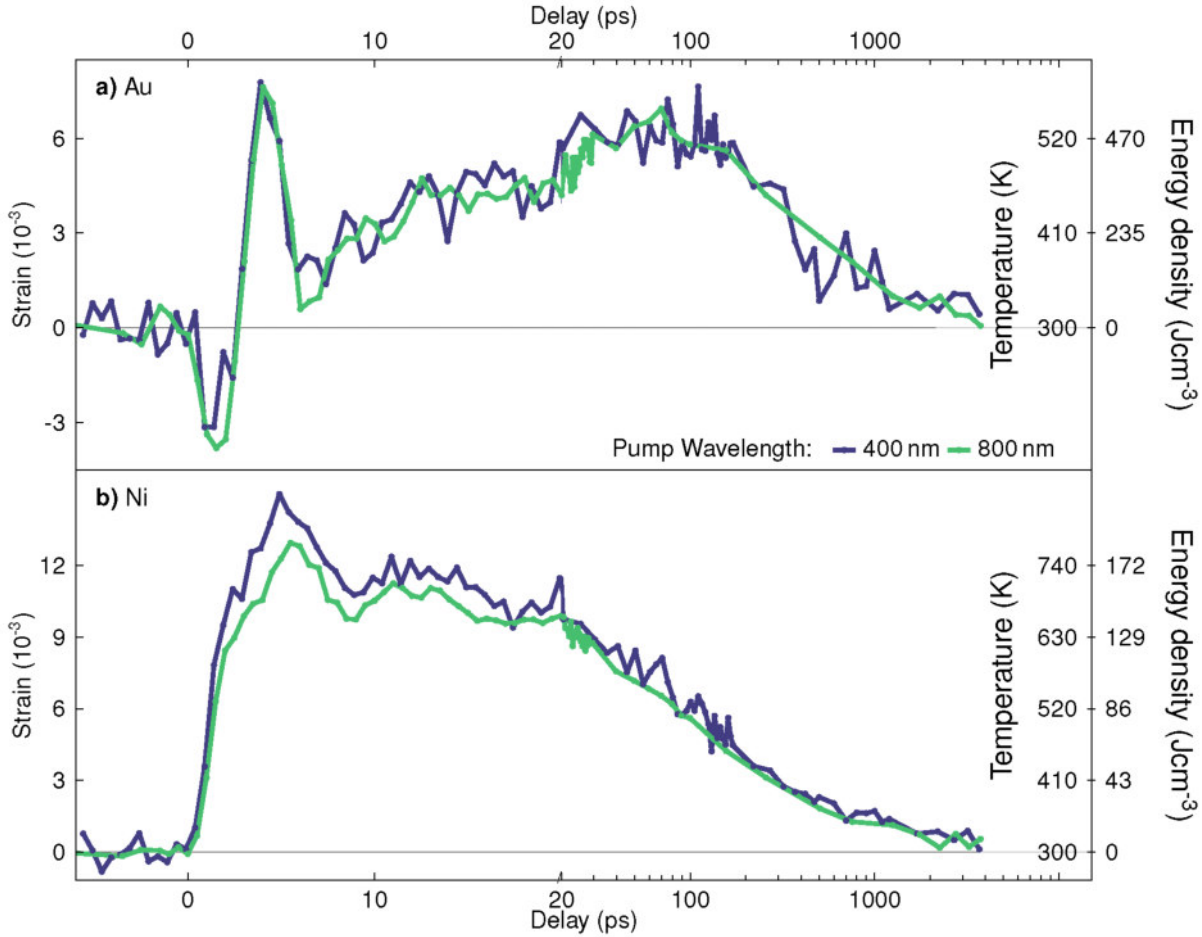


**Figure 7.2: Time resolved X-ray diffraction measurements of strain and calculated temperature and energy density for the Nickel sample GN1.** X-ray measurements of the a) Gold and b) Nickel Bragg peak. Left axis: strain  $\epsilon$  of the layer measured by the change of Bragg peak position. Outer right axis: energy density  $\rho^Q$  of the layer calculated from the specific heat  $C$  and the ultrafast expansion coefficient  $\alpha^{uf}$ . Inner right axis: corresponding temperature. The red line corresponds to an 800 nm, the blue line to a 400 nm pump pulse. The amplitude for the measurement at 400 nm is scaled for comparison. The incident fluence for 800 nm was around  $F_{inc} = 9 \text{ mJ}/\text{cm}^2$ . The red graph for Nickel pumped at 800 nm is used for comparing the magnetic and the lattice subsystem in their time-dependent behaviour. Figure originally from Pudell et al. [6].

### 7.1.2 Absorption Comparison

To compare the lattice and spin system dynamics extracted from two different experimental setups it is necessary to compare the experimental conditions regarding excitation and absorption. The incident fluence  $F_{\text{inc}}$  is a factor which scales the calculated temperature axis. The thoughts behind the adjustment of the fluence from two setups are described on the example of the Nickel sample geometry. The fluence itself is calculated equally for both measurements according to appendix B.

Figure 7.3 a) sketches the sample geometry in the UXRD setup. The X-ray probe beam enters at a Bragg angle of around  $27^\circ$  to the sample surface and has a high penetration depth, while the 800 nm pump beam enters at  $47^\circ$ . On the right the optical setup is shown. The 400 nm probe beam is incident at  $90^\circ$  to the sample surface. The pump beam is nearly parallel to the probe beam, deviating only about 1 to  $2^\circ$ . The ratio between the size of pump and probe beam spot on the sample was in both cases around 1/3. Both laser systems are working at a repetition rate of 1 kHz. For the X-Ray measurements no external magnetic field was applied, so the magnetisation of the Nickel samples was oriented in plane. The MOKE measurements in polar geometry required a magnetic field out of plane. The most important difference in

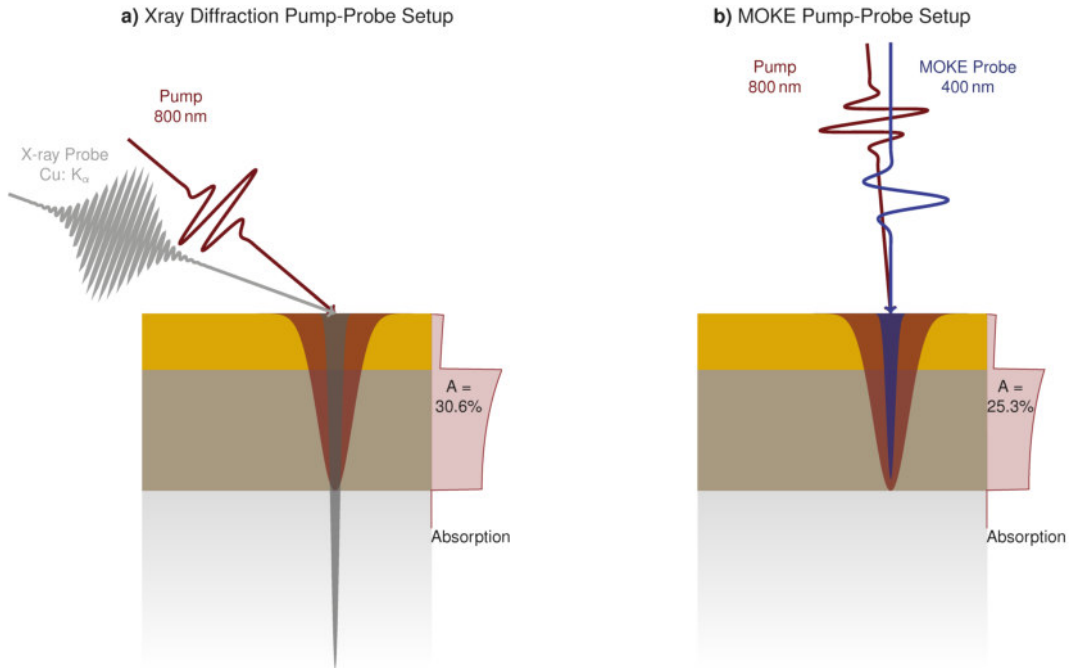


**Figure 7.3: Schematic UXRD and MOKE experimental measurement geometries.** Subfigure a) shows the geometry for the UXRD measurement: the pump pulse has an incident angle of  $47^\circ$ . The angle of the X-ray probe beam depends on the detected Bragg peak, so in case of the Nickel layer it is  $27^\circ$  from the sample surface. Subfigure b) represents the setup of the optical MOKE measurements. The probe and the pump beam are incident close to  $90^\circ$  from the sample surface. The graphs on the right side of the layers show the calculated absorption profile of the layers after excitation. The difference of 5% in the absorption results from different angle of incidence of the pump beam in the measurement setups.

the experimental conditions is the incident angle of the pump pulse. This causes a difference in absorbed fluence. The absorption of the single layers in the bilayer system cannot be assumed to be following a simple Lambert-Beer law. For the determination of the absorbed fluence, we used a multilayer absorption calculation package for Python based on [122]. This calculation takes the difference in absorption caused by different real and imaginary index of refraction for each layer into account as presented by [123]. The results for the two incident angles are shown in figure 7.3. As can be seen in both calculations shown on the right side of the sample layers, the majority of laser energy is deposited into the Nickel layer directly. Integration of the absorption gives a difference of around 5% between  $47^\circ$  and  $90^\circ$  with 800 nm light.

If the measurements carried out with the UXRD setup are compared to magneto-optical data at certain fluences, it is usually scaled with the fluence difference. This is possible if a linear relation between lattice strain and deposited energy is expected. The magneto-optical measurements are highly non-linear in response and they can therefore not be scaled.

## 7.2 Dependence of the Magnetisation on the Transient Lattice Temperature

In the previous section the analysis process from the X-ray detected Bragg peak shift to the lattice temperature was described. This section will now illustrate the process of calculating the lattice temperature dependent remagnetisation from the time resolved MOKE trace. Figure 7.4 demonstrates this process and the relation of all the discussed quantities. The rectangles on the left hand side of the schematics indicate the measured quantity with the respective method at the bottom: The strain measurement was obtained with UXRD measurements, the MOKE measurements give the magnetic field dependent magnetisation change and the absolute magnetisation is determined with vibrating sample geometry (VSM) measurements. The arrows indicate the necessary connection to extract additional information from the measurements. The time resolved lattice temperature can be obtained with the relation discussed in section 7.1.1, connecting the lattice strain and lattice temperature with the ultrafast expansion coefficient  $\alpha^{uf}$ . The assumption that the MOKE signal is proportional to the magnetisation in the sample results in the time dependent magnetisation change in the sample. This assumption is not unambiguously valid on ultrashort timescales (see section 3.3), but there is no indication that longer timescales are affected. The measurement of the absolute magnetisation depending on the ambient temperature  $T_a$  in a static, equilibrium setup (so  $T_a = T_e = T_p = T_s$ ) leads to the magnetisation curve  $M(T)$ . As indicated by the arrows on the right hand side, the time dependence of lattice temperature  $T_p(t)$  can be mapped onto the magnetisation time dependence  $M(t)$ , which results in a new temperature dependent magnetisation curve  $M(T_p)$ . The resulting green box describes the comparison that can now be made: Is the remagnetisation occurring after ultrafast excitation  $M(T_p)$  comparable to the static temperature magnetisation dependence  $M(T)$ ?

The graph below illustrates this process of data analysis with exemplary data of the granular Iron Platinum sample at an incident fluence of  $F_{inc} = 8.5 \text{ mJ/cm}^2$ . In total three parameter axis are connected via the measurements of the two degrees of freedom: a time axis (x-axis), a temperature axis (z-axis) and a magnetisation axis (y-axis).

The UXRD data is shown in purple on the back plane. The solid line represents the averaged and interpolated lattice temperature  $T_p(t)$ , which is shown on the z-temperature axis. The x-axis represents the delay time  $t$  and is shared with the magneto-optical response  $M(t)$ . This is shown in blue in the bottom plane. The y-axis represents the magnetisation  $M$  normalized by to the saturation magnetisation at room temperature. The magnetisation axis is shared with the third plane on the side. It depicts the relation between magnetisation and temperature,  $M(T)$ . The grey line is obtained from static VSM measurements on a similar sample. The green data points represent the final result of mapping the remagnetisation with a time dependent magnetisation value to the lattice temperature time dependence,  $M(T_p)$ . The three boxes with a bright green to yellow colour show the exact mapping of three points. Yellow represents the value where the lattice is crossing the Curie temperature  $T_c$ . The bright green shows the relation of magnetisation and temperature at a medium recovery state. The third green lines describe a value close to the maximum recovery observed with this delay length. After 700 ps the magnetisation has obviously not fully recovered to the saturated room temperature value.

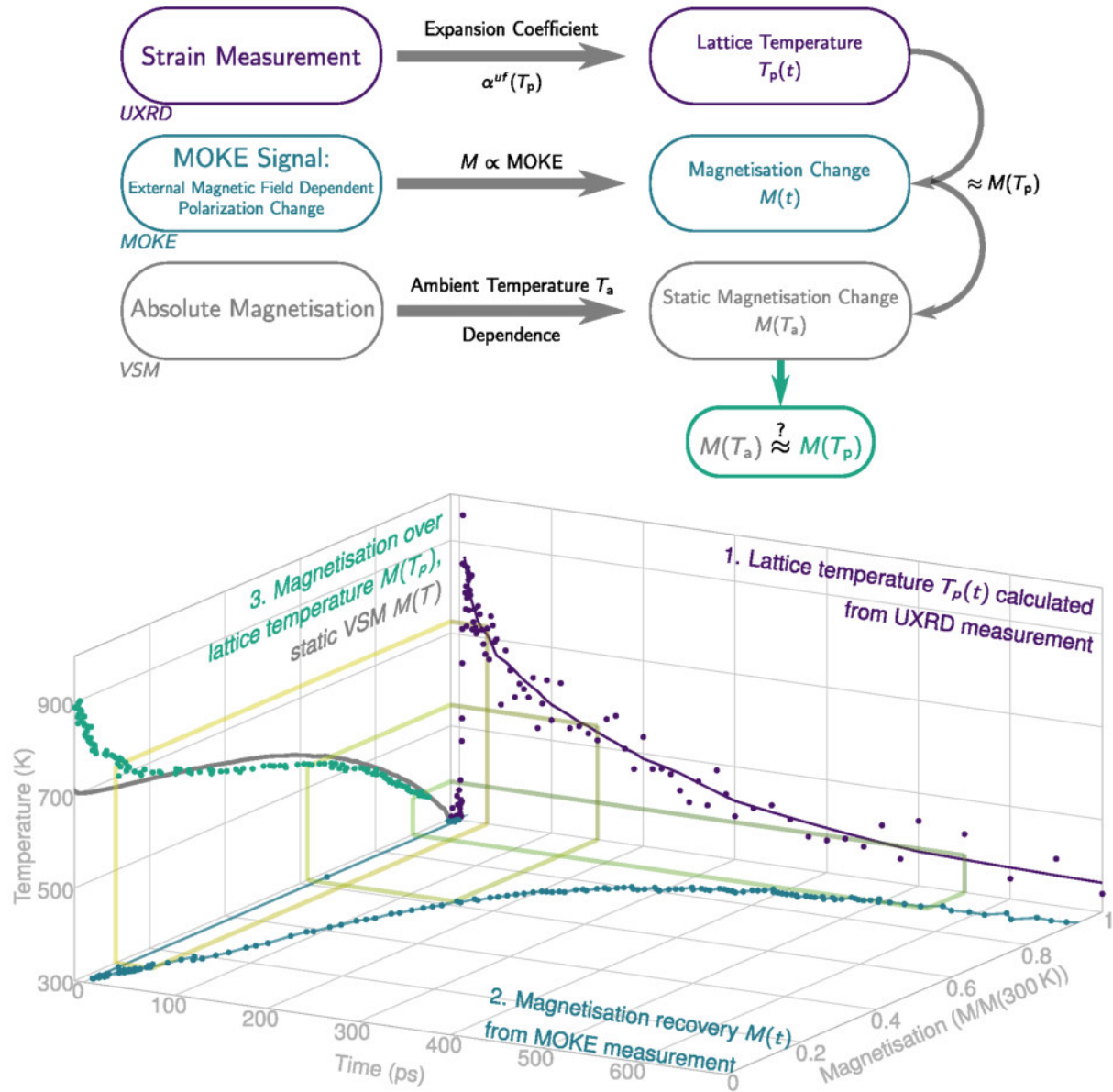


**Figure 7.4: Concept for the combination of UXRD and MOKE measurement to calculate magnetisation dependence on the lattice temperature  $T_p$ .** The flowchart outlines the process of data analysis to combine the time resolved measurements of MOKE and UXRD to extract the magnetisation dependence on the lattice temperature,  $M(T_p)$ , and compare this relation with the static measurement of magnetisation on ambient temperature  $M(T)$ , measured with VSM.

The 3D-plot demonstrates this procedure with exemplary data of the granular FePt sample. The measurement was performed with an incident fluence of  $F_{\text{inc}} = 8.5 \text{ mJ/cm}^2$  and with an external field of  $B_{\text{ext}} = 0.3 \text{ T}$  applied during the MOKE measurement. The X-ray experiment had no external field applied.

The time dependent lattice temperature  $T_p$  in purple on the back plane of the plot was obtained with an UXRD measurement. The time resolved remagnetisation dependence at the bottom plane in blue was obtained by measuring MOKE. The static magnetisation dependence on ambient temperature  $M(T)$  is shown in grey on the side plot. It was obtained with VSM measurements on a similar sample. From the combination of the time resolved lattice temperature  $T_p$  and the magnetisation recovery over time  $M(t)$  the relation between transient magnetisation and lattice temperature  $M(T_p)$  is calculated. This result is shown as the green points on the left side panel. Three connecting cycles highlight the determination of the magnetisation temperature at certain time delays. The yellow cycle is connected to the time delay when the lattice temperature drops below the Curie temperature. At the same time delay the magnetisation recovery has reached a value of 10% remagnetisation under the assumption that the minimum is close to full demagnetisation. Plotted in the temperature dependence of the magnetisation in the side plot this results in a recovery of 10% at the Curie temperature.

### 7.2.1 Expansion Coefficient $\alpha$

As seen from the schematic flowchart of the data analysis in figure 7.4 and the description in section 7.1.1, a value for the thermal expansion coefficient  $\alpha$  is necessary to calculate the lattice temperature from the strain measurements. For this calculation it is not sufficient to use the  $\alpha$  measured in equilibrium conditions. Instead an ultrafast expansion coefficient has to be determined. The difference between the equilibrium value and the value obtained for ultrafast excitation is explained by the Poisson effect [6, 124]. In equilibrium, the lattice can expand in plane upon heating. On ultrafast timescales, this expansion is not possible for symmetry reasons. The in plane expansion leads to an out of plane contraction via the Poisson effect. This missing out of plane contractive stress results in a larger expansion. The ratio of ultrafast to equilibrium expansion coefficients,  $\alpha^{uf}(T_p)/\alpha^{eq}$ , is calculated to be 2.2 for Nickel with a (100) surface orientation. The effect is even more important for FePt: The continuous film is an invar material [125], which shows no temperature dependent out of plane expansion under equilibrium conditions. The granular sample even contracts until a certain threshold temperature. Above this temperature it expands again. However, the ultrafast expansion out of plane is not zero.

An estimation for the linear expansion coefficient can be made by calculating the temperature increase in the sample according to the absorbed fluence  $F_a$  and the heat capacity  $C$ , see the equation 7.5.

$$\begin{aligned}\Delta T &= \frac{F_a}{dC} \\ &= \frac{F_{inc} \cdot A}{dC} \\ &= \frac{6 \text{ mJ/cm}^2 \cdot 0.25}{3.5 \cdot 10^6 \text{ Jm}^{-3}} \\ &\approx 440 \text{ K}\end{aligned}\tag{7.5}$$

The absorbed fluence  $F_a$  is determined from the incident fluence  $F_{inc}$  and the absorption  $A$ . The absorption calculations for the FePt sample according to section 7.1.2 lead to a value of 25%. This results in a temperature increase of approximately  $\Delta T = 440 \text{ K}$ . This knowledge can be applied to equation 7.6 in order to estimate the thermal expansion coefficient based on the measured strain  $\epsilon$  in the first picoseconds. The data and explanation for this calculation can be found in von Reppert et al. [98], the calculation in the publication was performed with a different incident fluence.

$$\begin{aligned}\alpha^{uf} &= \frac{\epsilon}{\Delta T} \\ &= \frac{4.5 \cdot 10^{-3}}{440 \text{ K}} \\ &\approx 1.0 \cdot 10^{-5} \text{ 1/K}\end{aligned}\tag{7.6}$$

This leads to an out of plane thermal expansion coefficient for the continuous film after ultrafast excitation of  $\alpha_{\text{FePt, cont}}^{uf} = 1.0 \cdot 10^{-5} \text{ 1/K}$ .

As discussed before in section 5.2 the granular sample has a distribution of absorption percentages depending on the grain positioning. This increases the uncertainty for an estimation of  $\alpha_{\text{FePt, gran}}^{uf}$ . For further calculations we estimate an upper bound of the expansion coefficient for the granular sample to be identical to the continuous sample. To estimate a lower bound we can assume that approximately the same incident and absorbed fluence leads to half of the expansion after about 5 ps [98], and hence the ultrafast expansion coefficient is approximately half. The values for the expansion coefficients are collected in table 7.1.

These significant uncertainties of the out of plane expansion coefficient make the quantitative analysis difficult. However, as can be seen in equation 7.4, the expansion coefficient is primarily a scaling factor for the lattice temperature. Other parameters which also scale the axis relatively to the magnetisation are the absorption and the error in fluence determination. Qualitative analysis about the difference in remagnetisation recoveries can be made even with the uncertainties in these parameters. In the following

Sample	$\alpha^{uf}$ [ $10^{-5}$ 1/K]	Estimation
Nickel (GN1, GN2, GMN)	2.8	Poisson corrected equilibrium $\alpha$ [6, 124]
FePt continuous	1	Initial temperature jump after excitation, equation 7.6
FePt granular	0.5-1	$\alpha^{uf}$ for the continuous film

**Table 7.1:** Thermal expansion coefficients after ultrafast excitation used for calculations of the lattice temperature  $T_p$  in the following sections.

the results of the calculated  $M(T_p)$  (green curve in figure 7.4) are presented and compared to the statically obtained  $M(T)$  curve.

### 7.2.2 Nickel GN2

In figure 7.5  $M(T_p)$  for the Nickel sample GN2 is calculated for the two fluences a) 5.0 (blue) and b) 9.0 mJ/cm<sup>2</sup> (green). In the left column plots a) and b) the results are presented for the exact used fluences, in the plots c) and d) on the right hand side the calculation is rescaled by the factor indicated in the centre between the figures. In this case a factor of 0.9 is a very slight variation and can be explained by minimal deviation in the fluence determination and conversion between the two setups. The rescaling has been done to overlap the highest resulting demagnetisation value with the static magnetisation curve, as it would be a possible value.

But with or without rescaling, it is apparent that the remagnetisation path changes for a lower and higher fluence. For the lower fluence the magnetisation values are not aligned with the static dependence of temperature. The magnetisation recovers more slowly at high temperatures and more rapidly at lower temperatures than in a static magnetisation curve. The transient  $M(T)$  dependence during the measurement is described by a linear temperature dependence rather than the  $T^{3/2}$ -law at lower temperatures. On the contrary the remagnetisation after a higher temperature increase follows the static magnetisation curve closely. The temperature calculation also predicts the lattice temperature to be above the Curie point. The ferromagnetic layer should undergo a phase transition to the paramagnetic phase. So the temperature dependence of the remagnetisation dynamics changes, if the sample was heated above phase transition.

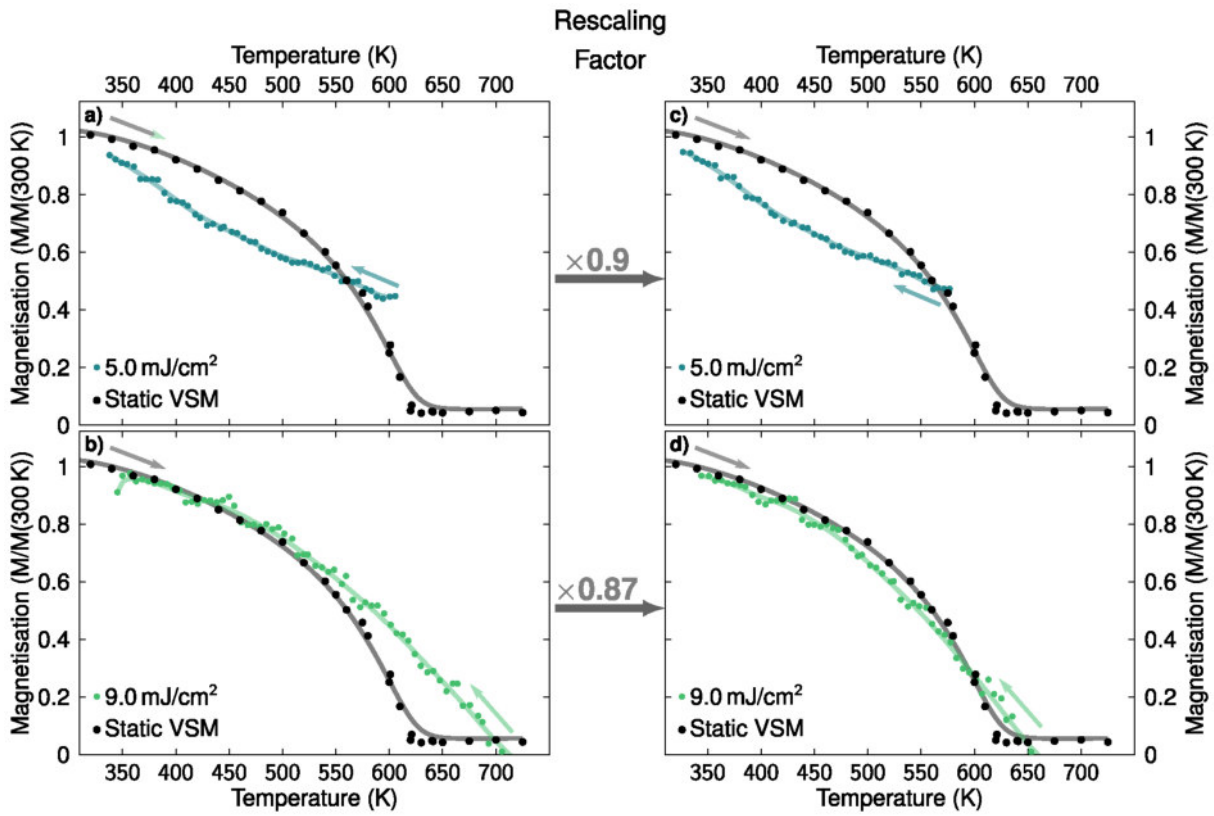


**Figure 7.5:** Calculated  $M(T_p)$  and statically obtained  $M(T)$  for the Nickel sample GN2. The graphs for  $M(T_p)$  in figures a) and b) are calculated with the original fluence value and the expansion coefficient  $\alpha^{uf}$  from table 7.1. The graphs for  $M(T_p)$  in plots c) and d) are rescaled by the factor indicated in the centre of the figure. This factor was chosen such that  $M(T)$  and  $M(T_p)$  overlap at the beginning of the measurement. The arrows on the curves indicate the direction of temperature change.

### 7.2.3 Nickel GN1

The calculations for the Nickel sample GN1 in figure 7.6 reveal a larger deviation between the calculated magnetisation and the static magnetisation curve. To shift the magnetisation value according to the lattice temperature, correction factors up to 3.2 are necessary. This deviation is too large, to originate from the standard uncertainty in the fluence calculations. An additional assumption which is part of the analysis process is the absorption in the layer, as described on section 7.1.2. It is possible that the absorption in this specific sample differs from the Nickel sample GN2, as the VSM measurements also reveal an unusual magnetic behaviour with unexpectedly large Curie temperature. A modification of the Curie temperature could be caused by mixing the composition of the Nickel layer. This also has a possible impact on absorption properties.

Nevertheless, the rescaled data of the remagnetisation reveals a similar behaviour as observed for the Nickel sample GN2.

For a small excitation with  $1.8 \text{ mJ/cm}^2$  (purple) the remagnetisation recovers minimal at high temperatures and increases closer to the ambient temperature. Both dependences are linear. However, the first recovery is most difficult to determine, because the X-ray data for the lattice temperature has the additional contribution of the longitudinal acoustic phonon and its reflections at the interfaces. Nevertheless, it is clear that the remagnetisation does not follow the static magnetisation curve.

At the medium fluence of  $5.0 \text{ mJ/cm}^2$  (blue) the remagnetisation does not follow the static magnetisation curve. It displays a linear dependence on temperature as seen before for the GN2 sample.

The excitation with a fluence of  $9.0 \text{ mJ/cm}^2$  (green) displays a more diverse temperature dependence: At the highest temperatures far beyond the Curie temperature the remagnetisation is small with decreasing temperature. In a phase transition to the paramagnetic phase this would be expected as the magnetisation depends linear on the applied magnetic field, and the susceptibility  $\chi$  connecting magnetisation and temperature has also an approximately linear dependence in the paramagnetic phase. The slope of magnetisation recovery increases at temperatures closer to the Curie temperature, but it is still linear. When the temperature falls below the Curie point, the magnetisation starts to follow the static magnetisation curve, as it was observed as well for the Nickel sample GN2.

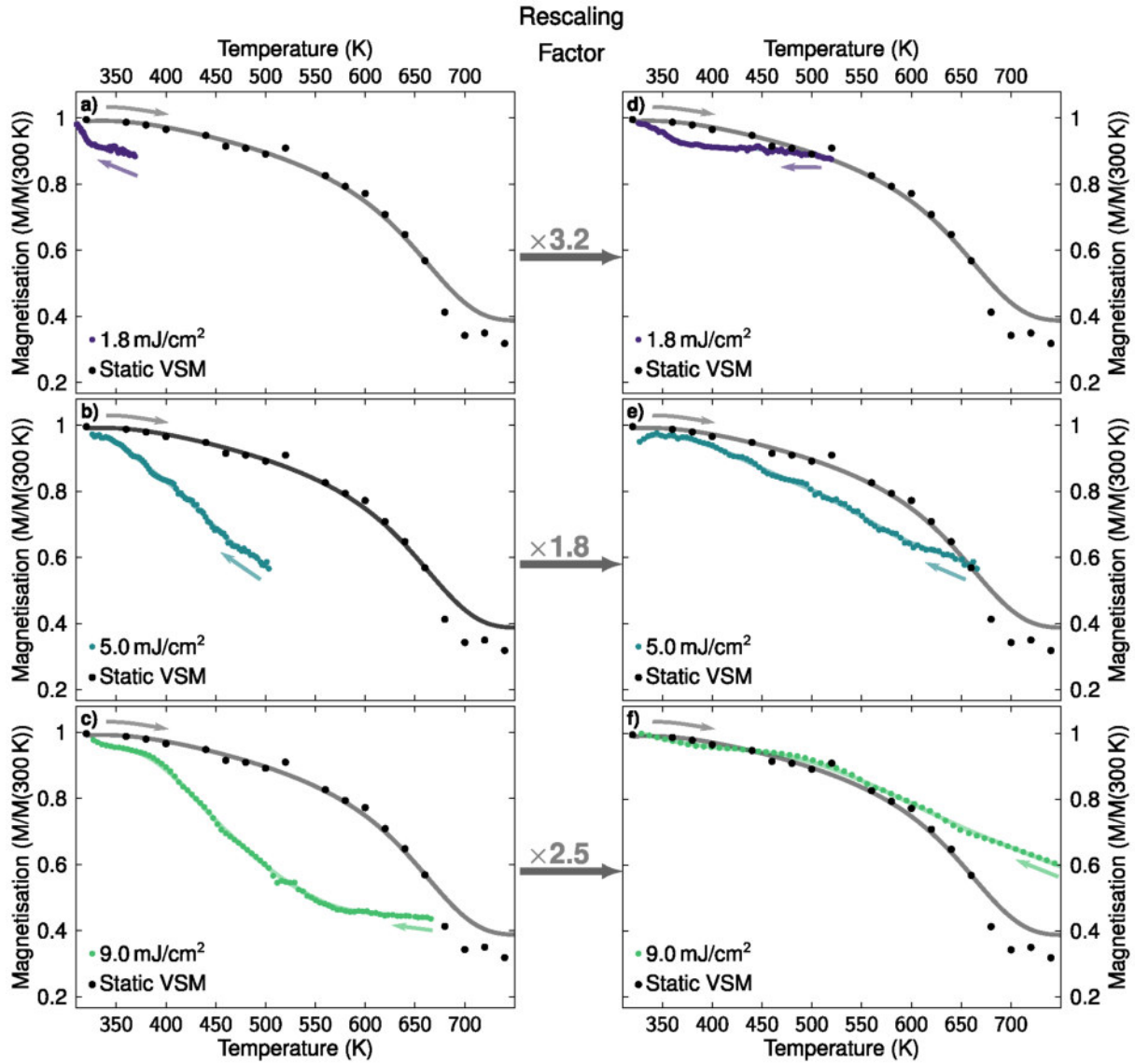


**Figure 7.6:** Calculated  $M(T_p)$  and statically obtained  $M(T)$  for the Nickel sample GN1. The graphs for  $M(T_p)$  in figures a), b) and c) are calculated with the original fluence value and the expansion coefficient  $\alpha^{uf}$  from table 7.1. The graphs for  $M(T_p)$  in plots d), e) and f) are rescaled by the factor indicated in the centre of the figure. This factor was chosen such that  $M(T)$  and  $M(T_p)$  overlap at the beginning of the measurement, in case of f) such that the magnetisation below the Curie temperature overlap. The arrows on the curves indicate the direction of temperature change.

#### 7.2.4 FePt Continuous

A similar trend to the Nickel samples can be seen in the calculations for the continuous FePt thin film. Figure 7.7 a) presents the remagnetisation for different applied magnetic fields and a high fluence of  $9.0 \text{ mJ/cm}^2$  (dots). The initial lattice temperature is well above the Curie temperature, which makes a phase transition very likely. The shape of the magnetisation gain with temperature decrease depends largely on the strength of the magnetic field applied. For high fields, a significant amount of magnetisation recovered before the Curie point was passed. After this crossing, the remagnetisation follows the static magnetisation curve. Noticeable, at lower fields this is not achieved: The remagnetisation follows an always increasing gain of magnetisation with decreasing temperature. Also, a slightly lower fluence of  $8.4 \text{ mJ/cm}^2$  plotted with star markers changes the remagnetisation over temperature significantly. The magnetisation increase above the Curie temperature is much lower than for a higher fluence with an equal strength of applied field. Below the Curie temperature the magnetisation recovery gets higher with decreasing temperature, displaying the opposite relation of derivative change. The derivative of the magnetisation curve to temperature in the equilibrium case is largest close to the Curie temperature. This measurement was obtained from a different spot on the sample, therefore an impact of structural difference is also possible.

The influence of the external magnetic field is also clearly visible at lower fluences shown in the two subplots b) and c) in figure 7.7. A higher field leads to an earlier magnetisation gain until the static curve is reached. The data also supports the observations of the field-dependent MOKE traces: at higher fluence the impact of an external field on the remagnetisation shape is more pronounced than for low fluences. Figure 7.7 c) with data obtained after  $3.0 \text{ mJ/cm}^2$  incident fluence the change in the magnetisation depending on the applied magnetic field is small. In 7.7 b) with  $5.0 \text{ mJ/cm}^2$  excitation the difference is already significant. The remagnetisation after  $9.0 \text{ mJ/cm}^2$  incident excitation is varied greatly with the magnetic field.

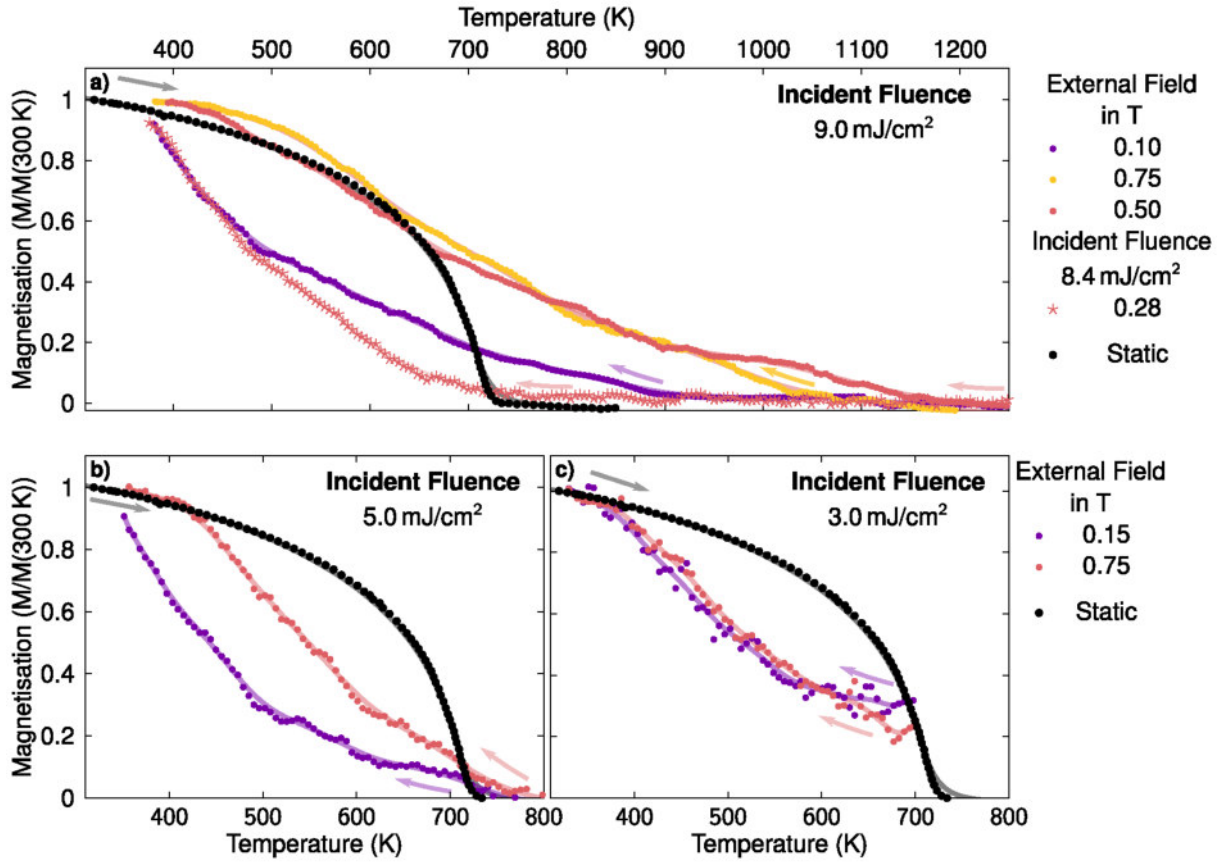


**Figure 7.7:** Calculated  $M(T_p)$  and statically obtained  $M(T)$  for the FePt continuous film. Subplot a) shows  $M(T_p)$  curves obtained with varying values for the applied external field at an incident fluence of  $F_{\text{inc}} = 9.0\text{ mJ/cm}^2$ . The curve marked with pink stars represents a measurement with an incident fluence of  $8.4\text{ mJ/cm}^2$ . Comparison of the applied magnetic fields of  $B_{\text{ext}} = 0.15\text{ T}$  (purple) and  $B_{\text{ext}} = 0.75\text{ T}$  (pink) are shown for incident fluences of b)  $F_{\text{inc}} = 5.0\text{ mJ/cm}^2$  and c)  $F_{\text{inc}} = 3.0\text{ mJ/cm}^2$ . Arrows indicate the direction of temperature variation.

### 7.2.5 FePt Granular

The remagnetisation of the granular sample qualitatively different than all other investigated samples. The uncertainty in the thermal expansion coefficient  $\alpha^{uf}$  and the average absorption on the probed spot on the sample makes a quantitative analysis difficult. Figure 7.8 displays the effect of the upper bound of  $\alpha^{uf} = 1.0 \cdot 10^{-5}$  (dots) and lower estimation of  $\alpha^{uf} = 0.5 \cdot 10^{-5}$  (stars). The static VSM measurement is also an approximation, as it was taken from a similar sample. It is evident that the scaling of the curves is important for absolute temperature values. However, the shape of the  $M(T_p)$  magnetisation curve does not change. Surprisingly, the magnetisation curves for low and high fluence coincide, so the remagnetisation dynamics is not different for small or complete demagnetisation. Figure 7.9 a) shows the results for three different fluences, b) the magnetic field dependence for the high fluence  $F_{inc} = 10.0 \text{ mJ/cm}^2$  is presented. In these calculations the upper boundary of  $\alpha^{uf}$  was used. As it was seen from the transient MOKE measurements in figure 5.23, the external magnetic field has only a small effect on the remagnetisation, contrary to the continuous FePt film. The similarity in the path of remagnetisation for all magnetisation curves might be attributed to the morphology of the sample. Due to the small size of the nanoparticles, domain wall motion cannot be a driving force for remagnetisation. Another possible influencing parameter might be the limited visibility of nanograins that are only partially demagnetised. As explained in section 5.3.2, the largest contribution to the measured magneto-optical signal originates from the particles that are heated enough to have a sufficiently low coercive field to be switched. The particles that are only exhibiting reduced saturation magnetisation and are not switched might follow the slower remagnetisation pattern as seen for the low fluence excitation of the Nickel samples.

The measurements in figure 7.9 a) and b) were not taken on the same spot on the sample which can explain the small difference in shape between the magnetisation curves in a) and b).

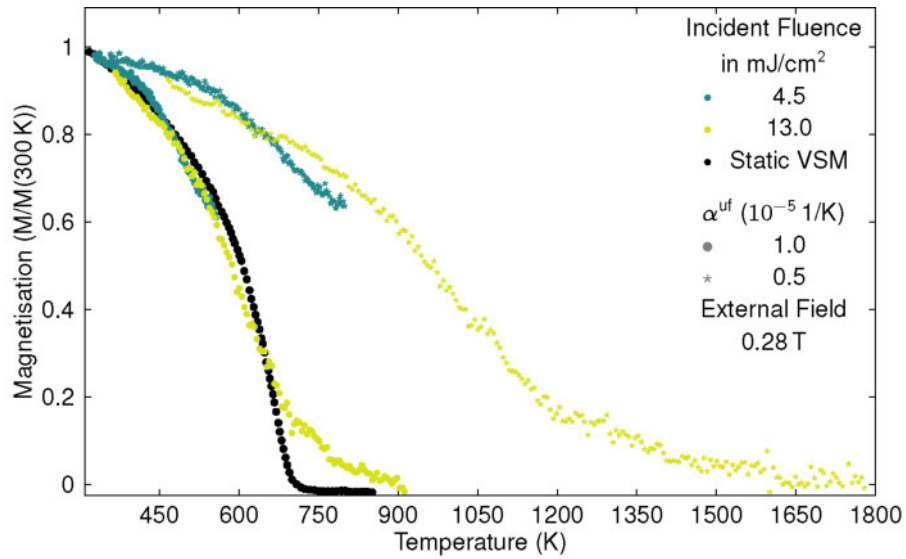


**Figure 7.8: Calculated  $M(T_p)$  and statically obtained  $M(T)$  for the FePt granular film depending on the thermal expansion coefficient  $\alpha^{uf}$ .** The plot shows  $M(T_p)$  curves obtained at the incident fluences of 4.5 and 13.0 mJ/cm<sup>2</sup> at the applied external field of  $B_{ext} = 0.28 \text{ T}$ . The black line represents a static VSM measurement. The two sets of  $M(T_p)$  are calculated by using different values for the expansion coefficient,  $\alpha^{uf} = 0.5 \cdot 10^{-5}$  (stars) and  $\alpha^{uf} = 1.0 \cdot 10^{-5}$  (dots).

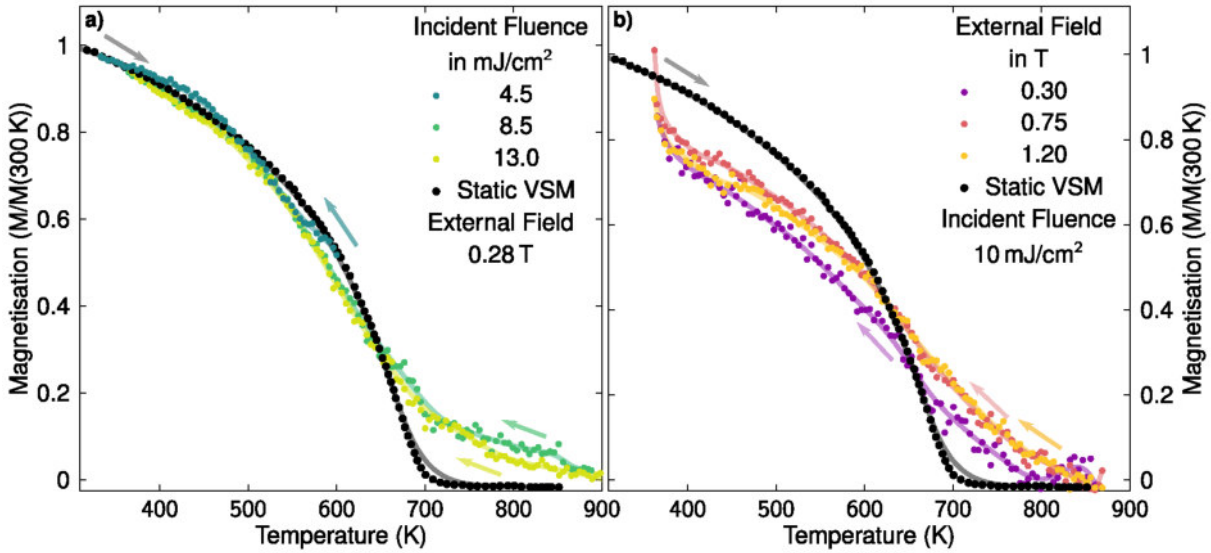


**Figure 7.9:** Calculated  $M(T_p)$  and statically obtained  $M(T)$  for the FePt granular film. Subplot a) shows  $M(T_p)$  curves obtained with varying values for the incident fluence at the applied external field of  $B_{ext}=0.28$  T. Subplot b) shows  $M(T_p)$  curves obtained at the incident fluence of  $F_{inc}=10.0$  mJ/cm<sup>2</sup> and various external applied fields. Arrows indicate the direction of temperature variation.

### 7.3 Comparison of Lattice and Spin Dynamics

Figure 7.10 presents the combination of UXRD and MOKE measurements with calibrated fluences for the Nickel sample GN2. The measurement of the UXRD curve with a fluence of  $F_{inc} = 6.1$  mJ/cm<sup>2</sup> is scaled according to the fluence it is compared to (see appendix B) as only linear effects regarding the scaling of the lattice constant with fluence are expected. The right y-axis in figure 7.10 a) shows the derived lattice temperature  $T_p$ , as described in section 7.1. The Curie temperature  $T_c$  as estimated from the VSM measurements is indicated. The vertical grey line represents the time region of intersection for both functions describing the remagnetisation behaviour, as shown in sections 6.3.

Figure 7.10 b) displays the remagnetisation dynamics measured for different fluences. The dotted lines indicate the linear and exponential fit performed as described in section 5.5 in chapter 5. The time scale of the figure changes from linear to exponential at 20 ps. The X-ray measurements suggest that the lattice temperature  $T_p$  is above the Curie temperature  $T_c$  for a significant amount of time of at least 30 ps. As seen from the magnetisation versus lattice temperature calculations in the previous section this predicts the transition to a paramagnetic phase after excitation until that time is passed.

As discussed in chapter 6, not only in Iron Platinum samples but also in Nickel layers the general shape of remagnetisation is determined by two distinct regions: a linear remagnetisation following the ultrafast demagnetisation transitioning into a second exponential recovery with a clear distinct break between the two regimes. The grey line with shading indicates this crossing of the two functions for the measurement of  $F_{inc} = 8.5$  mJ/cm<sup>2</sup>. The temperature of the lattice at this time  $t_{int}$  indicates that the Curie temperature is reached. Conclusively, this indicates that the slow remagnetisation in the beginning of the measurements is the marking of the paramagnetic phase, in which only a small amount of magnetisation is regained by applying a constant magnetic field. The cooling of the lattice and therefore the spin system enables a larger magnetisation with a constant magnetic field. A short time of transition between the linear and exponential recovery may be the result of the smoothed phase transition between para- and ferromagnetic state. The transition period marks the tail of the static magnetisation curve, where the long-range order is established again at short distances and favoured by the presence of an external field. Below the Curie temperature the magnetisation is recovered exponentially in time in the ferromagnetic phase.

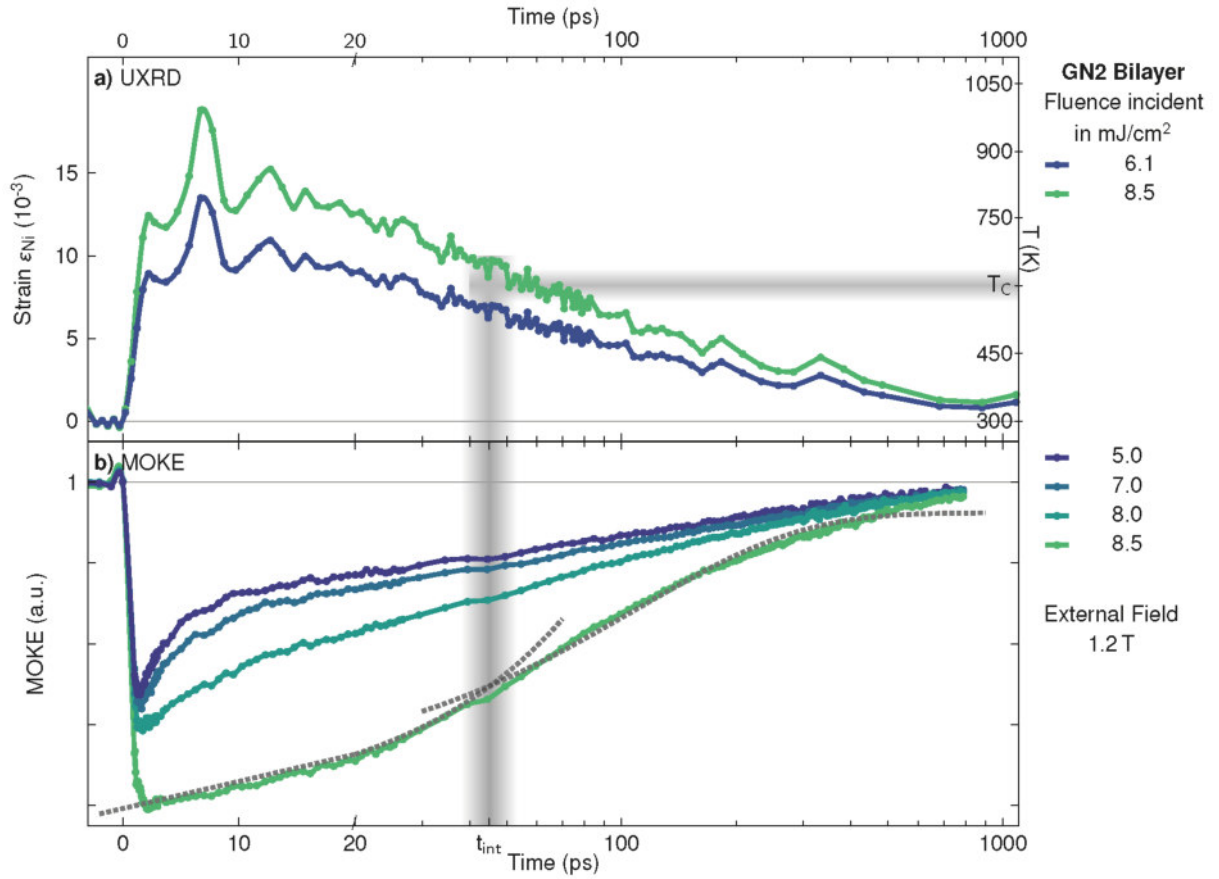


**Figure 7.10: Comparison of a) UXRD and b) MOKE measurements for the Nickel sample GN2.** The y-axis on the right hand side of the upper plot corresponds to the calculated lattice temperature  $T_p$  calculated from the strain  $\epsilon_{Ni}$ , the Curie temperature  $T_c$  extracted from the VSM measurements is indicated. The grey shade indicates the expected uncertainty in fluence calibration and Curie temperature estimation. Subplot b) shows the MOKE data for different fluences. For a fluence of 8.5 mJ/cm<sup>2</sup> the linear and exponential fits are shown with black dotted lines. The grey line with the shade represents the determined crossing time of both functions and a respective uncertainty. The X-ray data was obtained at  $F_{inc} = 6.1$  mJ/cm<sup>2</sup>.

The shift of the crossing point to earlier times at decreasing fluence corresponds to the earlier phase transition: Less energy is absorbed by the system, the general temperature increase is smaller.

In figure 7.11 this behaviour is shown for the Nickel trilayer as well. For this sample, the Curie temperature is not measured, so the grey line indicates a temperature between the two known temperatures for the other Nickel samples:  $T_c = 650$  K. When the lattice temperature  $T_p$  falls below that point, the magnetisation recovery follows an exponential function as observed for Nickel sample GN2.

The decrease of the lattice temperature until the Curie temperature is passed is accompanied by the linear magnetisation recovery. In this sample the linear magnetisation recovery at a fluence of  $F_{\text{inc}} = 9.6$  mJ/cm<sup>2</sup> is very small. Depending on the fit boundaries for the linear function also a negative slope can be seen. A better signal to noise ratio would be necessary to determine, if this decrease is the indication for a type II demagnetisation. For all other samples the observed demagnetisation behaviour was mostly following the type I behaviour, which predicts an immediate remagnetisation after the ultrafast demagnetisation. On the other hand the type II demagnetisation describes the demagnetisation with a fast and a slow component lasting several picoseconds.

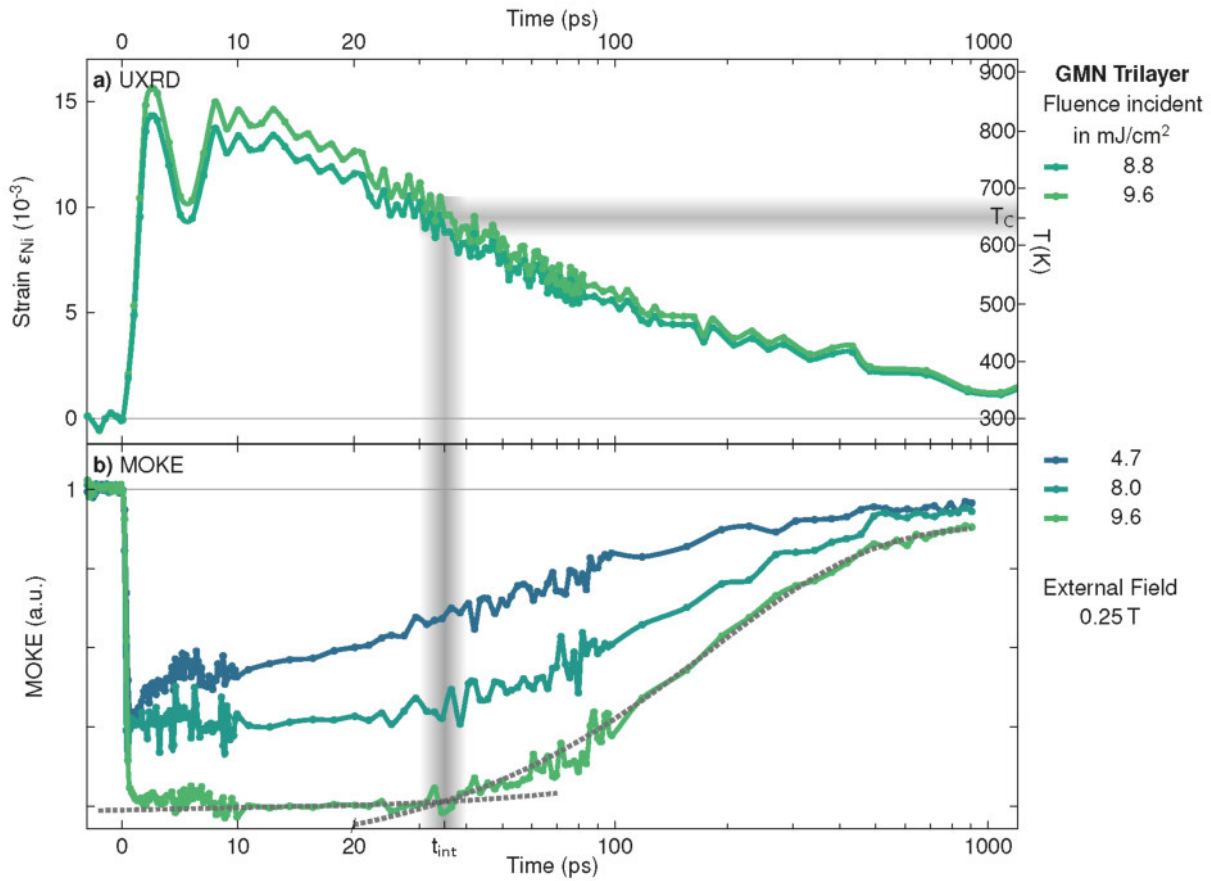


**Figure 7.11: Comparison of a) UXRD and b) MOKE measurements for the Nickel sample GMN.** The y-axis on the right hand side of the upper plot corresponds to the calculated lattice temperature  $T_p$  calculated from the strain  $\epsilon_{\text{Ni}}$ , the Curie temperature  $T_c$  for this sample is not known. But an estimated value based on the measurements of the other two samples is indicated. The grey shade indicates the expected uncertainty in fluence calibration and Curie temperature estimation. Subplot b) shows the MOKE data for different fluences. For a fluence of 9.6 mJ/cm<sup>2</sup> the linear and exponential fits are shown with black dotted lines. The grey line with the shade represents the determined crossing time of both functions and a respective uncertainty. The X-ray data was obtained at  $F_{\text{inc}} = 8.8$  mJ/cm<sup>2</sup>.

The data from the two methods for the Nickel sample GN1 is shown in figure 7.12. Compared to the other measurements, the Curie temperature  $T_c$  and interception time  $t_{\text{int}}$  between the two fit functions does not

overlap. The lattice temperature  $T_p$  indicates that the lattice is above the Curie temperature for a significant shorter time period than the transition of remagnetisation regimes in the MOKE data. As shown in section 7.2, the  $M(T_p)$  calculation also reveals an offset in temperature compared to the static measurement. The significantly higher Curie temperature (see section 6.2) and possibly superparamagnetic phase are strong indicators for a structural anomaly, which could lead to a different absorption compared to the expected value for a Nickel layer. The black curve indicates the possible expected lattice temperature progression expected from the MOKE time trace. This represents a measurement with significantly higher absorption or higher excitation fluence.

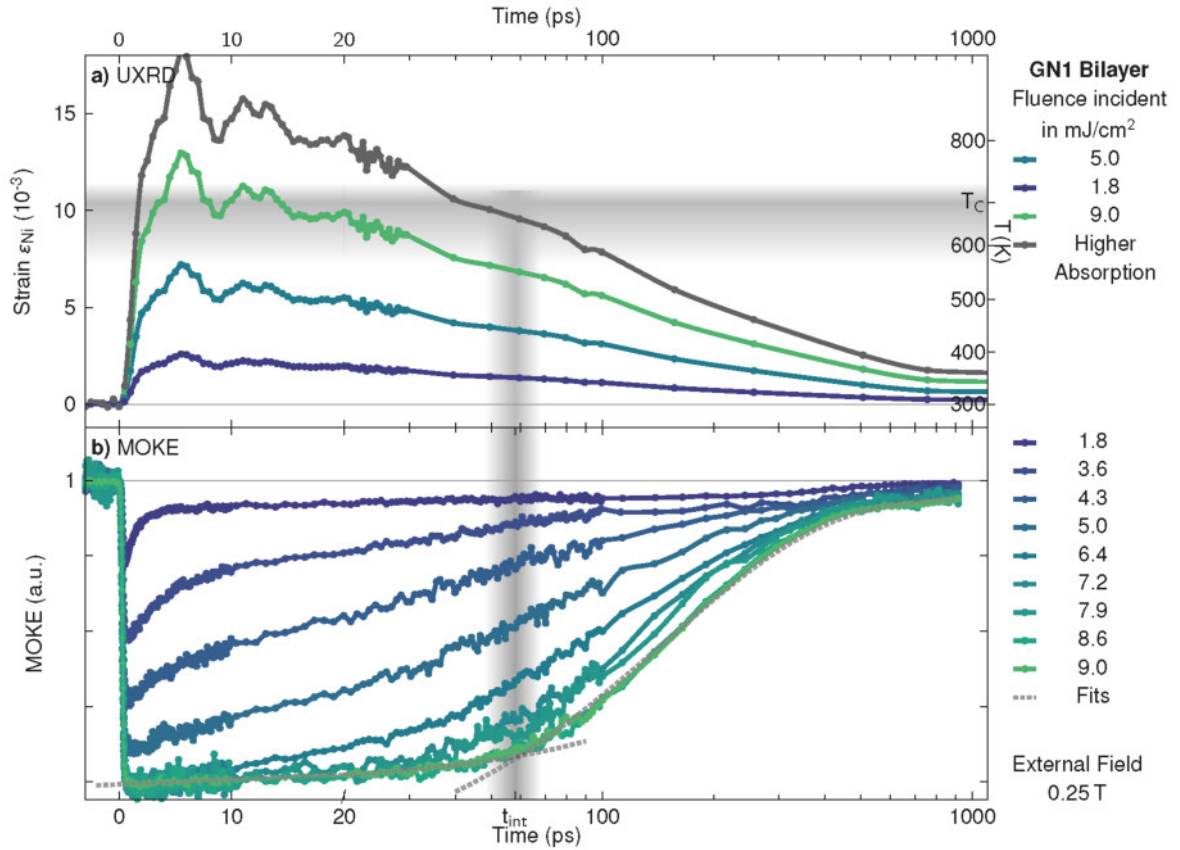


**Figure 7.12: Comparison of a) UXRD and b) MOKE measurements for the Nickel sample GN1.** The y-axis on the right hand side of the upper plot corresponds to the calculated lattice temperature  $T_p$  calculated from the strain  $\epsilon_{Ni}$ , the Curie temperature  $T_c$  extracted from the VSM measurements is indicated in with the grey line. The grey shade indicates the expected uncertainty in fluence calibration and Curie temperature estimation. Subplot b) shows the MOKE data for different fluences. For a fluence of 9.0 mJ/cm<sup>2</sup> the linear and exponential fits are shown with black dotted lines. The grey line with the shade represents the determined crossing time of both functions and a respective uncertainty. The X-ray data was obtained at  $F_{inc} = 9.0$  mJ/cm<sup>2</sup>.

Generally a temperature profile of lattice and electron temperature exists after excitation [126]. The magnetic signal will be a mix of different layers in the thin film: The surface might be above phase transition, while the interface of substrate and magnetic layer is still below the Curie temperature. However, the film thickness of all samples is small, most likely below the penetration depth of the light. Therefore in these measurements the temperature can be interpreted as constant across the film thickness. For thicker layers the depth absorption profile has to be taken into account.

## 7.4 Summary

For all samples the remagnetisation behaviour can be described in two recovery regimes in the time domain. The first one is dominant in the first tens of picoseconds of remagnetisation. Depending on sample and pumping parameters the transition to the second one is shifted in time. The second regime is determining the recovery until the sample is cooled to room temperature.

**Fluence Dependence** The first remagnetisation regime is changing from a fast recovery which is described by an exponential function to a very slow, nearly stagnant recovery with increasing fluence. The latter can be approximated by a linear function.

The transition between both time dependences is shifted to later times with higher fluences. The transition also gets more clear and distinct.

**Magnetic Field Dependence** Besides the dependence on the incident fluence, the remagnetisation behaviour also significantly changes with the applied field magnitude. Generally, the magnetisation recovers faster with a higher field applied, but the timing  $t_{\text{int}}$  of the transition between the remagnetisation functions is independent from the applied field. The impact of the field is increased when the fluence is higher. So when the magnetisation is destroyed significantly, the applied field magnitude speeds up the remagnetisation. In figure 7.7 this effect is translated into the  $M(T_p)$  curve.

**Lattice Temperature** The comparison of the magnetisation recovery obtained with optical MOKE observation and the lattice temperature extracted from UXRD measurements reveals that the samples have been above the Curie temperature for a significant time after the ultrafast excitation with high fluence. Combined with the hysteresis measurement of the Iron Platinum samples displayed in figures 5.8 and 5.9 it can be concluded that the magnetisation was nearly fully destroyed by the heating of the ultrafast laser pulse at sufficiently high fluence. Consequently, a phase transition from ferromagnetic to a paramagnetic state is observed in the magnetic measurements. This coincides well with the transition between the linear transient remagnetisation recovery and the following exponential recovery. With decreasing fluence, the phase transition from the excited paramagnetic to a ferromagnetic state is shifted to earlier times in the transient MOKE traces. At low fluence the temperature increase in the sample is smaller and the Curie temperature is not surpassed. The shape of the hysteresis for low fluence in figure 5.8 as well as the remagnetisation after the measurement in figure 5.7 indicate that a reduction of net magnetisation but no irreversible magnetisation change is observed. The first remagnetisation regime at this excitation level is therefore mainly a ferromagnetic recovery.

You et al. [13] presented the measurement of a Nickel sample with a layer thickness of 400 nm. The remagnetisation dynamics measured with all-optical MOKE were described by two time scales as well. They approximated the first slow recovery with an exponential term. Accordingly to the sample thickness they attributed the first remagnetisation timescale to a partial phase transition appearing in the excited region close to the surface of the sample. It is clear that a part of the sample is above the temperature for phase transition and other layers are still below the critical temperature, when a thicker sample is pumped with high fluence. As Kuiper et al. [12] have theoretically shown, the amount of demagnetisation of a Nickel layer does depend strongly on the film thickness as well as the temperature increase caused by the absorbed pump pulse. Their findings indicate that the net temperature increase necessary to reach a full phase transition grows with the film thickness above laser penetration depth, which is stated between 10 and 20 nm. In comparison to the samples presented in this thesis this supports the result that the Iron Platinum samples were fully demagnetized, as their thickness is below 10 nm. Also the Nickel samples are sufficiently thin to neglect any temperature variation in between the layer thickness. This is not true for the sample of You et al., which they considered in the absorbed fluence calculation.

Another experiment has been conducted by Zhao et al. [14]. They investigated FePt continuous films with varying thickness. Their data reveals the crucial importance of the film thickness. It is possible to see that a linear, slow component in the remagnetisation occurs when the film is thinner (6 nm), while with the same fluence a 15 nm layer is recovering exponentially and the magnetisation is only reduced to 50% compared to 10% for the thinner layer.

The observed demagnetisation behaviour was mostly following the type I behaviour, which predicts a remagnetisation after the ultrafast demagnetisation. The type II demagnetisation, which would describe the demagnetisation with a fast and a slow component lasting several picoseconds, might have been observed in the Nickel trilayer GMN, as described in the previous section. Mendil et al. [7] reported a transition to a type II behaviour for a granular Iron Platinum sample at high fluence. For Nickel it was already discussed from Roth et al. [9] that the parameters of fluence and ambient temperature define the transition in demagnetisation behaviour for Nickel. In all samples but GMN the damage threshold was reached before a second order demagnetisation could be identified. So despite measuring under conditions which would be predicted to lead to a type II demagnetisation, this was mostly not observed. A possible influence that could be investigated further is the presence of the Gold capping layer.

#### 7.4.1 Nickel

Figure 7.13 summarizes the time resolved performed measurements on the sample GN1. The top graph shows the data of the time resolved X-ray measurement obtaining the change in the lattice constant  $\Delta c$  along the out of plane axis, parallel to the sample surface normal. During this measurement no magnetic field was applied, so the spin system is aligned along an easy axis in plane. However, in this case the weak effect of magnetostriction in Nickel can be neglected. The centre graph depicts the results for the fluence dependent transient polar MOKE measurements. Here a magnetic field is applied out of plane. The strength of this field is sufficiently large to tilt the effective field  $B_{\text{eff}}$  determining the magnetisation direction out of plane. The change in magnetisation projected onto this axis is the measured quantity, as shown in the schematic inset on the right hand side. At the bottom the different states of the unit cell are illustrated. The grey lines in the measured data indicate the timings of the sketches. In the first state the unit cell is in equilibrium and thermalized. So no excitation is present, the sample is at ambient temperature and the spins are aligned along the axis of the effective magnetic field  $B_{\text{eff}}$ . After the excitation with an ultrafast laser pulse, the electrons absorbed the energy and are now in a state of a hot electron Fermi distribution. Within  $t \approx 10$  fs the electronic system thermalizes. Subsequently the energy is distributed into the spin system and the lattice system. A shorter coupling time to the spin system causes the spins to be fully demagnetised after around 200 fs. The lattice expands within a time of 2 ps, the in plane direction is blocked in case of ultrafast excitation. After that all subsystems of the Nickel layer begin to cool by distributing the energy to other layers. In this case this means mainly to the substrate, but also to the thin Gold layer for up to 80 ps [6]. After 200 ps the magnetisation is more than half recovered and the lattice has relaxed to less than half of the expansion. The sample does not recover fully to the initial state before excitation on the timescale of 1 ns.

The long term recovery time scale calculated by You et al. was  $\tau = 75$  ps. The values determined for the thin films presented in this thesis are on average above this value. They range from 100 to 200 ps. This can be explained by the thin layer, which lost the majority of all the magnetisation ordering in the excitation process. The film investigated by You et al. has a significantly larger thickness, so that the depth profile of the magnetisation is different and the contained magnetisation in lower layers can influence the remagnetisation process.

The determined remagnetisation over temperature determined by You et al. presented in the supplementary material of reference [13] is similar to the magnetisation recovery calculated for medium excitation fluence

in figure 7.6 b) for the Nickel sample GN1 or figure 7.7 a) and b) for the Iron Platinum continuous film: The excited magnetisation recovery does not follow the static magnetisation curve, but rather follows an approximately linear  $M(T_p)$  curve. For the thin samples at very high fluence the entire layer is driven above the Curie temperature. During the following relaxation process the  $M(T_p)$  curve approaches the static  $M(T)$  temperature dependence, because all information of the magnetization is lost during the excitation.

In particular this Nickel sample GN1 has shown some unexpected properties like an increased Curie temperature, indications for superparamagnetism (see chapter 6, section 6.2) and superposition of different external field dependencies in hysteresis measurements (see appendix E). Nevertheless, the overall characteristics and observations of the magnetisation recovery are reproducible and very well comparable to the other samples investigated in this work.

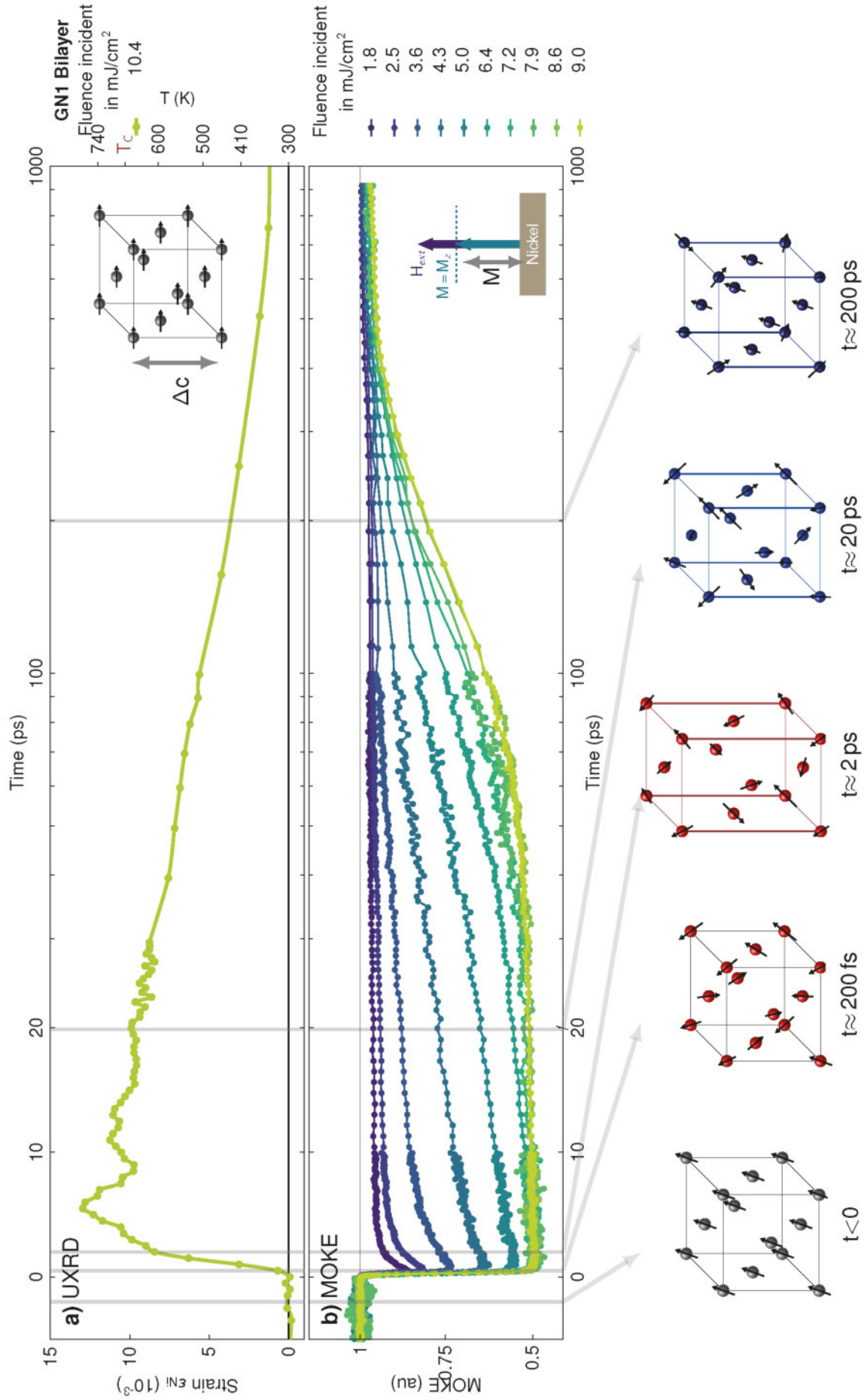


**Figure 7.13: Summary of measured quantities in the Nickel-Gold Bilayer GN1.** The first graph a) displays the data from UXRD measurements with a unit cell of Nickel in the top right corner showing the direction of the measured out of plane lattice constant  $c$ . No magnetic field was applied during the X-ray measurements so the spins are aligned along the easy axis in plane. The centre graph shows the TR-MOKE measurements for different fluences. In the right hand side the direction of the measured magnetisation is shown. At the bottom the processes in the unit cell are illustrated according to the time scale. See the main text for further details.

### 7.4.2 Iron Platinum

The lattice dynamics for the Iron Platinum (FePt) samples have been obtained with the same method and setup described earlier in section 7.1. A graphical summary of the dynamics observed for the continuous and granular film including sketches of the unit cell are shown in figure 7.15 and figure 7.16, respectively.

Here it is of particular interest that the granular sample shows an out of plane contraction, when it is excited in a free-standing configuration as shown by Reid et al. [99]. The sample measured with a substrate as seen in figure 7.16 on the other hand displays an expansion after a short contraction which is only present for lower fluence [98]. This short contraction as initial response to the excited laser pulse cannot be detected in the continuous film, shown in figure 7.15. Here only a rapid out of plane expansion can be observed.

The contraction of the grains can be attributed to the ultrafast demagnetisation. The loss of out of plane magnetisation causes the expansive stress contribution of magnetostriction to decrease. An initial in plane expansion of the lattice is accompanied by an out of plane contraction [99]. The in plane expansion does not occur in the continuous sample, because of the homogeneously distributed in plane stress. The equally applied in plane stress results in no force acting on the atoms in the in plane directions, so that their position is only altered out of plane. An excited spot could expand in plane only after a sound wave has travelled along the excited area, which is usually in the time domain of nanoseconds.

The hypothesis of the loss of magnetisation being the cause for the lattice contraction of the grains was tested with a double pulse experiment. Preliminary experimental results show that after the initial pump pulse induced a contraction, the second pump pulse only results in lattice expansion, if the time delay between both pump pulses is less than 50 ps. When the second pump pulse arrives after 50 ps, a second contraction can be observed.

Another difference to the Nickel samples is that the out of plane expansion of the lattice cannot be observed in equilibrium conditions. It is only present after the ultrafast excitation.

The magnetisation recovery shown in the MOKE measurements in figures 7.15 b) and 7.16 b) exhibit many similarities. The two timescales for remagnetisation are observed in both FePt samples. The continuous film is heated above phase transition for a significant time of close to 100 ps after an excitation with  $8.5 \text{ mJ/cm}^2$ . The hysteresis measurements confirm the hypothesis that the sample is fully demagnetized and heated above the phase transition. The change of the hysteresis both in time and depending on the incident fluence is clearly visible in this figure 7.15 as well as in the hysteresis matrix displayed in figure 5.8.

As seen in section 5.3, with higher fluence the coercive field of the hysteresis is reduced. Also the steepness of the hysteresis at the coercive field is reduced, so  $m_{\text{coer}} = \partial M / \partial B_{\text{ext}}$  is decreasing. A high incident fluence leads to an increase the temperature in the sample persists over a time of 1 ms, causing an effect of static heating: The saturation magnetisation is reduced for the transient reference hysteresis 1 ms after excitation compared to a low fluence measurement (see figure 5.15). This also reduces the absolute demagnetisation value.

The ultrafast remagnetisation for the continuous sample and for the granular sample are comparable, but some differences could be identified. The FePt grains have a much higher coercive field, so that the applied external field range is not sufficient to measure the major hysteresis loop (see section 5.3.2). However, due to the effect of heat-assisted switching the excitation with different fluences changes the magnetic signal according to the temperature increase, and for a sufficiently high fluence some grains will switch. Their coercive field is reduced to a value in the external field range. Figure 7.14 shows a possible distribution of switched particles during transient hysteresis measurements. This distribution was adopted from the measurements of Granitzka et al. [100], solely the lowest and highest absorption bars were shifted for visual representation. The static purple hysteresis was used as a reference to scale

the transient reference hysteresis. The exact ratio between transient hysteresis and static hysteresis is not known for this experiment, but for this explanation it is assumed that for the highest incident fluence of  $F_{\text{inc}} = 8.5 \text{ mJ/cm}^2$  the vast majority of particles has been switched during the measurement. Therefore this hysteresis was used as scaling reference. The relative hysteresis amplitudes from the measurement have been kept. The absorption distribution of the particle is displayed in the bar plot 7.14 b). This figure

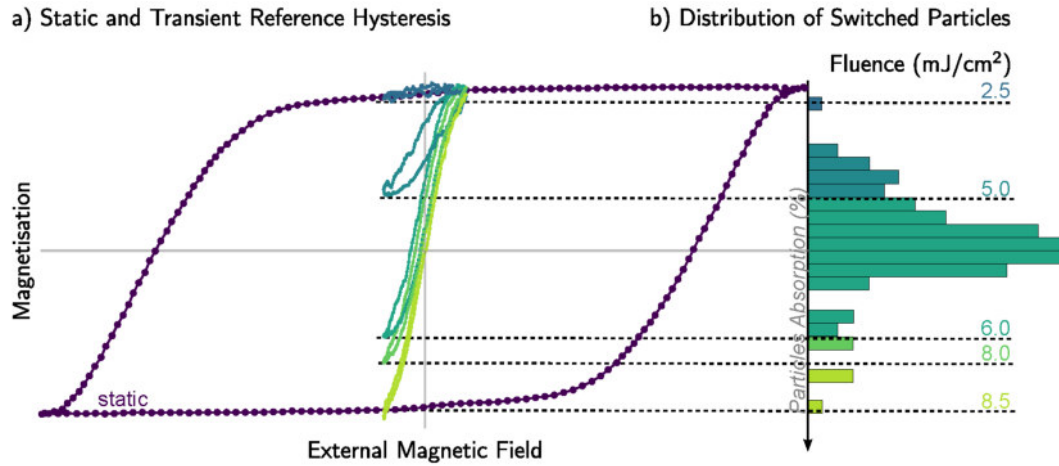


**Figure 7.14: Concept for correlation between fluence dependent transient hysteresis and switching particle fractions of the FePt granular film.** The hysteresis measurements in a) are scaled proportionally to the static hysteresis measurement (purple). The distribution of particle absorption in b) is related to each hysteresis measured at the respective incident fluence with the ratio between switched and not-switched particles indicated by the dotted line.

is created to illustrate the general concept of switching a different amount of particles with increasing fluence.

As has been observed in the matrix of the granular hysteresis measurements in figure 5.9, the lowest fluence of  $2.5 \text{ mJ/cm}^2$  does not increase the sample temperature high enough to reduce the coercive field inside the measurement range. The observed magnetisation reduction is equivalent to the small reduction of magnetisation along the remanence slope. The ultrafast magneto-optical demagnetisation is caused by a small change in magnetisation saturation due to temperature increase. Therefore the change in the transient hysteresis is characterised by a shift of the centre of the hysteresis compared to the equilibrium hysteresis, not a change in shape.

If the pump fluence is doubled, some particles absorb an energy amount high enough to switch the magnetisation direction. The hysteresis is open and deviates from the static reference, but in the excitation process the reduction of the saturation magnetisation is still visible (see 5.9, second row). Besides the switching particles the amount of not-switched particles is still significant, so that the transient hysteresis compared to the transient reference hysteresis is not centred around zero.

An additional small increase in fluence to  $6.0 \text{ mJ/cm}^2$  leads to a substantial change in the transient reference hysteresis magnitude. So with a relatively small increase in energy, a significant amount of additional particles can be switched. The transient hysteresis shortly after excitation is now centred around zero, so the amount of particles that contribute to the signal by a change in saturation magnetisation are small compared to the switched particles. The coercive field of the hysteresis decreases with increasing fluence, as it was also observed for the continuous sample.

A further increase of the fluence leads to a further increase in the magnetisation amplitude. The time resolved measurements at high fluence of  $13.0 \text{ mJ/cm}^2$  indicate a static heating effect as observed for the continuous samples as well (see section 5.4.2). Even without the static hysteresis loop and an exact value for the absorption of the grains (compared to the continuous film) this static heating indicates additionally to the shape of the calculated temperature dependent remagnetisation curves and the estimated lattice

temperature that the sample was heated above the Curie temperature. As seen before for the other samples the crossing of the first remagnetisation regime and the second one can be assigned to the transition between paramagnetic and ferromagnetic phase.

In comparison to all other samples the impact of the magnitude of the applied magnetic field is not significant. The change of the applied magnetic fields compared to the static coercive field is also smaller than for the continuous FePt sample, but even in a small ratio the continuous sample shows a significant change in the remagnetisation behaviour. Also in contrast to all other measurements, the temperature dependence of the remagnetisation  $M(T_p)$  closely follows the static magnetisation curve at all incident fluence values, as shown in section 7.2.5. Because both samples are made of the same magnetic material, the differences in remagnetisation have to be found in the geometric boundaries created by the granular structure and the surrounding carbon matrix. The arrangement in grains reduces the possibility of altering the magnetisation via domain wall motion. However, the grain boundaries increase the likelihood of defects in the crystal structure, at which domain nucleation appears. The particles are most likely in a single domain state in equilibrium, but their switching mechanism is not limited to the single domain rotation of a Stoner-Wolfahrt particle [48]. Comparing the remagnetisation speed for the continuous film and the granular film, the granular film has on average a faster recovery of the magnetisation at equal experimental conditions of fluence and external applied field. This could be caused by an overall different absorption of energy, but also by the faster switching mechanism of domain nucleation instead of a remagnetisation driven by domain wall motion. This hypothesis is also backed by the fact that the speed increase with higher applied field can be caused by increasing domain wall motion, as this is growing linear with the applied magnetic field (see chapter 2). Contrary to that is the maximum remagnetisation rate in the first time regime observed only for the granular sample. At  $6.0 \text{ mJ/cm}^2$  the linear remagnetisation is significantly larger than for lower or higher incident fluences. This effect strongly depends on the applied magnetic field.

A cinematic animation of the unit cells after excitation covering the first picoseconds can be found in the appendix F and is playable in the electronic version of this thesis.

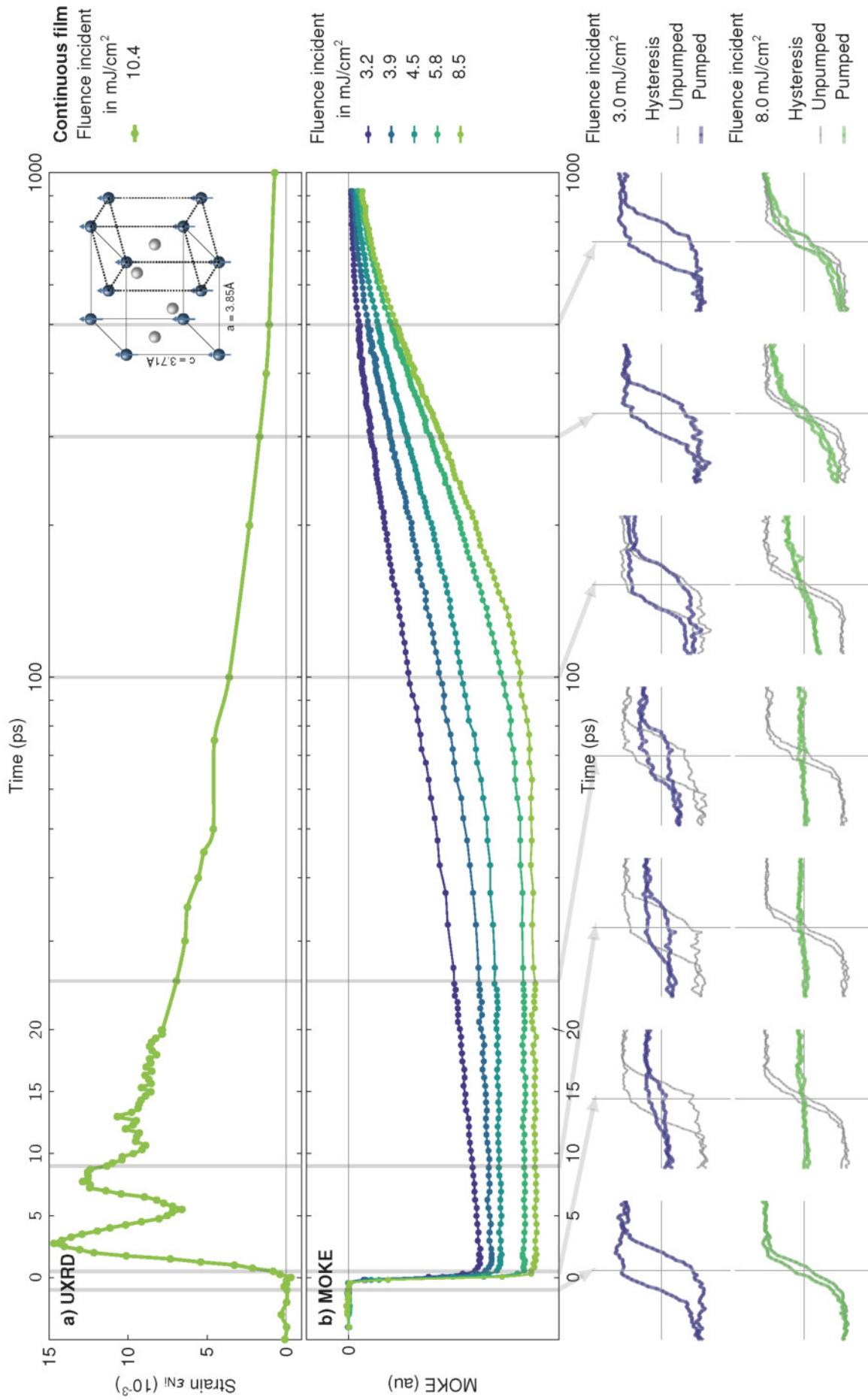


**Figure 7.15: Summary of measured quantities in the FePt continuous film.** The first graph a) displays the data from UXRD measurements with a unit cell of FePt in the top right corner showing the direction of the measured out of plane lattice constant  $c$ . The centre graph shows the TR-MOKE measurements for different fluences. At the bottom the time resolved hysteresis measurements are displayed for two incident fluences (3.0 and 8.0  $\text{mJ}/\text{cm}^2$ ). The corresponding times in the measurements and connected with the arrows.

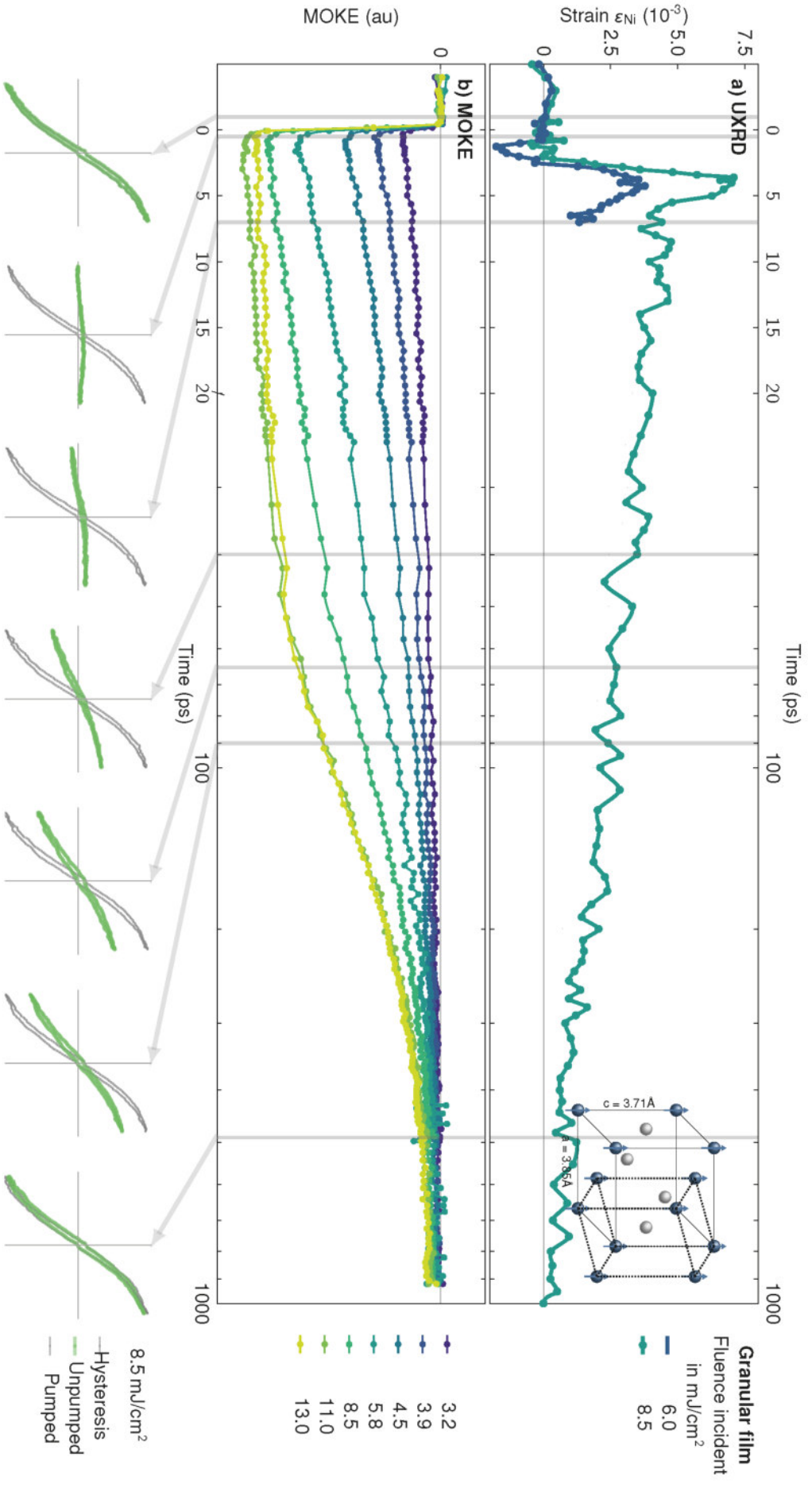


**Figure 7.16: Summary of measured quantities in the FePt granular film.** The first graph a) displays the data from UXRD measurements with a unit cell of FePt in the top right corner showing the direction of the measured out of plane lattice constant  $c$ . A second excitation fluence is added for the first picoseconds to highlight the contraction visible at medium fluences. The centre graph shows the TR-MOKE measurements for different fluences. At the bottom the time resolved hysteresis measurements for an incident fluence of  $8.5 \text{ mJ/cm}^2$  are presented. The corresponding times are indicated as grey lines in the measurements and connected with the arrows.

## 8 | Conclusion

In this thesis the remagnetisation dynamics of several thin magnetic films after ultrafast laser excitation were presented and discussed. The special focus was the combination of the dynamics of the lattice subsystems with the time resolved magnetic response. In that regard two measurement techniques of ultrafast time resolved properties were employed to understand the interaction of different subsystems in condensed matter.

The time resolved magneto-optical properties of three different sample systems have been obtained with a time resolved magneto-optical Kerr effect (MOKE) setup developed for this thesis. The lattice dynamics has been observed with ultrafast X-ray diffraction (UXRD) measurement. The extraction of the lattice temperature from these measurements made it possible to connect the magnetisation recovery over time  $M(t)$  with the temperature of the lattice  $T_p$ . The resulting temperature dependent magnetisation curves  $M(T_p)$  enabled the comparison of this non-equilibrium state after laser excitation and the magnetisation measured in equilibrium conditions  $M(T)$ .

The magneto-optical measurements revealed characteristics in the remagnetisation that were shared for all samples. The recovery of the magnetisation after destroying the magnetic order with an ultrafast laser pulse depends both on the absorbed fluence and the applied magnetic field. In all sample systems the magnetisation dynamics for high and low fluence measurements could be divided into two distinct time regimes distinguished by a clear transition. For low fluence this first remagnetisation regime dominating in the first picoseconds is fast, while the second regime of recovery is slower. Both regimes can be described by exponential functions. With increasing fluence the first function slows down and transitions to an approximately linear behaviour. It also dominates over a longer period of time, up to about 90 ps until the transition occurs. The second remagnetisation remains exponential for all fluences.

Not only the fluence has a significant impact on the remagnetisation, but also the applied external field. The field influences the speed of magnetisation recovery. For the first remagnetisation this means that the slope of the linear function increases with higher field values. The second regime also increases in speed, but additionally it is described less accurately by a simple exponential function. The influence of the external applied field is stronger with increasing fluence. In contrast to the fluence the applied field shifts the timing of the transition between the two time domains of magnetisation recovery only negligibly.

The comparison of time resolved measurements of UXRD and MOKE enables a correlation between lattice temperature  $T_p$  and time resolved magnetisation. This comparison reveals that for high fluences the distinct transition point between the two remagnetisation functions is associated to the surpassing of the Curie temperature. This is supported by the fluence dependence of the transition time. For higher fluence a larger temperature increase occurs in the sample, which shifts the cooling below a certain temperature to later times. The external magnetic field however has a very small influence on the cooling, therefore the time at which the Curie temperature is reached is not changed. The surpassing of the Curie temperature could be confirmed by measuring the transient hysteresis after excitation. They show that the continuous film of Iron Platinum is excited above phase transition and the magnetisation is fully quenched for high fluence.

The constructed magnetisation versus lattice temperature curves  $M(T_p)$  for the granular sample resemble the  $M(T)$  curve of the equilibrium measurements. The presence of a higher external field only raises the saturation magnetisation slightly, the temperature dependence is not changed significantly. Also different starting temperatures for the remagnetisation created by varied incident fluences only change the starting point on the static remagnetisation curve. The results for the continuous magnetic layers are different, especially in low fluence regimes. Here both Nickel and Iron Platinum follow an approximately linear

temperature dependence of the magnetisation value on the transient remagnetisation curve. This causes the magnetisation after excitation to be lower than the static reference value at each temperature. At high temperature far above the phase transition a linear dependence on temperature is replaced after cooling below phase transition with a temperature dependence comparable to the static curve. The magnetic field changes this behaviour significantly. It does not only shift the saturation magnetisation, but causes a faster remagnetisation compared to lower fields.

This remagnetisation dynamics shows that the dynamic remagnetisation is influenced by other parameters than the temperature. The difference between the granular sample and the continuous layers suggests the driving mechanism of remagnetisation is determining the transient dynamics of remagnetisation. The morphology of the granular sample prohibits the magnetisation to be switched by far travelling domain wall movements. However, it gives rise to domain nucleation by an increase of impurities and defects at the grain boundaries.

The results of the combination of both techniques have shown promising results that enrich the discussion about the coupling of different subsystems of a magnetic material. Therefore the experiments are combined in the near future to perform both UXRD measurements as well as MOKE measurements at the same time. This improves the quality of comparison, because the energy absorbed by the sample and the investigated sample spot are identical for both procedures. All experimental conditions will be ensured to be identical. Together with the measurement of transient reflected intensity a powerful experimental setup is created, which has access to all subsystems of the three temperature model (3TM): electron, lattice and spin system.

But also the MOKE setup developed in this work can give further results about magnetisation dynamics. In addition to the properties presented temperature dependent measurements in a range from 16 K to 400 K can be performed. This enables the observation of temperature dependence of magnetisation rotation mechanisms.

## Bibliography

1. Aristotle. *De anima* (Critical edition. Leiden and New York : E.J. Brill, 1994, 1994).
2. Stöhr, J. & Siegmann, H. C. *Magnetism: From fundamentals to nanoscale dynamics* (Springer, Berlin, 2006).
3. Beaurepaire, Merle, Daunois & Bigot. „Ultrafast spin dynamics in ferromagnetic nickel“. *Physical review letters* **76**, 4250–4253 (1996).
4. Weller, D., Mosendz, O., Parker, G., Pisana, S. & Santos, T. S. „L1<sub>0</sub> FePtX-Y media for heat-assisted magnetic recording“. *physica status solidi (a)* **210**, 1245–1260 (2013).
5. Hofherr, M. *et al.* „Speed and efficiency of femtosecond spin current injection into a nonmagnetic material“. *Physical Review B* **96** (2017).
6. Pudell, J. *et al.* „Layer specific observation of slow thermal equilibration in ultrathin metallic nanostructures by femtosecond X-ray diffraction“. *Nature communications* **9**, 3335 (2018).
7. Mendil, J. *et al.* „Resolving the role of femtosecond heated electrons in ultrafast spin dynamics“. *Scientific reports* **4**, 3980 (2014).
8. Conrad, U., Güdde, J., Jähnke, V. & Matthias, E. „Ultrafast electron and magnetization dynamics of thin Ni and Co films on Cu(001) observed by time-resolved SHG“. *Applied Physics B* **68**, 511–517 (1999).
9. Roth, T. *et al.* „Temperature Dependence of Laser-Induced Demagnetization in Ni: A Key for Identifying the Underlying Mechanism“. *Physical Review X* **2** (2012).
10. Cheskis, D., Porat, A., Szapiro, L., Potashnik, O. & Bar-Ad, S. „Saturation of the ultrafast laser-induced demagnetization in nickel“. *Physical Review B* **72**, 012413 (2005).
11. Atxitia, U., Chubykalo-Fesenko, O., Walowski, J., Mann, A. & Münzenberg, M. „Evidence for thermal mechanisms in laser-induced femtosecond spin dynamics“. *Physical Review B* **81**, 173 (2010).
12. Kuiper, K. C., Malinowski, G., Longa, F. D. & Koopmans, B. „Nonlocal ultrafast magnetization dynamics in the high fluence limit“. *Journal of Applied Physics* **109**, 07D316 (2011).
13. You, W. *et al.* „Revealing the Nature of the Ultrafast Magnetic Phase Transition in Ni by Correlating Extreme Ultraviolet Magneto-Optic and Photoemission Spectroscopies“. *Physical Review Letters* **121** (2018).
14. Zhao, J., Cui, B., Zhang, Z., Ma, B. & Jin, Q. Y. „Ultrafast heating effect on transient magnetic properties of L1<sub>0</sub>-FePt thin films with perpendicular anisotropy“. *Thin Solid Films* **518**, 2830–2833 (2010).
15. O’Grady, P. F. *Thales of Miletus: The beginnings of western science and philosophy* (Routledge, [Place of publication not identified], 2017).
16. Baigrie, B. S. *Electricity and magnetism: A historical perspective* (Greenwood Press, Westport, Conn., 2007).
17. Blundell, S. *Magnetism in condensed matter* 1. Reprinted. (Oxford Univ. Press, Oxford, 2003).
18. Coey, J. M. D. *Magnetism and magnetic materials* Repr (Cambridge Univ. Press, Cambridge, 2013).

19. Gross, R. & Marx, A. *Festkörperphysik* (Oldenbourg, München, 2012).
20. Fiorillo, F., Appino, C. & Pasquale, M. in *The Science of Hysteresis* 1–190 (Elsevier, 2006).
21. Weiss, P. „La variation du ferromagnétisme avec la température“. *Comptes Rendus des Séances de l'Académie des Sciences*, 1136–1139 (1906).
22. Weiss, P. „L'hypothèse du champ moléculaire et la propriété ferromagnétique“. *Journal de Physique Théorique et Appliquée* **6**, 661–690 (1907).
23. Mohn, P. *Magnetism in the Solid State: An Introduction* Corrected Second Printing (Springer-Verlag Berlin Heidelberg, Berlin, Heidelberg, 2006).
24. Piamonteze, C., Miedema, P. & de Groot, F. M. F. „Accuracy of the spin sum rule in XMCD for the transition-metal L edges from manganese to copper“. *Physical Review B* **80** (2009).
25. McCord, J. „Progress in magnetic domain observation by advanced magneto-optical microscopy“. *Journal of Physics D: Applied Physics* **48**, 333001 (2015).
26. Dennis, C. L. *et al.* „The defining length scales of mesomagnetism: a review“. *Journal of Physics: Condensed Matter* **14**, R1175–R1262 (2002).
27. Beach, G. S. D., Nistor, C., Knutson, C., Tsoi, M. & Erskine, J. L. „Dynamics of field-driven domain-wall propagation in ferromagnetic nanowires“. *Nature materials* **4**, 741–744 (2005).
28. Hubert, A. & Schäfer, R. *Magnetic domains: The analysis of magnetic microstructures* Corr. print., [Nachdr.] (Springer, Berlin, ca. 2011).
29. Faraday, M. „On the magnetization of light and the illumination of magnetic lines of force“. *Philosophical Magazine and Journal of Science* **3** (1846).
30. Kerr, J. „XLIII. On rotation of the plane of polarization by reflection from the pole of a magnet“. *The London, Edinburgh, and Dublin Philosophical Magazine and Journal of Science* **3**, 321–343 (1877).
31. Oppeneer, P. in *Handbook of magnetic materials* (ed Buschow, K. H. J.) 229–422 (Elsevier North Holland, Amsterdam and Boston, 2006).
32. Hamrle, J. *Magneto-optical determination of the in-depth magnetization profile in magnetic multilayers*. Thesis (Université Paris Sud - Paris XI, 2003).
33. Bruno, P., Suzuki, Y. & Chappert, C. „Magneto-optical Kerr effect in a paramagnetic overlayer on a ferromagnetic substrate: A spin-polarized quantum size effect“. *Physical Review B* **53**, 9214–9220 (1996).
34. Oppeneer, P. M., Maurer, T., Sticht, J. & Kübler, J. „Ab initio calculated magneto-optical Kerr effect of ferromagnetic metals: Fe and Ni“. *Physical Review B* **45**, 10924–10933 (1992).
35. Pershan, P. S. „Magneto–Optical Effects“. *Journal of Applied Physics* **38**, 1482–1490 (1967).
36. Hamrle, J., Ferré, J., Nývlt, M. & Višňovský, Š. „In-depth resolution of the magneto-optical Kerr effect in ferromagnetic multilayers“. *Physical Review B* **66**, 635 (2002).
37. Haider, T. „A Review of Magneto-Optic Effects and Its Application“. *International Journal of Electromagnetics and Applications*, 17–24 (2017).
38. Shinagawa, K. in *Magneto-Optics* (eds Sugano, S. & Kojima, N.) (Springer, Berlin and Heidelberg, 2000).
39. Azzam, R. M. A.-G. & Bashara, N. M. *Ellipsometry and polarized light* Reprint (North-Holland, Amsterdam, 1989).
40. Born, M. *Principles of Optics* (Elsevier Science, 1980).

41. Ebert, H. „Magneto-optical effects in transition metal systems“. *Reports on Progress in Physics* **59**, 1665–1735 (1996).
42. Getzlaff, M. in *Fundamentals of Magnetism* iii (Elsevier, 2013).
43. Grolier, V., Ferré, J., Maziewski, A., Stefanowicz, E. & Renard, D. „Magneto–optical anisometry of ultrathin cobalt films“. *Journal of Applied Physics* **73**, 5939–5941 (1993).
44. Mougin, A., Cormier, M., Adam, J. P., Metaxas, P. J. & Ferré, J. „Domain wall mobility, stability and Walker breakdown in magnetic nanowires“. *Europhysics Letters (EPL)* **78**, 57007 (2007).
45. Metaxas, P. J. *et al.* „Creep and flow regimes of magnetic domain-wall motion in ultrathin Pt/Co/Pt films with perpendicular anisotropy“. *Physical review letters* **99**, 217208 (2007).
46. Rohart, S. *Basic concepts on magnetization reversal (1): Static properties : coherent reversal and beyond*. Targosite, 2011.
47. Tudosa, I. *et al.* „The ultimate speed of magnetic switching in granular recording media“. *Nature* **428**, 831–833 (2004).
48. Skomski, R. *Simple models of magnetism* Reprinted. (Oxford Univ. Press, Oxford, 2009).
49. Cox, A., Dalrymple, G. B. & Doell, R. R. „Reversals of the Earth’s Magnetic Field“. *Scientific American* **216**, 44–54 (1967).
50. Azzawi, S., Hindmarch, A. T. & Atkinson, D. „Magnetic damping phenomena in ferromagnetic thin-films and multilayers“. *Journal of Physics D: Applied Physics* **50**, 473001 (2017).
51. Losby, J. E., Sauer, V. T. K. & Freeman, M. R. „Recent Advances in Mechanical Torque Studies of Small-scale Magnetism“. *Journal of Physics D: Applied Physics* **51**, 483001 (2018).
52. Jiang, L. & Tsai, H.-L. „Improved Two-Temperature Model and Its Application in Ultrashort Laser Heating of Metal Films“. *Journal of Heat Transfer* **127**, 1167 (2005).
53. Knorren, R., Bennemann, K. H., Burgermeister, R. & Aeschlimann, M. „Dynamics of excited electrons in copper and ferromagnetic transition metals: Theory and experiment“. *Physical Review B* **61**, 9427–9440 (2000).
54. Koopmans, B. in *Handbook of magnetism and advanced magnetic materials* (eds Kronmüller, H. & Parkin, S. S. P.) 1589–1613 (John Wiley & Sons, Hoboken NJ, 2007).
55. Koopmans, B. *et al.* „Explaining the paradoxical diversity of ultrafast laser-induced demagnetization“. *Nature materials* **9**, 259–265 (2010).
56. Maldonado, P., Carva, K., Flammer, M. & Oppeneer, P. M. „Theory of out-of-equilibrium ultrafast relaxation dynamics in metals“. *Physical Review B* **96**, 173 (2017).
57. Connelly, D. L., Loomis, J. S. & Mapother, D. E. „Specific Heat of Nickel near the Curie Temperature“. *Physical Review B* **3**, 924–934 (1971).
58. Bigot, J.-Y. & Vomir, M. „Ultrafast magnetization dynamics of nanostructures“. *Annalen der Physik* **525**, 2–30 (2013).
59. Agranat, M. B., Ashitkov, A. B., Granovskii, A. B., Rukman & G.I. „Interaction of picosecond laser pulses with the electron, spin, and phonon subsystems of nickel“. *SOVIET PHYSICS JETP* **59** (1984).
60. Hohlfeld, J., Matthias, E., Knorren, R. & Bennemann, K. H. „Nonequilibrium Magnetization Dynamics of Nickel“. *Physical review letters* **78** (1997).
61. Koopmans, B., van Kampen, M., Kohlhepp, J. T. & de Jonge, W. J. M. „Femtosecond spin dynamics of epitaxial Cu(111)/Ni/Cu wedges“. *Journal of Applied Physics* **87**, 5070–5072 (2000).

62. Beaupre, E. *et al.* „Spin dynamics in CoPt3 alloy films: A magnetic phase transition in the femtosecond time scale“. *Physical Review B* **58**, 12134–12137 (1998).
63. van Kampen, M. *et al.* „All-optical probe of coherent spin waves“. *Physical review letters* **88**, 227201 (2002).
64. Hansteen, F., Kimel, A., Kirilyuk, A. & Rasing, T. „Nonthermal ultrafast optical control of the magnetization in garnet films“. *Physical Review B* **73**, 1376 (2006).
65. Kalashnikova, A. M. *et al.* „Impulsive excitation of coherent magnons and phonons by subpicosecond laser pulses in the weak ferromagnet FeBO3“. *Physical Review B* **78**, 1008 (2008).
66. Atoneche, F. *et al.* „Large ultrafast photoinduced magnetic anisotropy in a cobalt-substituted yttrium iron garnet“. *Physical Review B* **81** (2010).
67. Lambert, C.-H. *et al.* „All-optical control of ferromagnetic thin films and nanostructures“. *Science (New York, N.Y.)* **345**, 1337–1340 (2014).
68. Hassdenteufel, A. *et al.* „All-optical helicity dependent magnetic switching in Tb-Fe thin films with a MHz laser oscillator“. *Optics express* **22**, 10017–10025 (2014).
69. Hassdenteufel, A. *et al.* „Dependence of all-optical magnetic switching on the sublattice magnetization orientation in Tb-Fe thin films“. *Applied Physics Letters* **105**, 112403 (2014).
70. Gorchon, J. *et al.* „Single shot ultrafast all optical magnetization switching of ferromagnetic Co/Pt multilayers“. *Applied Physics Letters* **111**, 042401 (2017).
71. Wilson, R. B. *et al.* „Ultrafast magnetic switching of GdFeCo with electronic heat currents“. *Physical Review B* **95** (2017).
72. Yang, Y. *et al.* „Ultrafast magnetization reversal by picosecond electrical pulses“. *Science advances* **3**, e1603117 (2017).
73. Radu, I. *et al.* „Transient ferromagnetic-like state mediating ultrafast reversal of antiferromagnetically coupled spins“. *Nature* **472**, 205–208 (2011).
74. Mathias, S. *et al.* „Probing the timescale of the exchange interaction in a ferromagnetic alloy“. *Proceedings of the National Academy of Sciences of the United States of America* **109**, 4792–4797 (2012).
75. Stamm, C. *et al.* „Femtosecond modification of electron localization and transfer of angular momentum in nickel“. *Nature materials* **6**, 740–743 (2007).
76. Carley, R. *et al.* „Femtosecond laser excitation drives ferromagnetic gadolinium out of magnetic equilibrium“. *Physical review letters* **109**, 057401 (2012).
77. Eich, S. *et al.* „Band structure evolution during the ultrafast ferromagnetic-paramagnetic phase transition in cobalt“. *Science advances* **3**, e1602094 (2017).
78. Rhie, H.-S., Dürr, H. A. & Eberhardt, W. „Femtosecond electron and spin dynamics in Ni/W(110) films“. *Physical review letters* **90**, 247201 (2003).
79. Steiauf, D. & Fähnle, M. „Elliott-Yafet mechanism and the discussion of femtosecond magnetization dynamics“. *Physical Review B* **79** (2009).
80. Krauß, M. *et al.* „Ultrafast demagnetization of ferromagnetic transition metals: The role of the Coulomb interaction“. *Physical Review B* **80**, 208 (2009).
81. Carpena, E. *et al.* „Dynamics of electron-magnon interaction and ultrafast demagnetization in thin iron films“. *Physical Review B* **78** (2008).
82. Ibach, H. & Lüth, H. *Festkörperphysik: Einführung in die Grundlagen ; mit 18 Tafeln und 104 Übungen* 7. Aufl. (Springer, Berlin, 2009).

83. Salvatella, G. *et al.* „Ultrafast demagnetization by hot electrons: Diffusion or super-diffusion?“ *Structural dynamics (Melville, N.Y.)* **3**, 055101 (2016).
84. Battiato, M., Carva, K. & Oppeneer, P. M. „Superdiffusive spin transport as a mechanism of ultrafast demagnetization“. *Physical review letters* **105**, 027203 (2010).
85. Malinowski, G. *et al.* „Control of speed and efficiency of ultrafast demagnetization by direct transfer of spin angular momentum“. *Nature Physics* **4**, 855–858 (2008).
86. Schellekens, A. J., de Vries, N., Lucassen, J. & Koopmans, B. „Exploring laser-induced interlayer spin transfer by an all-optical method“. *Physical Review B* **90** (2014).
87. Mueller, B. Y. *et al.* „Feedback effect during ultrafast demagnetization dynamics in ferromagnets“. *Physical review letters* **111**, 167204 (2013).
88. Oppeneer, P. M. & Liebsch, A. „Ultrafast demagnetization in Ni: theory of magneto-optics for non-equilibrium electron distributions“. *Journal of Physics: Condensed Matter* **16**, 5519–5530 (2004).
89. Ding, H., Pütter, S., Oepen, H. & Kirschner, J. „Experimental method for separating longitudinal and polar Kerr signals“. *Journal of Magnetism and Magnetic Materials* **212**, 5–11 (2000).
90. Loriot, V., Hertz, E., Faucher, O. & Lavorel, B. „Measurement of high order Kerr refractive index of major air components“. *Optics Express* **17**, 13429 (2009).
91. Willig, L. *Labware\_UDKM*. 2018.
92. Renard, V. *et al.* „Nonintrusive monitoring and quantitative analysis of strong laser-field-induced impulsive alignment“. *Physical Review A* **70** (2004).
93. Marceau, C. *et al.* „Femtosecond filament induced birefringence in argon and in air: Ultrafast refractive index change“. *Optics Communications* **283**, 2732–2736 (2010).
94. Stephens, R. E. & Malitson, I. H. „Index of refraction of magnesium oxide“. *Journal of Research of the National Bureau of Standards* **49**, 249 (1952).
95. Rehren, T. *et al.* „5,000 years old Egyptian iron beads made from hammered meteoritic iron“. *Journal of Archaeological Science* **40**, 4785–4792 (2013).
96. Reardon, A. C. *Metallurgy for the non-metallurgist* (ASM International, Materials Park, Ohio, 2011).
97. MacDonald, D. & Hunt, L. B. *A history of platinum and its allied metals* (Matthey, London, 1982).
98. Reppert, A. v. *et al.* „Ultrafast laser generated strain in granular and continuous FePt thin films“. *Applied Physics Letters* **113**, 123101 (2018).
99. Reid, A. H. *et al.* „Beyond a phenomenological description of magnetostriction“. *Nature communications* **9**, 388 (2018).
100. Granitzka, P. W. *et al.* „Magnetic Switching in Granular FePt Layers Promoted by Near-Field Laser Enhancement“. *Nano letters* **17**, 2426–2432 (2017).
101. Hovorka, O. *et al.* „The Curie temperature distribution of FePt granular magnetic recording media“. *Applied Physics Letters* **101**, 052406 (2012).
102. Becker, J. *et al.* „Laser induced spin precession in highly anisotropic granular L1 0 FePt“. *Applied Physics Letters* **104**, 152412 (2014).
103. He, P. *et al.* „Quadratic scaling of intrinsic Gilbert damping with spin-orbital coupling in L10 FePdPt films: experiments and Ab initio calculations“. *Physical review letters* **110**, 077203 (2013).
104. Chen, Z. *et al.* „Spin waves and small intrinsic damping in an in-plane magnetized FePt film“. *Applied Physics Letters* **101**, 222402 (2012).

105. Mizukami, S. *et al.* „Fast magnetization precession observed in L10-FePt epitaxial thin film“. *Applied Physics Letters* **98**, 052501 (2011).
106. Iihama, S. *et al.* „Observation of Precessional Magnetization Dynamics in L1<sub>0</sub>-FePt Thin Films with Different L1<sub>0</sub> Order Parameter Values“. *Japanese Journal of Applied Physics* **52**, 073002 (2013).
107. Weller, D. *et al.* „Review Article: FePt heat assisted magnetic recording media“. *Journal of Vacuum Science & Technology B, Nanotechnology and Microelectronics: Materials, Processing, Measurement, and Phenomena* **34**, 060801 (2016).
108. Wicht, S. *et al.* „Atomic resolution strain analysis in highly textured FePt thin films“. *Journal of Applied Physics* **119**, 115301 (2016).
109. Kazantseva, N., Nowak, U., Chantrell, R. W., Hohlfeld, J. & Rebei, A. „Slow recovery of the magnetisation after a sub-picosecond heat pulse“. *EPL (Europhysics Letters)* **81**, 27004 (2008).
110. Pisana, S. *et al.* „Effects of grain microstructure on magnetic properties in FePtAg-C media for heat assisted magnetic recording“. *Journal of Applied Physics* **113**, 043910 (2013).
111. Sparrow, G. *Nickel* (Benchmark Books/Marshall Cavendish, New York, 2005).
112. Enghag, P. *Encyclopedia of the elements: Technical data, history, processing, applications* (Wiley-VCH, Weinheim, 2004).
113. Cheng, C. F. & Schwitter, C. M. „Nickel in Ancient Bronzes“. *American Journal of Archaeology* **61**, 351 (1957).
114. Choi, G.-M., Moon, C.-H., Min, B.-C., Lee, K.-J. & Cahill, D. G. „Thermal spin-transfer torque driven by the spin-dependent Seebeck effect in metallic spin-valves“. *Nature Physics* **11**, 576–581 (2015).
115. Choi, G.-M., Wilson, R. B. & Cahill, D. G. „Indirect heating of Pt by short-pulse laser irradiation of Au in a nanoscale Pt/Au bilayer“. *Physical Review B* **89** (2014).
116. Eschenlohr, A. *et al.* „Ultrafast spin transport as key to femtosecond demagnetization“. *Nature materials* **12**, 332–336 (2013).
117. Eschenlohr, A. *et al.* „Reply to 'Optical excitation of thin magnetic layers in multilayer structures'“. *Nature materials* **13**, 102–103 (2014).
118. J. I. Gittleman, Y. Goldstein & S. Bozowski. „Magnetic Properties of Granular Nickel Films“. *Phys Rev B* **5** (1972).
119. Schick, D. *et al.* „Normalization schemes for ultrafast x-ray diffraction using a table-top laser-driven plasma source“. *The Review of scientific instruments* **83**, 025104 (2012).
120. Zamponi, F. *et al.* „Femtosecond hard X-ray plasma sources with a kilohertz repetition rate“. *Applied Physics A* **96**, 51–58 (2009).
121. Schick, D. *et al.* „Ultrafast reciprocal-space mapping with a convergent beam“. *Journal of Applied Crystallography* **46**, 1372–1377 (2013).
122. Windt, D. L. „IMD—Software for modeling the optical properties of multilayer films“. *Computers in Physics* **12**, 360 (1998).
123. Khorsand, A. R., Savoini, M., Kirilyuk, A. & Rasing, T. „Optical excitation of thin magnetic layers in multilayer structures“. *Nature materials* **13**, 101–102 (2014).
124. Lee, H.-S. & Park, H.-H. „Band Structure Analysis of La<sub>0.7</sub>Sr<sub>0.3</sub>MnO<sub>3</sub> Perovskite Manganite Using a Synchrotron“. *Advances in Condensed Matter Physics* **2015**, 1–7 (2015).

125. Nicula, R. *et al.* „Thermal stability, thermal expansion and grain-growth in exchange-coupled Fe–Pt–Ag–B bulk nanocomposite magnets“. *Journal of Alloys and Compounds* **622**, 865–870 (2015).
126. Rethfeld, B., Ivanov, D. S., Garcia, M. E. & Anisimov, S. I. „Modelling ultrafast laser ablation“. *Journal of Physics D: Applied Physics* **50**, 193001 (2017).



# Appendix



## A Hardware Setup

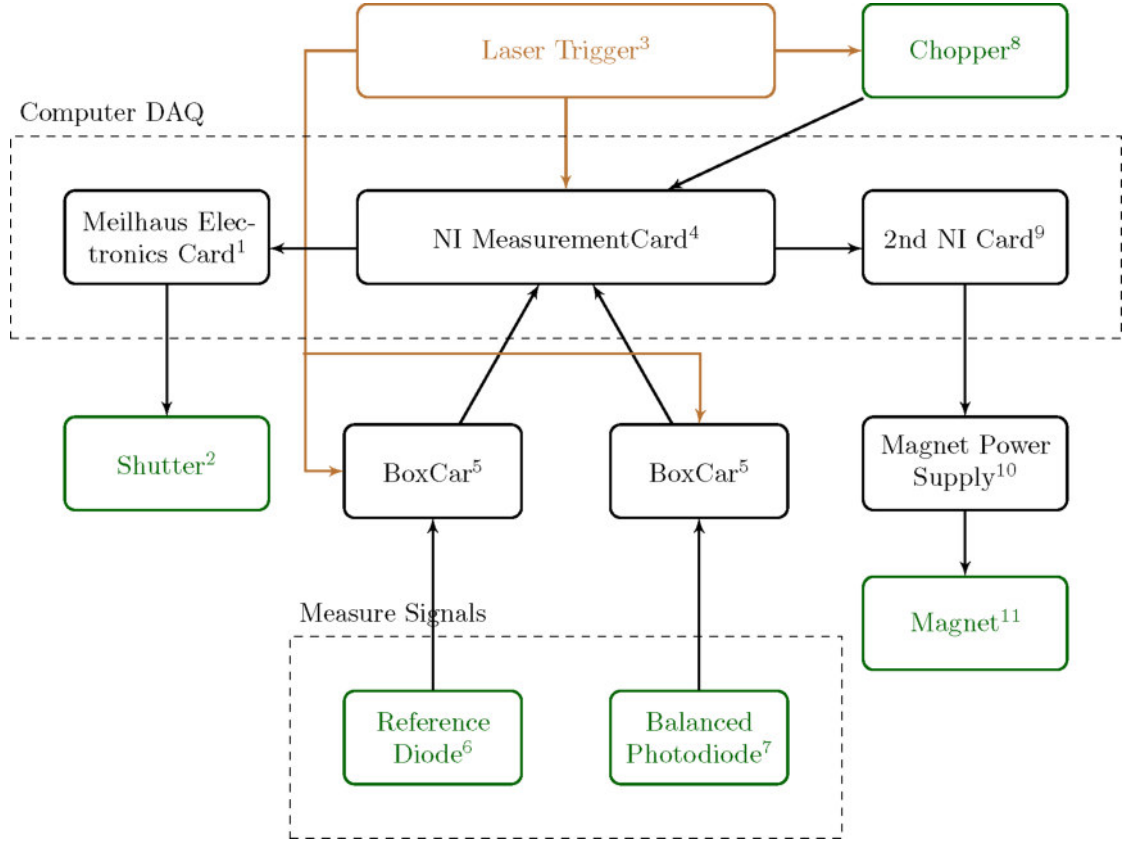


**Figure A.1: Hardware components of MOKE-setup.** Green: Objects on the optical table, black: electronic parts that can be moved, copper: laser trigger determining the timings of the measurement

<sup>1</sup>Meilhaus Electronics RedLab

<sup>2</sup>self-made with motor from Kuhnke

<sup>3</sup>Laser System described in chapter 4, section 4.1

<sup>4</sup>NI PCIe-6251, National Instruments

<sup>5</sup>SR250, Stanford Research System

<sup>6</sup>DET36A/M, Thorlabs

<sup>7</sup>PDB210A/M, Thorlabs

<sup>8</sup>Chopper Controller: MC1000A, Thorlabs

<sup>9</sup>NI USB 6003, National Instruments

<sup>10</sup>Kepeco BOP 36-6ML

<sup>11</sup>Buckley Systems LTO



## B Fluence Determination

The parameter *fluence* is used as an indicator for how much energy is absorbed in the sample from the pump pulse. For this thesis, this parameter was particularly important, because the results of two laboratories had to be compared with an accurate value. The incident fluence is listed throughout the thesis, because it does not depend on the absorption of the sample. For some samples the absorption parameters were not fully known or are under discussion.

The incident fluence  $F_{\text{inc}}$  was calculated according to equation .1. The angle  $\alpha$  indicates the deviation from normal incidence. It projects the beam profile measured at normal incidence to the larger footprint under grazing incidence.

$$F_{\text{inc}} = \frac{E_p}{A} \sin(\alpha) \quad (.1)$$

Here  $E_p$  refers to the energy in one pulse. So it is defined by the input power  $P$  and the repetition rate  $r$ :

$$E_p = \frac{P}{r}. \quad (.2)$$

The area  $A = x_0 y_0 \pi$  of the pump spot on the sample is determined by a CCD measurement of the pump beam. It returns a 2D image from which the 2D Gaussian shape is extracted by integrating over both dimensions. An example image for the bilayer of Nickel and gold (GN1, see chapter 6) MOKE measurement of the  $F_{\text{inc}} = 9.0 \text{ mJ/cm}^2$  is shown in figure B.1. It shows the CCD image and the integrated intensity graphs with the gauss fits. The beam size parameter used for calculations is the 1/e-intensity reduction, which is indicated by the green lines and labels,  $x_0$  and  $y_0$ . Table B.1 summarizes the parameters for the determination of the incident fluence  $F_{\text{inc}}$  for both laboratories exemplary for the  $F_{\text{inc}} = 9.0 \text{ mJ/cm}^2$  measurement shown in figure 7.12. For both laboratories the ratio between pump and probe pulse diameter is similar. It is kept at 1/3 of the pump beam, to probe an approximately evenly excited area of the sample. The conversion factor results from the difference of the fluence and the different absorption expected at the different incident angles. For the demonstrated calculations in table B.1 the incident fluence was similar, so that no conversion is necessary. If the UXR and MOKE measurements were done at different fluence, the UXR measurement was scaled with this factor. This is only reasonable, when the lattice response is scaling approximately linear with the excitation energy. Therefore the scaling was done for measurements of nickel in chapter 6, but not for measurements of Iron Platinum in chapter 5, as this material did not show linear dependence.

	Xray Measurement (PXS)	MOKE Measurement (Femtomag)
Repetition Rate $r$ (Hz)	1000	1000
Laser Power $P$ (mW)	300	105
Incident Angle $\alpha$ (°)	44	0
1/e-Width $x_0$ ( $\mu\text{m}$ )	1801	1149
1/e-Width $y_0$ ( $\mu\text{m}$ )	1682	1536
Incident Fluence $F_{\text{inc}}$ (mJ/cm <sup>2</sup> )	8.76	9.01
	$\approx 8.8$	$\approx 9.0$
Conversion Factor	0.97	

**Table B.1: Fluence determination and comparison for UXR and MOKE.** Measurement parameters and resulting fluence for the bilayer nickel sample (GN1, figure 7.12) at  $F_{\text{inc}} = 9.0 \text{ mJ/cm}^2$  for both measurement setups.

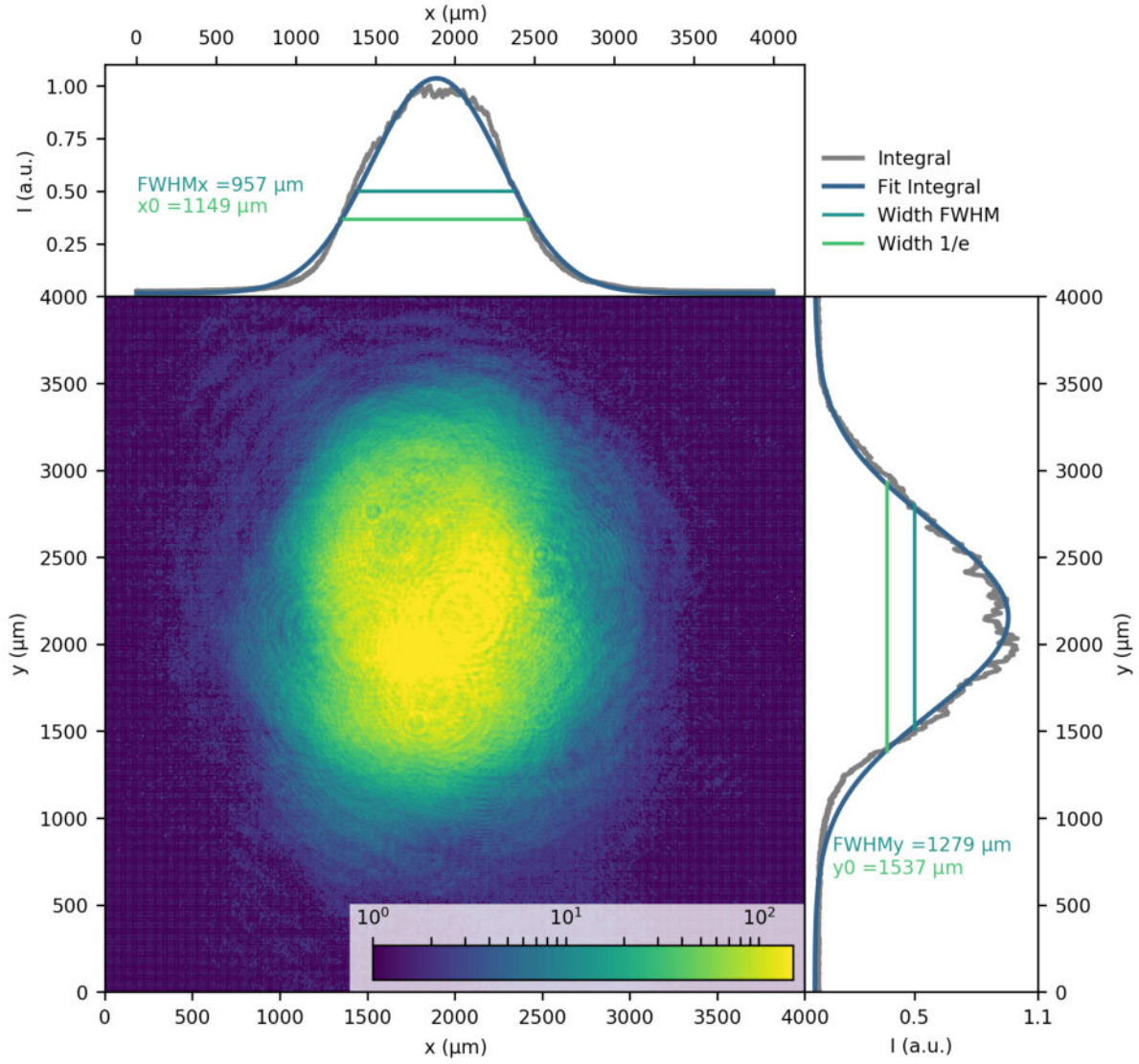


**Figure B.1: Pump beam profile of the MOKE setup.** CCD image of the pump beam profile with the integrated profiles (grey) and the respective gauss fits of  $x$  and  $y$  (blue). The bright blue and green lines indicate the position of FWHM and  $1/e$ -widths in both dimensions.

## Gauss Profile

A crucial part of the fluence calculation is the assumption about the excited area which absorbs the incident energy. If the fluence is not only a comparison parameter for different excitation values but also a measure for the absolute absorbed energy, it is necessary to evaluate the beam profile as well as the ratio between pump and probe beam.

If the fluence is estimated with the assumption that all of the incident energy  $E$  is absorbed in the circle with the radius of the FWHM values, the resulting fluence  $F_{\text{FWHM}}$ , equation .3, is larger than the peak fluence  $F_{\text{peak}}$ , equation .4. Instead of the FWHM value the value for the reduction of the gaussian intensity to  $1/e$  can be used. This leads to the estimation of the peak fluence, and therefore corrects the absorbed energy by a factor of  $\ln(2) \approx 0.69$ . A cylinder with the radius of  $x_0$  has the same volume as the gaussian distribution.

$$F_{\text{FWHM}} = \frac{E}{2\pi \ln(2) x_{\text{FWHM}}^2} \quad (.3)$$

$$F_{\text{peak}} = \frac{E}{2\pi x_0^2} \quad (.4)$$

To take into account that the probe beam has a certain profile as well, it is possible to calculate a weighted fluence average depending on the size of the probe spot. This correction depends on the ratio between pump and probe beam diameter. For measurements in this work this ratio was kept at 3/1, at which the correction only leads to small changes and is therefore not necessary.

For both setups a 2D Gauss profile was used as an approximation of the pumped area. The fluence was determined with a footprint of  $1/e$  of the gauss profile.



## C Labware UDKM

This chapter describes the elements of the graphical user interface (GUI) and the saved data for the MOKE application. The source code and the technical description can be found in [91].

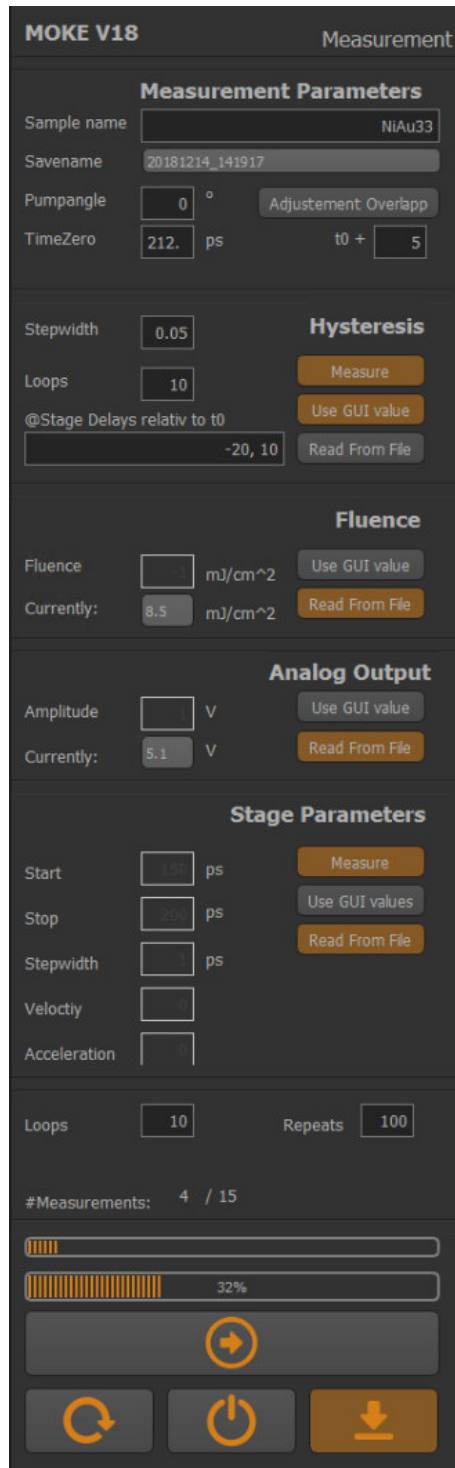


**Figure C.1:** Screenshot of the MOKE application side panel.

### Side Panel

The side panel of the MOKE measurement application allows the determination of the measurement parameters, is responsible for the additional data that is saved and displays the progress of the measurement.

The label at the top right hand side indicates if the application is run in the normal *Measurement* mode or in *Debug* mode. In the debugging mode the hardware interface is only simulating the connected hardware and data is randomly generated. This can be used for testing new programming implementations.

In the section *Measurement Parameters* the parameters for saving are set. It also displays the directory name, under which all measurements of the started session are saved. It is currently determined by the date. The sample name, pumping angle and the time zero are saved in a file which only stores the measurement parameters. So it is a collection of all input values for the measurement saved in this date. The button *Adjustment Overlap* moves the delay stage to one position, calculated as offset from the time zero as shown in the line below. This makes it possible to manually align the overlap of the pump and probe beam by maximising the magneto-optical signal. It also allows for checking different spots on the sample and comparing their magneto-optical response.

The next section labelled *Hysteresis* sets the measurement values for the hysteresis measurement. If the button *Measure* is not toggled (orange and grey indicate the toggled and untoggled states), the hysteresis will not be measured and the section of the flowchart 4.5 will be skipped. To visualize the effect the other buttons and input lines are disabled if no measurement will be performed. The next two buttons enable the input methods for the delay times at which the time resolved hysteresis is measured. This can be set either by writing the times relative to time zero in the line on the left side (*Use GUI value*) or with a text file which is located in the application folder (*Read From File*). Only one method can be chosen, the buttons are linked and cannot be activated at the same time. The syntax is as demonstrated here with -20, 10: Numbers separated by a comma. The parameters *Stepwidth* and *Loops* set the number of repeated measurements of the

whole hysteresis and the stepwidth of the output voltage of the measurement card, which is translated into magnetic field.

The section *Fluence* controls the fluence settings during the measurement. If the value in the line labelled *Fluence* is set to -1, then nothing will happen. This reduces the possibility of wrong numbers saved in the measurement and parameter data files. A -1 indicates that the fluence has been set manually and has to be calculated separately. Otherwise the input method can be chosen as before: Either input as a number in the GUI or read it from a separate file. In this case the GUI entry can only be a single number. Additionally the grey field displays the fluence that is currently set. This is particularly helpful when the fluence is read from a text file and cannot be seen directly during the measurement. The fluence is entered in the unit  $\text{mJ}/\text{cm}^2$  and refers to the incident fluence. The description of how it is calculated can be found in B or in the source code.





The strength of the external magnetic field during the time resolved MOKE measurements is set in the section *Analog Output*. It is set in the unit *Volt* and is a direct measure of the output of the DAQ card. This voltage is translated from the power supply into Ampere, which are applied on the magnet. The exact translation between voltage, ampere and the resulting magnetic field depend on the power supply, the magnet itself and the shape and distance of the magnetic pole shoes. Therefore a reference hysteresis of the current setting must be obtained if any changes in the setup have been made. As before the value for the measurement can be written in the GUI field labelled *Amplitude* or loaded from an external text file if more than one measurement is required. The current value of the measurement is displayed as well.

The following section for the *Stage Parameters* determine the settings for the delay stage. As before the state of the button *Measure* determines if a time resolved MOKE measurement is performed or not. The choice of how the stage vector parameter is set functions as described before for the hysteresis panel. The stage vector read from the GUI is only linear. So a start and stop position determines the beginning and the end of the measurement, the stepwidth defines the time steps of the measurement. The unit for the vector is entered in picoseconds which gets internally converted into mm for the actual stage movement. Other units would be possible to implement, but the usage of ps for this setup proved to be sufficient. When the stage vector is created by reading it from an external file it can be constructed of several linear sections. The syntax for the vector components in the external file is as follows: Start (float), Stop (float), Stepwidth (float) \newline. Every line added to this list will be added to the vector. The velocity and the acceleration of the stage can be left at 0, which will chose the default value of the connected hardware.

The parameter *Loops* determines how often the pump probe measurement for both magnetic field directions is repeated. So a loop value of 10 does result in 20 single pump probe measurements. The parameter *Repeats* defines the number of values taken for averaging one point in the pump and unpumped measurement. It declares the value for each pumped and unpumped value, so 100 repeats results in the DAQ card collecting 100 pumped and 100 unpumped data points at one stage delay.

The label *#Measurements* shows the current measurement with respect to the total number of all measurements. This is calculated as the sum of all hysteresis measurements and all time-resolved MOKE measurements. The small progress bar below visualizes the total progress. Here it is the sum of all actual points at which data is collected. So in the hysteresis measurement the number of set currents are added, in the time resolved measurement the number of stage positions are counted. Both are added depending on the number of loops, length of the fluence vector and length of the voltage vector.

The larger progress bar shows the progress for the current measurement. It also counts the steps that have to be made to obtain all data points.

The buttons determine the actions  start,  restart,  exit program and  save (toggled: yes, untoggled: no).

At the bottom of the application window a status bar shows additional information about the status of the measurement (hardware initialization, current stage position, data saving, etc.).

## Main Data Window

The largest plot in the application window represents the main data visualization window. In the running measurements it switches the focus between the hysteresis and the time-resolved MOKE data depending on the current measurement. If the overlap adjustment is chosen, it displays the current pump-probe value. The user can choose to view different plots by switching the focused tabs. As seen in figure C.2 currently there are 5 different options: MOKE measurement, hysteresis, relative intensity (this currently is referring to the intensity change of both single diodes of the balanced photodiode) and the pump and probe values separately for the current measurement.

The current position of the stage during time resolved measurements is indicated with a small blue vertical line.

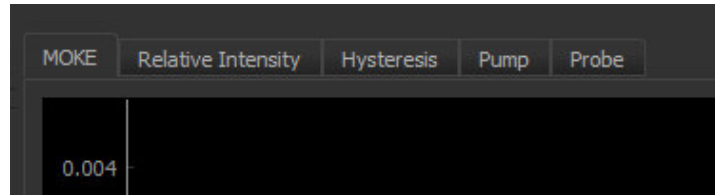


**Figure C.2:** Tabs of the main data window for switching between different measurements.

## Additional Data Windows

Below the largest plot there are two smaller windows. These represent the pump probe data for the current MOKE measurement depending on the applied magnetic field. The tabs allow to switch between the averaged pump probe traces or an overlapping plot of all loops. This is useful for monitoring the state of the sample, so for example to observe if the sample is deteriorating over time.



## D Molecule Excitation

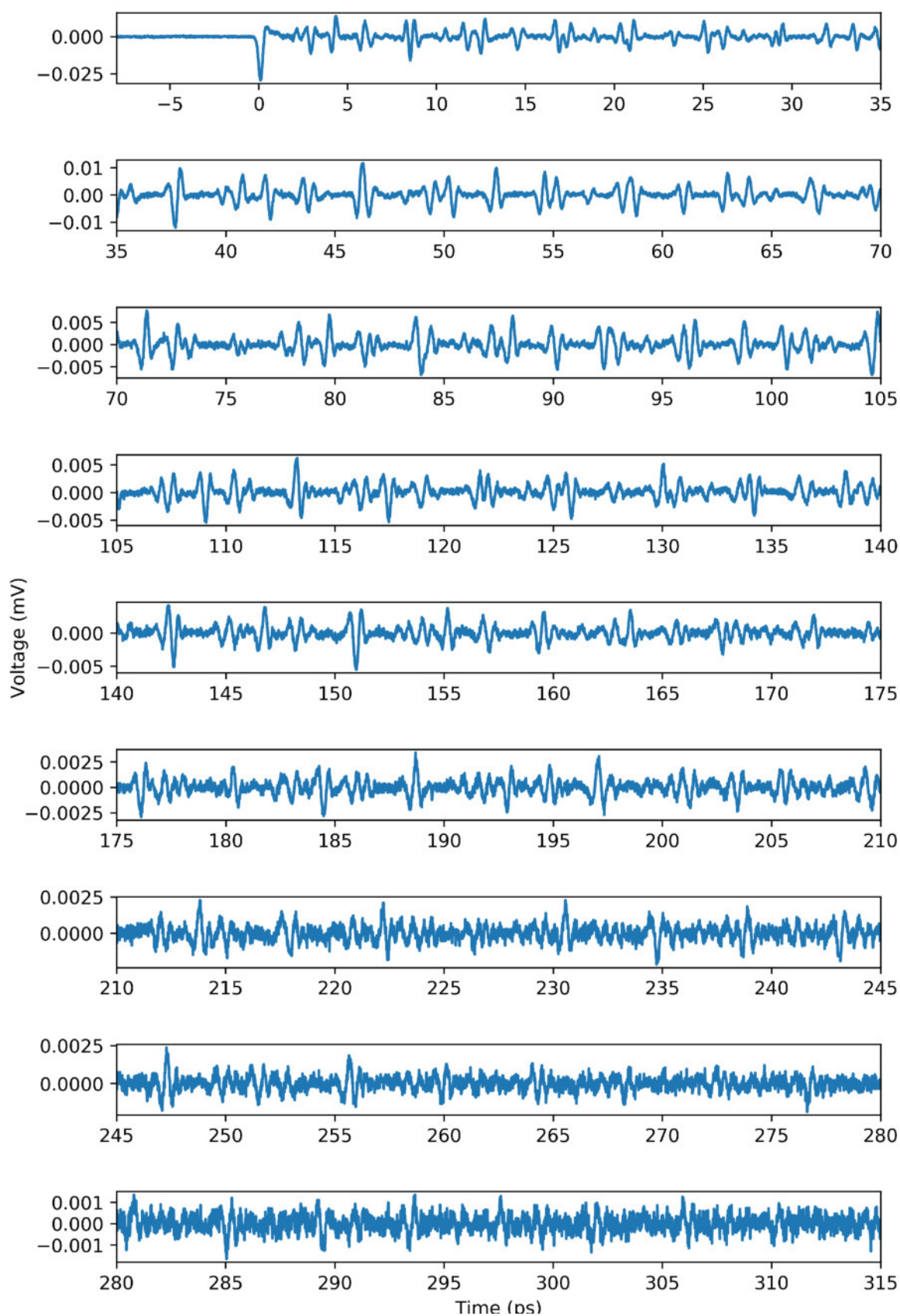


**Figure D.1: Electronic Kerr signal measured from the rotational alignment of molecules (see 4, section 4.7.1).** The peak magnitudes decrease, but stay above the noise level for approximately 310 ps.



## E Hysteresis Measurements of Nickel, Gold and MgO

The hysteresis measurements of the sample GN1 (discussed in chapter 6) presented a surprising behaviour. Besides the expected ferromagnetic contribution of the magnetic Nickel layer a quadratic contribution was observed. This appeared both in static measurements and excited states, see the plot b) of figure E.1. If the hysteresis only represented a paramagnetic contribution at the saturation magnetisation for Nickel a possible explanation would have been the substrate. This can have an impact on the measurement because a part of the probe beam is reflected from the back of the substrate. The substrate is transparent for optical light and therefore can show a large Kerr rotation due to the Faraday effect. But as expected for a paramagnetic hysteresis the Kerr rotation changes sign with the magnetic field, as the measurement E.1 a) shows.

The measurements were performed on single Gold layers as well and are presented in figure E.2. A sample with a Gold layer of 50 nm on top of a 2 mm MgO substrate is plotted in b). It does not show any significant magnetisation dependent Kerr signals. But the hysteresis of a thin Gold layer with only 5 nm on MgO in plot a) exhibits the same behaviour as the assumption made from the GN1 hysteresis: A quadratic signal which does not change the sign depending on the magnetic field. This could indicate that interface effects of the thin Gold layer with Nickel creates an unexpected magneto-optical signal change.

The quadratic effect could not be seen for any other of the investigated Nickel samples.

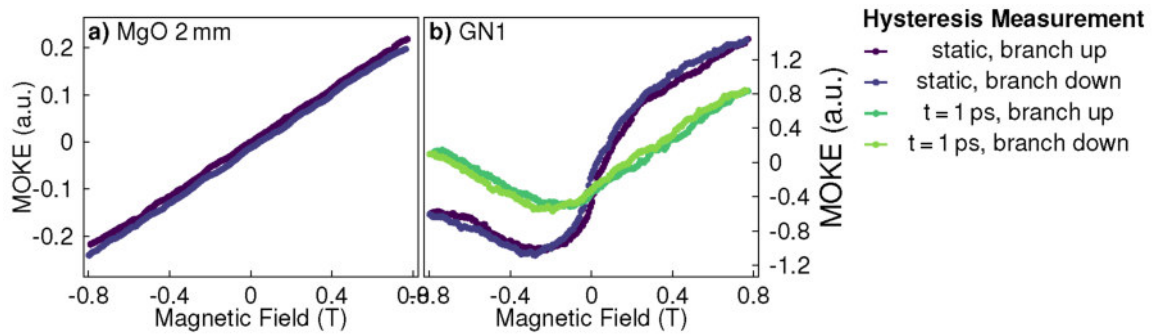


**Figure E.1: Hysteresis Measurements of MgO and GN1.** Left: Paramagnetic hysteresis of MgO. Right: Kerr rotation of the GN1 sample. In addition to the ferromagnetic Nickel signal a quadratic contribution could be observed. This contribution is also visible in the pumped state at a delay of maximum demagnetisation (1 ps), when the ferromagnetic hysteresis is suppressed.

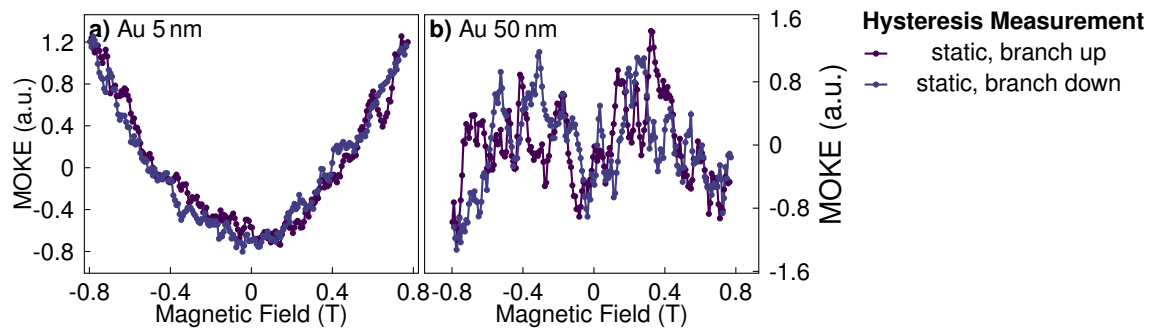


**Figure E.2: Hysteresis Measurement of Gold Films.** Left: A clear external field dependent Kerr rotation was observed for a 5 nm thin film. Right: For a 50 nm gold layer no Kerr signal was obtained.



## F Animations

### Precession Detection

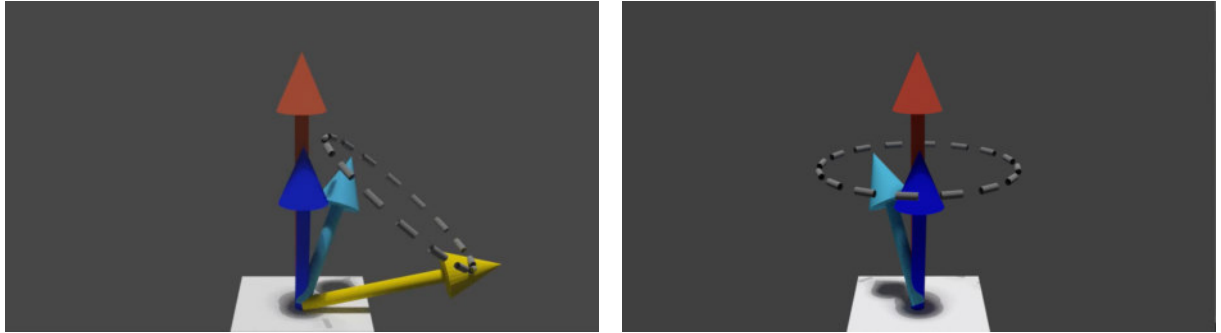


**Figure F.1:** These animations are a visualization of the precessional magnetisation dynamics and the detection in the polar MOKE geometry. They are equivalent to the explanation of the sample geometry in section 4.2. The animation on the left side represents the situation that the anisotropy of the thin film points mostly in plane (yellow arrow), the external field (red arrow) is pointing in the out of plane direction. As a result the magnetisation (bright blue) is tilted. In case of a polar MOKE setup with detection sensitivity in direction of the external field, the blue arrow represents the measurement signal. If the magnetisation starts a precession, the blue arrow will change in amplitude, a signal can be measured. In the animation on the right, the anisotropy is either very small compared to the external applied field, or the direction of the applied field and the anisotropy are parallel. In this case the magnetisation is also aligned along the field. If a precession of the spin would be triggered, the projection of the magnetisation to the detected z-axis does not change in amplitude, so no precession is measured.

### Iron Platinum Unit Cell

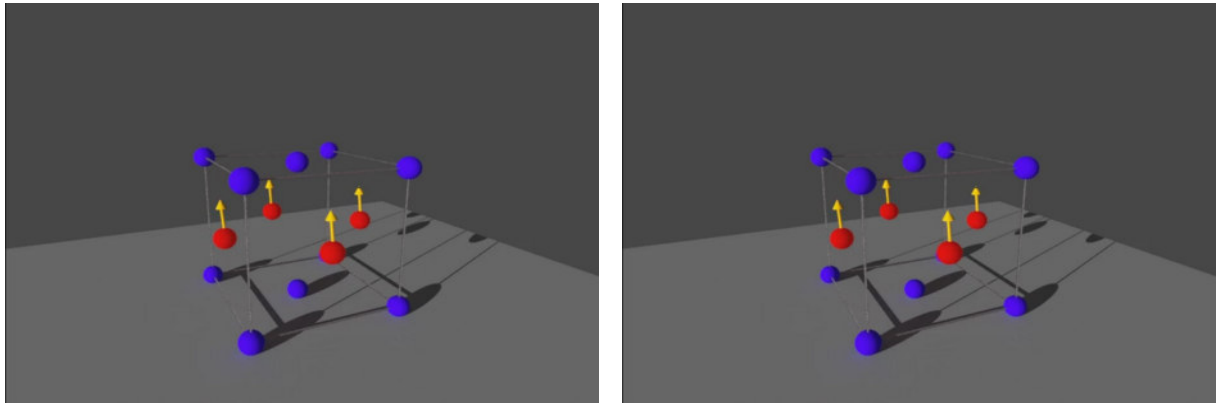


**Figure F.2:** These animations represent a cinematic visualization of the first picoseconds after the excitation of the Iron Platinum unit cell. The left animation represents the continuous thin film. After the energy is deposited in the electrons (represented by glowing atoms), the phononic system (glowing lattice) and the spin system (disorder of spins leading to no net magnetisation), the lattice expands out of plane without in plane movement. The animation on the right indicates the behaviour of a unit cell in the granular sample. Contrary to the continuous sample, the first lattice movement occurs with an in plane expansion and out of plane contraction<sup>1</sup>. After about 2 ps the lattice starts to expand out of plane.

<sup>1</sup>The glowing of the atoms appears later than in the continuous film animation. That is a currently appearing not intended technical mistake.

The animations can be played in PDF-Viewers supporting VPlayer. That includes for example *Adobe Acrobat Reader DC* or *Xodo*. Sometimes the animations have to be clicked twice to start.



# Acknowledgement

I feel very lucky to live my dreams, to be able to do what I want the most. And in doing so I had a lot of help and support from many people, giving me encouragement, criticism, inspiration and hope. Most of them for a time exceeding my PhD years. With these lines I would like to thank all of them and I hope to do it justice.

First and foremost I want to thank Matias Bargheer, for giving me the opportunity to work and introduce a new topic to the UDKM group, for the constant support, motivation and freedom to experiment and discover. Thank you for supporting and helping to realize my dream to work in Australia during my master thesis. But also for having more faith in me than I ever had since we met the first time 10 years ago.

I want to thank the FIT graduate school and the Helmholtzzentrum Berlin for financially enabling my work.

Special thanks to the Gregory Malinowski and the Institut Jean Lamour of the Université de Lorraine in Nancy for having me as a guest, allowing me to measure my samples in their setups and supporting this work with lots of discussions!

I want to thank all of my colleagues from the UDKM group. I always enjoyed the lively discussions between so many divers inspired and motivated people with all kinds of topics: problems in the lab, discussing the results of experiments or simply the most absurd topics imaginable.

A special thanks to Lena Maerten and Matthias Rössle, who helped me in particular in the beginning to organize and set up a new laser laboratory for my experiments.

Also thank you to Marc Herzog and Jan Pudell, who were present in the later stages of the lab, helping me to improve the hardware and laser settings as well as nourishing me with late night sushi sessions ;).

Marc, Jan and Alexander von Reppert also supported this work by doing the experiments on the X-ray plasma source and helping me to understand the results in numerous discussions, thank you!

And another special thanks to Felix Stete and Wouter Koopman, for being my rocks in the times of particularly turbulent waters and enduring my constant self doubts. Also thanks to Felix for being my eyes and ears whenever a design decision has to be made.

Also thank you to all the other members of the group that I have not named yet. In total I have spent nearly 8 years (with breaks) here and all of you have influenced my life and work, thank you!

I would also like to take the opportunity to thank the department of physics and astronomy. The warm and energetic atmosphere between students and professors had the most surprising effect on me and I benefited tremendously in my personal development from the opportunities I was given as part of the student council and the faculty council. I gained more experience in soft social skills and more self growth than any lecture could communicate and teach.

All of that was topped by the many people I studied physics with. I am very grateful to have been part of a very inspiring and motivating year, with many diverse people encouraging each other and being united in the wish to improve and to understand. I will remember many late night sessions discussing physics problems on black and white boards with very varying levels of math understanding and levels of abstract thinking :). I will also remember many nights of laughter and fun playing games with my friends.

In particular I want to thank Antje, Josie, Nadin and Levke, for being with me from the start, enduring all of my strange traits and preferences, encouraging me and being not discouraged by my overall very positive attitude about the present and the future. But I still feel a bit annoyed by the fact that it had to be me that was showered in coffee in the train after our very first lecture :). But still thanks for your

compassion! Without you the past 10 years would not have been that amazing for me! I wish I could share my joy and happiness with you.

This level of mutual support was not only present during my university years. I am very thankful that I have an amazing group of friends also from my school years. I want to thank all of you for all those years, for keeping the contact with me even when the distance is far and for being the first people believing in me when I wanted to study physics and reach Australia. So thank you Aishe, Ellie, Tifte, Jojo and Isa!

There are also many people that I have met during my life, that touched my heart and inspired me, both emotionally and rationally, mostly without realising the impact or without even knowing me personally.

Thank you!

Last but not least I want to thank my parents for supporting me and accepting me for who I am.

## Declaration of Authorship

I hereby declare that the thesis was written independently and without assistance except where otherwise indicated. Third parties other than the referenced sources and aids were not used.

This thesis was not previously presented to another examination board or audit authority and has not been published.

.....

Lisa Willig

Potsdam, June 17, 2019